Experimental and Numerical Modeling of Surf Zone Hydrodynamics

by

Daniel T. Cox, Nobuhisa Kobayashi
and Akio Okayasu

RESEARCH REPORT NO. CACR-95-07
June, 1995

Center for Applied Coastal Research
Ocean Engineering Laboratory
University of Delaware
Newark, DE 19716

ACKNOWLEDGMENTS

This work was sponsored by the U.S. Army Research Office, University Research Initiative under contract No. DAAL03-92-G-0116 and by the National Science Foundation under grant No. CTS-9407827. Dr. Okayasu was supported by the Foundation of International Exchanges, Yokohama National University, during his stay at the University of Delaware.

This work was originally submitted by Daniel T. Cox in the Spring of 1995 as a dissertation to the Faculty of the University of Delaware in partial fulfillment of the requirements for the degree of Doctor of Philosophy in Civil Engineering.

TABLE OF CONTENTS

LIST OF FIGURES

LIST OF TABLES

ABSTRACT

Detailed laboratory measurements were made of the free surface elevations and velocities for the case of regular waves spilling on a 1:35 impermeable slope. The velocity profiles were measured at several vertical lines in the cross-shore direction to include the shoaling region seaward of breaking, the break point, the transition region, and the inner surf zone. Each vertical line included measuring points at a fraction of the grain height above the rough, fixed bottom. A logarithmic layer was found to exist in the bottom boundary layer for most of the phases over a wave period seaward of the break point and in the surf zone. A regression analysis was used at each phase to estimate the shear velocity and bottom roughness from the phase-averaged horizontal velocities in the lower portion of the bottom boundary layer. The bottom friction factor was estimated from a quadratic friction equation based on the estimated shear velocity and measured horizontal velocity above the bottom boundary layer. The quadratic friction equation with the fitted friction factor was shown to predict the temporal variation of the bottom shear stress within a factor of two. The bottom roughness estimated from the grain size assuming rough turbulent flow was shown to agree qualitatively with the measured values. The cross-shore variation of the friction factor estimated from a semi-theoretical formula developed for non-breaking waves was shown to agree within a factor of two of the measured values.

The data were used to investigate the processes of wave generated turbulence. An order of magnitude analysis of the turbulent kinetic energy transport

equation indicated an approximate local equilibrium of turbulence for shallow water waves in the surf zone. Estimates were found for common surf zone turbulence parameters. The calibrated values were used to show that the eddy viscosity varies gradually over depth and is nearly time-invariant and that the local equilibrium of turbulence is a reasonable approximation for spilling waves in the inner surf zone.

The data were also used to evaluate the capabilities and limitations of a time-dependent, one-dimensional numerical model. The model predicted the cross-shore variation of the wave profile reasonably well. The computed depth-averaged horizontal velocity represented the vertical profile of the measured horizontal velocity below the wave trough level reasonably well except in the transition region. The computed vertical velocity estimated from the continuity equation represented the measured vertical velocity at least qualitatively except under the wave crest. The temporal variation of the bottom shear stress was predicted poorly, because errors in the computed horizontal velocity were magnified in the computed bottom shear stress and because the friction factor is not really constant as assumed in the model.

Chapter 1

INTRODUCTION

More than half of the population of the United States lives within 50 miles of the coastlines (Holman *et al.* 1990). The coastal regions are especially important for our quality of life. Most of the American coastline is suffering from erosion (Holman *et al.* 1990) and will continue to erode with the increasing rise in sea level.

A goal of coastal research is to develop numerical models for predicting sediment transport. A primary simplification is to consider either along-shore or cross-shore coastal evolution. Cross-shore beach profile models are appropriate over time scales of hours to days, typical of the duration of storms. Hedegaard, *et al.* (1992) presented six cross-shore coastal models, most of which rely on the time-averaged momentum and energy equations for predicting the wave height and setup (Battjes and Janssen 1978). The comparisons of these models with large scale laboratory data indicated the deficiencies of these models with respect to the low frequency and swash motions. The study also indicated the importance of the vertical velocities near the break point for the bar formation.

An advance towards predictive sediment transport modeling would be to develop a time-dependent numerical model for the surf and swash zone which could predict the temporal variations of the fluid velocities, shear stress and turbulent

intensity. These predicted hydrodynamics could then be used to drive a sediment transport model. The numerical model would require the implementation of a turbulence model for the surf zone and proper specification of the conditions at the bottom boundary layer. However, our understanding of wave breaking and bottom boundary layer processes is limited (Holman *et al.* 1990). In particular, few studies have been made of the bottom boundary layer inside the surf zone. For this dissertation, an experiment was conducted in a laboratory flume to determine proper length and velocity scales for the turbulent flow in a surf zone and to estimate the temporal variation of the bottom shear stress under breaking waves. It is within the context of the development of a two-dimensional cross-shore, time-dependent numerical model that the results from this experiment are presented.

1.1 Literature Review

Several reviews have been made of coastal hydrodynamics and sediment transport processes. Peregrine (1983) gave a qualitative review of the dynamics of wave breaking. The review focused on the transition of the organized motion to a turbulent bore, relying on visualization techniques, observations of surf zone waves and numerical simulations. Battjes (1988) reviewed the modeling of several kinds of fluid motions in the surf zone. The review focused on short-term, time-averaged fluid dynamics, but excluded sediment transport processes and morphological evolution. The review of Kobayashi (1988) focused on the cross-shore hydrodynamics of incident wind waves and low frequency motions as well as the cross-shore sediment transport and resulting beach profile evolution. Horikawa (1981) and Komar and Holman (1986) reviewed coastal sediment processes. Although our understanding of nearshore hydrodynamics and coastal processes has improved over the last several decades, all of the above reviews indicated that our understanding of the interactions of the fluid motions and coastal morphology is

far from complete.

Field measurements of wave generated turbulence are limited. Thornton (1979) measured the fluid motions under a variety of wave types. The turbulent component was extracted by correlating the velocity records with the free surface measurements. With this method, he found little difference among the wave types with respect to the turbulent intensity as a percent of the wave induced velocity. Flick and George (1990) measured fluid motions of surf zone waves on a natural beach using hot film anemometers. The turbulence intensity was estimated using Taylor's hypothesis of frozen turbulence. They concluded that the length scale of surf zone turbulence is on the order of the bore height, or equivalently, the local depth. The resolution of the measurements was not sufficient to indicate whether the velocity scales were dependent on the local shallow water wave speed. George *et al.* (1994) increased the spatial resolution of the previous study and in their analysis suggested a velocity scaling based on a bore dissipation model (Thornton and Guza 1983). Both papers cited the difficulty of using hot film probes due to breakage under harsh field conditions. It is also important to note the inherent difficulty in extracting the turbulent signal, in particular, for random, multi-directional waves.

In addition to the use of hot film anemometry, considerable progress has been made with laboratory measurements of fluid motions with improved techniques such as laser Doppler velocimetry (LDV) (e.g., Adrian 1983) and particle image velocimetry (PIV) (e.g., Adrian 1991). Flick *et al.* (1981) measured fluid motions of spilling and plunging waves in a laboratory flume using hot film anemometers. They reported on the intensity of the turbulence due to wave breaking with respect to the organized wave motion. Also, they noted the difference in the turbulence intensity between plunging and spilling breakers in the transition

zone, that is, from the break point to the quasi-steady bore region of the inner surf zone (Svendsen *et al.* 1978). Stive (1980) studied the internal velocity fields of spilling and plunging breakers using laser Doppler velocimetry. The results qualitatively supported the turbulent mixing layer model of Peregrine and Svendsen (1978). Battjes and Sakai (1981) presented the velocity field in a spilling breaker generated by a steady current over a submerged hydrofoil. The flow field behind the breaker was compared to a turbulent wake. Nadaoka and Kondoh (1982), Nadaoka *et al.* (1989), and Okayasu *et al.* (1986) have also shown the structure of the turbulent flow field under breaking waves in the surf zone. Hattori and Aono (1985) studied the turbulent structure of a spilling wave using a split-type hot film velocimeter to measure the horizontal and vertical velocities simultaneously. The break point was stabilized by a composite slope, where the broken wave propagated onto a flat section of beach.

Sakai *et al.* (1982) presented the distribution of turbulence for spilling waves and (nearly) plunging waves. They indicated that as the wave type changed from spilling to plunging, the offshore turbulent intensity would decrease relative to the onshore turbulent intensity. Ting and Kirby (1994) measured the fluid motions under spilling and plunging breakers. They indicated a seaward correlation between the mean flow and turbulence for a spilling breaker and a landward correlation for a plunging breaker. They suggested that the change in beach profile for storm waves (typically spilling breakers) and swell waves (typically plunging breakers) could result from the different correlations of the mean flow and turbulence of these waves. Nadaoka *et al.* (1988) discussed the existence of obliquely descending eddies. They suggested that these highly turbulent, intermittent eddies may hit the bottom and induce sediment suspension. Using flow visualization, Sakai *et al.* (1986) also showed an obliquely descending eddy and discussed the vortex formation in a plunging breaker. Sakai *et al.* (1984) and Okayasu *et al.*

(1988) have shown the distribution of the time-averaged Reynolds stress in the surf zone. Recently, Lin and Rockwell (1994) used PIV techniques to show the instantaneous structure of a spilling wave formed by a uniform current over a submerged hydrofoil.

It is important to note the difficulty in separating the turbulent and wave-induced velocities. In the field, waves are inherently random and multi-directional which precludes the use of ensemble averaging. Methods based on Taylor's hypothesis applied to oscillatory flow (e.g., George *et al.* 1994; Flick and George 1992) are subject to the selective rejection of data during flow reversal which may bias the results (George *et al.* 1994). Defining the turbulent signal as those which are incoherent with the free surface oscillation (e.g., Thornton 1979; Hattori and Aono 1985) may bias the results since large eddies may affect the free surface profile (Nadaoka *et al.* 1989). Frequency filters (e.g., Nadaoka and Kondoh 1982) are limited since there is no clear cutoff between the organized wave motion and the turbulent intensity, that is, the frequency of the wave motion is on the same order of turbulent intensity of the large-scale vortices. Moving averages (e.g., Battjes and Sakai 1981; Sakai *et al.* 1982) are essentially limited for the same reason, and the results are subject to the choice of the averaging interval. Ensemble-averaging or phase-averaging is a less subjective technique; however, it includes irregular breaking of monochromatic waves as turbulence and smears the effects of large vortices in the turbulent signal. Although considered the best defined way to separate the organized and turbulent motions (Svendsen 1987), the phase-averaging technique can not be extended to field measurements of random, multi-directional waves.

In contrast to the turbulence due to breaking waves in the surf zone, more studies on bottom boundary layer flows due to currents and non-breaking waves

have been made in the field and laboratory, and theories to describe these flows have been applied more successfully. Grant *et al.* (1983) and Grant *et al.* (1984) presented near bottom velocity measurements for wind driven currents and wind wave oscillations over the Northern California continental shelf. They estimated the mean bottom shear stress and bottom roughness by a logarithmic fit of the current velocities measured near the bottom. They indicated the importance of the wave-current interactions in determining the mean bottom shear stress and roughness felt by the current outside the bottom boundary layer. Similarly, Huntley and Hazen (1988) measured near bottom velocities on the Nova Scotia continental shelf and confirmed the importance of the wave-current interactions in determining the mean bottom shear stress. Madsen *et al.* (1993) measured the near bottom velocities on the North Carolina inner shelf during an extreme storm event and estimated the bottom shear stress, bottom roughness, and equivalent Nikuradse sand grain roughness. The importance of bottom shear stress estimates for sediment transport modeling can be seen, for example, in Hanes and Bowen (1985) and Trowbridge and Young (1989).

Grant and Madsen (1986) reviewed the present understanding of the bottom boundary layer for wind-driven flow over the continental shelf. In their review, they discussed separately the wave bottom boundary layer and the wave-current bottom boundary layer. For purely sinusoidal flow, Jonsson (1966) related the maximum horizontal fluid velocity outside the bottom boundary layer to the maximum bottom shear stress through a semi-empirical wave friction factor. In his formulation, he neglected the phase shift between the shear stress and the velocity outside the boundary layer. Kamphius (1975) determined an empirical wave friction factor diagram with a number of tests measuring the bottom shear stress directly in an oscillating water tunnel. Trowbridge and Madsen (1984a) used a time-dependent eddy viscosity to model the wave friction factor, and their results

agreed well with the measurements of Jonsson and Carlsen (1976). Trowbridge and Madsen (1984b) showed the importance of a time-varying eddy viscosity for time-averaged second-order phenomena such as mass transport. Recently, Madsen (1994) developed a spectral model for combined wave and current flows in the bottom boundary layer.

Laboratory measurements of the near bottom velocities have been made for several flow conditions. Jonsson and Carlsen (1976) measured the near bottom velocity in an oscillating water tunnel using a micro-propeller. The bottom shear stress was estimated by a logarithmic fit of the velocities measured in the bottom boundary layer. The bottom roughness, wave friction factor and boundary layer thickness were also estimated. Bakker and van Doorn (1978) measured the near bottom velocity using laser-Doppler velocimetry in a wave flume with a current superimposed. Roughness elements were added to obtain a turbulent boundary layer at the bottom. Sleath (1987) measured the near bottom velocities in an oscillating water tunnel for several rough bed conditions. The friction factor was estimated by integration of the velocity deficit in the bottom boundary layer. The bottom roughness was estimated from the grain size. Jensen *et al.* (1989) measured the turbulent boundary layer flow in an oscillatory water tunnel for smooth and rough bottoms at large Reynolds numbers. In the smooth bed case, the bottom shear stress was measured directly using a flush mounted hot film probe. For the rough bed cases, the bottom shear stress was estimated by a logarithmic fit of the bottom velocities. Klopman (1994) made detailed measurements of the velocity profiles under combined wave-current motion. Simons *et al.* (1992) measured the bottom shear stress directly for the case of waves and currents crossing at right angles. Simons *et al.* (1994) made similar measurements using random waves. In all cases of the works cited above, the waves were non-breaking. Diegaard *et al.* (1992) presented measurements of the temporal variation of the bottom shear

stress measured directly by a hot film probe on a smooth bed under non-breaking and breaking waves.

1.2 Outline of Dissertation

The dissertation is organized as follows. Chapter 2 discusses the formulation of the two-dimensional, time-dependent numerical model for predicting the wave transformation and velocity profiles in the surf zone. The formulation includes an analysis of the turbulent kinetic energy transport equation and the implementation of a simple turbulence model based on the mixing length concept. Development of the numerical solution of the two-dimensional model is beyond the scope of this dissertation.

Chapter 3 discusses the experimental setup and procedures. The design of the experiment includes a bottom roughness provided by natural sand grains to increase the thickness of the bottom boundary layer. For the first time, velocity measurements are made at a fraction of the grain height above the bottom so that estimates can be made of the temporal variation of the bottom shear stress and bottom roughness under breaking waves. Additional velocity measurements are made in the bottom boundary layer at locations offset by a small horizontal distance from each measuring line to check the variability of the measurements due to irregularities of the bottom and to check the reliability of the method to estimate the bottom shear stress and bottom roughness. Only one set of spilling breakers are used for this experiment; and although the importance of plunging versus spilling breakers has been noted in the literature, it is not of primary interest here. The extent of a vertical measuring line is from inside the bottom boundary layer to just above trough level. Measurements from trough level to wave crest with the aerated roller region are not possible at present.

Chapter 4 discusses the reduction of the data. Regular waves are used so that the turbulent signal can be extracted by phase-averaging. The usefulness of other methods such as frequency filters, running averages, correlation methods, and methods based on the frozen turbulence assumption are inferred from the literature. A rigorous comparison of these methods would require data sets which include several types of wave breaking, monochromatic and random waves with normal incidence, and multi-directional waves. This chapter presents the temporal variation of the phase-averaged free surface elevations and statistics and the phase-averaged velocities and turbulent stresses. The higher order statistics of skewness and kurtosis are discussed briefly in connection with a conditional sampling technique to analyze large eddies.

Chapter 5 discusses the bottom boundary layer analysis and the estimates of the bottom shear stress and bottom roughness. The logarithmic profile is shown to exist for the bottom boundary layers seaward of breaking and inside the surf zone. The bottom shear velocity and bottom roughness are estimated using a logarithmic fit of the measuring points in the bottom portion of the boundary layer. The estimates of the bottom shear velocity are used to evaluate the extension of simple theories developed for non-breaking waves in predicting the temporal and spatial variations of the bottom shear stress and bottom roughness under breaking waves.

Chapter 6 discusses the wave generated turbulence in relation to the assumption of a local equilibrium of turbulence for wave breaking. This assumption of the local production of turbulence being equal to the local dissipation is often applied to simple surf zone models. The relations between the eddy viscosity, the turbulence scales, the turbulent kinematic energy, the shear stress, and the vertical gradient of the horizontal velocity are discussed. Two empirical coefficients

are introduced, and the temporal and spatial variations of these coefficients are determined. The validity of the local equilibrium assumption is evaluated using the calibrated coefficients for the present data.

In Chapter 7, the governing equations of Chapter 2 are further simplified by integrating over depth (Kobayashi *et al.* 1987) to yield a one-dimensional, time-dependent model for which a numerical solution has been developed (Kobayashi and Wurjanto 1992; Kobayashi and Poff 1994). Comparisons are made between the data and the numerical model, and an evaluation is made of the model's sensitivity to three input specifications. The three input specifications of interest are the empirical friction factor, the location of the seaward boundary of the model, and the specification of the input time series at the seaward boundary. The ability of the model to predict the measured velocity profile is discussed. The vertical velocity profile estimated using the continuity equation together with the computed depth-averaged velocity is compared to the data. The limitations of the numerical model in predicting the temporal variation of the bottom shear stress is discussed.

Chapter 8 summarizes the dissertation and discusses the applicability of the results. The chapter concludes with suggestions on further extensions of this work.

The results of Chapter 6 appear in Cox *et al.* (1994b), and the results of Chapter 5 and Chapter 7 appear in Cox *et al.* (1994c).

Chapter 2

VERTICALLY TWO-DIMENSIONAL MODEL IN SHALLOW WATER

Numerical modeling of the fluid flow in the nearshore region is complicated by the turbulence associated with wave breaking. Simulations by direct solution of the Navier-Stokes equations have been made for breaking waves in two dimensions (e.g., Sakai *et al.* 1986; Petit *et al.* 1994), but these models are limited by computational intensity to only a few waves. Schäffer *et al.* (1992) introduced the concept of surface rollers to a two-dimensional Boussinesq model and obtained reasonable agreement in predicting the free surface elevations in the surf zone. However, their semi-empirical model is based on potential flow theory and will not predict the turbulent flow field outside the roller region. Recently, Wei *et al.* (1995) adopted an eddy viscosity concept to a time-dependent Boussinesq model and found reasonable agreement for the free surface elevations of random waves measured in a laboratory flume. Alternatively, a numerical model based on the two-dimensional continuity and Reynolds equations is proposed in the following.

2.1 Continuity and Reynolds Equations

A two-dimensional, time-dependent model is formulated here to solve the free surface elevations and velocity profiles in the surf zone. The two dimensions are in the cross-shore plane. The two-dimensional continuity and Reynolds

equations are given as (e.g., Tennekes and Lumley 1972)

$$\frac{\partial u_j}{\partial x_j} = 0 \tag{2.1}$$

$$\frac{\partial u_i}{\partial t} + u_j \frac{\partial u_i}{\partial x_j} = -\frac{1}{\rho}\frac{\partial p}{\partial x_i} - g\delta_{i2} + \frac{1}{\rho}\frac{\partial \tau_{ij}}{\partial x_j} \tag{2.2}$$

where use is made of the repeated indices, $i = 1, 2$; t is time; x_1 is the onshore directed horizontal coordinate; x_2 is the vertical coordinate, positive upward with $x_2 = 0$ at the still water level (SWL); u_1 is the horizontal velocity; u_2 is the vertical velocity; ρ is the fluid density, assumed constant; p is the pressure; g is the gravitational acceleration; δ_{i2} is the Kronecker delta; and τ_{ij} is the sum of turbulent and viscous stresses. The viscous stresses are neglected in the following. Reynolds averaging has been used for the turbulent stresses in Eq 2.2, and it is noted that that the time scale of the turbulent motion in the surf zone may be of the same order as the wave motion. The lack of a clear cut-off is discussed in Chapter 4 with respect to the method used to separate the turbulence from the wave motion.

The turbulent shear stresses, τ_{ij}, may be expressed as (e.g., Rodi 1980)

$$\tau_{ij} = \rho\left[\nu_t\left(\frac{\partial u_i}{\partial x_j} + \frac{\partial u_j}{\partial x_i}\right) - \frac{2}{3}k\delta_{ij}\right] \tag{2.3}$$

in which ν_t is the turbulent eddy viscosity; and k is the turbulent kinetic energy per unit mass given by

$$k = -\frac{1}{2\rho}(\tau_{11} + \tau_{22} + \tau_{33}) \tag{2.4}$$

For an idealized two-dimensional turbulent flow, $\partial u_3/\partial x_3 = 0$ so that Eq 2.3 yields

$$\tau_{13} = \tau_{31} = 0 \;\; ; \;\; \tau_{23} = \tau_{32} = 0 \;\; ; \;\; \tau_{33} = -\frac{2}{3}\rho k \tag{2.5}$$

where x_3 is the horizontal coordinate normal to x_1. Eq 2.4 reduces to

$$k = -\frac{3}{4\rho}(\tau_{11} + \tau_{22}). \tag{2.6}$$

2.2 Turbulence Model

The turbulence model is introduced here, and details are presented in Chapter 6. The transport equation of the turbulent kinetic energy, k, is normally written as (e.g., ASCE 1988)

$$\frac{\partial k}{\partial t} + u_j \frac{\partial k}{\partial x_j} = \nu_t \left(\frac{\partial u_i}{\partial x_j} + \frac{\partial u_j}{\partial x_i} \right) \frac{\partial u_i}{\partial x_j} + \frac{\partial}{\partial x_j} \left(\frac{\nu_t}{\sigma_k} \frac{\partial k}{\partial x_j} \right) - C_d^{3/4} \frac{(k)^{3/2}}{\ell} \tag{2.7}$$

where σ_k is an empirical constant associated with the diffusion of k. The turbulent eddy viscosity, ν_t, may be expressed as

$$\nu_t = C_d^{1/4} \ell \sqrt{k} \tag{2.8}$$

in which ℓ is the turbulent mixing length, and C_d is an empirical coefficient. Typical values of C_d and σ_k for *steady* turbulent flow are $C_d \simeq 0.08$ and $\sigma_k \simeq 1.0$ (Launder and Spalding 1972). The value of C_d is determined in Chapter 6 for the unsteady motion of non-breaking and breaking waves under the assumption of the approximate local equilibrium of turbulence.

The mixing length ℓ in Eq 2.8 may be specified simply as

$$\ell = \begin{cases} \kappa(x_2 - z_b) & \text{for } x_2 < \left(\overline{C_\ell} h/\kappa + z_b \right) \\ \\ \overline{C_\ell}\, h & \text{for } x_2 \geq \left(\overline{C_\ell} h/\kappa + z_b \right) \end{cases} \tag{2.9}$$

where κ is the Kármán constant ($\kappa \simeq 0.4$); z_b is the bottom elevation; h is the instantaneous water depth; and $\overline{C_\ell}$ is an empirical coefficient related to the eddy size. $\overline{C_\ell}$ is written with an overbar to show that it is time-invariant and to differentiate it from C_ℓ used later. The coefficient for the unsteady flow, C_ℓ, and the time-averaged value, $\overline{C_\ell}$, will also be determined in Chapter 6.

To simplify Eqs 2.1 and 2.2 with Eqs 2.3, 2.8, 2.7, and 2.9, the dimensionless variables are introduced following Kobayashi and Wurjanto (1992):

$$t' = \frac{t}{T_r};\quad x_1' = \frac{x_1}{T_r\sqrt{gH_r}};\quad x_2' = \frac{x_2}{H_r};\quad u_1' = \frac{u_1}{\sqrt{gH_r}};\quad u_2' = \frac{u_2}{H_r/T_r} \tag{2.10}$$

$$p' = \frac{p}{\rho g H_r};\quad \nu_t' = \frac{\nu_t}{{H_r}^2/T_r};\quad k' = \frac{k}{gH_r/\sigma};\quad \ell' = \frac{\ell}{H_r/\sqrt{\sigma}};\quad \sigma = \frac{T_r\sqrt{gH_r}}{H_r} \tag{2.11}$$

where the primes indicate dimensionless quantities, T_r and H_r are the characteristic wave period and height of the shallow water waves, and σ is the ratio between the horizontal and vertical length scales. The order of magnitude of k, ℓ, and ν_t is estimated such that the normalized variables k', ℓ', and ν_t' are of $O(1)$ or less as shown in Chapter 6.

In the following, the standard notations of $x_1 = x$, $x_2 = z$, $u_1 = u$, and $u_2 = w$ are used. Substitution of Eqs 2.10 and 2.11 into Eqs 2.1 and 2.2 yields the normalized continuity equation and the momentum equations which are simplified assuming $\sigma^2 \gg 1$. The exact continuity equation is

$$\frac{\partial u'}{\partial x'} + \frac{\partial w'}{\partial z'} = 0. \tag{2.12}$$

The approximate horizontal momentum equation is expressed as

$$\frac{\partial u'}{\partial t'} + u\frac{\partial u'}{\partial x'} + w'\frac{\partial u'}{\partial z'} = -\frac{\partial}{\partial x'}\left(p' + \frac{2k'}{3\sigma}\right) + \frac{\partial \tau'}{\partial z'} \tag{2.13}$$

with

$$\tau' = \nu_t'\frac{\partial u'}{\partial z'} \tag{2.14}$$

and

$$\nu_t' = C_d^{1/4}\ell'\sqrt{k'} \tag{2.15}$$

where τ' is the normalized shear stress. The approximate vertical momentum equation is given as

$$0 = -\frac{\partial}{\partial z'}\left(p' + z' + \frac{2k'}{3\sigma}\right). \tag{2.16}$$

The normalized free surface is located at $z' = \eta'$ where $\eta' = \eta/H_r$, and the kinematic free surface boundary condition is given as

$$\frac{\partial \eta'}{\partial t'} + u' \frac{\partial \eta'}{\partial x'} - w' = 0 \quad \text{at } z' = \eta'. \tag{2.17}$$

The conditions of zero normal and tangential stresses at the free surface for $\sigma^2 >> 1$ can be shown to be

$$p' + \frac{2k'}{3\sigma} = 0 \quad \text{at } z' = \eta' \tag{2.18}$$

$$\tau' = \nu_t' \frac{\partial u'}{\partial z'} = 0 \quad \text{at } z' = \eta'. \tag{2.19}$$

The kinematic bottom boundary condition is specified as

$$w' = u' \frac{\partial z_b'}{\partial x'} \quad \text{at } z' = z_b', \tag{2.20}$$

and the no-slip bottom boundary condition is specified as

$$u' = 0 \quad \text{at } z' = z_b' \tag{2.21}$$

It is noted that use of Eq 2.21 reduces Eq 2.20 to

$$w' = 0 \quad \text{at } z' = z_b'. \tag{2.22}$$

Integration of Eq 2.16 with respect to z' and applying the boundary condition Eq 2.18 yields the pressure p' in the form

$$p' = \eta' - z' - \frac{2k'}{3\sigma}. \tag{2.23}$$

Substituting Eq 2.23 into Eq 2.13 simplifies the x'-momentum equation to

$$\frac{\partial u'}{\partial t'} + u' \frac{\partial u'}{\partial x'} + w' \frac{\partial u'}{\partial z'} = -\frac{\partial \eta'}{\partial x'} + \frac{\partial \tau'}{\partial z'}. \tag{2.24}$$

For the turbulent kinetic energy transport equation, substituting Eqs 2.10 and 2.11 into Eq 2.7 under the assumption of $\sigma^2 \gg 1$ gives

$$\sigma^{-1} \left(\frac{\partial k'}{\partial t'} + u' \frac{\partial k'}{\partial x'} + w' \frac{\partial k'}{\partial z'} \right) = \tau' \frac{\partial u'}{\partial z'} + \sigma^{-1} \frac{\partial}{\partial z'} \left(\frac{\nu_t'}{\sigma_k} \frac{\partial k'}{\partial z'} \right) - C_d^{3/4} \frac{k'^{3/2}}{\ell'} \tag{2.25}$$

where the first and third terms on the right-hand-side are the production and dissipation terms, respectively. Eq 2.25 indicates that the production and dissipation of k' are dominant under the assumption of $\sigma^2 \gg 1$.

Considering the empirical nature of Eq 2.25 with the coefficients σ_k and C_d as well as the uncertainty of the free surface boundary condition of k' even for steady turbulent flow (Rodi 1980), Eq 2.25 may be simplified further by neglecting the terms of the order σ^{-1}, and the resulting equation is expressed in dimensional form as

$$\frac{\tau}{\rho}\frac{\partial u}{\partial z} \simeq C_d^{3/4}\frac{k^{3/2}}{\ell} \tag{2.26}$$

which implies the local equilibrium of turbulence. Substitution of $\tau/\rho = \nu_t \partial u/\partial z$ and Eq 2.8 into Eq 2.26 yields

$$k = \frac{|\tau|}{(\rho\sqrt{C_d})} \tag{2.27}$$

and

$$\nu_t = \ell^2 \left|\frac{\partial u}{\partial z}\right|. \tag{2.28}$$

In Chapter 6, Eq 2.27 is used with these assumptions to determine the appropriate value of C_d. Eq 2.28 corresponds to the standard mixing length model (ASCE 1988) and is used with Eq 2.8 to determine C_ℓ and $\overline{C_\ell}$ in Eq 2.9. The degree of the local equilibrium of turbulence is assessed using Eq 2.26 with the calibrated coefficients C_d and $\overline{C_\ell}$. The one-dimensional model derived by integrating Eqs 2.12 and 2.24 from the bottom to the free surface is summarized in Chapter 7, and comparisons are made with the data. The following chapter discusses the experimental setup and procedure.

Chapter 3

LABORATORY EXPERIMENT

Previous experimental studies of the turbulence due to wave breaking (e.g., Stive 1980; Okayasu *et al.* 1986; Nadaoka *et al.* 1989) and of the bottom boundary layer under oscillatory flow conditions (e.g., Jonsson and Carlsen 1976; Jensen *et al.* 1989) were cited in Chapter 1. It was also mentioned that with the exception of Deigaard *et al.* (1992), there are no measurements of the bottom shear stress under breaking waves. In this chapter, the experimental setup and procedure to measure the detailed structure of the bottom boundary layer under breaking waves is presented. This experiment is also described in Okayasu and Cox (1995).

3.1 Experimental Apparatus

This section is divided into subsections to discuss separately the experimental apparatus, including the wave flume, the physical bottom roughness, the wave gages, the laser-Doppler velocimeter, and the data acquisition system.

3.1.1 Wave Flume

The experiment was conducted in August and September, 1993, in the Precision Wave Tank located in the Ocean Engineering Laboratory at the University of Delaware. The flume was 33 m long, 0.6 m wide and 1.5 m deep. The side walls

were glass for the length of the flume except near the wavemaker. The horizontal bottom section and the side walls near the wavemaker were constructed of marine plywood. The impermeable 1:35 bottom slope was constructed of Corian™, a smooth material used commercially for kitchen countertops. A hydraulically actuated piston wavemaker with a 1 m stroke was located at the far end of the flume and was controlled by an IBM 286 PC. Several movable instrument carriages spanned the top of the flume on which wave gages and the laser-Doppler velocimeter lens were mounted. The flume was filled with tap water, and the water depth in the constant depth section was 0.4 m. The water temperature was 23° C.

3.1.2 Bottom Roughness

A physical bottom roughness was added to the impermeable 1:35 slope to increase the boundary layer roughness and boundary layer thickness. The bottom roughness was prepared using natural sand from Rehobeth Beach, Delaware. The sand was washed to remove any dirt and organic material, dried, and then sieved in the diameter range 0.71–1.41 mm. The sieved sands were remixed such that the median grain diameter was $d_{50} = 1.0$ mm. A thin layer of sand was glued onto Plexiglas™sheets using epoxy resin. After drying, loose or poorly adhered grains were removed with a wire brush. Each sheet was then inspected for large irregularities in the bottom roughness. The 1.2 m long by 0.6 m wide Plexiglas sheets were mounted over the entire Corian slope using a double-sided transfer tape, and the gaps between adjoining sheets were less than the median grain diameter.

Figure 3.1 is a photograph of the bottom roughness taken at a low magnification (×6) and shows the typical irregularities in the distribution of the sand

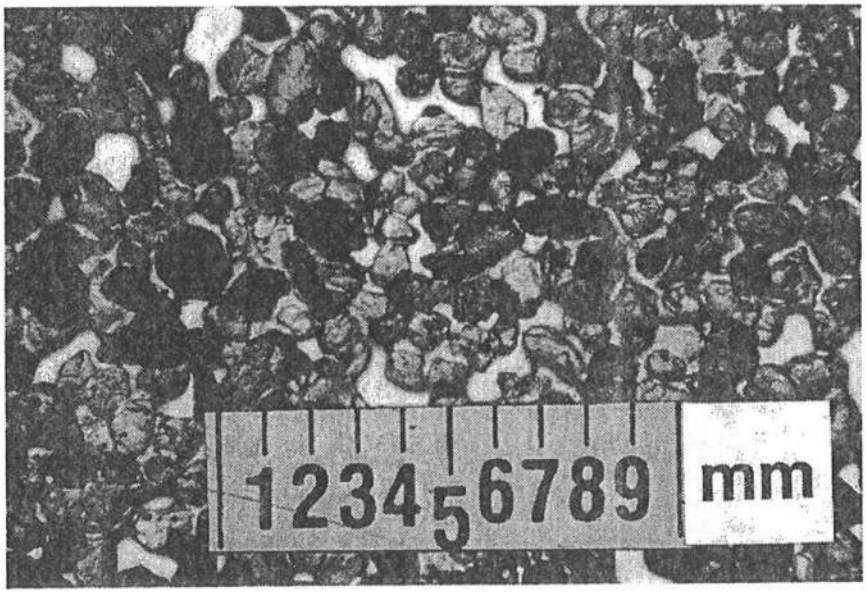

Figure 3.1: Photograph of Bottom Roughness at Low Magnification (courtesy of William Cox).

grains on the Plexiglas. The thickness of the physical roughness above the Plexiglas is essentially the height of one sand grain with median diameter $d_{50} = 1.0$ mm. Figure 3.2 is a photograph of the bottom roughness taken with a scanning electron microscope at a high magnification ($\times 20$) and shows the variation in the shapes of the individual grains.

3.1.3 Wave Gages

Six capacitance type wave gages were used simultaneously to measure the free surface elevations of both non-breaking and breaking waves. It is noted that, in principle, capacitance wave gages cannot be used to measure the free surface elevation of a turbulent bore due to aeration (Ting and Kirby 1994). However, the air content of the most densely entrained laboratory wave is approximately 2 to 4% (Stive 1980). For the spilling breakers in this experiment, the air content

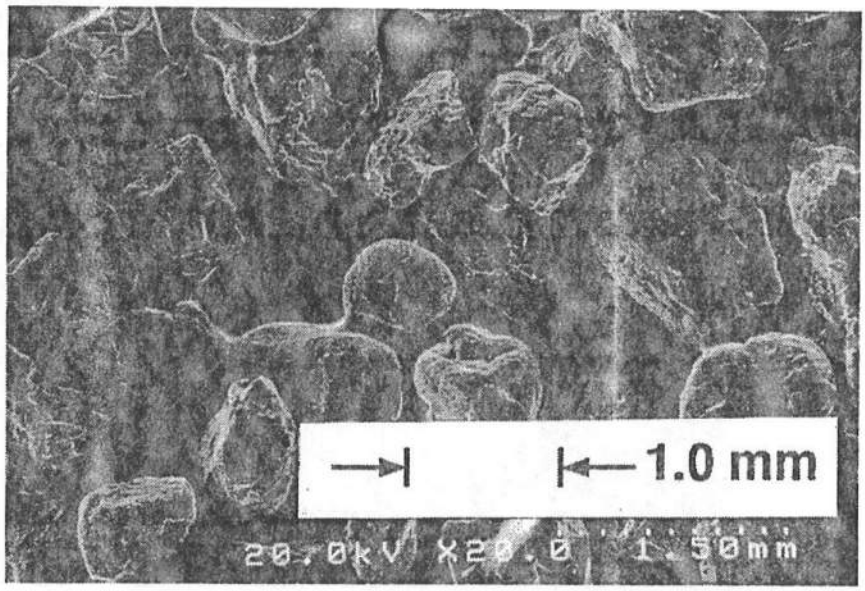

Figure 3.2: Photograph of Bottom Roughness at High Magnification (courtesy of William Cox).

was likely to be less. Therefore, the estimates of the free surface fluctuations for the breaking waves measured by the capacitance wave gages are sufficiently accurate for the requirements of this experiment. The gages were calibrated at the beginning and end of each day, and the gain in the calibration curves was linear for all gages with little offset due to voltage drift. The phase-averaged free surface elevation and standard deviation envelope presented in Chapter 4 will show that the repeatability of the wave form was excellent seaward of breaking.

3.1.4 Laser-Doppler Velocimeter

The velocities were measured in the cross-shore, x-z plane using laser-Doppler velocimetry (LDV) which is a well established technique for fluid measurements (e.g., Adrian 1983). A Dantec fiber-optic LDV was powered by a Lexel Model 95 argon-ion laser. The LDV was operated in backscatter mode with the

laser powered at 0.8 W, drawing a current of 18.5 A. A pair of Dantec Type 57N10 and Type 57N25 burst spectrum analyzers (BSAs) with Type 55N12 frequency shifters were used for processing the backscatter signal. This system was used to reduce the noise which is typical from measuring near a solid boundary. The operating mode was set such that when a particle passed through the measuring volume, both the arrival time and the velocities were recorded. Since the particle arrival time is irregular, the sampling intervals of the velocity time series were irregular. The conversion to a time series with a regular sampling interval is discussed in Section 3.3.3.

3.1.5 Data Acquisition

Two data acquisition systems were used with the synchronization provided by an external trigger. The wave gage signals were recorded on an IBM 386 PC with a MetraByte DAS-16F data acquisition board which was used with a sampling rate of 100 Hz. The velocity signals from the BSAs were recorded on a Zenith 486 PC running the BURSTware software (Dantec Electronik 1991). The effective sampling rate ranged between 1,400 and 1,700 samples per second. The data files were collected on the hard disk of the 486 PC and were later transferred by FTP/PC software to a Unix-based workstation for postprocessing.

3.2 Experimental Setup

This section discusses the experimental setup, including the cross-shore placement of the measuring lines, the measuring point locations for a given measuring line, and the positioning of the laser-Doppler optics.

3.2.1 Measuring Line Locations

Figure 3.3 shows a schematic setup of the experiment with the location of the six wave gages and the six measuring lines. Wave gages 1 to 3 were located near the wavemaker with a spacing of 0.7 m between gages 1 and 2 and a spacing of 0.3 m between gages 2 and 3. Wave gage 1 was about one wavelength from the wavemaker. Wave gage 6 was located in the surf zone at $x = 8.4$ m, where x is the horizontal coordinate shown in Figure 3.3. Gages 1 to 3 were used collectively for synchronization and, in a separate study, to analyze the reflection and long wave components in the flume. Wave gage 4 was located at measuring line 2, which was the start of wave breaking defined as the onset of aeration in the tip of the wave crest. Gages 4 and 6 were used to check the variability of breaking and broken waves in the flume. Wave gage 5 was located above the measuring volume of the laser-Doppler which is indicated in Figure 3.3 by the circle and cross-hair. When the measuring volume was at measuring line 2, wave gage 4 was moved to measuring line 1.

The two cross-shore components of velocity were measured along six vertical measuring lines which are denoted L1, L2, ..., L6 for brevity. The horizontal spacing of the measuring lines was on the order of 1 m, and their cross-shore position can be characterized as follows: L1 is seaward of breaking; L2 is at the break point, defined as the onset of aeration in the tip of the wave crest; L3 is in the

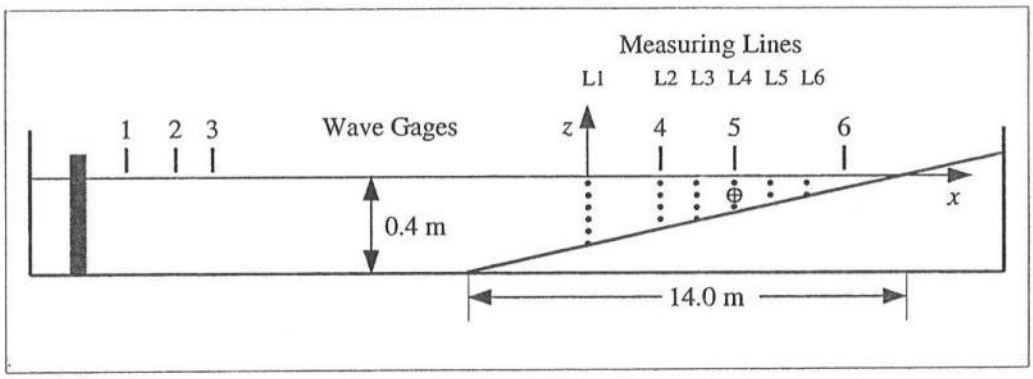

Figure 3.3: Experimental Setup.

transition region where the wave form goes from organized motion to a turbulent bore; and L4, L5, and L6 are in the inner surf zone where the saw-toothed wave shape is a well-developed turbulent bore. The horizontal locations and still water depths of the measuring lines are listed in Table 3.1 where x is the horizontal coordinate, positive onshore with $x = 0$ m at the first measuring line; and d is the depth below the still water level. The distance from L1 to the still water shore line is 9.8 m.

For each measuring line, there were approximately twenty measuring points between the rough bottom and the wave trough level. The vertical spacing of the measuring points was on the order of 1 cm except near the bottom where measurements were made on the order of a fraction of the grain height. For each of the measuring lines L1 to L5, eight additional measuring points were taken near the bottom. These points were offset 2 cm in the x-direction to check the estimates of the location of the theoretical bottom discussed in Chapter 5. The coordinates of the measuring points are given in Table 3.2 where the vertical coordinate from the bottom, z_m, is defined in Section 3.3.2 and discussed in detail in Chapter 5.

Table 3.1: Horizontal Locations and Still Water Depths for L1 to L6.

Line No.	x (cm)	d (cm)
L1	0	28.00
L2	240	21.14
L3	360	17.71
L4	480	14.29
L5	600	10.86
L6	720	7.43

Table 3.2: Measuring Point Coordinates with Respect to z_m for L1 to L6.

	z_m (cm)					
	L1 [0.0 m]	L2 [2.4 m]	L3 [3.6 m]	L4 [4.8 m]	L5 [6.0 m]	L6 [7.2 m]
1	0.13	0.13	0.13	0.13	0.13	0.13
2	0.15	0.15	0.15	0.15	0.15	0.15
3	0.17	0.17	0.17	0.17	0.17	0.17
4	0.20	0.20	0.20	0.20	0.20	0.20
5	0.25	0.25	0.25	0.25	0.25	0.25
6	0.30	0.30	0.30	0.30	0.30	0.30
7	0.40	0.40	0.40	0.40	0.40	0.40
8	0.60	0.60	0.60	0.60	0.60	0.60
9	0.80	0.80	0.80	0.80	0.80	0.80
10	1.10	1.10	1.10	1.10	1.10	1.10
11	1.60	1.60	1.60	1.60	1.60	1.60
12	2.10	2.10	2.10	2.10	2.10	2.10
13	3.10	3.10	3.10	3.10	3.10	3.10
14	4.10	4.10	4.10	4.10	4.10	4.10
15	6.10	6.10	6.10	6.10	5.10	5.10
16	8.10	8.10	8.10	8.10	6.10	6.10
17	12.10	12.10	10.10	10.10	7.10	7.10
18	16.10	16.10	12.10	12.10	8.10	8.10
19	20.10	18.10	14.10	13.10	9.10	—
20	24.10	20.10	16.10	14.10	10.10	—
21	26.10	22.10	17.10	15.10	11.10	—
22	28.10	24.10	18.10	—	12.10	—
23	0.13^-	0.13^-	0.13^-	0.13^-	0.13^-	—
24	0.15^-	0.15^-	0.15^-	0.15^-	0.15^-	—
25	0.17^-	0.17^-	0.17^-	0.17^-	0.17^-	—
26	0.20^-	0.20^-	0.20^-	0.20^-	0.20^-	—
27	0.13^+	0.13^+	0.25^-	0.13^+	0.13^+	—
28	0.15^+	0.15^+	0.30^-	0.15^+	0.15^+	—
29	0.17^+	0.17^+	0.60^-	0.17^+	0.17^+	—
30	0.20^+	0.20^+	1.00^-	0.20^+	0.20^+	—

Note: Horizontal measuring line location, x_m, given in brackets. For offset measuring line values with (−) superscript, $x_m^- = x_m - 2$ cm, and with (+) superscript, $x_m^+ = x_m + 2$ cm.

3.2.2 Positioning of Laser-Doppler Optics

The lens of the laser-Doppler velocimeter was rotated in the x-z and y-z planes so that the measuring volume could be positioned just above the bottom roughness. The lens was rotated 45° in the x-z plane as shown in Figure 3.4. This figure shows the velocity vector measured by the shifted and unshifted green beams, a_1, and the blue beams, a_2. The measured instantaneous horizontal and vertical velocities, u_m and w_m, are given by

$$u_m = \frac{1}{\sqrt{2}}(a_2 + a_1) \tag{3.1}$$

$$w_m = \frac{1}{\sqrt{2}}(a_2 - a_1) \tag{3.2}$$

Estimating the velocity based on this rotated coordinate system required that the a_1 and a_2 velocity time series have the same sampling interval. Converting from time series with irregularly sampled data to time series with a constant sampling interval is discussed in Section 3.3.3.

In measuring at a fraction of a grain height from the bottom, considerable care was taken to avoid interference of bottom grains with the path of the laser beams. In the experimental work of Klopman (1994), a slightly curved false bottom was installed in the flume so that the middle portion of the bottom roughness was approximately 2 mm higher than the sides. For the present experiment, the sheets of the bottom roughness were mounted flat on the existing impermeable slope. To avoid interference with the path of the laser, the lens had to be rotated in the y-z plane as shown in Figure 3.5. The angle of rotation was $\phi \simeq 3°$ where $\cos 3° = 0.9986$. No correction was made for the rotation and a systematic error of less that 1% was introduced.

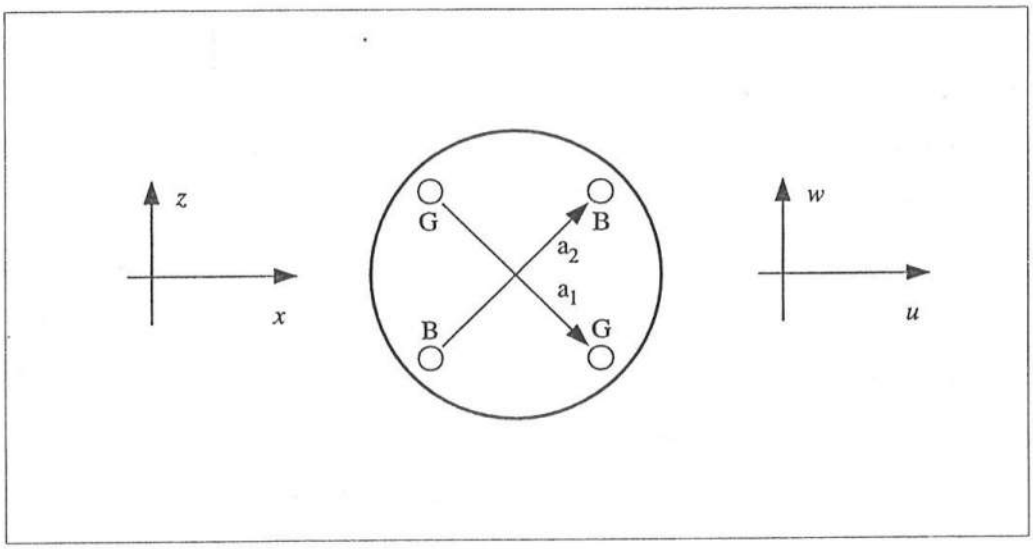

Figure 3.4: Lens Rotation in x-z Plane.

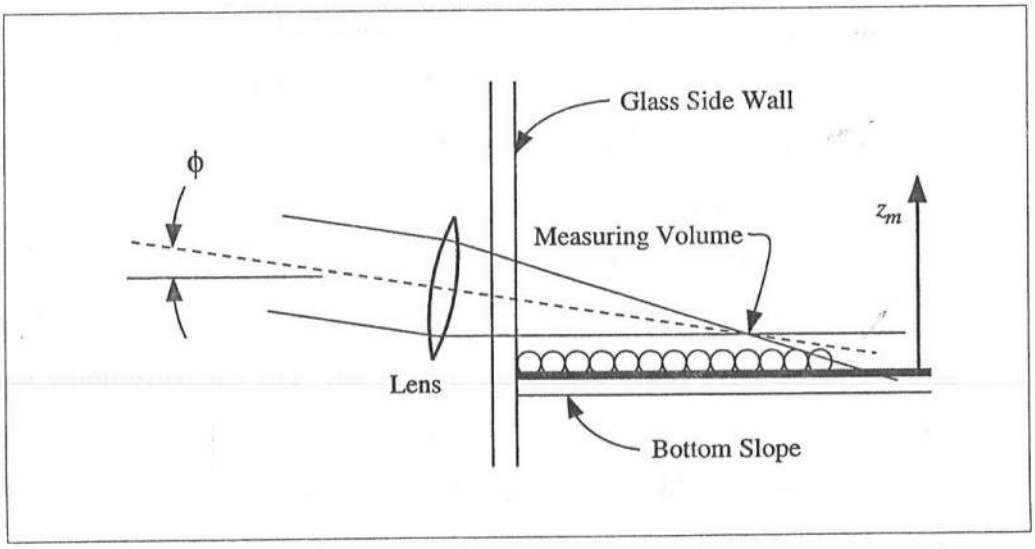

Figure 3.5: Lens Rotation in y-z Plane.

3.3 Procedure

The flow field was mapped by repositioning the measuring volume and repeating the waves. Before starting the measurements, waves were generated for approximately 30 minutes to eliminate transitional effects associated with the start of the wavemaker in still water. Monochromatic waves were generated and were characterized as spilling breakers. The wave period was 2.2 s, and the wave height was 17.10 cm at breaking. The free surface elevations at the six gages and the two velocity components at each measuring point were measured for 50 waves. Measurements proceeded from the bottom of the water column to the top, and the eight additional points near the bottom were taken at the end of the run.

3.3.1 Number of Waves

It was decided at the start of the experiment that the number of waves for each measuring point would be $N_w = 50$ waves. This number was chosen based on previous experience (Okayasu, personal communication) and is similar to other values in the literature for studies which used phase-averaging to separate the turbulent and wave induced velocities for waves breaking on plane slopes. Stive (1980) used a minimum of 20 waves, Nadaoka *et al.* (1989) used a minimum of 45 waves, and Okayasu *et al.* (1988) used 100 waves. Recently, Ting and Kirby (1994) used 102 waves and reported that the phase-averaged statistics of mean and variance were fairly stable for $N_w > 40$. For measurements of the bottom boundary layer in oscillating water tunnels, Jensen *et al.* (1988) used between 50 and 80 cycles, and Sleath (1987) used 200 cycles for a rough bottom with sand. Sleath (1987) reported no improvement in the statistics (presumably mean and variance) for the number of cycles greater than approximately 50.

3.3.2 Vertical Coordinates

Two vertical coordinated are used in this dissertation. The first coordinate is the z coordinate defined in Chapter 2 with $z = 0$ at the still water level. The second coordinate is z_m defined with respect to the bottom with $z_m = 0$ at the top of the Plexiglas sheet. During the experiment, the measuring volume of the laser-Doppler was lowered to the roughness layer until a signal could not be acquired due to partial obstruction of the laser beams. From this position, the measuring volume was raised 0.03 cm to take the first measurement, and the subsequent measurements were taken at 0.05, 0.07, 0.10 cm, etc. For the bottom boundary layer analysis in Chapter 5, it was convenient to have a positive displacement distance, and a constant value of 0.1 cm was added to the recorded elevations to give the measuring elevations 0.13, 0.15, 0.17, 0.2, etc. as they appear in Table 3.2. The choice of adding 0.1 cm was arbitrary and does not affect the calculations of the bottom roughness. However, the estimation of the displacement distance is not trivial; and this point is addressed in Chapter 5.

3.3.3 Resampling the Measured Velocities

Eqs 3.1 and 3.2 essentially required the velocity time series of a_1 and a_2 to be resampled with a constant sampling interval. Several methods were considered and are discussed in the following.

The first method considered is that used, for example, by the BURSTware software (Dantec Electronik 1991). The resampled velocity is simply the velocity corresponding to the measured velocity value immediately preceding the interval. This is analogous to using a frequency tracker. This method, however, does not use all of the measured values.

A second method is to fit a cubic spline through the data and compute the resampled velocity from the spline function. This method was considered since all the measured points would be used to compute the spline function. There are several cubic spline algorithms available: for example, the set of FORTRAN subroutines of the IMSL libraries (Visual Numerics 1991). Several IMSL subroutines were tested including CSIEZ, the basic cubic spline interpolant using the "not-a-knot" criterion; BSLSQ, combining a least-squares fit using splines with fixed knots; and BSVLS, combining a least-squares fit using splines with free knots. Both BSLSQ and BSVLS were tested with cubic and higher order splines. The idea for using a least-squares fit with splines is that it would weight heavier those intervals for which the number of measured velocities was greater. However, none of the cubic spline subroutines were reliable for the following reason. If a strict tolerance were set for the subroutine, the spline function would return an unrealistic spiked signal as it tried to fit the curve through densely sampled data. When the subroutine tolerance was set loose enough to avoid these spikes, then the spline function did not represent the higher frequency fluctuations in the measured signal, that is, the spline function appeared to smooth the data. As a result, the spline methods were abandoned in favor of the next method.

The resampling method adopted here is "bin-averaging." For this method, the time axis is divided into bins, and the resampled velocity is the average of all the measured velocities in that bin. If there are no measured data in that bin, the interval is considered to have a "signal dropout". This is analogous to the signal dropouts for frequency trackers. The choice of bin width is subjective, so several bin widths were used to check the sensitivity. One velocity time series was taken from a measuring point below trough level at L4 in the inner surf zone. The effective sampling of this time series was approximately 1,500 Hz. This time series was resampled four times with the sampling rates of 200 Hz, 100 Hz, 50 Hz

and 20 Hz. The spectra were computed for each resampled time series. Almost no difference could be detected in the energy levels below 10 Hz for the spectra corresponding to the 200 Hz, 100 Hz and 50 Hz sampling rates. The sampling rate of 100 Hz was selected since it corresponded to the sampling rate of the wave gage data and would facilitate the data analysis.

The free surface elevations and velocity time series were synchronized to the first zero-upcrossing of wave gage 1. The records were truncated to include 50 waves. The following chapter discusses the phase-averaging procedure to separate the turbulent and wave motions.

Chapter 4

PHASE-AVERAGED DATA

The difficulty in separating the turbulent and wave motions was noted in Chapter 1. The methods available to extract the turbulent signal include those based on Taylor's hypothesis of frozen turbulence (e.g., George *et al.* 1994), correlation with the free surface (e.g., Thornton 1979), frequency filters (e.g., Nadaoka and Kondoh 1982), moving averages (e.g., Battjes and Sakai 1981), and phase-averaging (e.g., Stive 1980). The phase-averaging method is adopted for this data set, and the method is explained in detail in this chapter.

This section is organized as follows. Section 4.1 presents the statistical moments of mean, variance, skewness and kurtosis, and other definitions. Definitions of the free surface and velocity statistics are presented separately since the velocity records contain signal dropouts which are not included in the calculations. Section 4.2 presents the phase-averaged free surface elevations and statistics. Section 4.3 presents the fluid velocities. Section 4.4 presents the turbulent stresses and dropout rates. Section 4.5 presents a comparison of the Froude-scaled, time-averaged horizontal turbulent intensity for the present data with data from the literature. Section 4.6 presents the skewness and kurtosis in connection with a conditional sampling technique for large eddies.

4.1 Statistical Moments

From Chapter 3, there are three time series of interest: $\eta_m(x,t)$, the measured free surface elevation at a given x sampled at a rate of $\Delta t = 0.01$ s; $u_m(x,z,t)$, the measured horizontal velocity at a given x and z averaged over the interval of $\Delta t = 0.01$ s; and $w_m(x,z,t)$, the measured vertical velocity at a given x and z averaged over the interval of $\Delta t = 0.01$ s. In the following, time is indicated by the discrete time level, t_{jn}, as

$$t_{jn} = t_j + (n-1)\,T \quad \text{for} \quad n = 1, 2, \ldots, N_w \tag{4.1}$$

with

$$t_j = (j-1)\Delta t \quad \text{for} \quad j = 1, 2, \ldots, J \tag{4.2}$$

where $T = 2.2$ s is the wave period, $N_w = 50$ is the number of waves, $\Delta t = 0.01$ s is the sampling interval, and $J = T/\Delta t = 220$ is the number of data points or phases per wave. The phase-averaged free surface elevation is indicated by the subscript a and is given as

$$\eta_a(x,t_j) = \frac{1}{N_w}\sum_{n=1}^{N_w} \eta_m(x,t_{jn}) \quad \text{for} \quad j = 1, 2, \ldots, J. \tag{4.3}$$

The variance of the free surface elevation, σ_η^2, is given as

$$\sigma_\eta^2(x,t_j) = \frac{1}{N_w - 1}\sum_{n=1}^{N_w} \left[\eta_m(x,t_{jn}) - \eta_a(x,t_j)\right]^2 \quad \text{for} \quad j = 1, 2, \ldots, J \tag{4.4}$$

and its square root, σ_η, is the standard deviation. It is noted that $(N_w - 1)$ is used for an unbiased estimate of the variance (e.g., Press *et al.* 1989).

The signal dropouts as defined in Chapter 3 are excluded in the phase-averaging of the measured horizontal and vertical velocities. The dropout rate, $R_N(x,z,t_j)$, expressed as a percent, is given as

$$R_N(x,z,t_j) = \left[1 - \frac{N_j(x,z,t_j)}{N_w}\right] \times 100 \tag{4.5}$$

where $N_j(x, z, t_j)$ is the number of data points of u_m and w_m excluding the signal dropout at a given phase and at a given (x, z) location. The criterion of $5 \leq N_j \leq 50$ at a given phase, t_j, was adopted. If there were fewer than 5 out of 50 velocity measurements at a given phase, the phase-averaged velocity was written as zero. For the data presented herein, the condition $N_j < 5$ occurred only after the passing of the wave crest when the measuring volume was out of the water. These zero recordings are included in the time averaging of quantities related to measured velocities for which the z-elevations were above trough level as explained later.

The phase-averaged horizontal and vertical velocities, u_a and w_a, are given as

$$u_a(x, z, t_j) = \frac{1}{N_j} \sum_{n=1}^{N_j} u_m(x, z, t_{jn}) \quad \text{for} \quad j = 1, 2, \ldots, J \tag{4.6}$$

$$w_a(x, z, t_j) = \frac{1}{N_j} \sum_{n=1}^{N_j} w_m(x, z, t_{jn}) \quad \text{for} \quad j = 1, 2, \ldots, J. \tag{4.7}$$

The horizontal and vertical velocity variances, σ_u^2 and σ_w^2, are given as

$$\sigma_u^2(x, z, t_j) = \frac{1}{N_j - 1} \sum_{n=1}^{N_j} [u_m(x, z, t_{jn}) - u_a(x, z, t_j)]^2 \quad \text{for} \quad j = 1, 2, \ldots, J \tag{4.8}$$

$$\sigma_w^2(x, z, t_j) = \frac{1}{N_j - 1} \sum_{n=1}^{N_j} [w_m(x, z, t_{jn}) - w_a(x, z, t_j)]^2 \quad \text{for} \quad j = 1, 2, \ldots, J. \tag{4.9}$$

The turbulent normal stresses may be assumed to be equal to $-\rho\sigma_u^2$ and $-\rho\sigma_w^2$ in the horizontal and vertical directions, where ρ is the fluid density. The phase-averaged covariance of the measured horizontal and vertical velocities, σ_{uw}, is given as

$$\sigma_{uw}(x, z, t_j) = \frac{1}{N_j - 1} \sum_{n=1}^{N_j} [u_m(x, z, t_{jn}) - u_a(x, z, t_j)] [w_m(x, z, t_{jn}) - w_a(x, z, t_j)] \quad \text{for} \quad j = 1, 2, \ldots, J. \tag{4.10}$$

The turbulent shear stress may be assumed to be equal to $-\rho\sigma_{uw}$. The correlation coefficient, γ_{uw}, is given as

$$\gamma_{uw}(x,z,t_j) = \frac{\sigma_{uw}(x,z,t_j)}{\sigma_u(x,z,t_j)\sigma_w(x,z,t_j)} \quad \text{for } j = 1,2,\ldots,J. \tag{4.11}$$

The correlation coefficient is dimensionless and in the range $-1 \leq \gamma_{uw} \leq 1$ where $\gamma_{uw} = 0$ indicates no correlation between u_m and w_m.

Additionally, the following symbols and notation are used for the phase-averaged quantities $j = 1,2,\ldots,J$, that is, in the range $0 \leq t_j \leq T$. An overbar indicates the mean or time average over one wave period of a phase-averaged quantity. For example, the wave setup or setdown, $\overline{\eta_a}$, is given

$$\overline{\eta_a(x)} = \frac{1}{J}\sum_{j=1}^{J}\eta_a(x,t_j). \tag{4.12}$$

In computing the time-averages for the phase-averaged velocities, the zero recordings for those z-elevations for which the measuring volume was exposed to air above the wave trough level are included in the time-averaged quantities. It is noted that the signal dropouts due to air entrainment or the irregular arrival time of the seeding particles are excluded from the phase-averaging.

The subscripts min and max indicate the minimum and maximum values with respect to t_j of a phase-averaged quantity. For example, the trough and crest elevations, $[\eta_a]_{min}$ and $[\eta_a]_{max}$, are given as

$$[\eta_a(x)]_{min} = \min\left[\eta_a(x,t_j) \mid j = 1,2,\ldots,J\right] \tag{4.13}$$

$$[\eta_a(x)]_{max} = \max\left[\eta_a(x,t_j) \mid j = 1,2,\ldots,J\right]. \tag{4.14}$$

For completeness, the higher order statistical moments are presented. The phase-averaged skewness of the horizontal and vertical velocity, ζ_u and ζ_w, are

given as (Press *et al.* 1989)

$$\zeta_u(x,z,t_j) = \frac{1}{N_j}\sum_{n=1}^{N_j}\left[\frac{u_m((x,z,t_{jn}) - u_a((x,z,t_j)}{\sigma_u}\right]^3 \quad \text{for } j = 1,2,\ldots,J \qquad (4.15)$$

$$\zeta_w(x,z,t_j) = \frac{1}{N_j}\sum_{n=1}^{N_j}\left[\frac{w_m((x,z,t_{jn}) - w_a((x,z,t_j)}{\sigma_w}\right]^3 \quad \text{for } j = 1,2,\ldots,J. \qquad (4.16)$$

The phase-averaged kurtosis of the horizontal and vertical velocity, κ_u and κ_w, are given as

$$\kappa_u(x,z,t_j) = \left\{\frac{1}{N_j}\sum_{n=1}^{N_j}\left[\frac{u_m((x,z,t_{jn}) - u_a((x,z,t_j)}{\sigma_u}\right]^4\right\} - 3 \quad \text{for } j = 1,2,\ldots,J \qquad (4.17)$$

$$\kappa_w(x,z,t_j) = \left\{\frac{1}{N_j}\sum_{n=1}^{N_j}\left[\frac{w_m((x,z,t_{jn}) - w_a((x,z,t_j)}{\sigma_w}\right]^4\right\} - 3 \quad \text{for } j = 1,2,\ldots,J, \qquad (4.18)$$

where the -3 term in Eqs 4.17 and 4.18 gives $\kappa_u = 0$ and $\kappa_w = 0$ for a normal distribution (Press *et al.* 1989). It is emphasized that these higher moments are less stable statistics, particularly for the small number of $5 \leq N_j \leq 50$; and their results should be interpreted with caution.

For all figures which show the temporal variation over the wave period, the phases are aligned with the zero-upcrossing of the free surface elevation at $t = (T/4) = 0.55$ s to facilitate comparisons of a given phase among the six measuring lines.

4.2 Free Surface Elevations

Figure 4.1 shows the temporal variation of the phase-averaged free surface elevations, η_a, and the standard deviation envelope, $\eta_a \pm \sigma_\eta$, for L1 to L6. For

L1, seaward of breaking, the standard deviation envelope is small, indicating repeatability of the wave form. At this location, the wave shape has a sharpened peak and flattened trough. For L2, the wave shape pitches forward, and there is a slight variation in the standard deviation envelope due to irregularities of wave breaking. For this spilling breaker, breaking is defined as the onset of aeration in the tip of the wave crest. For L3, the wave is in transition from organized wave motion to a turbulent bore. Here the value of σ_η is largest. In the inner surf zone for L4, L5, and L6, the wave shape is a well-developed turbulent bore. The values of σ_η are largest near the front face and top of the bore.

Figure 4.2 shows the cross-shore variation of the mean water level, $\overline{\eta_a}$, the free surface elevation maximum, $[\eta_a]_{max}$, and minimum, $[\eta_a]_{min}$, the wave height $H = [\eta_a]_{max} - [\eta_a]_{min}$, and the mean of the standard deviation, $\overline{\sigma_\eta}$, for L1 to L6 where x is the horizontal distance, positive onshore. The wave height and wave setdown increase until breaking after which the wave height decreases and the mean water level increases after breaking as has been observed by many researchers.

Figure 4.3 shows a detail of the cross-shore variation of free surface statistics, including the maximum and minimum of the standard deviations, $[\sigma_\eta]_{max}$ and $[\sigma_\eta]_{min}$. Both of these quantities are largest in the transition region for L3. It is interesting to note the cross-shore variation of $[\sigma_\eta]_{max}$ because it could be used to better quantify the transition region of the surf zone (e.g., Nairn *et al.* 1990 and references therein). Table 4.1 lists the free surface statistics where d is the depth below the still water level (SWL).

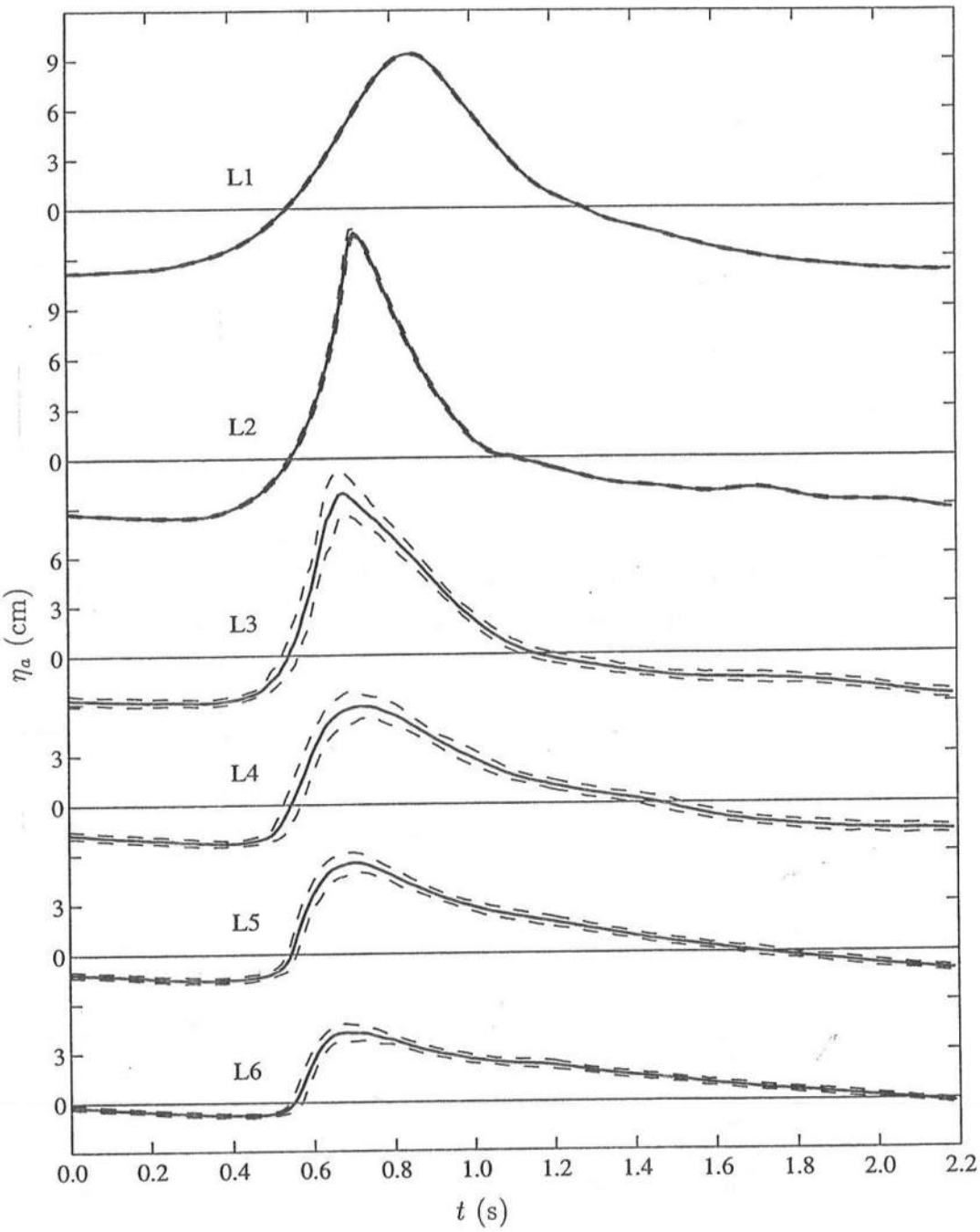

Figure 4.1: Temporal Variations of Phase-Averaged Free Surface Elevation, η_a (——), and Standard Deviation Envelope, $\eta_a \pm \sigma_\eta$ (– –), for L1 to L6.

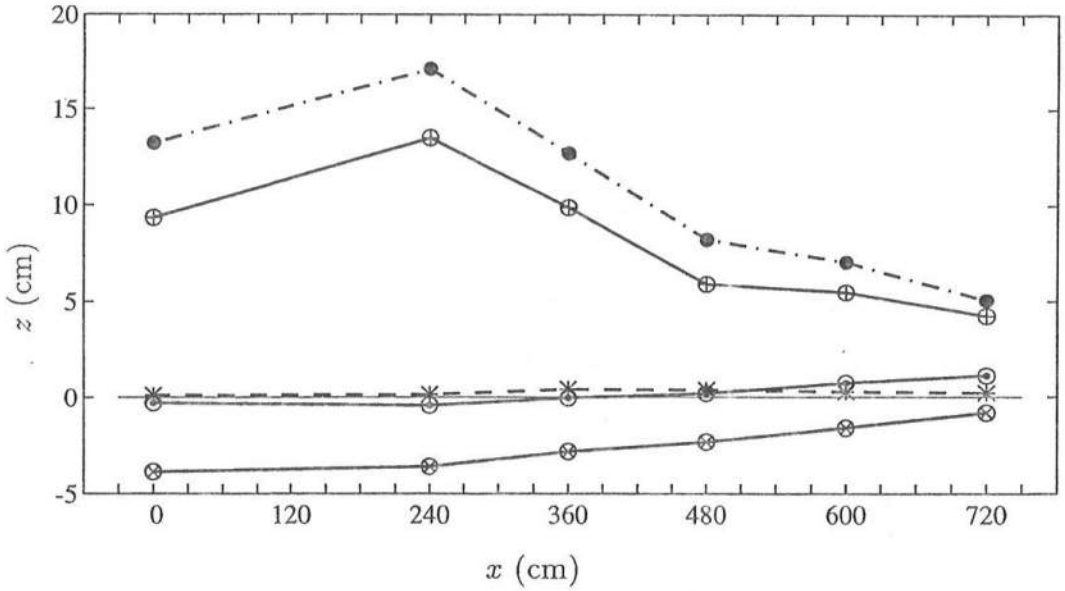

Figure 4.2: Cross-Shore Variations of Time-Averaged Free Surface Statistics with H ($\bullet$ $-\cdot-$); $[\eta_a]_{max}$ ($\oplus$ ——); $[\eta_a]_{min}$ ($\otimes$ ——); $\overline{\eta_a}$ ($\odot$ ——); and $\overline{\sigma_\eta}$ ($*$ – –) for L1 to L6.

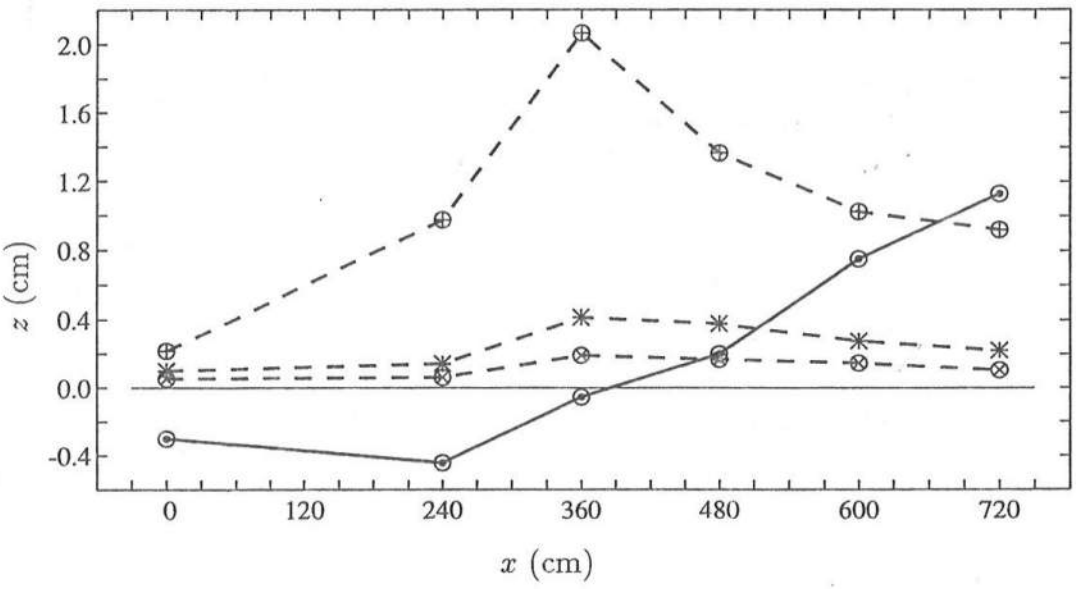

Figure 4.3: Cross-Shore Variations of Time-Averaged Free Surface Statistics with $\overline{\eta_a}$ ($\odot$ ——); $[\sigma_\eta]_{max}$ ($\oplus$ – –); $[\sigma_\eta]_{min}$ ($\otimes$ – –); and $\overline{\sigma_\eta}$ ($*$ – –) for L1 to L6.

Table 4.1: Phase-Averaged Free Surface Statistics for L1 to L6.

Line No.	x (cm)	d (cm)	H (cm)	$\overline{\eta_a}$ (cm)	$[\eta_a]_{min}$ (cm)	$[\eta_a]_{max}$ (cm)	$\overline{\sigma_\eta}$ (cm)	$[\sigma_\eta]_{min}$ (cm)	$[\sigma_\eta]_{max}$ (cm)
L1	0	28.00	13.22	-0.30	-3.88	9.34	0.10	0.05	0.22
L2	240	21.14	17.10	-0.44	-3.60	13.50	0.14	0.06	0.98
L3	360	17.71	12.71	-0.05	-2.82	9.89	0.41	0.19	2.06
L4	480	14.29	8.24	0.20	-2.33	5.91	0.38	0.17	1.37
L5	600	10.86	7.08	0.75	-1.60	5.48	0.28	0.15	1.03
L6	720	7.43	5.05	1.13	-0.82	4.23	0.22	0.11	0.92

4.3 Fluid Velocities

In this section, the fluid velocities of two representative measuring lines are shown in detail: L2 at breaking where there appears to be little effect of turbulence on the flow and L4 in the inner surf zone where the turbulent bore is well established.

Figure 4.4 shows the temporal variations of the phase-averaged velocities, u_a and w_a, and the free surface elevation, η_a, and the standard deviation envelope, $\eta_a \pm \sigma_\eta$ for L2. The horizontal velocity is fairly uniform vertically in the interior; and there are interesting variations in the bottom boundary layer, including the overshoot in the range $0.45 < t < 0.8$ s. The vertical velocity under the steep front of the breaking wave is large and approximately the same magnitude as the horizontal velocity at $t \simeq 0.6$ s. The same quantities shown in Figure 4.4 for L2 are shown in Figure 4.5 for L4, but the scale of the vertical axis and the velocity vectors in these two figures are not the same. In general, the pattern of the phase-averaged velocities looks similar before and after breaking. The presence of a bottom boundary is also apparent in the surf zone.

Measurements were made at approximately twenty points at each measuring line. To be concise in the next several figures, five representative measuring point elevations are chosen for L2 and L4. The elevations are denoted by (a) to (e), where point (a) is at or slightly below trough level, (b) and (c) are in the interior, (d) is near the top of the bottom boundary layer, and (e) is inside the bottom boundary layer. Figure 4.6 shows the (x, z) coordinates of these representative measuring points. The wave trough level and the bottom are indicated by light solid lines. Table 4.2 lists the representative measuring point locations. The coordinate z_m is the vertical coordinate with respect to the bottom as defined in Chapter 3 and discussed in detail in Chapter 5.

Figure 4.7 shows the temporal variation of the phase-averaged horizontal velocity, u_a, with the standard deviation envelope, $u_a \pm \sigma_u$, at the five vertical elevations for L2. The small envelope for elevations L2a to L2d shows that the flow field is repeatable and that little turbulence is transported from the surf zone or from the bottom boundary layer. There is an increase in σ_u for L2e in the bottom boundary layer as the flow begins to decelerate at $t = 0.7$ s. Figure 4.8 shows the temporal variation of the phase-averaged vertical velocities, w_a, with the standard deviation envelope, $w_a \pm \sigma_w$, for the five vertical elevations for L2. The values of σ_w in this figure are similar to σ_u in Figure 4.7.

The same horizontal velocity quantities of Figure 4.7 for L2 are plotted in Figure 4.9 for L4. There is an overall increase in σ_u due to wave breaking. The value of σ_u is largest for L4a near trough level and decreases below the still water level. For L4a, the curve of u_a is fairly smooth over the wave period, suggesting that phase-averaging over 50 waves may be sufficient to provide stable estimates of the mean and variance. For L4a, the maximum of σ_u occurs near $t \simeq 0.9$ s. For L4b, the maximum of σ_u occurs slightly later near $t \simeq 1.2$ s. For L4c and L4d, σ_u is fairly uniform across the wave period, suggesting that most of the turbulence generated by wave breaking is dissipated and the remainder is distributed over the entire period before reaching the bottom boundary layer. However, the turbulence level at L4e inside the surf zone is larger than that at L2e, indicating the presence of turbulence generated by wave breaking in the bottom boundary layer.

The same vertical velocity quantities of Figure 4.8 for L2 are shown in Figure 4.10 for L4. The value of σ_w relative to w_a is larger than that for the horizontal velocity in Figure 4.9. The turbulent component is of the same order of magnitude as the phase-averaged velocity. For L4e in the bottom boundary layer, σ_w is small since the component of the vertical fluctuations is probably

limited by the solid boundary.

Figure 4.11 shows the cross-shore and vertical variations of the mean, minimum and maximum of the phase-averaged horizontal velocity, $\overline{u_a}$, $[u_a]_{min}$, and $[u_a]_{max}$, for L1 to L6. Trough level is indicated by a light solid line. Except in the bottom boundary layer, $[u_a]_{min}$ and $[u_a]_{max}$ are fairly constant below the trough level for all six measuring lines. Figure 4.12 shows the cross-shore and vertical variations of the mean, minimum and maximum of the phase-averaged vertical velocity, $\overline{w_a}$, $[w_a]_{min}$, and $[w_a]_{max}$, for L1 to L6. The values of $[w_a]_{min}$ and $[w_a]_{max}$ increase approximately linearly from the bottom and are smaller than $[u_a]_{min}$ and $[u_a]_{max}$ near trough level. Figure 4.13 shows the detail of $\overline{u_a}$ and $\overline{w_a}$ from Figures 4.11 and 4.12. The mean vertical velocity, $\overline{w_a}$, is nearly zero for L1 and L2 but nonzero in the surf zone probably because of the circulation induced by the undertow, $\overline{u_a}$.

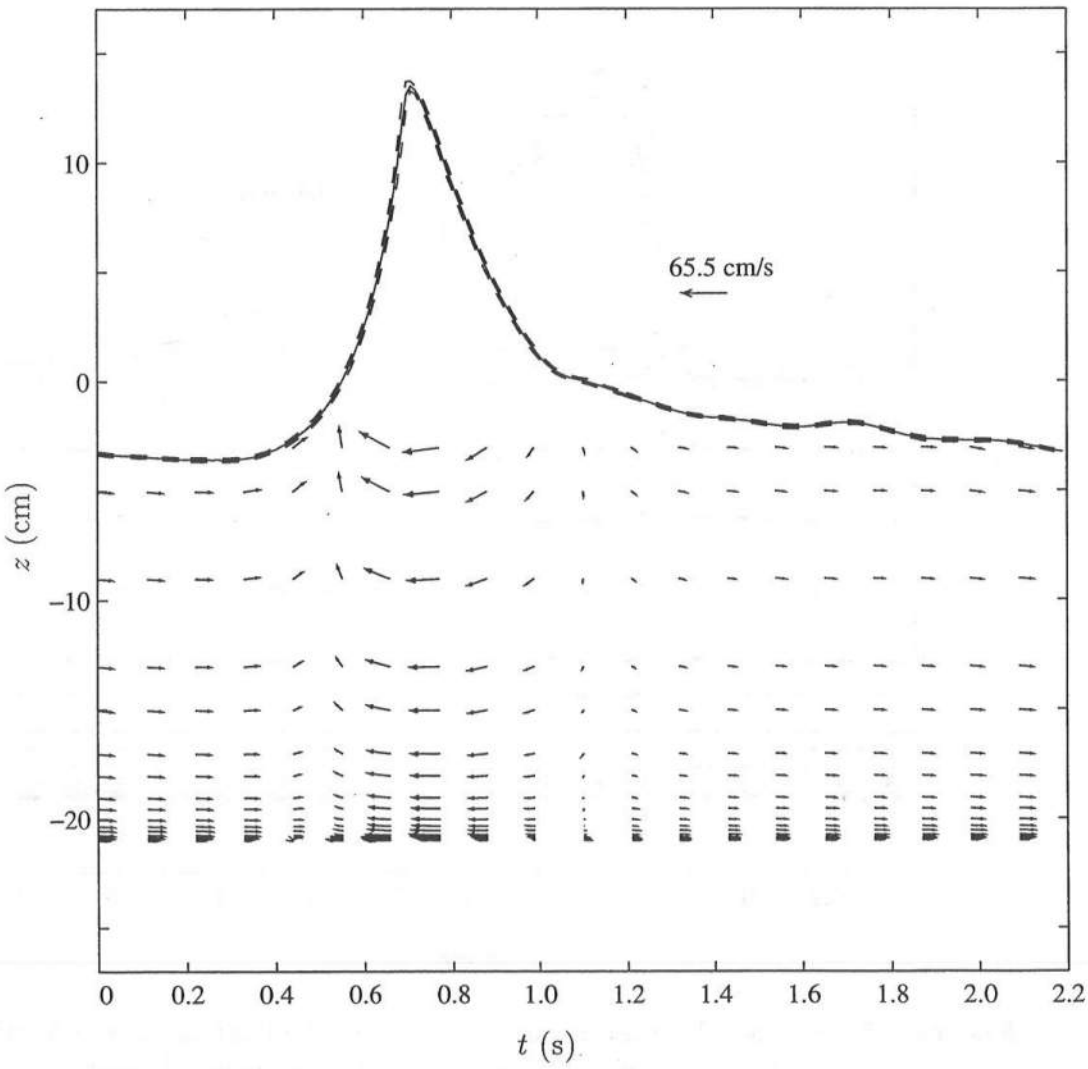

Figure 4.4: Temporal Variations of Phase-Averaged Horizontal and Vertical Velocity (⟵) with Phase-Averaged Free Surface Elevation, η_a (——), and Standard Deviation Envelope, $\eta_a \pm \sigma_\eta$ (– –), for L2.

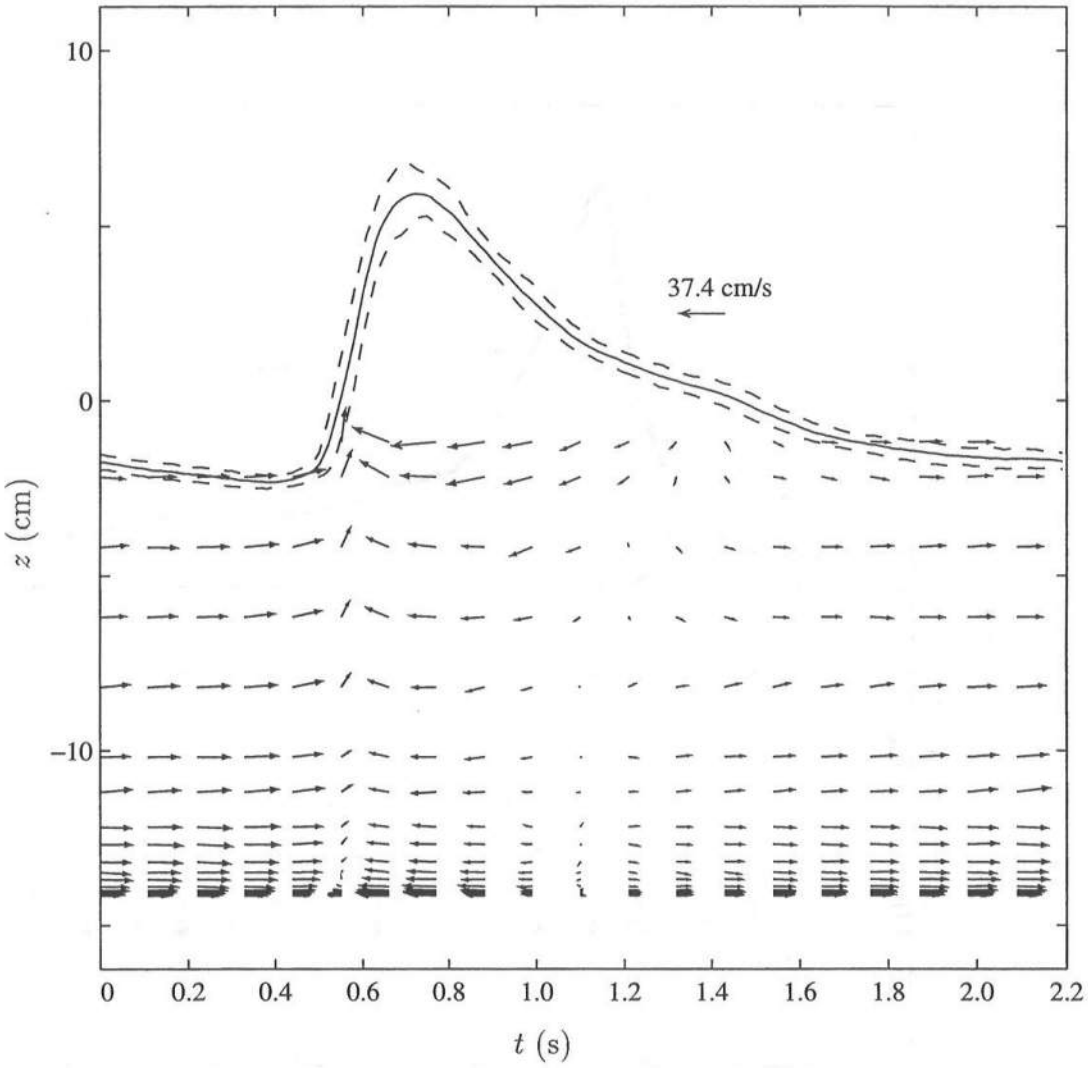

Figure 4.5: Temporal Variations of Phase-Averaged Horizontal and Vertical Velocity (⟵) with Phase-Averaged Free Surface Elevation, η_a (——), and Standard Deviation Envelope, $\eta_a \pm \sigma_\eta$ (– –), for L4.

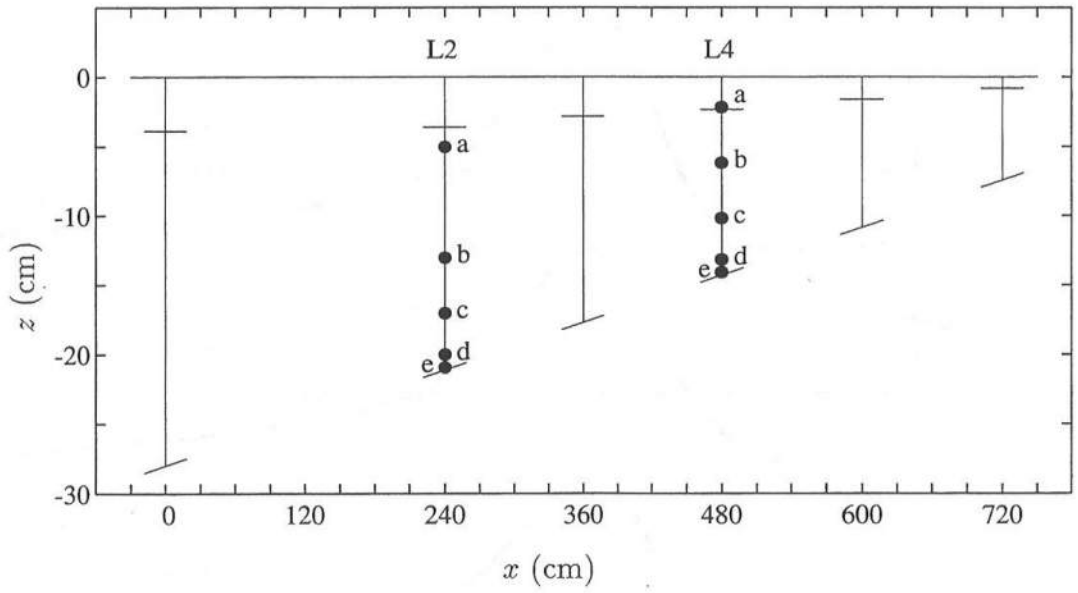

Figure 4.6: Representative Measuring Point Locations for L2 and L4.

Table 4.2: Vertical Coordinates of Representative Measuring Points for L2 and L4.

	L2 at x=240 cm		L4 at x=480 cm	
	z (cm)	z_m (cm)	z (cm)	z_m (cm)
a	-5.04	16.10	-2.19	12.10
b	-13.04	8.10	-6.19	8.10
c	-17.04	6.10	-10.19	4.10
d	-20.04	1.10	-13.19	1.10
e	-20.94	0.20	-14.09	0.20

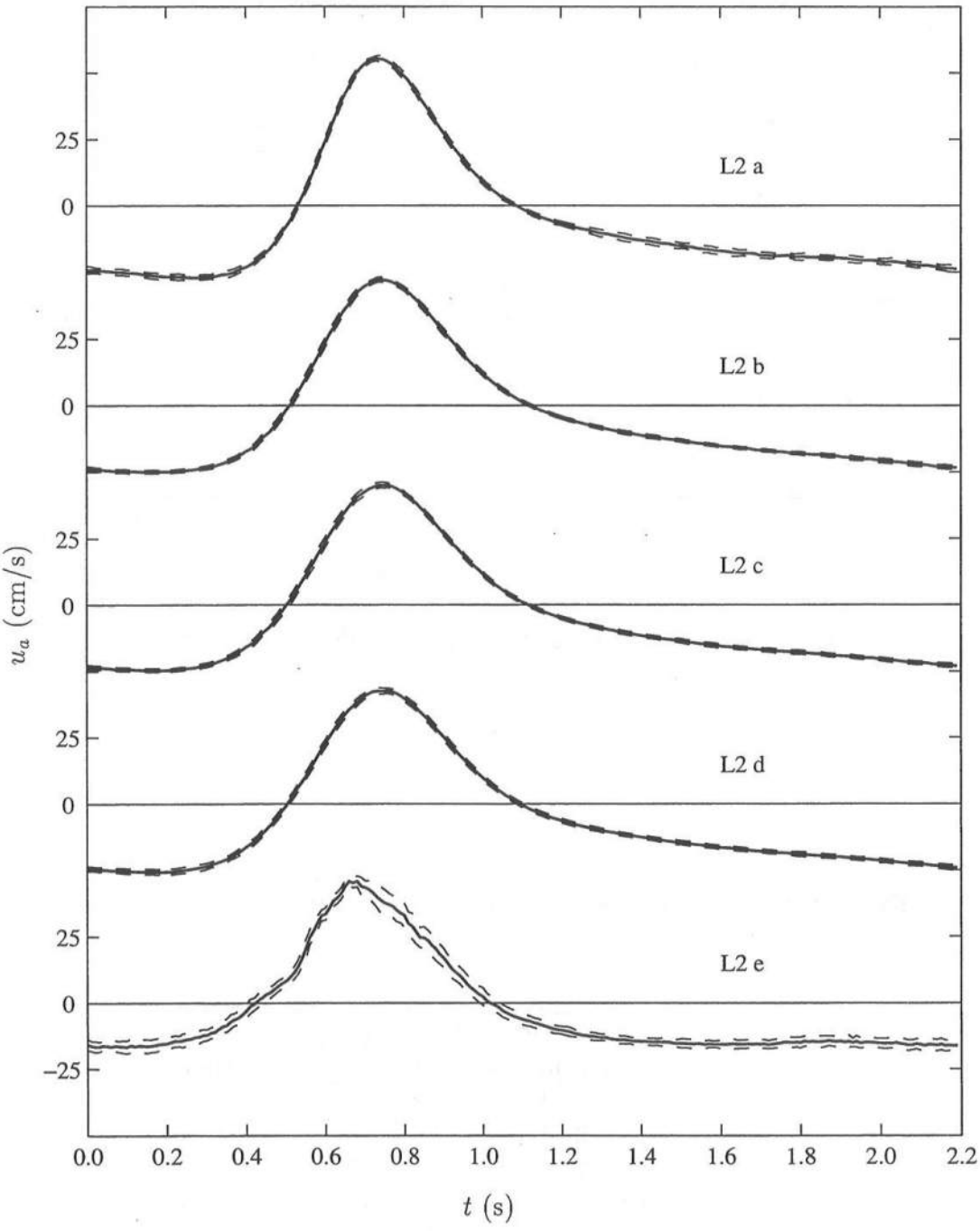

Figure 4.7: Temporal Variations of Phase-Averaged Horizontal Velocity, u_a (——), and Standard Deviation Envelope, $u_a \pm \sigma_u$ (– –), for Five Vertical Elevations for L2.

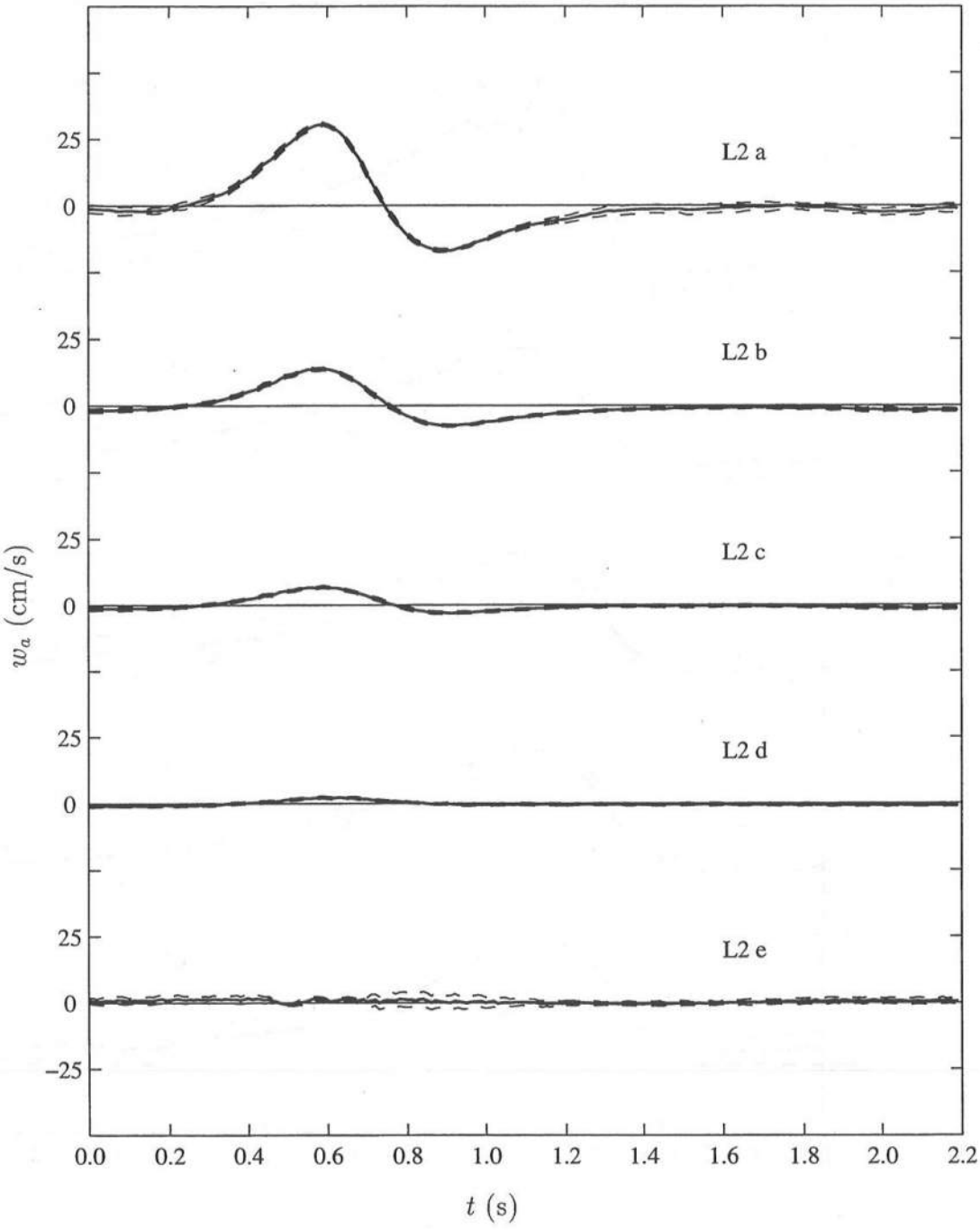

Figure 4.8: Temporal Variations of Phase-Averaged Vertical Velocity, w_a (——), and Standard Deviation Envelope, $w_a \pm \sigma_w$ (– –), for Five Vertical Elevations for L2.

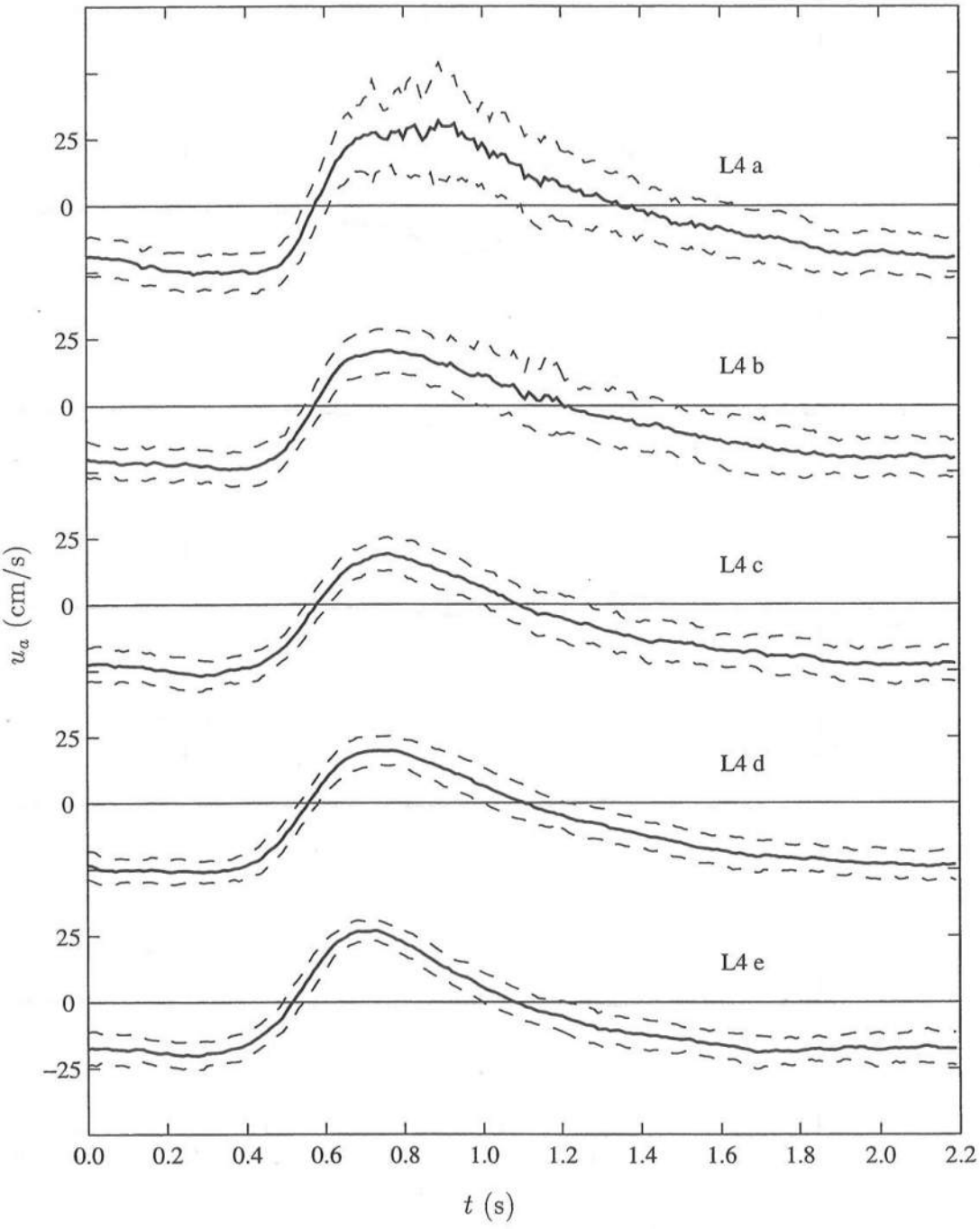

Figure 4.9: Temporal Variations of Phase-Averaged Horizontal Velocity, u_a (——), and Standard Deviation Envelope, $u_a \pm \sigma_u$ (– –), for Five Vertical Elevations for L4.

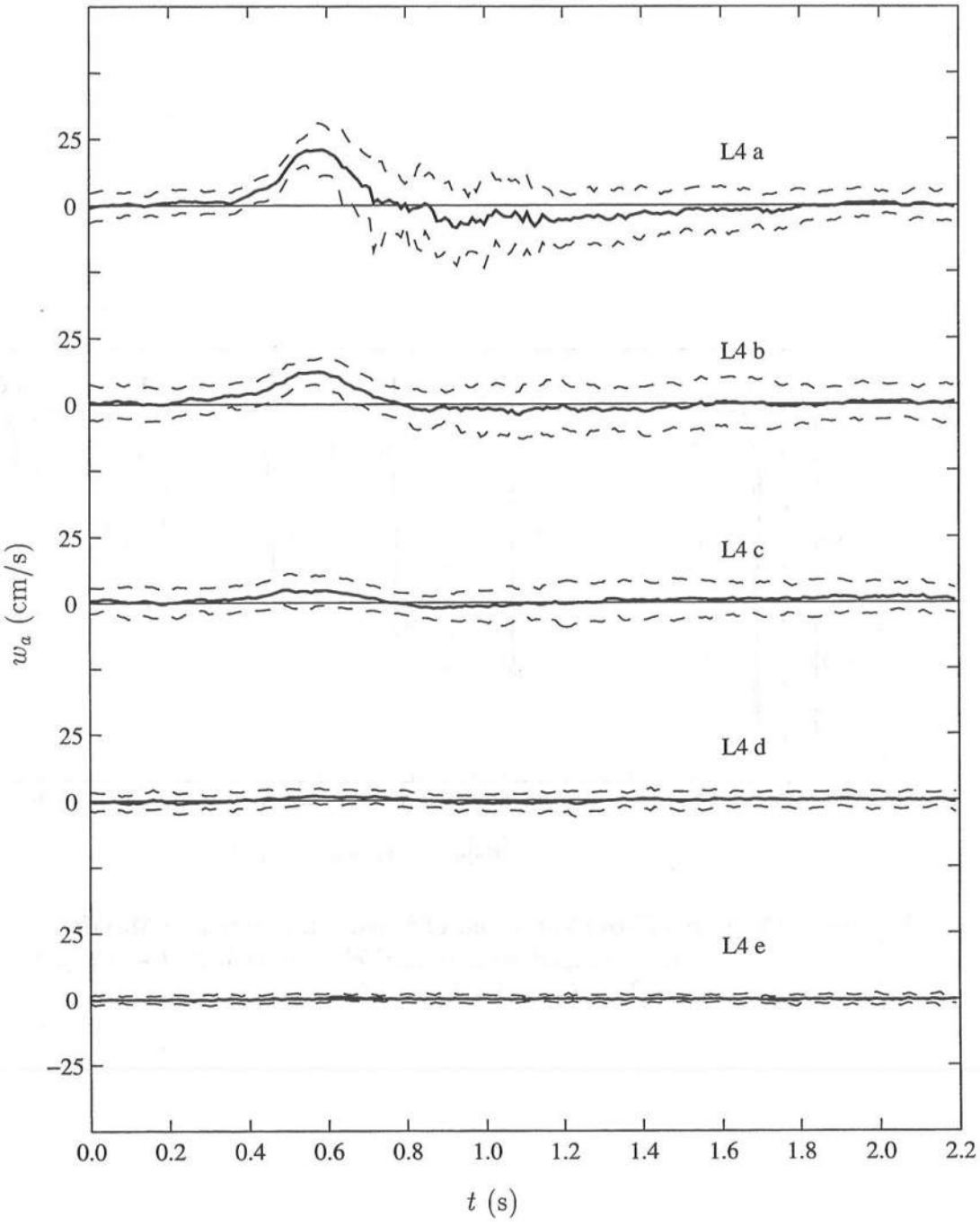

Figure 4.10: Temporal Variations of Phase-Averaged Vertical Velocity, w_a (——), and Standard Deviation Envelope, $w_a \pm \sigma_w$ (– –), for Five Vertical Elevations for L4.

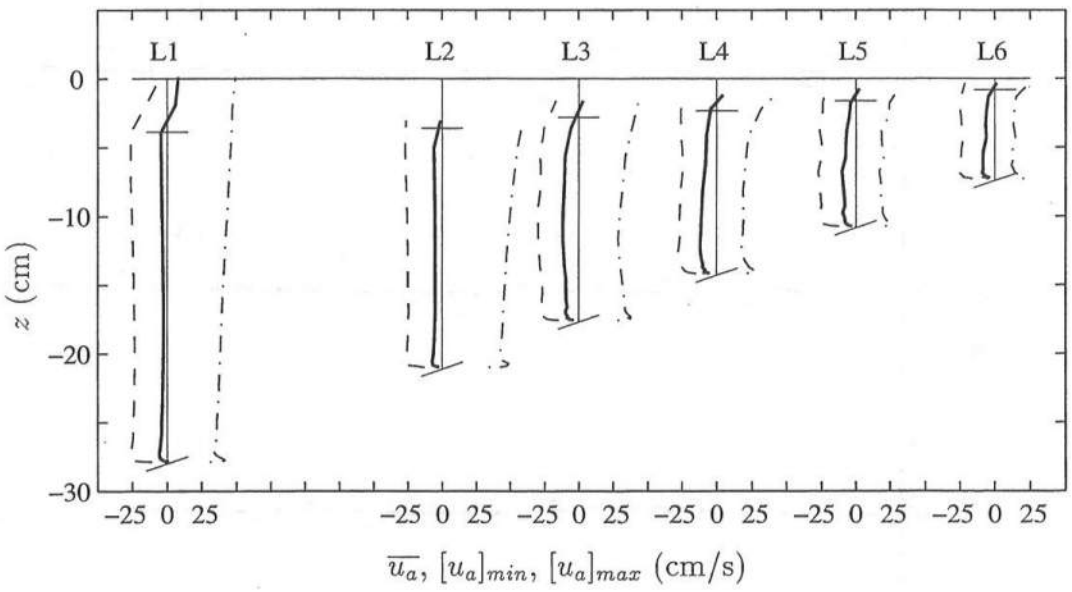

Figure 4.11: Cross-Shore Variations of Mean, Minimum and Maximum Values of Phase-Averaged Horizontal Velocity with $\overline{u_a}$ (——); $[u_a]_{min}$ (– –); and $[u_a]_{max}$ (–·–) for L1 to L6.

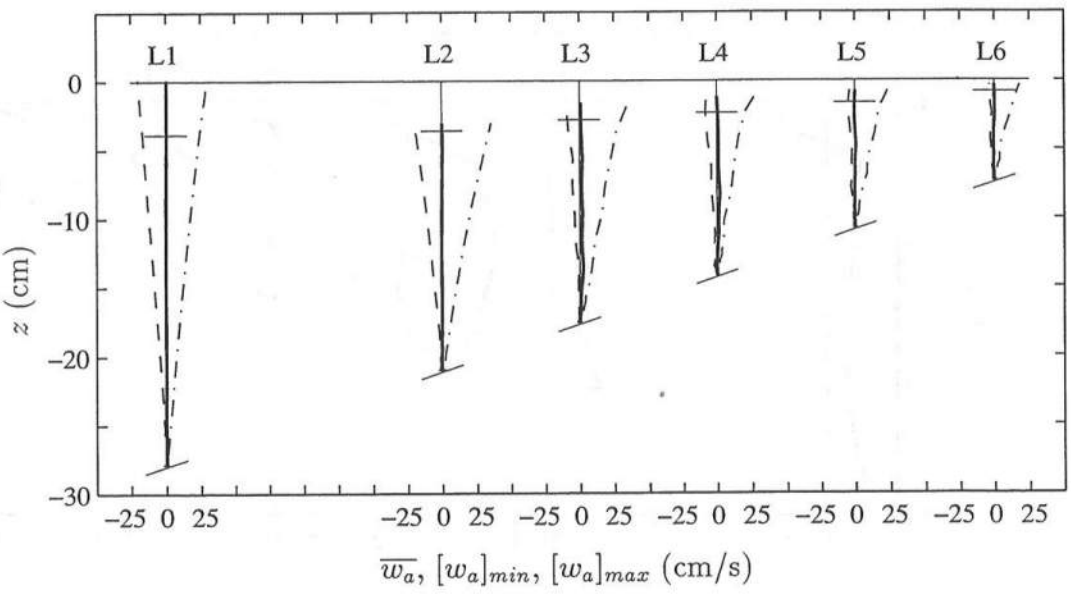

Figure 4.12: Cross-Shore Variations of Mean, Minimum and Maximum Values of Phase-Averaged Vertical Velocity with $\overline{w_a}$ (——); $[w_a]_{min}$ (– –); and $[w_a]_{max}$ (–·–) for L1 to L6.

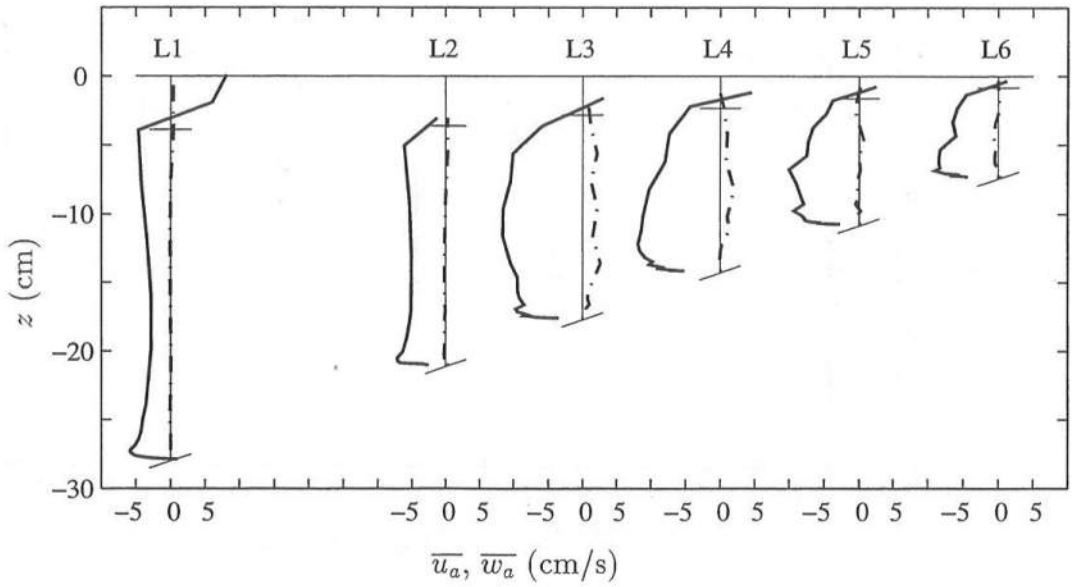

Figure 4.13: Comparison of Mean Horizontal and Vertical Velocities with $\overline{u_a}$ (——) and $\overline{w_a}$ (–·–) for L1 to L6.

4.4 Turbulent Stresses

Figure 4.14 shows the temporal variations of the phase-averaged horizontal velocity variance, σ_u^2, vertical velocity variance, σ_w^2, and velocity covariance, σ_{uw} for the five vertical elevations for L2. As stated in Section 4.1, the horizontal and vertical turbulent stresses may be estimated as $-\rho\sigma_u^2$ and $-\rho\sigma_w^2$, and the turbulent shear stress may be estimated as $-\rho\sigma_{uw}$. Like Figures 4.7 and 4.8 showing $u_a \pm \sigma_u$ and $w_a \pm \sigma_w$, Figure 4.14 shows almost no turbulence in the interior; and the turbulence seems to be confined to the bottom boundary layer.

The same quantities of Figure 4.14 for L2 are shown in Figure 4.15 for L4. This figure shows the downward decrease in turbulence generated by wave breaking. Also, the peak of the turbulence shifts downward. For L4a, the magnitude of the horizontal variance is larger than the vertical variances over most of the wave period except at $t \simeq 0.6$ s where they are approximately equal. Figure 4.5 showed that the phase-averaged vertical velocity is as large as the horizontal velocity at $t \simeq 0.6$ just below trough level. For L4c, σ_u^2 and σ_w^2 are approximately the same at each phase, and the turbulence seems to be more isotropic even though the phase-average vertical velocity is much less than the horizontal velocity at this elevation. For L4e, σ_u^2 is large than σ_w^2 since the vertical fluctuations may be limited by the solid boundary.

Figure 4.16 shows the temporal variations of the correlation coefficient, γ_{uw}, for the five vertical elevations for L2. For L2a to L2d interpretation of these curves is difficult because of the high noise in comparison to the low turbulence level. In the bottom boundary layer, however, the curve for L2e shows more clearly the variation of γ_{uw} due to the oscillatory boundary layer. Similar to Figure 4.16 for L2, Figure 4.17 shows the variation of γ_{uw} for L4. In this figure, $\gamma_{uw} < 0$ for most of the wave period of L4a, L4b, and L4c indicating a positive shear

stress due to wave breaking. For L4e in the bottom boundary layer, γ_{uw} is noisy; but the oscillatory trend is similar to L2e. It is noted that the 95% confidence intervals for the correlation coefficients are shown in Figures 4.16 and 4.17 and are computed following Bendat and Piersol (1986). The 95% confidence interval for the estimated γ_{uw} may be written

$$\gamma_{uw}(1-2\epsilon) \leq \gamma_{uw} \leq \gamma_{uw}(1+2\epsilon), \tag{4.19}$$

where

$$\epsilon = \frac{\sqrt{2}(1-\gamma_{uw}^2)}{|\gamma_{uw}|\sqrt{N_d}} \tag{4.20}$$

and N_d is the number of degrees of freedom for the covariance calculation which is related to the number of waves in the ensemble average and the dropout rate given as

$$N_d = 2\left(N_w - \frac{R_N}{2}\right) \tag{4.21}$$

where $N_w = 50$ waves and R_N is the dropout rate expressed as a percent.

Figure 4.18 shows the temporal variations of the dropout rate, R_N, for the five vertical elevations for L2. The dropout rate is the highest when the flow reverses and the velocities are near zero. At this point, there are fewer seeding particles moving through the measuring volume over a fixed time, increasing the likelihood of a dropout. In any case, the dropout rate was less than 30% even in the most extreme case. There is no significant vertical variation in R_N except in the bottom boundary layer where the flow is turbulent and R_N is reduced. In this case, the turbulent fluctuations increase the likelihood of seeding particles passing through the measuring volume even at those phases where the phase-averaged velocities are near zero. Figure 4.19 shows the dropout rate for L4 at the five vertical locations. The dropouts here are due to air entrainment associated with the breaking process. In general, the dropout rate pattern follows that of the velocity variances in Figure 4.15 with the dropout rate decreasing downward as

well as the phase shift in the peak dropout rate. In the bottom boundary layer for L4e, the dropout rate seems to be affected more by the flow reversal than aeration since curves L2e and L4e are similar.

Figure 4.20 shows the cross-shore and vertical variations of the mean, minimum and maximum horizontal velocity variances, $\overline{\sigma_u^2}$, $[\sigma_u^2]_{min}$, and $[\sigma_u^2]_{max}$, for L1 to L6. These values are multiplied by 0.01 cm^2/s^2 in Figures 4.20 to 4.23 for convenience. The largest value of $[\sigma_u^2]_{max}$ in Figure 4.20 occurs for L4. Similarly, Figure 4.21 shows the cross-shore and vertical variations of the mean, minimum and maximum vertical velocity variances, $\overline{\sigma_w^2}$, $[\sigma_w^2]_{min}$, and $[\sigma_w^2]_{max}$, for L1 to L6. In both of these figures, the region seaward of breaking appears to be affected very little by turbulence. Figure 4.22 shows the cross-shore and vertical variations of the time-averaged mean, minimum and maximum values of the horizontal and vertical velocity covariance, $\overline{\sigma_{uw}}$, $[\sigma_{uw}]_{min}$, and $[\sigma_{uw}]_{max}$, for L1 to L6. Figure 4.23 shows the detail of the cross-shore variations of $\overline{\sigma_u^2}$, $\overline{\sigma_w^2}$, and $\overline{\sigma_{uw}}$ from the preceding three figures. Comparison of $\overline{\sigma_u^2}$ and $\overline{\sigma_w^2}$ for L3 to L6 shows that they are about the same magnitude below trough level and decay linearly downward except in the lower portion of the water column where $\overline{\sigma_u^2}$ remains approximately constant over depth and $\overline{\sigma_w^2}$ tends to zero near the bottom.

Figure 4.24 shows the cross-shore and vertical variations of the mean correlation coefficient, $\overline{\gamma_{uw}}$, for L1 to L6. The values above trough level are not plotted since γ_{uw} is undefined when the measuring volume is out of the water. For L1 and L2, $\overline{\gamma_{uw}}$ is near zero in the upper two thirds of the measured water column and is negative in the lower portion. It is slightly positive in the bottom boundary layer. For L3 to L6, $\overline{\gamma_{uw}}$ is negative in general, except in the bottom boundary layer where it is slightly positive. In general, the negative correlation coefficient indicates a positive shear stress.

Figure 4.25 shows the cross-shore and vertical variations of the mean dropout rate, $\overline{R_N}$ for L1 to L6. For L3, the vertical variation $\overline{R_N}$ is similar to $[\sigma_u^2]_{max}$ in Figure 4.20 and $[\sigma_w^2]_{max}$ in Figure 4.21. For L4, the dropout rate does not increase in proportion to the level of turbulence; and for L5 and L6, the vertical variation is not similar at all. This is particularly true in the lower portion of the water column. In this region, the air bubbles entrained by the initial breaking process have surfaced, and the bubbles generated by the bore do not penetrate downward as far. Consequently, the dropout rate or aeration does not give a clear indication of turbulence in the inner surf zone for spilling waves.

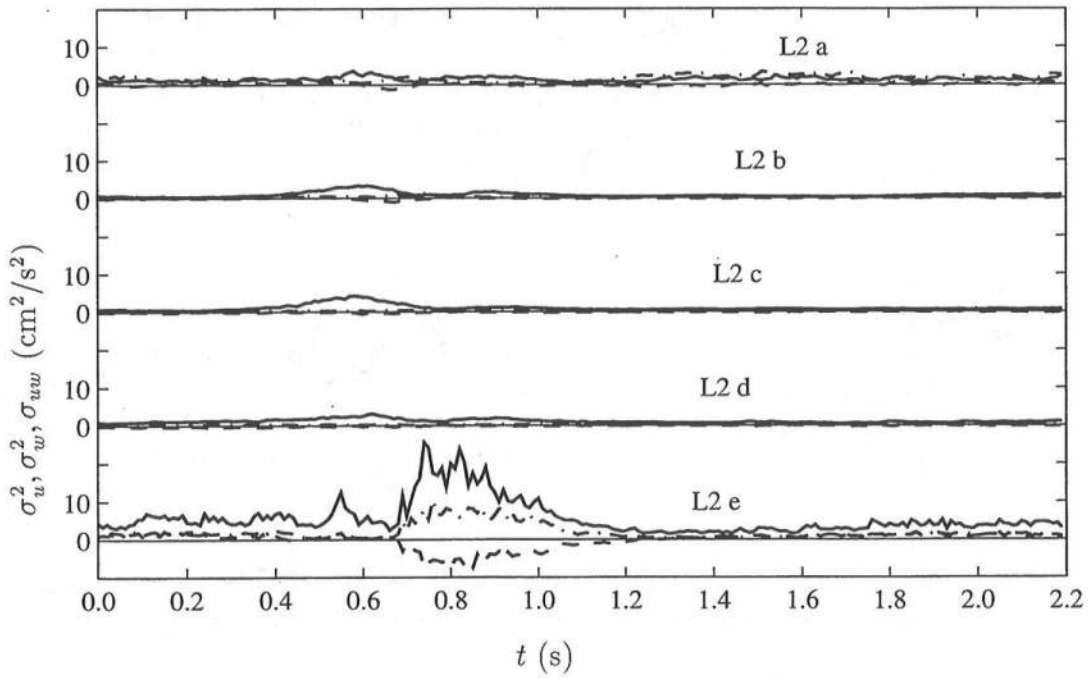

Figure 4.14: Temporal Variations of Phase-Averaged Horizontal Velocity Variance, σ_u^2 (——); Vertical Velocity Variance, σ_w^2 (–·–); and Covariance, σ_{uw} (– –) for Five Vertical Elevations for L2.

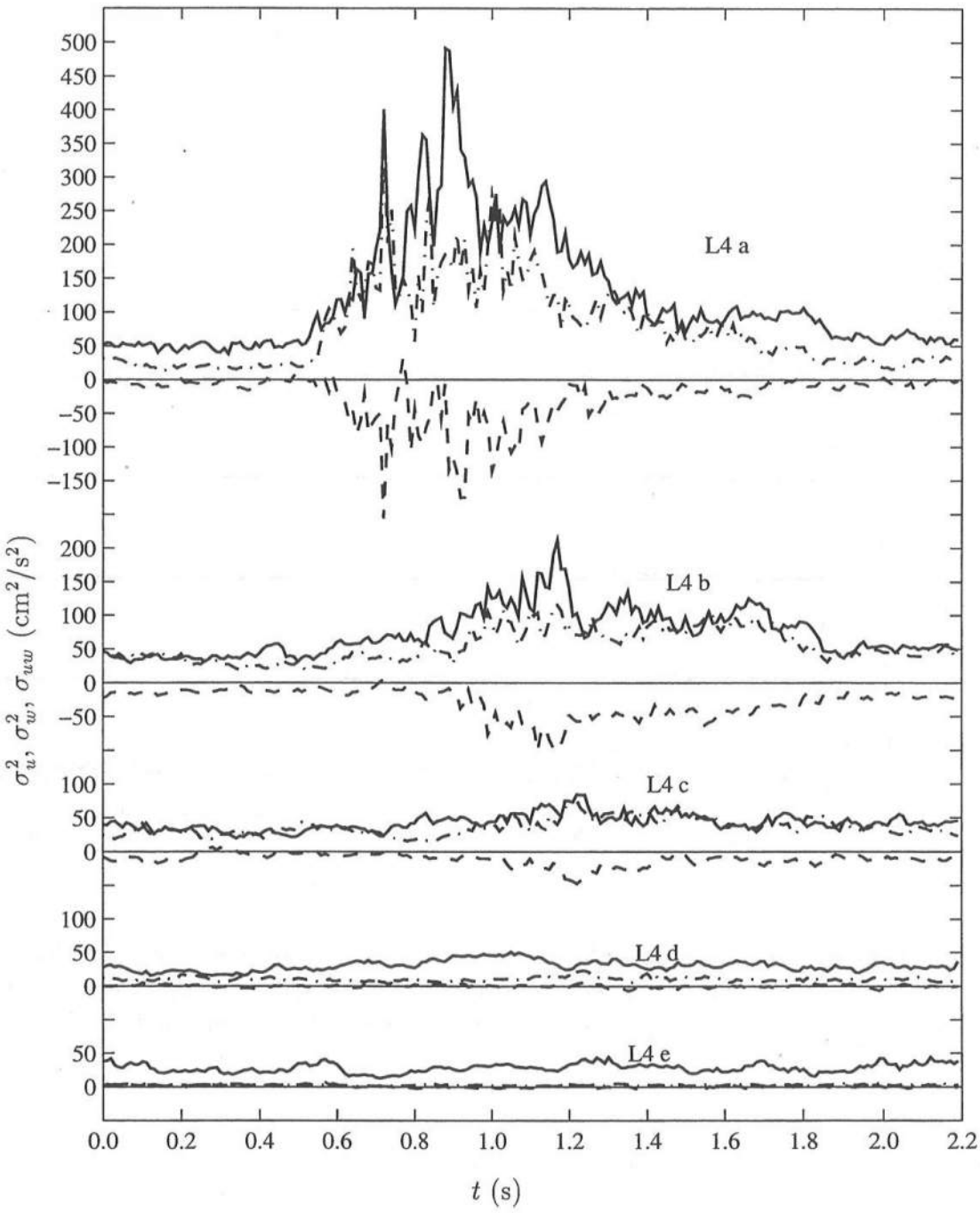

Figure 4.15: Temporal Variations of Phase-Averaged Horizontal Velocity Variance, σ_u^2 (——); Vertical Velocity Variance, σ_w^2 (-·-); and Covariance, σ_{uw} (– –) for Five Vertical Elevations for L4.

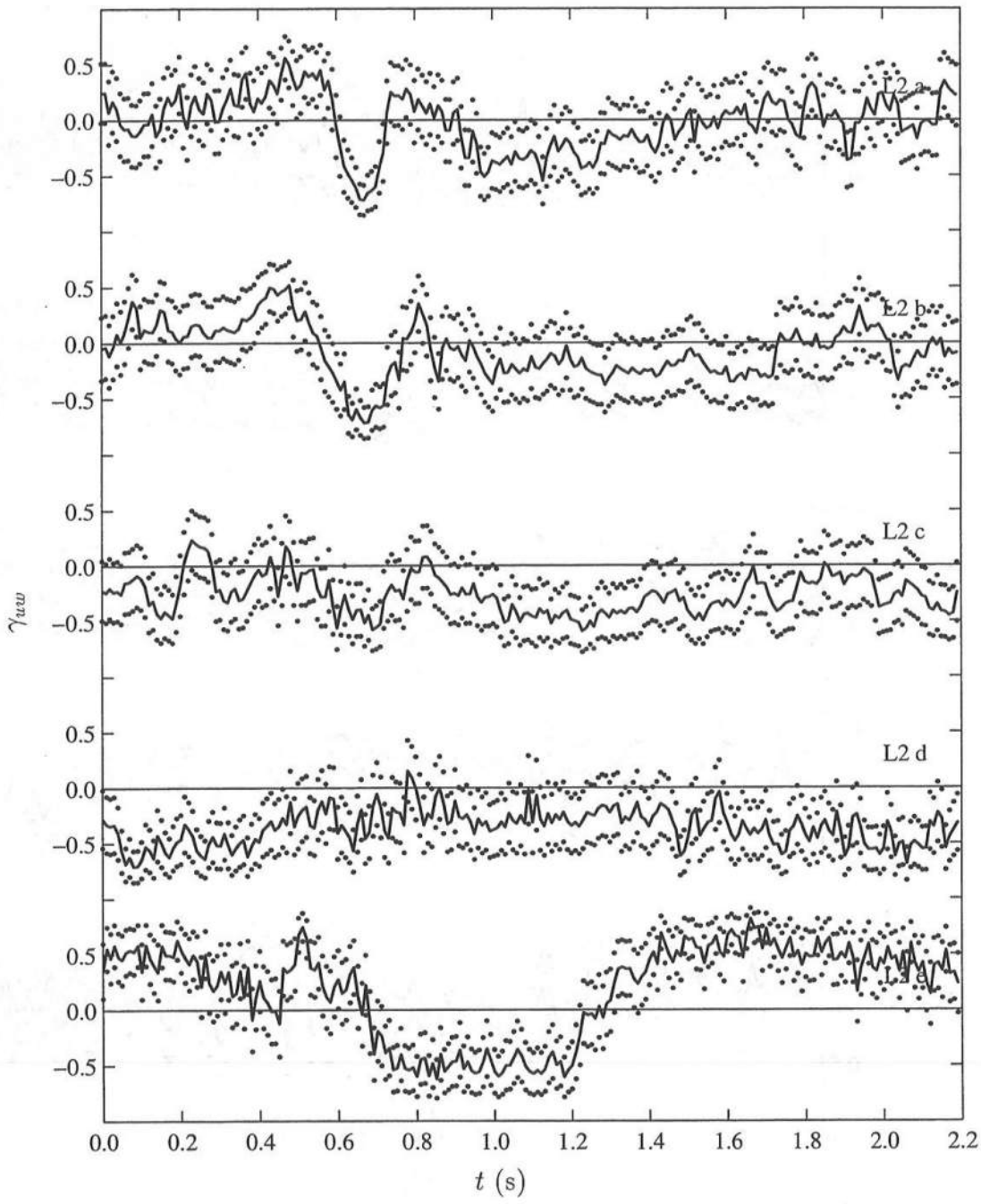

Figure 4.16: Temporal Variations of Phase-Averaged Correlation Coefficient, γ_{uw} (——), with 95% Confidence Interval (•) for Five Vertical Elevations for L2.

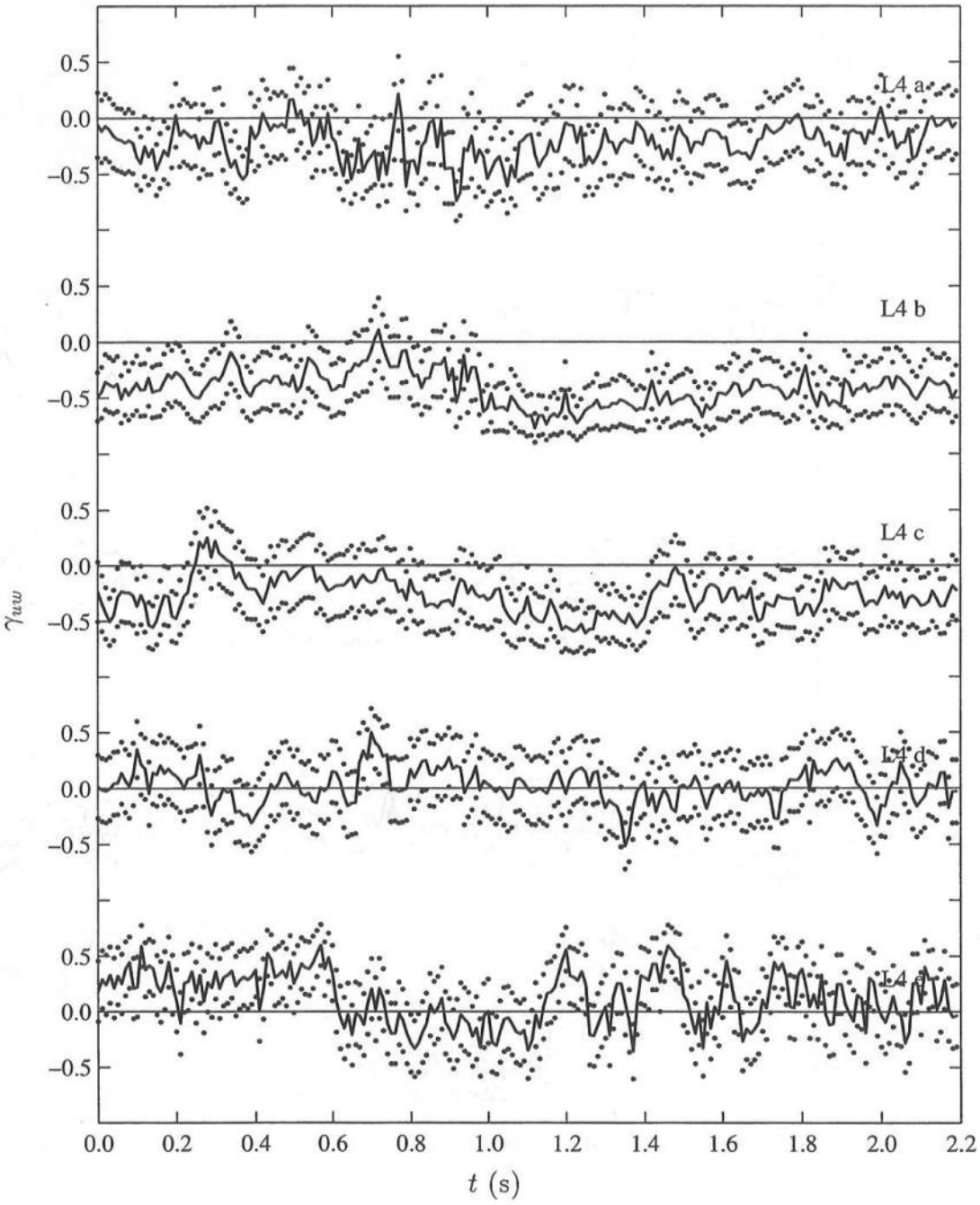

Figure 4.17: Temporal Variations of Phase-Averaged Correlation Coefficient, γ_{uw} (——), with 95% Confidence Interval (•) for Five Vertical Elevations for L4.

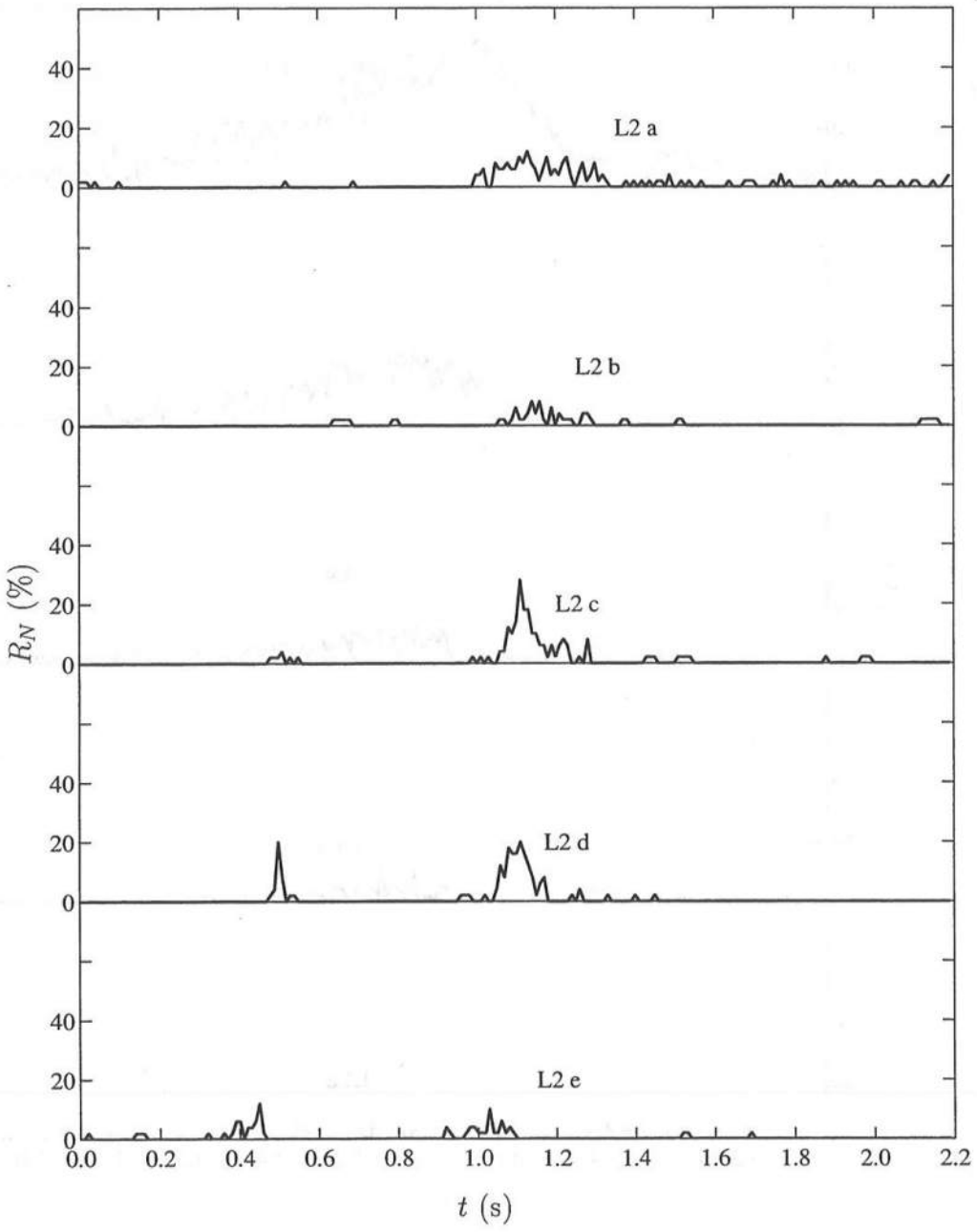

Figure 4.18: Temporal Variations of Phase-Averaged Dropout Rate, R_N, for Five Vertical Elevations for L2.

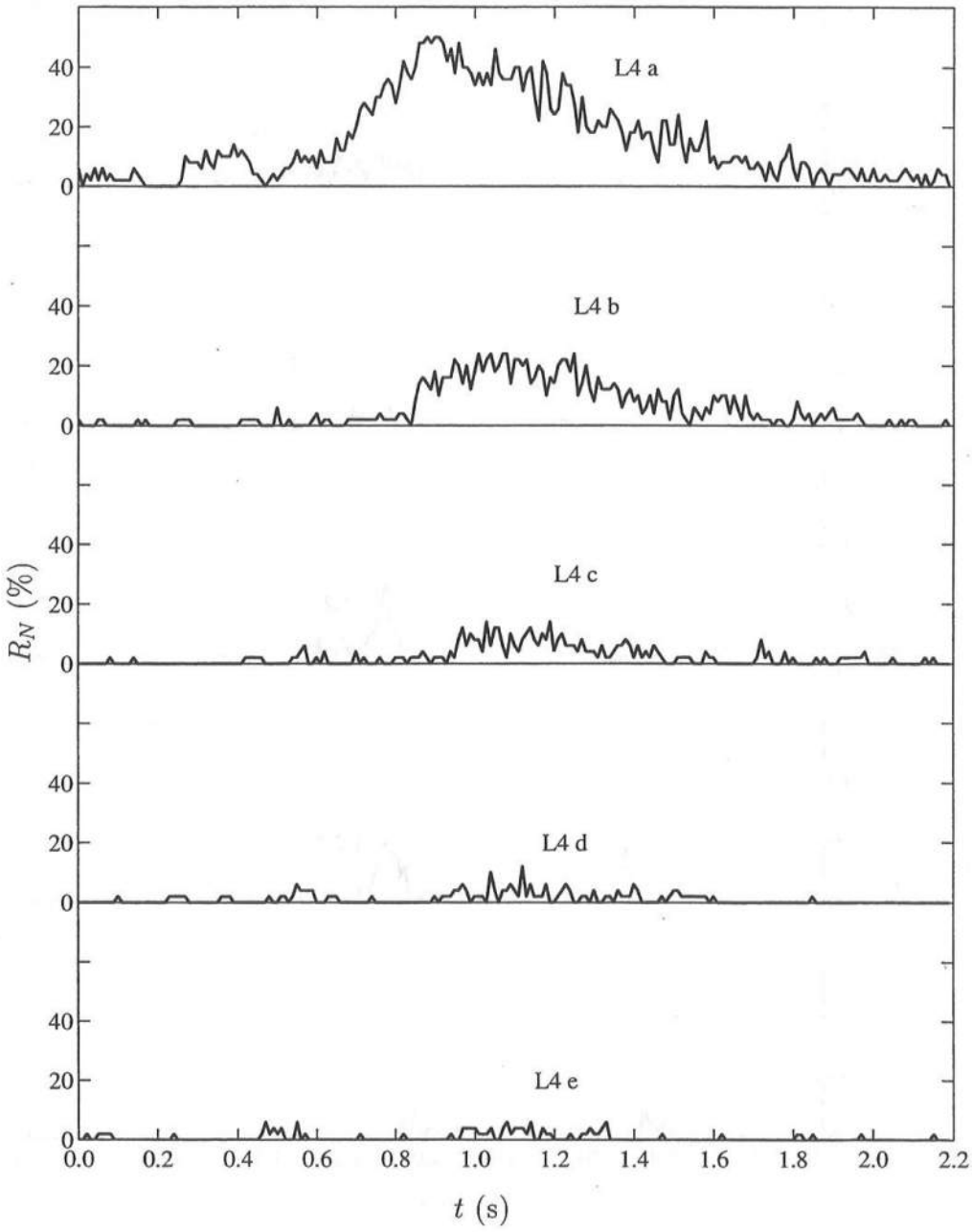

Figure 4.19: Temporal Variations of Phase-Averaged Dropout Rate, R_N, for Five Vertical Elevations for L4.

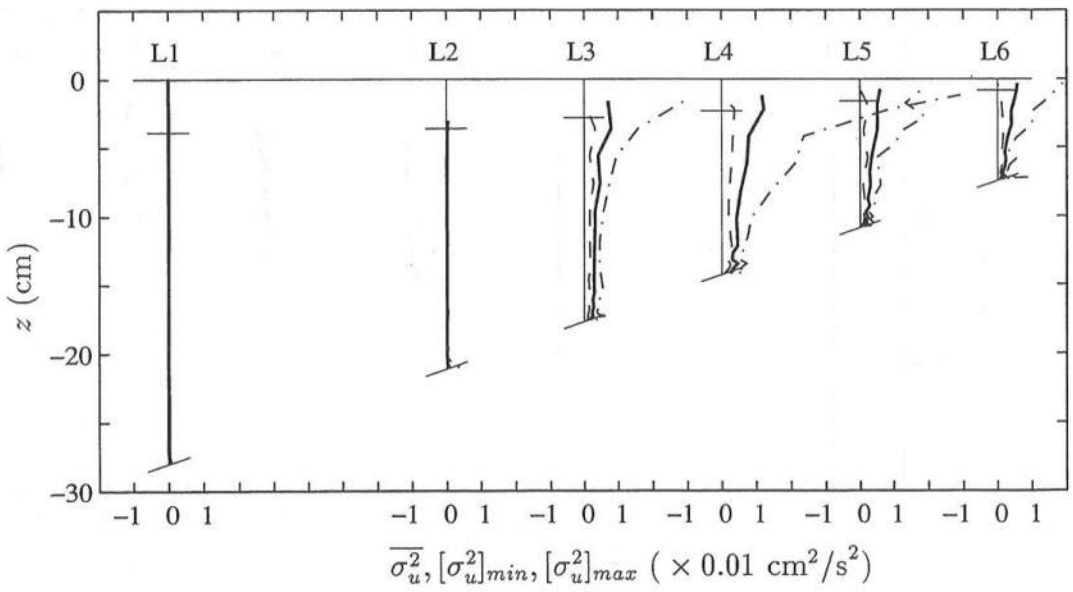

Figure 4.20: Cross-Shore Variations of Mean, Minimum and Maximum of Horizontal Velocity Variance with $\overline{\sigma_u^2}$ (——); $[\sigma_u^2]_{min}$ (– –); and $[\sigma_u^2]_{max}$ (–·–) for L1 to L6.

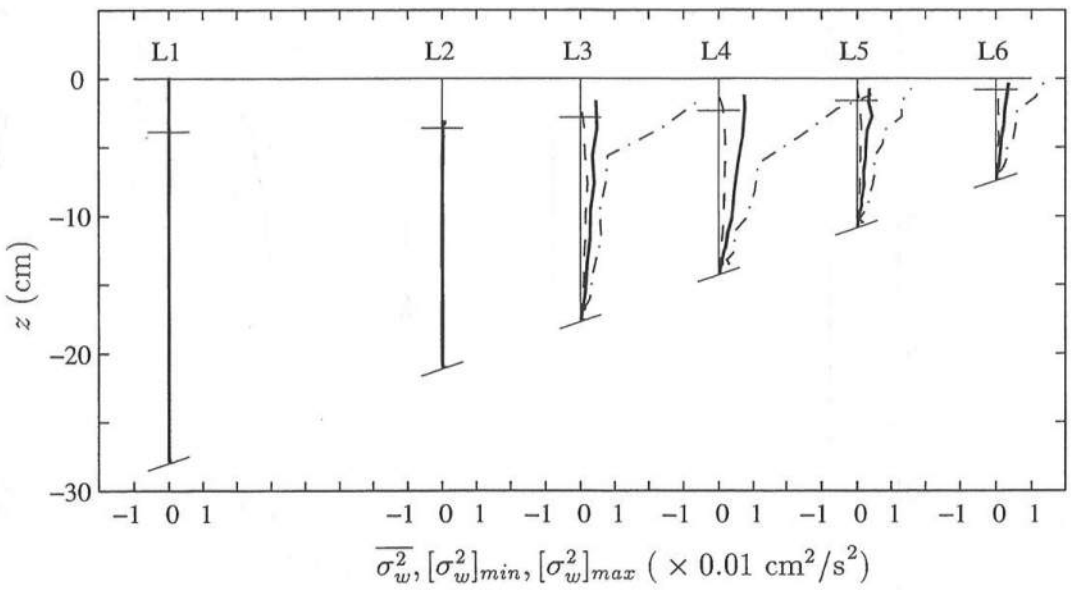

Figure 4.21: Cross-Shore Variations of Mean, Minimum and Maximum of Vertical Velocity Variance with $\overline{\sigma_w^2}$ (——); $[\sigma_w^2]_{min}$ (– –); and $[\sigma_w^2]_{max}$ (–·–) for L1 to L6.

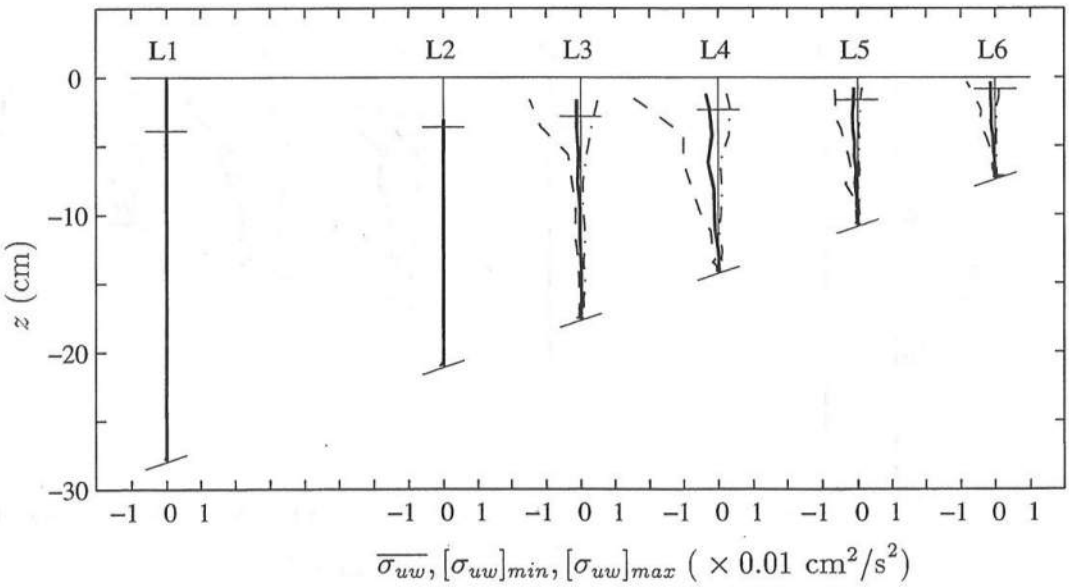

Figure 4.22: Cross-Shore Variations of Mean, Minimum and Maximum of Horizontal and Vertical Velocity Covariance with $\overline{\sigma_{uw}}$ (——); $[\sigma_{uw}]_{min}$ (– –); and $[\sigma_{uw}]_{max}$ (–·–) for L1 to L6.

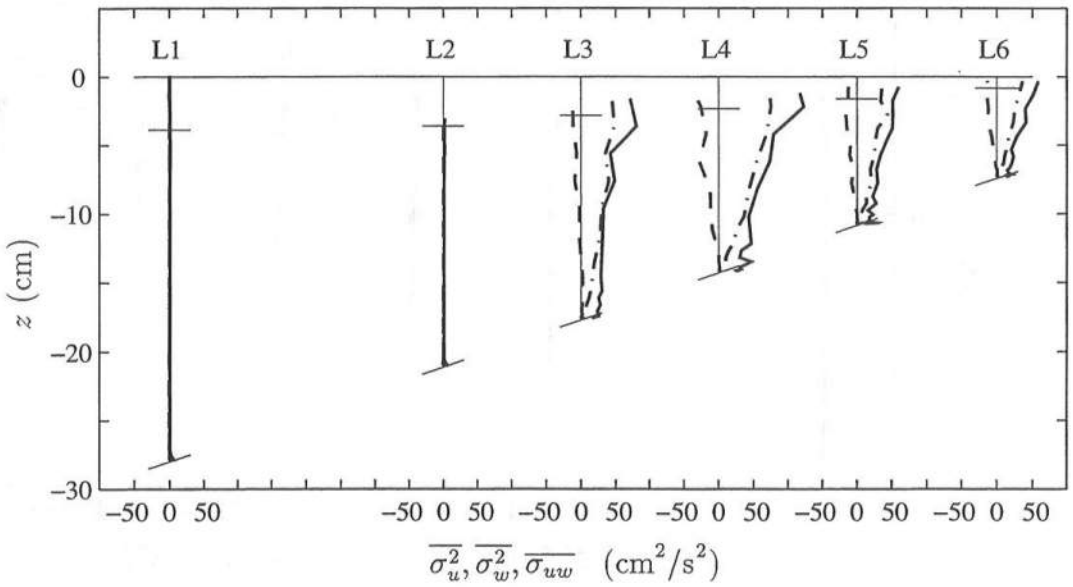

Figure 4.23: Cross-Shore Comparison of Mean Horizontal and Vertical Velocity Variances and Mean Covariance with $\overline{\sigma_u^2}$ (——); $\overline{\sigma_w^2}$ (–·–); and $\overline{\sigma_{uw}}$ (– –) for L1 to L6.

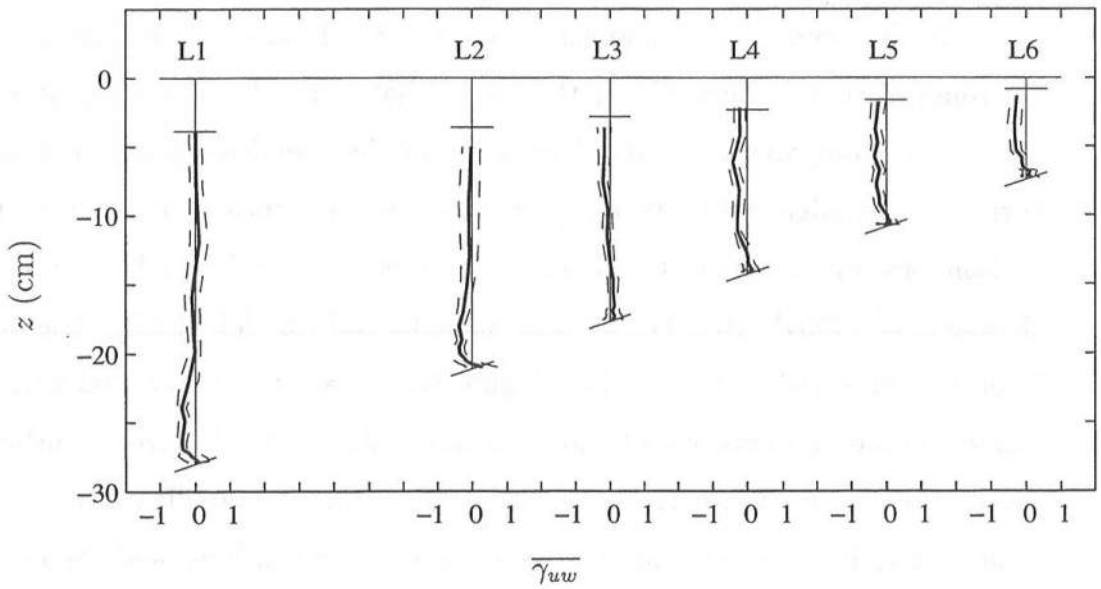

Figure 4.24: Cross-Shore Variations of Mean Correlation Coefficient, $\overline{\gamma_{uw}}$ (——), with One Standard Deviation Envelope (– –) for L1 to L6.

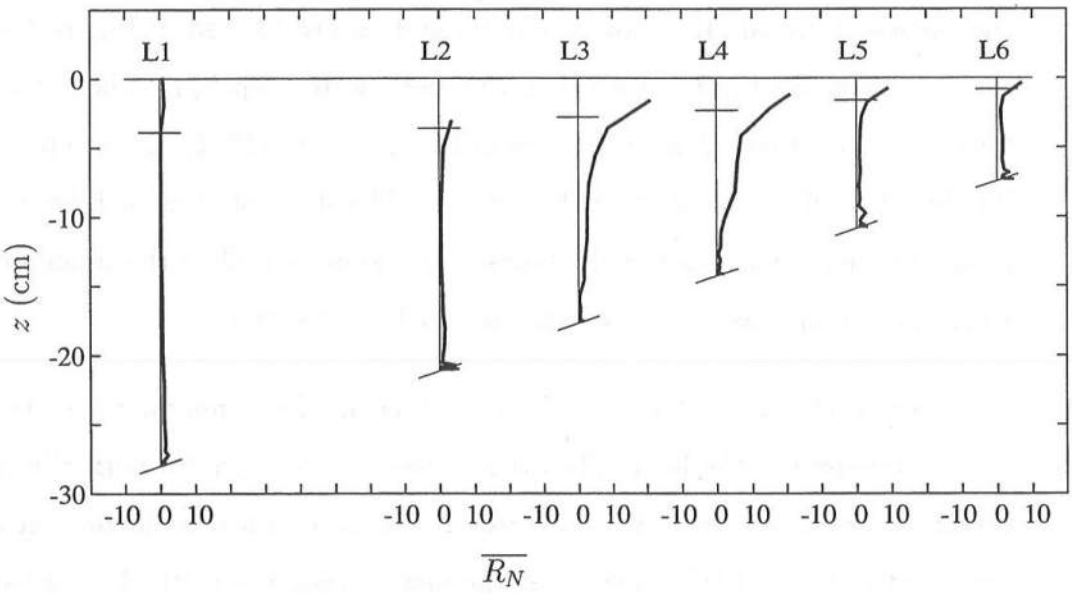

Figure 4.25: Cross-Shore Variations of Mean Dropout Rate, $\overline{R_N}$, for L1 to L6.

4.5 Comparison with Published Data

In this section, a comparison is made of the Froude-scaled, time-averaged horizontal turbulent intensity for the present data with data from the literature. Figure 4.26 compares the vertical variation of the Froude-scaled, time-averaged horizontal turbulent intensity, $\overline{\sigma_u}/\sqrt{g\overline{h}}$, where $\overline{h}$ is the mean water depth. Comparisons are made among the present measurements for L3 to L6, the data of George *et al.* (1994), Stive (1980), and Nadaoka and Kondoh (1982). The data of George *et al.* (1994) are from their Figure 8a and are for the natural surf zone, including random waves of both plunging and spilling type. The frozen turbulence assumption was used to extract the turbulent signal. The middle curve of George *et al.* (1994) indicates the mean value in several vertical bins, and the envelope is this mean ± 1 standard deviation plus the uncertainty in the data reduction. The data of Nadaoka and Kondoh (1982) are from their Figure 7 and are for Case 1, spilling waves on a 1:20 slope. Only the measuring lines inside the surf zone, i.e. P1 to P5, are shown in Figure 4.26. A frequency filter was used to extract the turbulent signal. It is noted that these data are plotted in Figure 4.26 using the still water depth, d, rather than the mean water depth, $\overline{h}$. The data of Stive (1980) are also taken from Figure 8a of George *et al.* (1994) and are presumably for Test 1, spilling waves on a 1:40 slope. The data plotted in Figure 4.26 include the measuring lines in the transition region as well as the inner surf zone. Phase-averaging was used to extract the turbulent signal.

Only the data of George *et al.* (1994) are for random, multi-directional waves measured in the field. The other three data sets are for normally incident, regular waves measured in the laboratory. The comparison of the present data set with that of Stive (1980) shows that the phase averaging method gives consistent results for laboratory waves of similar type. The comparison with Nadaoka and

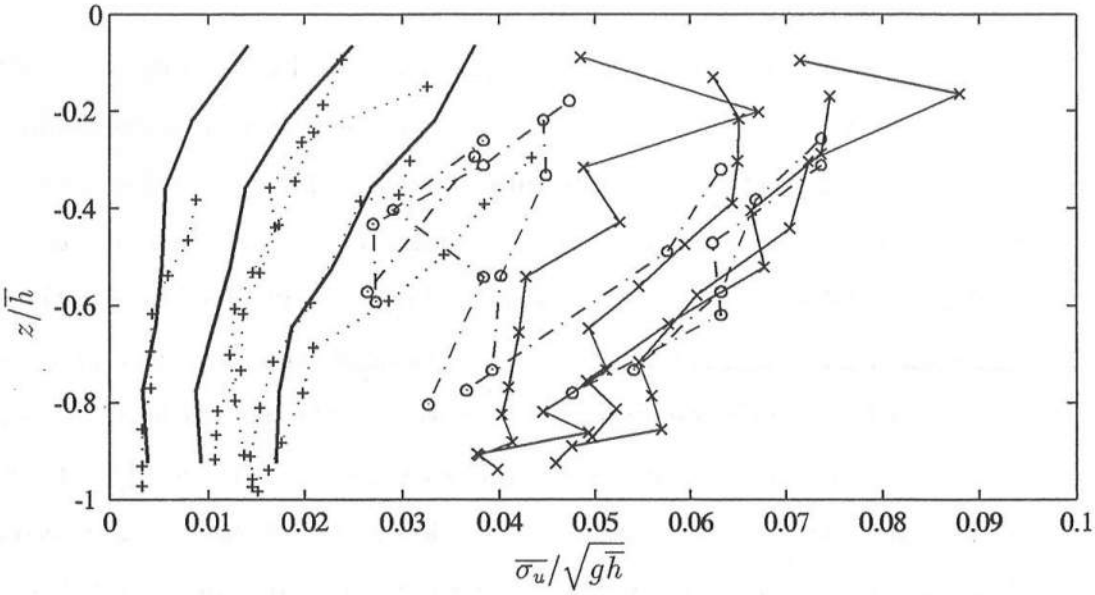

Figure 4.26: Comparison of Vertical Variation of Froude-Scaled Horizontal Turbulence Intensity with George *et al.* (1994) (——); Stive (1980) (o – – –); Nadaoka and Kondoh (1982) (+ · · · ·); Present Data L3 to L6 (× ——).

Kondoh (1982) indicates that the frequency filter may underestimate the turbulent signal as noted by other researchers (e.g., George *et al.* 1994). Nevertheless, it would be useful to have a relation between the turbulent signals from the two methods since phase averaging cannot be used for random waves in a natural surf zone. Interpretation of the data of George *et al.* (1994) is difficult, because of the method used to extract the turbulent signal, and because the waves were random and multi-directional. More work is necessary in this area.

4.6 Conditional Sampling for Large Eddies

A conditional sampling technique was used by Nadaoka *et al.* (1988) to relate sediment suspension in the surf zone and obliquely descending eddies, both of which are characterized by intermittent events. The motivation for their study was that sediment suspension due to spilling waves in the inner surf zone or bore region (L4 to L6 in the present study) might be affected less by the vertical diffusion or advection of wave generated turbulence and influenced predominantly by obliquely descending eddies left in the wake of the passing bore. A conditional sampling technique is applied here to remove the waves with the highest turbulence levels, and statistics of mean, variance, skewness and kurtosis are recomputed. Comparisons are made between the statistics computed for the total record and for the partial record with the large turbulent events removed. The figures are plotted as a function of depth and time, and the patterns in the reduction of the statistics are consistent with the idea of obliquely descending eddies. It is noted that this section does not treat the statistics rigorously since the confidence intervals and sensitivity are not reported. This section is included simply to add to the limited knowledge of the turbulent flow in the surf zone.

To illustrate the intermittent events, Figure 4.27 shows the temporal variation of the instantaneous measured horizontal and vertical velocities, u_m and w_m, for a portion of the wave record in the range $37.4 < t < 50.6$ s in the surf zone below trough level for L4b. The wave period is $T = 2.2$ s. The solid vertical lines are the signal dropouts, occurring in the u_m and w_m signals simultaneously. The dashed lines in the figure are the phase-averaged horizontal and vertical velocities, u_a and w_a, superposed at each wave period to show in some sense the definition of turbulence adopted in this dissertation. The turbulent signal is the difference between the solid and dashed lines. In general, this definition is reasonable; but

at the 22nd wave in the range 46.2 s $< t <$ 48.4 s, there is a large component included in the turbulent signal which may be due to organized motions such as an obliquely descending eddy. These large deviations are of interest in this section and are termed *intermittent events* since they do not occur for each wave period.

The conditional sampling technique adopted here is subject to an intuitive but reasonable critical level of turbulence in both the u_m and w_m records as explained in the following. The instantaneous turbulent velocity components of the measured horizontal and vertical velocity signals, u' and w', are given as

$$u'(x,z,t) = u_m(x,z,t) - u_a(x,z,t) \tag{4.22}$$

$$w'(x,z,t) = w_m(x,z,t) - w_a(x,z,t) \tag{4.23}$$

where the phase averaged velocities computed for the range $0 < t <$ 2.2 s are repeated over the 50 waves and the primes indicate turbulent fluctuations rather than normalized quantities as in Chapter 2. This turbulent signal at a given (x,z) location is divided into $N_w = 50$ segments starting with the phase of the zero-upcrossing from the free surface signal. This was done to minimize an intermittent event spanning two segments. The part of the first wave truncated before the first zero-upcrossing was added to the last wave to make 50 complete segments. The segmented turbulent signals at a given (x,z) location are written

$$[u'(t_j)]_n \quad \text{and} \quad [w'(t_j)]_n \tag{4.24}$$

where t_j is the discrete time over one segment, $t_j = (j-1)\Delta t$ for $j = 1, 2, \ldots, J$ with $J = 220$ points per segment; and n is the counter for each segment, $n = 1, 2, \ldots, N_w$ with $N_w = 50$ segments. The number of points *in a segment* excluding the dropouts at a given (x,z) location is $[N(x,z)]_n$ for $n = 1, 2, \ldots, N_w$. The mean horizontal and vertical turbulent velocities for each segment, $\left[\overline{u'}\right]_n$ and $\left[\overline{w'}\right]_n$,

excluding the dropouts, are given as

$$\left[\overline{u'}\right]_n = \frac{1}{[N]_n}\sum_{j=1}^{[N]_n}[u'(t_j)]_n \text{ for } n = 1,2,\ldots,N_w \tag{4.25}$$

$$\left[\overline{w'}\right]_n = \frac{1}{[N]_n}\sum_{j=1}^{[N]_n}[w'(t_j)]_n \text{ for } n = 1,2,\ldots,N_w. \tag{4.26}$$

The standard deviation of the horizontal and vertical turbulent velocities for each segment, $[\sigma_{u'}]_n$ and $[\sigma_{u'}]_n$, are given as

$$[\sigma_{u'}]_n = \left\{\frac{1}{[N]_n - 1}\sum_{j=1}^{[N]_n}\left([u'(t_j)]_n - \left[\overline{u'}\right]_n\right)^2\right\}^{1/2} \text{ for } n = 1,2,\ldots,N_w \tag{4.27}$$

$$[\sigma_{w'}]_n = \left\{\frac{1}{[N]_n - 1}\sum_{j=1}^{[N]_n}\left([w'(t_j)]_n - \left[\overline{w'}\right]_n\right)^2\right\}^{1/2} \text{ for } n = 1,2,\ldots,N_w. \tag{4.28}$$

The mean standard deviation of the horizontal and vertical turbulent velocities over all 50 segments, $\overline{[\sigma_{u'}]_n}$ and $\overline{[\sigma_{w'}]_n}$, at a given (x,z) location are given as

$$\overline{[\sigma_{u'}]_n} = \frac{1}{N_w}\sum_{n=1}^{N_w}[\sigma_{u'}]_n \tag{4.29}$$

$$\overline{[\sigma_{w'}]_n} = \frac{1}{N_w}\sum_{n=1}^{N_w}[\sigma_{w'}]_n\,. \tag{4.30}$$

Using the above definition, a critical turbulence level for the horizontal and vertical turbulent velocities at a given (x,z) location may be taken as

$$(\sigma_{u'})_{crit} = \alpha_{cr}\overline{[\sigma_{u'}]_n} \tag{4.31}$$

$$(\sigma_{w'})_{crit} = \alpha_{cr}\overline{[\sigma_{w'}]_n}, \tag{4.32}$$

where α_{cr} is a sensitivity parameter selected to be in the range $1.0 < \alpha_{cr} < 1.5$.

The condition for which a segment is assumed to contain an intermittent event is based on the standard deviation of the turbulent velocity of that segment

which exceeds the following critical turbulence level set for all the segments at that given (x, z) location,

$$[\sigma_{u'}]_n > (\sigma_{u'})_{crit} \quad \text{and} \quad [\sigma_{w'}]_n > (\sigma_{w'})_{crit} \quad \text{for } n = 1, 2, \ldots, N_w \tag{4.33}$$

In this way, the conditional sampling method accounts for the spatial variations in the turbulence level.

Using Eq 4.33, the velocity record at a given location is divided into two groups with the first consisting of intermittent events and the second consisting of the remaining segments. Table 4.3 lists the number of intermittent events, $[N_{ie}]_{ave}$, averaged over each measuring line in the surf zone for the range $1.0 < \alpha_{cr} < 1.5$. The number of intermittent events is fairly constant for a given α_{cr} for L4 to L6 where the bore is well established. For L3 where the wave is in transition, $[N_{ie}]_{ave}$ is consistently lower for a given α_{cr} with the exception of $\alpha_{cr} = 1.0$. The table indicates the sensitivity of the conditional sampling to the critical turbulence level and also indicates that there is no clear threshold which might separate the two groups. The lack of a clear threshold is probably because of the limitations of the point measurement technique and the nature of the descending eddy instead of the limited number of segments. If the intermittent events are due to obliquely descending eddies shed with the passing of a bore, and if these eddies are distributed randomly in the y-direction across the wave, then the eddy may not pass directly through the measuring volume. Another technique such as particle image velocimetry (Adrian 1991) could be applied to study the turbulent flow field in connection to intermittent events or obliquely descending eddies.

Despite the limitations of the point measurement technique, the relatively small number of waves, and the subjectivity of the conditional sampling method, the phase-averaged quantities are recomputed for the conditionally samples waves. Following Eqs 4.6 to 4.9 and Eqs 4.15 to 4.18, the mean, variance, skewness and

Table 4.3: Mean Number of Intermittent Events for Given α_{cr}.

Line No.	$[N_{ie}]_{ave}$ α_{cr} 1.0	1.1	1.2	1.3	1.4	1.5
L3	14.2	7.6	4.2	2.0	0.9	0.6
L4	14.2	9.1	5.2	3.1	2.1	1.6
L5	14.1	8.6	5.6	3.9	2.1	1.2
L6	14.0	9.4	6.2	4.5	2.7	1.2

kurtosis are computed for the second group of waves consisting of those segments whose turbulence level was below the critical value. These quantities are denoted with a hat. The statistics of the first group of waves, those segments whose turbulence level exceeded the critical value, were not computed since the sample size was small. Repeating the caveat from Section 4.1, the skewness and kurtosis are less stable statistics, and their results should be interpreted with caution.

For the following figures, the value of $\alpha_{cr} = 1.1$ was selected since it gave a reasonable number of intermittent events as listed in Table 4.3. Assuming an eddy size of 10 cm in the 60 cm wide tank, this would give a cross-tank "eddy density" of about 17%. For observations fixed in the x-z plane, one would expect about 8 or 9 waves out of 50 to contain intermittent events. The effect of conditional sampling for this choice of α_{cr} for the four lines listed in Table 4.3 removes about nine waves with the highest turbulence levels. As a result, the choice of $\alpha_{cr} = 1.1$ may be reasonable qualitatively.

Figure 4.28 shows the vertical variations of the phase-averaged horizontal and vertical velocities without conditional sampling, u_a and w_a, and with conditional sampling, $\hat{u}_a$ and $\hat{w}_a$, at six phases for L4. The free surface elevation

and bottom location are marked by a light solid line. The effect of conditional sampling on u_a and w_a is small except for a slight change in u_a at $t = 2T/6$ near upper portion of the measured water column.

Figure 4.29 shows the vertical variations of the horizontal and vertical velocity variances without conditional sampling, σ_u^2 and σ_w^2, and with conditional sampling, $\hat{\sigma}_u^2$ and $\hat{\sigma}_w^2$, at six phases for L4. The variances are noticeably reduced with conditional sampling. The pattern for both the horizontal and vertical variances is a reduction in the variance over a fixed portion of the water column at a given phase. At $t = 2T/6$, the variance is reduced only in the upper portion of the water column; at $t = 3T/6$ and $t = 4T/6$, the variance is reduced mostly in the middle; and at $t = 5T/6$, the vertical variance is reduced near the bottom. At $t = 0$ and $t = T/6$, the variance is unchanged. This pattern is consistent with the idea of an obliquely descending eddy. The conditional sampling shows that a fair amount of turbulent energy is contained in a few number of waves passing a given point in the surf zone where the bore is well established for a spilling breaker.

Figure 4.30 shows the vertical variation of the horizontal and vertical velocity skewness without conditional sampling, ζ_u and ζ_w, and with conditional sampling, $\hat{\zeta}_u$ and $\hat{\zeta}_w$, at six phases for L4. To reduce the noise in this and the following figure, the quantities shown are the average of the value at the given phase and the two nearest points. For example, the horizontal velocity skewness without conditional sampling at six phases is given as

$$\zeta_u\left[t = nT/6\right] = \frac{1}{5}\left[\zeta_u^{nj-2} + \zeta_u^{nj-1} + \zeta_u^{nj} + \zeta_u^{nj+1} + \zeta_u^{nj+2}\right] \tag{4.34}$$

where $n = 0, 1, \ldots, 5$ and $j = 37$ corresponding approximately to $T/6$ for $J = 220$ phases per wave period. Qualitatively, it is interesting to note the sign of the skewness for only those curves without conditional sampling. The horizontal velocity skewness is generally positive everywhere except at $t = 0$ and $t = T/6$

near the free surface where the sign is negative and for all phases near the bottom where the skewness is noisy. For the vertical velocity skewness, the signs are reversed. With the conditional sampling, the skewness is reduced in a pattern similar to the variance in Figure 4.29 although it is less pronounced.

Figure 4.31 shows the vertical variations of the horizontal and vertical velocity kurtosis without conditional sampling, κ_u and κ_w, and with conditional sampling, $\hat{\kappa}_u$ and $\hat{\kappa}_w$, at six phases for L4. Again, this figure shows a fair amount of noise even with the 5-point smoothing given in Eq 4.34. The physical interpretation of the kurtosis is that it amplifies extreme events. A record of suspended sediment concentrations near the bottom in the surf zone is characterized by a spiked and intermittent signal (e.g., Beach and Sternberg 1988). This signal would have a large value of kurtosis compared to the wave record taken directly above. It is thought that obliquely descending eddies would increase the kurtosis of the turbulent signal since they are intermittent events of high intensity. Comparing the two curves with and without conditional sampling for both the horizontal and vertical kurtosis, it can be seen that there is a general reduction in the kurtosis with the removal of the conditionally sampled waves following the pattern of the previous two figures.

Although it is no surprise that removing the largest deviations from the record reduces these statistics, it is interesting to see that the pattern of the reduction seems consistent with the idea of obliquely descending eddies. This analysis also indicates limitations in discerning three-dimensional eddies from point measurements.

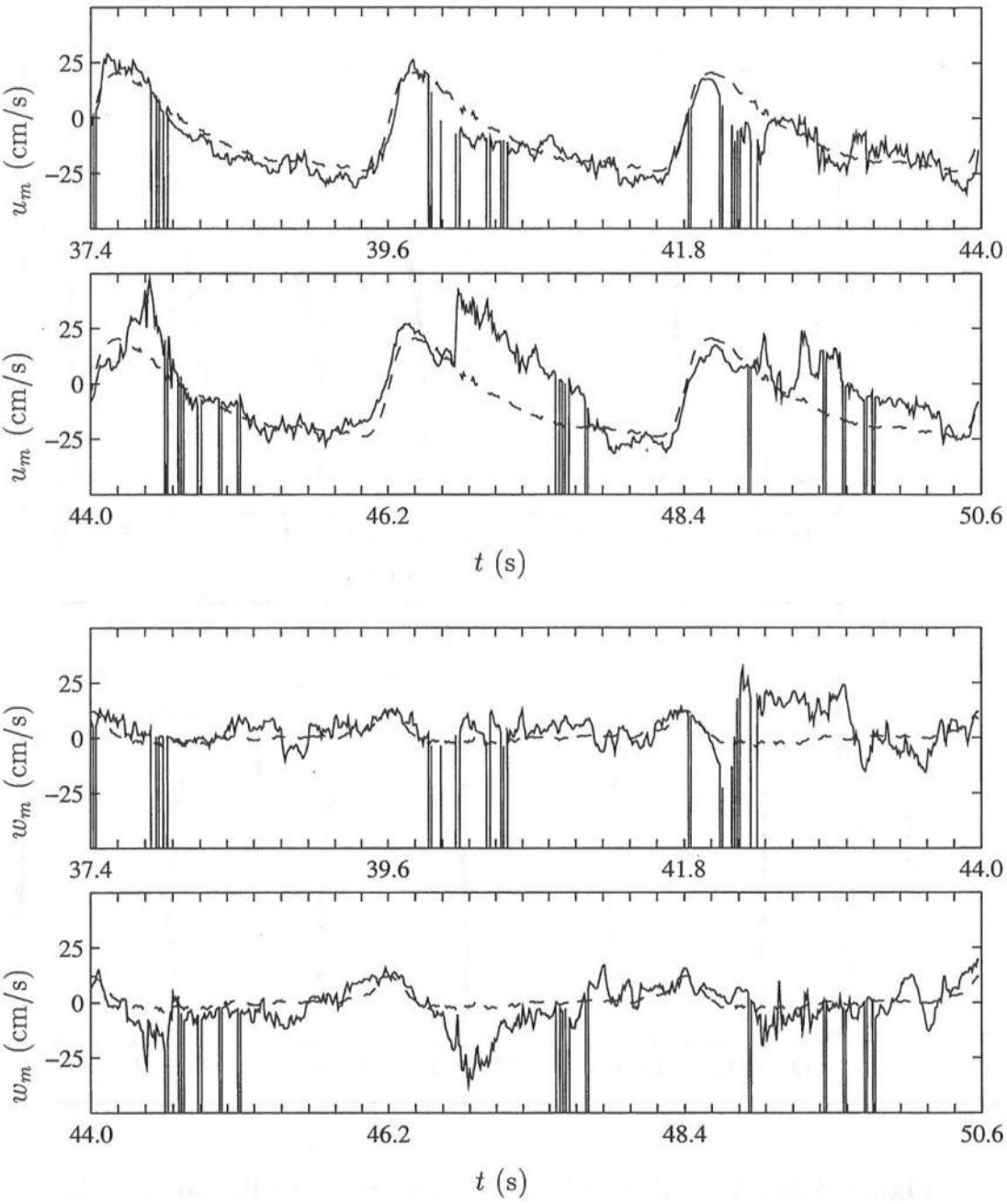

Figure 4.27: Temporal Variations of Measured Horizontal Velocity, u_m (——), and Phase-Averaged Horizontal Velocity, u_a (– –), (Top Two Panels); Temporal Variations of Measured Vertical Velocity, w_m (——), and Phase-Averaged Vertical Velocity, w_a (– –), (Bottom Two Panels), for Six Wave Periods for L4b.

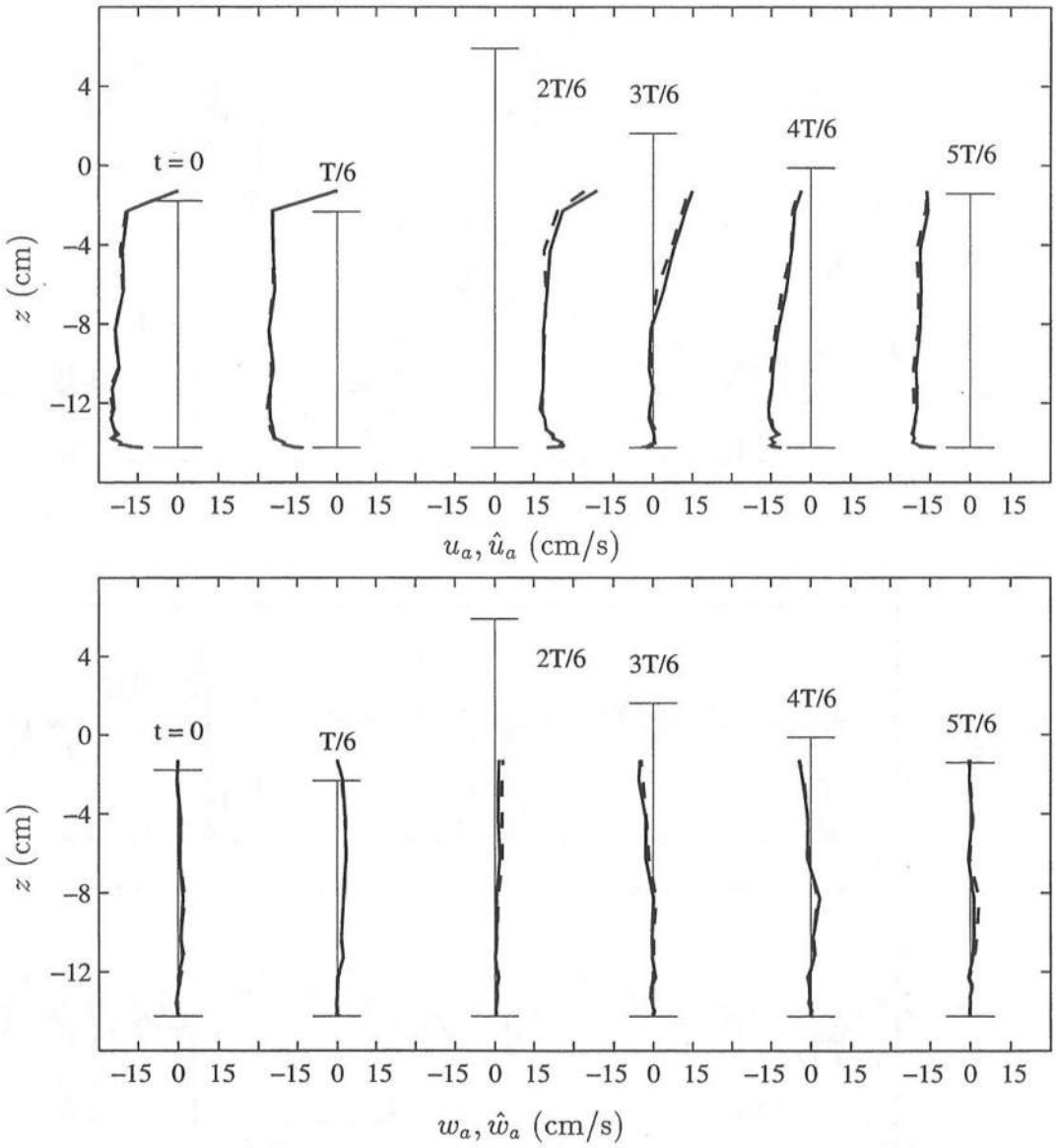

Figure 4.28: Vertical Variations of Phase-Averaged Horizontal Velocity without Conditional Sampling, u_a (——), and with Conditional Sampling, $\hat{u}_a$ (– –), (Top); Vertical Variations of Phase-Averaged Vertical Velocity without Conditional Sampling, w_a (——), and with Conditional Sampling, $\hat{w}_a$ (– –), (Bottom), at Six Phases for L4.

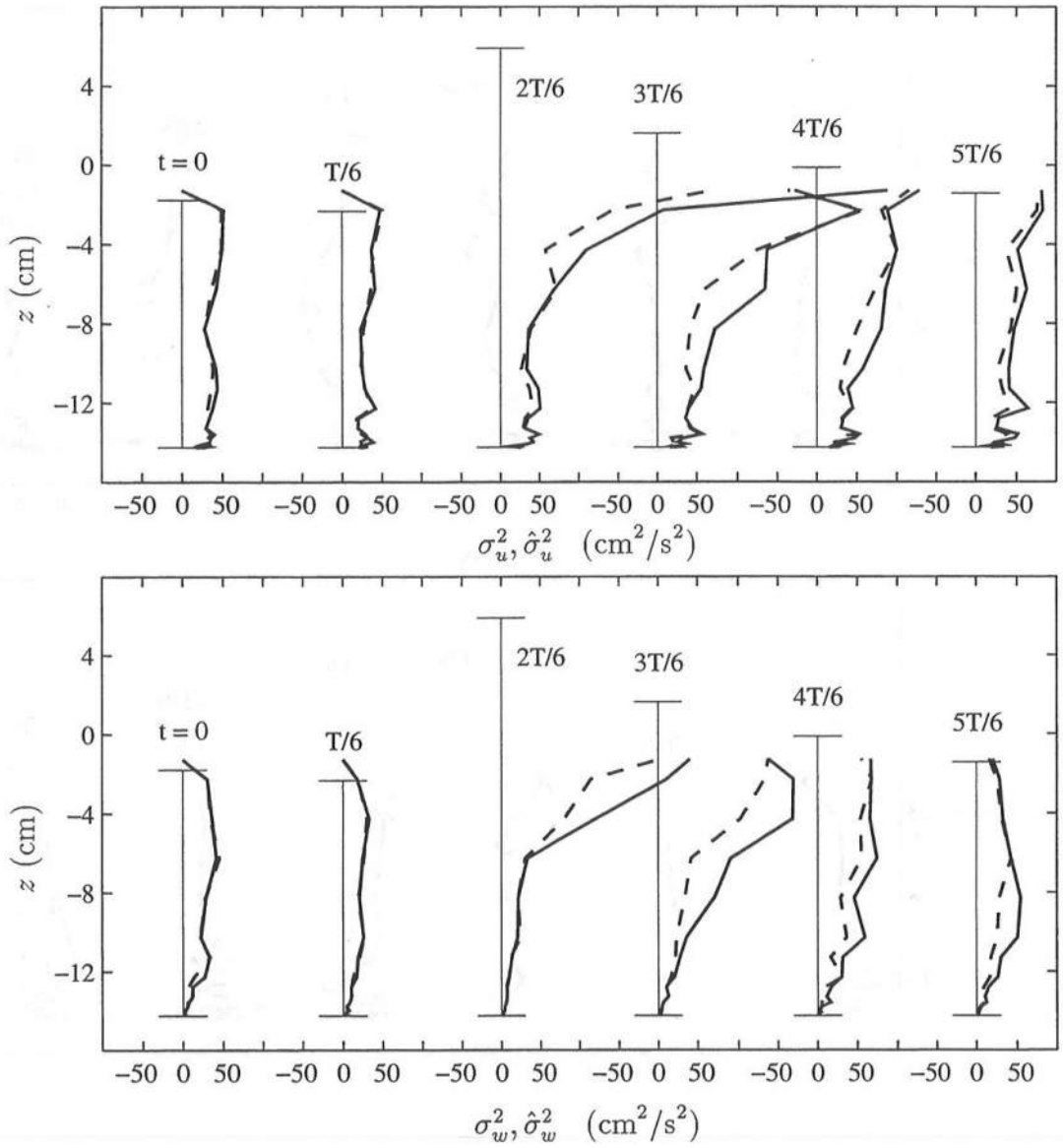

Figure 4.29: Vertical Variations of Phase-Averaged Horizontal Velocity Variance without Conditional Sampling, σ_u^2 (——), and with Conditional Sampling, $\hat{\sigma}_u^2$ (– –), (Top); Vertical Variations of Phase-Averaged Vertical Velocity Variance without Conditional Sampling, σ_w^2 (——), and with Conditional Sampling, $\hat{\sigma}_w^2$ (– –), (Bottom), at Six Phases for L4.

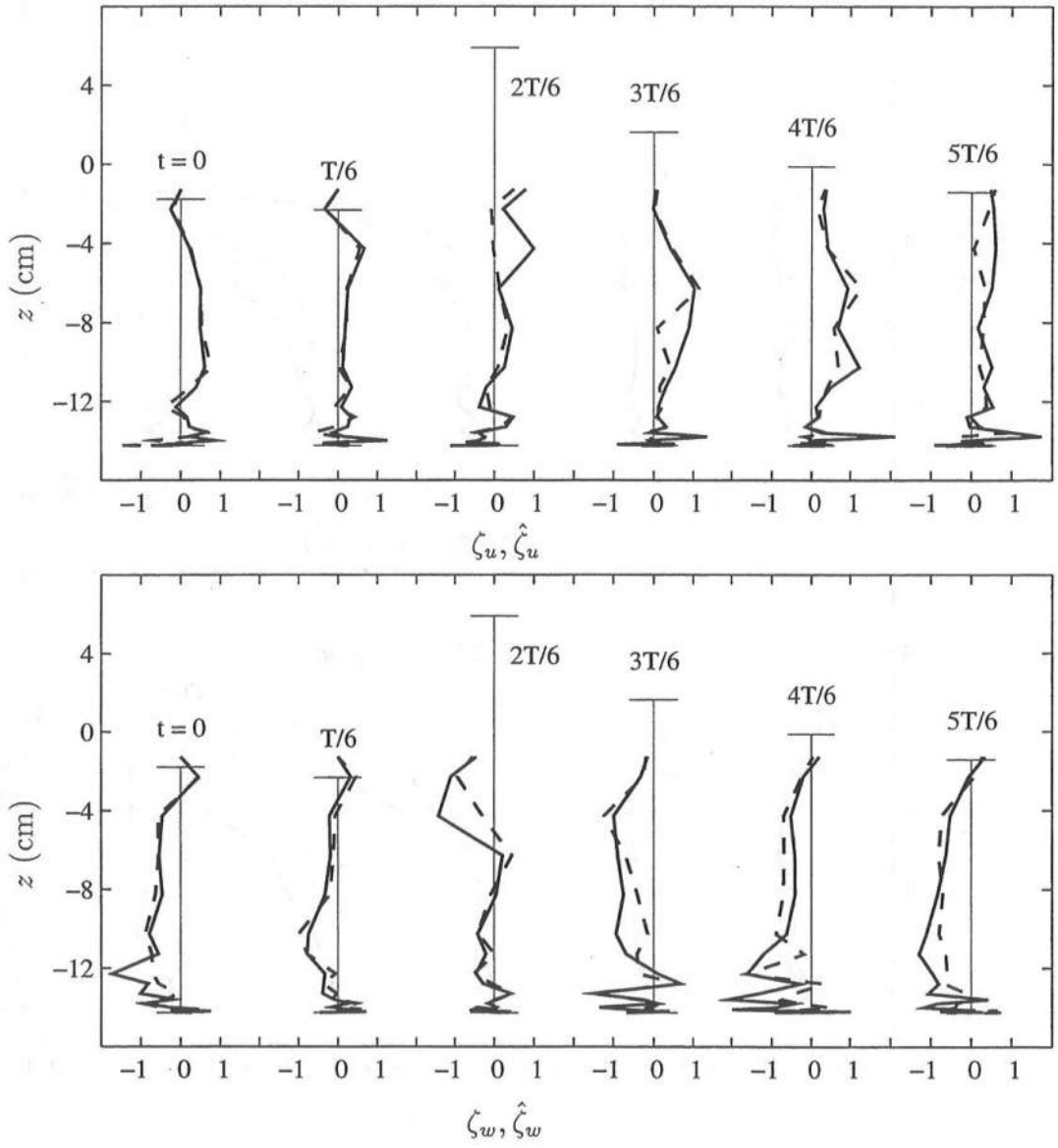

Figure 4.30: Vertical Variations of Phase-Averaged Horizontal Velocity Skewness without Conditional Sampling, ζ_u (——), and with Conditional Sampling, $\hat{\zeta}_u$ (– –), (Top); Vertical Variations of Phase-Averaged Vertical Velocity Skewness without Conditional Sampling, ζ_w (——), and with Conditional Sampling, $\hat{\zeta}_w$ (– –), (Bottom), at Six Phases for L4.

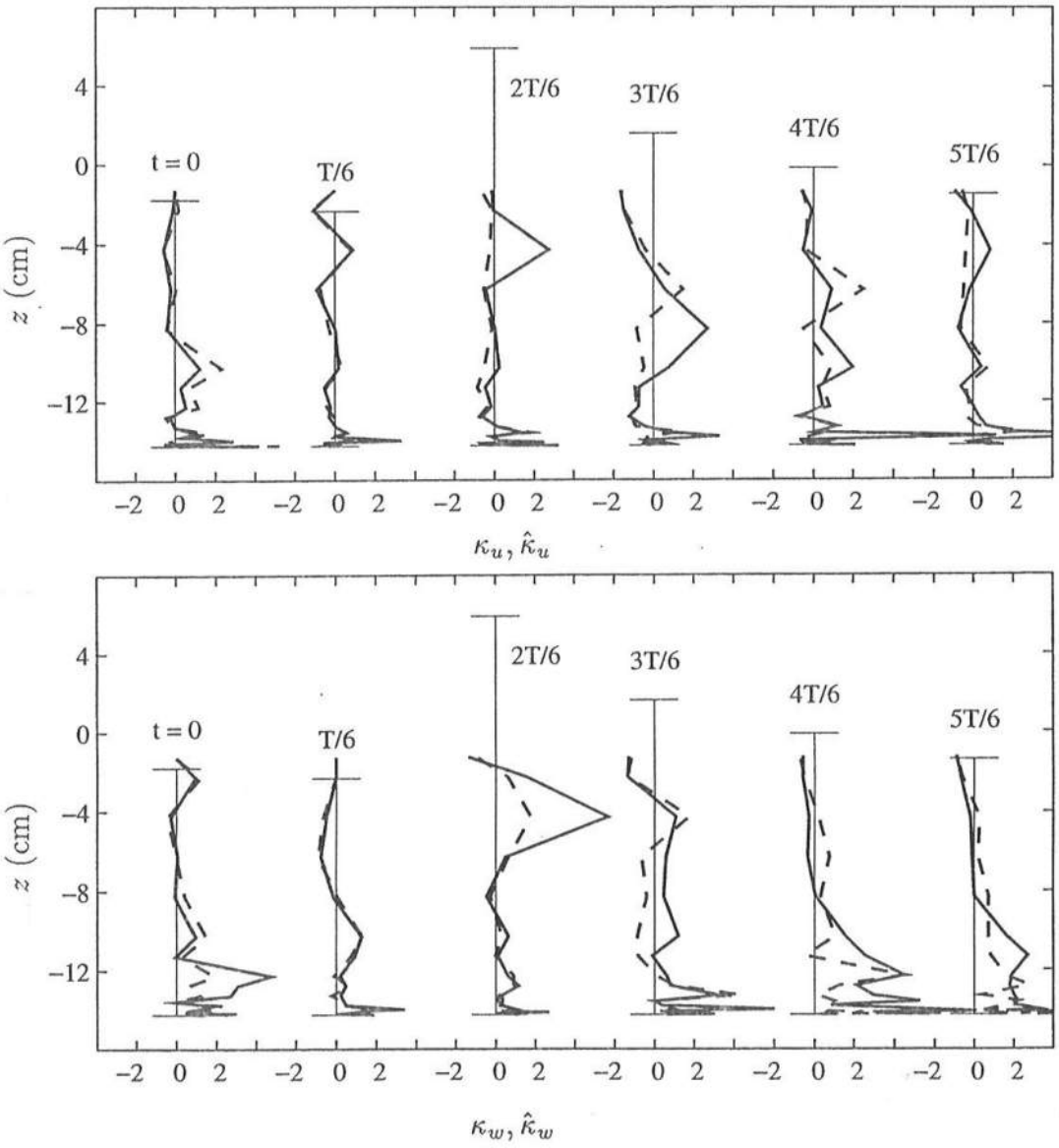

Figure 4.31: Vertical Variations of Phase-Averaged Horizontal Velocity Kurtosis without Conditional Sampling, κ_u (——), and with Conditional Sampling, $\hat{\kappa}_u$ (– –), (Top); Vertical Variations of Phase-Averaged Vertical Velocity Kurtosis without Conditional Sampling, κ_w (——), and with Conditional Sampling, $\hat{\kappa}_w$ (– –), (Bottom), at Six Phases for L4.

Chapter 5

BOTTOM BOUNDARY LAYER ANALYSIS

A general introduction to boundary layer theory in the context of coastal processes was given in the literature review in Chapter 1, and the importance of estimating the bottom shear stress for sediment transport models was noted. In this chapter, the temporal variations of the bottom shear stress under breaking waves are estimated using the phase-averaged horizontal velocities presented in Chapter 4. The focus of this chapter is to show the applicability of models developed under non-breaking waves in predicting the shear stress and bottom roughness in the surf zone.

In studying the bottom boundary layer, several quantities are of interest including estimates of the bottom shear stress, the bottom roughness, and the thickness of the boundary layer. Several methods have been used to estimate the bottom shear stress. Direct measurements by means of a flush mounted hot film probe have been used for oscillatory flows over a smooth bottom (e.g., Jensen *et al.* 1989; Deigaard *et al.* 1992) and by means of a shear plate for flows over a rough bottom (e.g., Kamphius 1975; Simons *et al.* 1992, 1994). A second method to estimate the bottom shear stress involves integrating the velocity deficit in the bottom boundary layer (e.g., Sleath 1987). However, this method neglects the nonlinear advection terms. This assumption may be valid for flow in an oscillating water tunnel, but is likely to be incorrect for measurements under breaking waves.

Also, this method is more difficult to apply for surf zone measurements since the shear stress is not zero above the bottom boundary layer. Further, this method does not give an estimate of the bottom roughness. A third method involves a logarithmic fit of the measured velocities in the bottom boundary layer and has been applied to flows measured over the continental shelf (e.g., Grant *et al.* 1983) and oscillating water tunnel experiments (e.g., Jonsson and Carlsen 1976; Jensen *et al.* 1989). The logarithmic fit method also gives an estimate of the bottom roughness which can be related to the Nikuradse equivalent sand roughness.

This chapter is organized as follows. Section 5.1 gives a definition of the theoretical bottom location and describes the measuring point locations near the bottom. Section 5.2 discusses the theoretical background of the logarithmic velocity region. Section 5.3 discusses the logarithmic fit using the least-squares method and presents the estimates of the temporal variation of the bottom shear velocity and bottom roughness. Section 5.4 discusses the sensitivity of the estimates to the bottom displacement. Section 5.5 discusses the near bottom shear stress estimates by the measurements of the horizontal and vertical velocity covariance in comparison to the bottom shear stress estimates by the least-squares method. Section 5.6 discusses the estimates of the bottom shear velocity and bottom roughness with the eight additional measuring points. These points were taken at a horizontal offset of $\Delta x = \pm 2$ cm, and the results of this section indicate the sensitivity of the estimates to irregularities in the rough bottom. Section 5.7 discusses the thickness of the wave boundary layer since velocity measurements just outside the boundary layer are used in the next section. Section 5.8 discusses the bottom friction and compares the estimates of the shear velocity from the least-squares method to estimates using the velocity outside the bottom boundary layer. This section also discusses the bottom roughness estimates.

5.1 Bottom Definition

This section discusses the bottom definition and the location of the measuring points near the bottom.

Figure 5.1 shows a schematic detail of the bottom boundary layer with the bottom roughness. There are two vertical coordinates as mentioned in Section 3.3.2, where the vertical coordinate, z, is defined with $z = 0$ at the still water level (SWL) and the vertical coordinate, z_m, is defined with respect to the bottom roughness with $z_m = 0$ at the top of the Plexiglas sheet. The relation between the two vertical coordinates is given as

$$z_m = z + d \tag{5.1}$$

where d is the depth below the SWL to the Plexiglas. The theoretical bottom location of zero horizontal velocity with respect to the z axis, $z = z_b$, is given as

$$z_b = d_* + z_0 - d \tag{5.2}$$

where z_0 is the bottom roughness height and d_* is the displacement distance as explained in the next section.

Figure 5.1 also shows schematically the roughness elements composed of sand grains with a median diameter $d_{50} = 1$ mm. The median roughness height is indicated by a light dashed line, and the theoretical bottom location is indicated by a light solid line. The measuring points are indicated by the solid circles and indicate that the first measuring point from the bottom is a fraction of the grain height above the median roughness height.

Figure 5.2 shows a schematic for the measuring points locations well inside the bottom boundary layer for a given measuring line. The main measuring line for which the measuring points extend from the bottom to the wave trough level

is indicated by Δx^0. Eight additional measuring points were taken at two offset measuring lines denoted Δx^- and Δx^-, where the horizontal offset distance is -2 cm and $+2$ cm, respectively. Only four measuring points were taken in each offset measuring line. This system of eight points with two offset measuring lines was used for L1, L2, L4, and L5. For L3, all of the eight additional points were in the same measuring line at Δx^-. For L6, no additional measuring points were included. The eight additional measuring lines will be used in Section 5.6 to show the sensitivity of the results to irregularities in the bottom roughness.

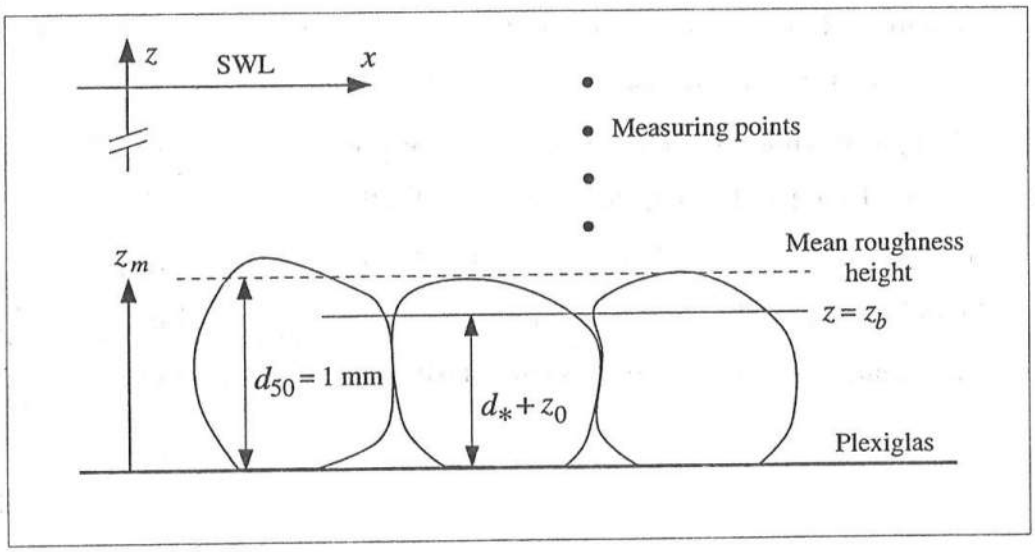

Figure 5.1: Detail of Bottom Boundary Layer with Bottom Roughness (not to scale).

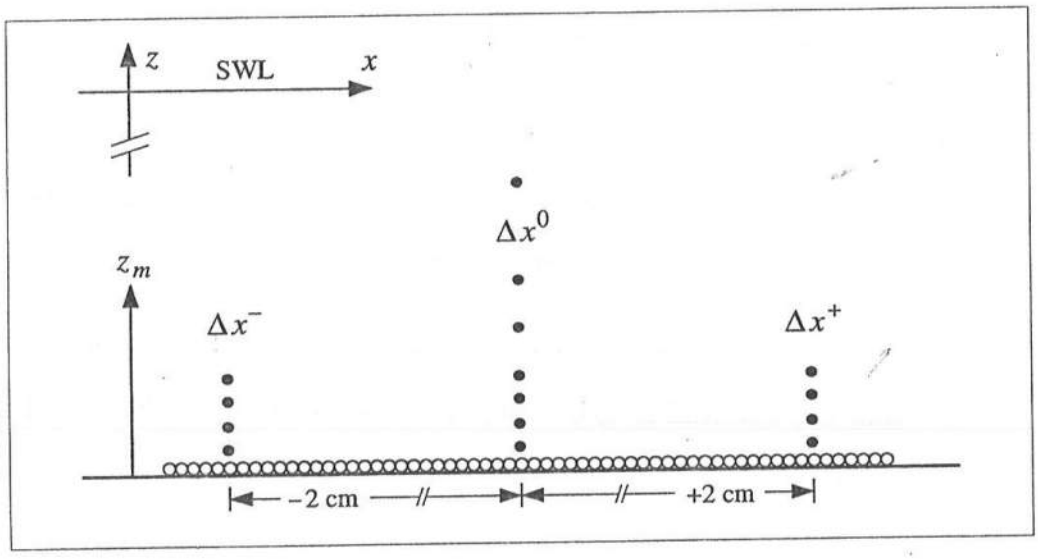

Figure 5.2: Measuring Point Locations Well Inside Bottom Boundary Layer (not to scale).

5.2 Logarithmic Velocity Region

The theoretical derivation of the logarithmic velocity region is presented here following Yaglom (1979). The assumptions used to derive the equation for the logarithmic velocity region are emphasized.

The case considered is for a steady turbulent wall flow without a pressure gradient. The coordinate system is similar to that used throughout this dissertation: x is the horizontal coordinate, positive in the direction of the flow; and z_m is the vertical coordinate, positive upward with $z_m = 0$ at the bottom. The dimensional parameters for the case of a smooth bottom are the kinematic viscosity, ν, a vertical length scale, δ, and a velocity scale which is taken as the shear velocity, u_*, where

$$u_* = \left(\frac{\tau_b}{\rho}\right)^{1/2} \tag{5.3}$$

and ρ is the fluid density and τ_b is the bottom shear stress. The bottom shear stress for the case of a smooth bottom is given by

$$\tau_b = \rho\nu\frac{\partial u}{\partial z_m} \tag{5.4}$$

where $u = u(z_m)$ is the mean horizontal velocity and will be taken as the phase-averaged horizontal velocity $u = u_a$ later.

There are two independent length scales: a viscous length scale, $\delta_v = \nu/u_*$, and the external length scale, δ, which will be the boundary layer thickness. A dimensional analysis for the mean flow velocity gives

$$u(z_m) = u_*\Phi\left(\frac{u_* z_m}{\nu}, \frac{z_m}{\delta}\right) \tag{5.5}$$

and for the velocity gradient

$$\frac{du(z_m)}{dz_m} = \frac{u_*}{z_m}\phi\left(\frac{u_* z_m}{\nu}, \frac{z_m}{\delta}\right) \tag{5.6}$$

where Φ and ϕ are universal functions related by

$$\phi(r_1, r_2) = r_1 \frac{\partial \Phi}{\partial r_1} + r_2 \frac{\partial \Phi}{\partial r_2} \tag{5.7}$$

with $r_1 = (u_* z_m/\nu) = z_m/\delta_v$ and $r_2 = z_m/\delta$.

Considering only fully developed turbulent flows implies both

$$Re = \frac{u_1 \delta}{\nu} >> 1 \tag{5.8}$$

and

$$Re_* = \frac{u_* \delta}{\nu} = \frac{\delta}{\delta_v} >> 1 \tag{5.9}$$

where Re is the Reynolds number, u_1 is the free stream velocity, and Re_* is the shear Reynolds number. It can be argued from Eq 5.9 that near the wall the influence of the length scale δ is small so that Eqs 5.5 and 5.6 give

$$\left.\begin{aligned} u(z_m) &= u_* \Phi\left(\frac{u_* z_m}{\nu}\right) \\ z_m \frac{\partial u}{\partial z_m} &= u_* \phi\left(\frac{u_* z_m}{\nu}\right) \end{aligned}\right\} z_m << \delta \tag{5.10}$$

where

$$\Phi(r_1) = \int_0^{r_1} \frac{\phi(r_1)}{r_1} dr_1. \tag{5.11}$$

This is Prandtl's universal law of the wall. A second argument can be made that away from the wall, the influence of the viscosity is small so that Eqs 5.5 and 5.6 give

$$\left.\begin{aligned} u_1 - u(z_m) &= u_* \Phi_1\left(\frac{z_m}{\delta}\right) \\ z_m \frac{\partial u}{\partial z_m} &= u_* \phi_1\left(\frac{z_m}{\delta}\right) \end{aligned}\right\} z_m >> \delta_v \tag{5.12}$$

where

$$\Phi_1(r_2) = \int_{r_2}^{1} \frac{\phi_1(r_2)}{r_2} dr_2. \tag{5.13}$$

This is Kármán's velocity defect law.

Assuming an overlap region where both Eqs 5.10 and 5.12 are valid yields a logarithmic solution given by (Yaglom 1979)

$$u(z_m) = u_* \left[A \ln \left(\frac{u_* z_m}{\nu} \right) + B \right] \tag{5.14}$$

$$u_1 - u(z_m) = u_* \left[-A \ln \left(\frac{z_m}{\delta} \right) + B_1 \right] \tag{5.15}$$

where A, B, and B_1 are constants. The thickness of this logarithmic layer for which Eqs 5.14 and 5.15 are valid is not precisely defined; however, it is estimated to be $z_m \simeq 0.1\delta$ or roughly 10% of the boundary layer thickness. The inverse of A is the Kármán constant

$$\frac{1}{A} = \kappa \simeq 0.4 \tag{5.16}$$

and the value of $\kappa = 0.40$ is used in this dissertation. The variability of the Kármán constant is discussed in Yaglom (1979).

Yaglom (1979) considers next the flow over a rough boundary with a mean roughness height, h_r, where h_r is much larger than the viscous length scale $\delta_v = (\nu/u_*)$. It is assumed that the roughness height is much less than the boundary layer thickness, $h_r << \delta$, and that Kármán's velocity defect law still applies within the boundary layer but away from the wall. Near the wall, the effects of the wall roughness can be included to modify the logarithmic solution as

$$u(z_m) = \frac{u_*}{\kappa} \ln \left(\frac{z_m}{z_0} \right) \tag{5.17}$$

where z_0 is the roughness height which includes the effects of the wall roughness such as the roughness size, shape, and distribution.

Yaglom (1979) includes the vertical shift of the coordinate origin so that Eq 5.17 becomes

$$u(z_m) = \frac{u_*}{\kappa} \ln \left(\frac{z_m - d_*}{z_0} \right) \quad \text{for } z_m \geq (d_* + z_0) \tag{5.18}$$

where d_* is the displacement distance. Jackson (1981) gives a physical interpretation to d_*, indicating that it is "the level at which the mean drag on the surface appears to act." The displacement distance is discussed again in Section 5.4. The least-squares method used to solve Eq 5.18 is discussed in the following section.

5.3 Least-Squares Method to Estimate Bottom Shear Velocity and Bottom Roughness

The logarithmic profile was derived in the previous section assuming a steady flow. In the following, it is assumed that a logarithmic profile near the bottom could exist at each phase over one wave period and that u in Eq 5.18 can be replaced by the phase-averaged horizontal velocity, u_a, so that the logarithmic velocity for a rough bottom can be expressed,

$$u_a(z_m) = \frac{u_*}{\kappa} \ln\left(\frac{z_m - d_*}{z_0}\right) \quad \text{for } z_m \geq (d_* + z_0) \tag{5.19}$$

where $\kappa \simeq 0.4$ is the Kármán constant. This equation can be rewritten as

$$\ln(z_m - d_*) = \frac{\kappa}{u_*} u_a + \ln(z_0) \tag{5.20}$$

and can be reduced to the linear equation

$$Y_i = \beta X_i + \alpha \quad \text{for } i = 1, 2, \ldots, n \tag{5.21}$$

where

$$X_i = [u_a]_i \quad \text{and} \quad Y_i = \ln\left[(z_m)_i - d_*\right] \tag{5.22}$$

with

$$\beta = \kappa / u_* \quad \text{and} \quad \alpha = \ln(z_0) \tag{5.23}$$

The index i refers to the measuring point elevation starting from the lowest point at $i = 1$; and the number of points used for the logarithmic fit is taken as $n = 4$, 5, or 6 as discussed below. The measuring point elevations were listed in Table 3.2 in Chapter 3.

The shear velocity, u_*, and bottom roughness, z_0, will be computed at each measuring line at a given phase using the least-squares procedure based on Eq 5.21. This procedure will be applied in two ways denoted Method A and Method B.

Method A uses only the horizontal velocity measurements at the main measuring line, Δx^0. The values for u_* and z_0 are computed three times at a given phase for $n = 4$, 5, and 6. The best fit among $n = 4$, 5, and 6 is decided by the square of the correlation coefficient, and only one value for u_* and z_0 is selected at a given phase. This is made clear in the context of the figures in this section. Method B is applied at L1, L2, L4 and L5 where eight additional measuring points were made. For Method B, only four bottom points are used so that $n = 4$. The values for u_* and z_0 are computed three times at a given phase using the three lines at Δx^0, Δx^-, and Δx^+. The best fit is determined by the square of the correlation coefficient, and only one value for u_* and z_0 is selected. It is noted that the phase shift due to the horizontal offset is neglected for Method B. Method A* for L3 is the same at Method A except that the offset line Δx^- is used. Only the figures for Method A are presented in this section, and the results of Method B are presented separately in Section 5.6. The purpose of Method A with a variable n is to give the best estimate of u_* and z_0 for the limited number of data points available for the logarithmic fit. The purpose of Method B is to show the variability of the least-squares method due to irregularities in the bottom roughness.

In was noted in the previous section that the logarithmic velocity layer holds up to approximately 10% of the boundary layer thickness. Since the boundary layer thickness is approximately 1 cm for this experiment as will be shown in Section 5.7, the thickness of the logarithmic velocity layer is approximately 0.1 cm. The measuring point elevations in the bottom boundary layer are approximately

$$(z_m)_{i=6} - d_* \simeq 0.22 \text{ cm} \qquad (z_m)_{i=3} - d_* \simeq 0.09 \text{ cm}$$

$$(z_m)_{i=5} - d_* \simeq 0.17 \text{ cm} \qquad (z_m)_{i=2} - d_* \simeq 0.07 \text{ cm}$$

$$(z_m)_{i=4} - d_* \simeq 0.12 \text{ cm} \qquad (z_m)_{i=1} - d_* \simeq 0.05 \text{ cm}$$

for this experiment so that the use of $n = 4$, 5, or 6 is slightly above the 10%

guideline.

The least-squares method based on Eq 5.21 is summarized here where Benjamin and Cornell (1970) is used as a reference. The sample means are defined as

$$\overline{X} = \frac{1}{n}\sum_{i=1}^{n} X_i \;\; ; \;\; \overline{Y} = \frac{1}{n}\sum_{i=1}^{n} Y_i. \tag{5.24}$$

The sample variances are defined as

$$S_x^2 = \frac{1}{n}\sum_{i=1}^{n}(X_i - \overline{X})^2 \;\; ; \;\; S_y^2 = \frac{1}{n}\sum_{i=1}^{n}(Y_i - \overline{Y})^2, \tag{5.25}$$

where $1/n$ is used rather than $1/(n-1)$ for the sample. The sample covariance is defined as

$$S_{xy} = \frac{1}{n}\sum_{i=1}^{n}(X_i - \overline{X})(Y_i - \overline{Y}). \tag{5.26}$$

The sample correlation coefficient is defined as

$$\gamma_{xy} = \frac{S_{xy}}{S_x S_y}, \tag{5.27}$$

where $\gamma_{xy} = 1.0$ indicates that the points are collinear. The expected or mean values of β and α are denoted by a hat and are estimated by

$$\hat{\beta} = \frac{S_{xy}}{S_x^2} = \frac{\gamma_{xy} S_y}{S_x} \;\; ; \;\; \hat{\alpha} = \overline{Y} - \hat{\beta}\overline{X}. \tag{5.28}$$

For small n, the t-distribution with $(n-2)$ degrees of freedom is recommended by Benjamin and Cornell (1970) to estimate the 95% confidence intervals of α and β

$$\alpha = \hat{\alpha} \pm \varepsilon(n) S_A \tag{5.29}$$

$$\beta = \hat{\beta} \pm \varepsilon(n) S_B, \tag{5.30}$$

where $\varepsilon = 4.3$, 3.2 and 2.8 for $n = 4$, 5 and 6, respectively. The variances S_A^2 and S_B^2 included in Eqs 5.29 and 5.30 are estimated as

$$S_B^2 = \frac{S^2}{n S_x^2} \;\; ; \;\; S_A^2 = \frac{S^2}{n}\left[1 + \frac{(\overline{X})^2}{S_x^2}\right] \tag{5.31}$$

with

$$S^2 = \frac{n}{(n-2)}(1-\gamma_{xy}^2)S_y^2, \tag{5.32}$$

where S^2 is an estimate of the average of the squared residuals based on the linear regression using Eq 5.21.

The shear velocity and bottom roughness are estimated at each phase for which the square of the correlation coefficient, γ_{xy}^2, exceeds a critical value, $[\gamma_{xy}^2]_{crit}$,

$$\gamma_{xy}^2 > [\gamma_{xy}^2]_{crit}. \tag{5.33}$$

The critical value adopted herein is $[\gamma_{xy}^2]_{crit} = 0.95$. The sensitivity of the results to this choice are discussed in Section 5.4. The number of phases for which Eq 5.33 holds is denoted by N_γ. As mentioned previously, u_* and z_0 are computed three times at a given phase for the location Δx^0 and using $n = 4$, 5, and 6 for Method A. Only one set of values of u_* and z_0 corresponding to the n value with the highest γ_{xy}^2 value will be used at a given phase. This value of γ_{xy}^2 at a given phase is denoted $[\gamma_{xy}^2]_{max}$. The mean of the highest correlation coefficients at phases exceeding the critical value is $\overline{[\gamma_{xy}^2]_{max}}$. This is an average over particular phases of the wave and is not a time-average in the strict sense. Similarly for Method B, u_* and z_0 are computed three times at a given phase for $n = 4$ and at the three locations Δx^0, Δx^-, and Δx^+. Only one set of values is used at a given phase; and the definitions of N_γ, $[\gamma_{xy}^2]_{max}$, and $\overline{[\gamma_{xy}^2]_{max}}$ for Method B are similar to Method A except that the chosen values of u_* and z_0 correspond to the highest correlation coefficient at a given Δx. These definitions will be made clear in the context of the figures.

Figures 5.3 to 5.8 show the results of the least-squares method for L1 to L6 using Method A and an adopted d_*. The choice of d_* is discussed in Section 5.4. The top panel of Figure 5.3 shows the vertical variation of the phase-averaged horizontal velocity in the bottom boundary layer at 22 phases. The vertical axis

is a logarithmic scale and indicates the alignment of the bottom n points. The phases are aligned with the free surface elevations in Figure 4.1, for example, the wave front appears around $t = 0.6$ s for L1.

The second panel of Figure 5.3 shows the temporal variation of γ^2_{xy} in the range $0.5 \leq \gamma^2_{xy} \leq 1.0$ for the three n values. The thin horizontal line indicates $[\gamma^2_{xy}]_{crit} = 0.95$. The curves indicate that the logarithmic profiles are well established for several phases in both the onshore and offshore directions for L1 and that the least-squares fit method is not applicable for the phases where the flow reverses.

The third and fourth panels of Figure 5.3 show the temporal variations of the fitted shear velocity, u_*, and bottom roughness, z_0, for the three n values. Comparing with the second panel, it is apparent that only those phases satisfying $\gamma^2_{xy} > [\gamma^2_{xy}]_{crit}$ are plotted. The temporal variation of u_* is smooth and nonsinusoidal, consistent with the top panel. The sensitivity of u_* and z_0 to n is small at a given phase. The bottom roughness z_0 is small but increases systematically before the flow reversal.

Figures 5.4 to 5.8 show results similar to Figure 5.3 but, in general, have fewer estimates of u_* and z_0 for which Eq 5.33 holds. Hence, all of the figures for L1 to L6 are shown for completeness.

Figures 5.9 to 5.14 show the values selected at a given phase based on the maximum correlation coefficient. The top panel of Figure 5.9 shows the temporal variation of the maximum correlation coefficient squared, $[\gamma^2_{xy}]_{max}$, of the three curves from the second panel of Figure 5.3. The maximum correlation coefficient squared is plotted in the range $0.95 < [\gamma^2_{xy}]_{max} < 1.00$ and shows that for many of the phases, $[\gamma^2_{xy}]_{max} > 0.99$.

The second panel of Figure 5.9 shows the corresponding n value. There is no clear correlation between the n values and phases for L1 to L6, and the method of choosing u_* and z_0 based on the maximum γ_{xy}^2 values seems reasonable without adding bias.

The third panel shows the value of u_* selected at each phase from Figure 5.3 and the 95% confidence intervals calculated using Eq 5.30 where $\beta = \kappa/u_*$. The confidence interval decreases as $[\gamma_{xy}^2]_{max}$ and n increase as may be seen from Eqs 5.30 to 5.32.

The fourth panel shows the value of z_0 selected at each phase and the 95% confidence limits calculated using Eq 5.29 where $\alpha = \ln(z_0)$. The bottom roughness is fairly constant over most of the phases but increases unrealistically before the flow reversal.

The figures in this section show that the temporal variations of the bottom shear velocity and bottom roughness can be estimated with a reasonable confidence interval both seaward of breaking and inside the surf zone using the logarithmic fit of the horizontal velocities measured well inside in the bottom boundary layer except for the phases of flow reversal.

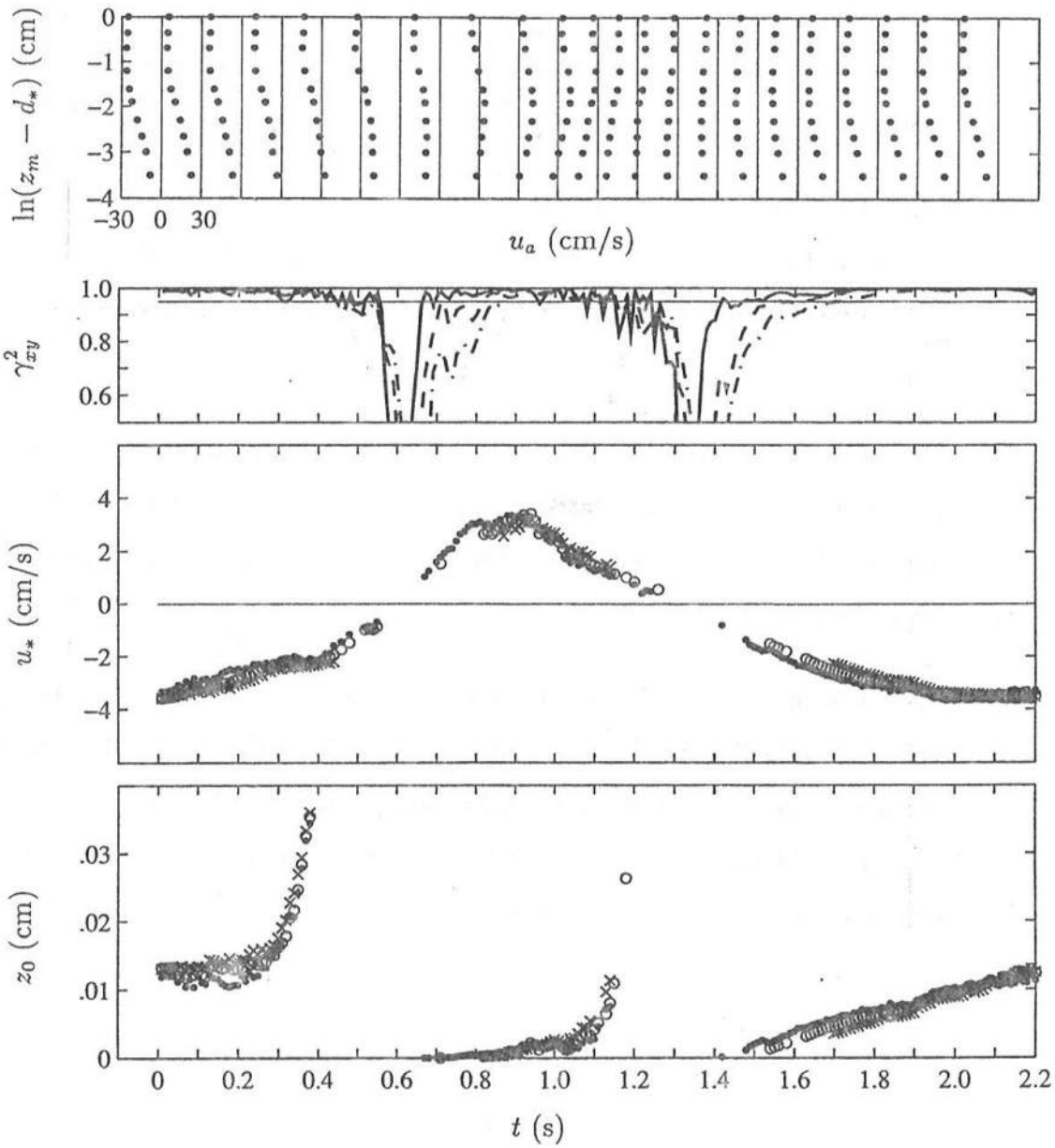

Figure 5.3: Vertical Variations of Phase-Averaged Horizontal Velocity, u_a (•), at 22 Phases (Top); Temporal Variations of Correlation Coefficient Squared, γ^2_{xy}, for $n = 4$ (——), $n = 5$ (– –), and $n = 6$ (–·–), (Second); Shear Velocity, u_*, for $n = 4$ (•), $n = 5$ (○), and $n = 6$ (×), (Third); and Bottom Roughness, z_0, same notation as above (Bottom); for $d_* = 0.10$ cm and for L1, Method A.

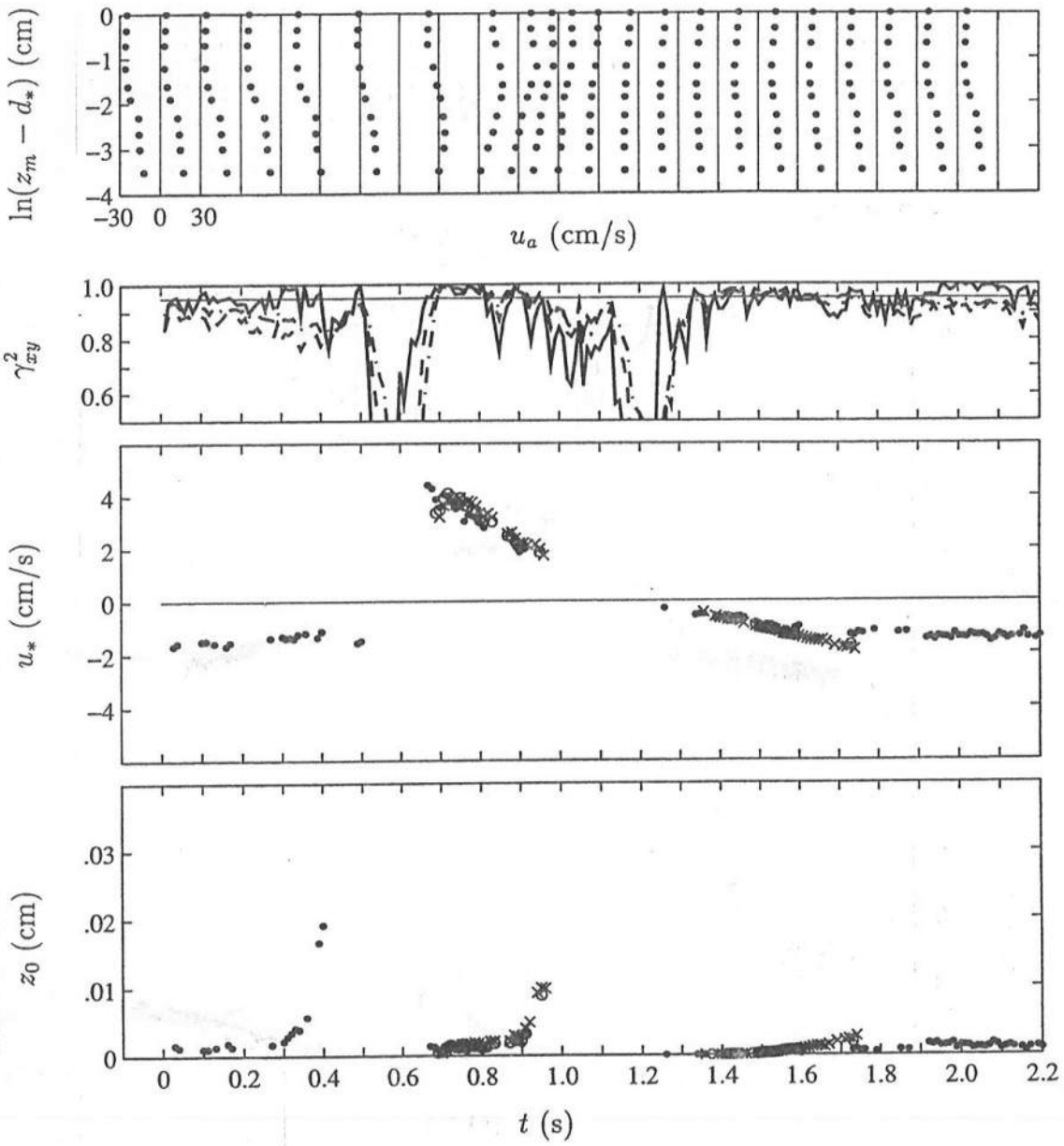

Figure 5.4: Vertical Variations of Phase-Averaged Horizontal Velocity, u_a (•), at 22 Phases (Top); Temporal Variations of Correlation Coefficient Squared, γ^2_{xy}, for $n = 4$ (——), $n = 5$ (– –), and $n = 6$ (–·–), (Second); Shear Velocity, u_*, for $n = 4$ (•), $n = 5$ (○), and $n = 6$ (×), (Third); and Bottom Roughness, z_0, same notation as above (Bottom); for $d_* = 0.10$ cm and for L2, Method A.

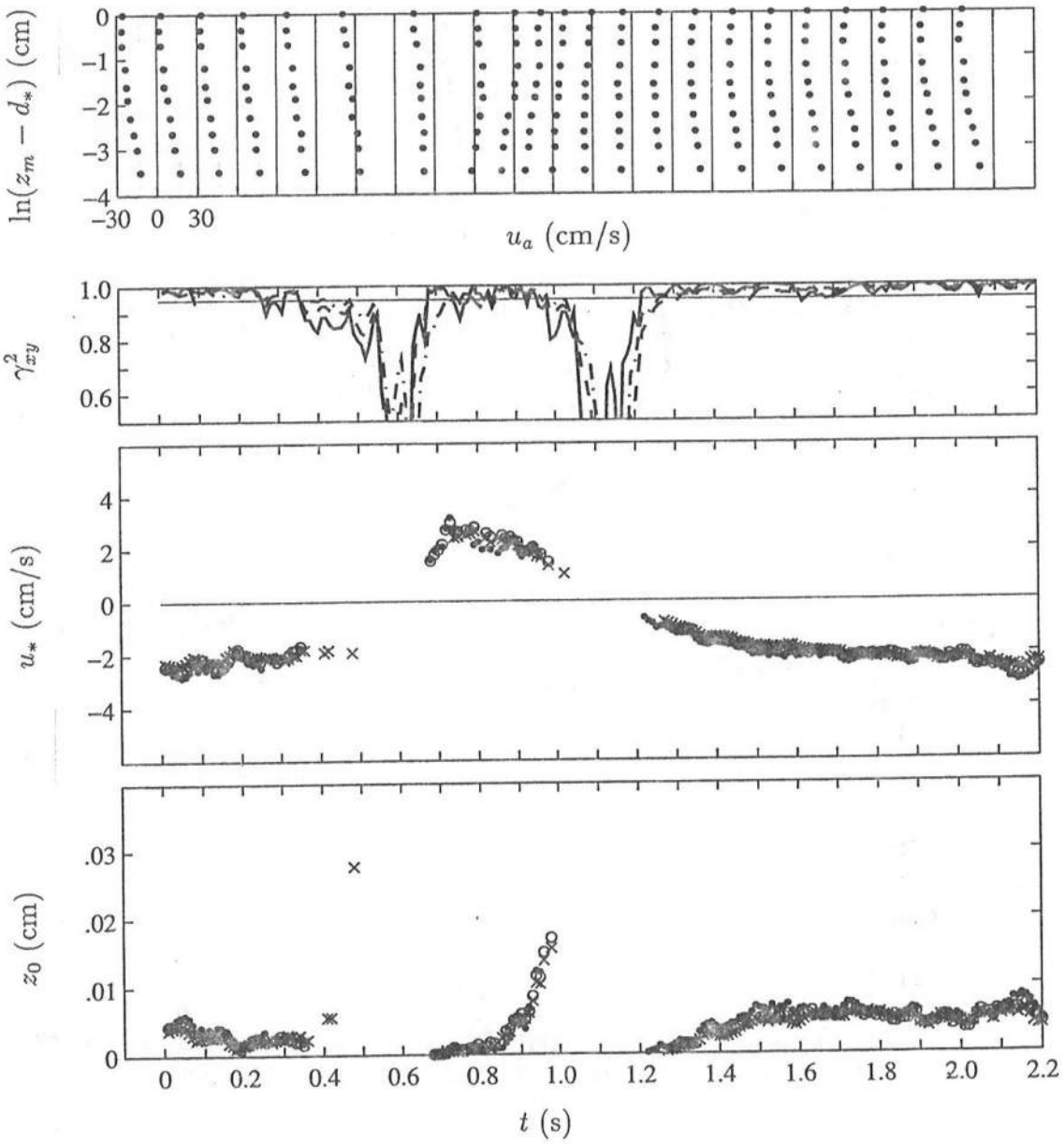

Figure 5.5: Vertical Variations of Phase-Averaged Horizontal Velocity, u_a (•), at 22 Phases (Top); Temporal Variations of Correlation Coefficient Squared, γ^2_{xy}, for $n = 4$ (——), $n = 5$ (– –), and $n = 6$ (–·–), (Second); Shear Velocity, u_*, for $n = 4$ (•), $n = 5$ (○), and $n = 6$ (×), (Third); and Bottom Roughness, z_0, same notation as above (Bottom); for $d_* = 0.10$ cm and for L3, Method A.

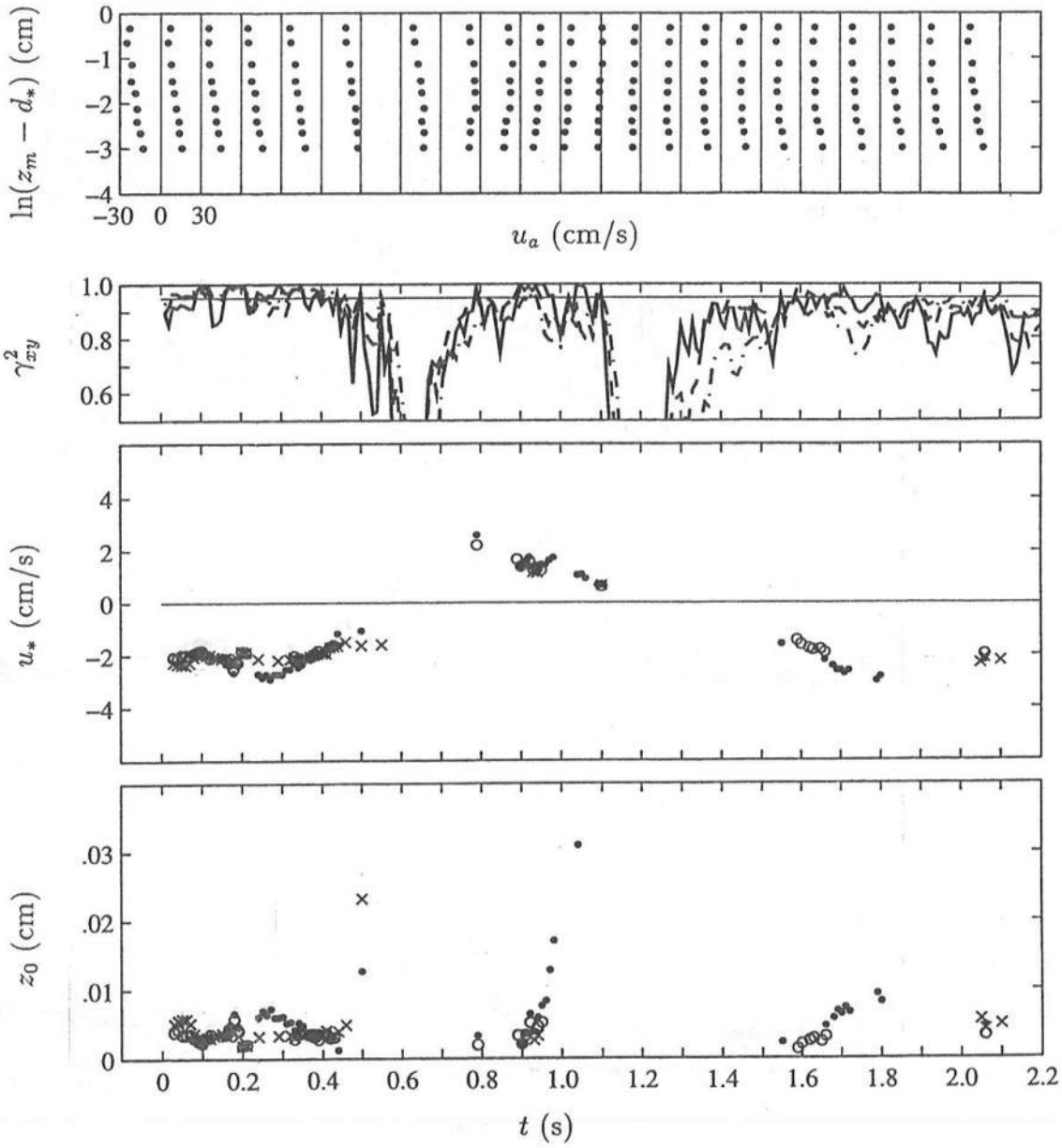

Figure 5.6: Vertical Variations of Phase-Averaged Horizontal Velocity, u_a (•), at 22 Phases (Top); Temporal Variations of Correlation Coefficient Squared, γ^2_{xy}, for $n = 4$ (——), $n = 5$ (– –), and $n = 6$ (–·–), (Second); Shear Velocity, u_*, for $n = 4$ (•), $n = 5$ (○), and $n = 6$ (×), (Third); and Bottom Roughness, z_0, same notation as above (Bottom); for $d_* = 0.08$ cm and for L4, Method A.

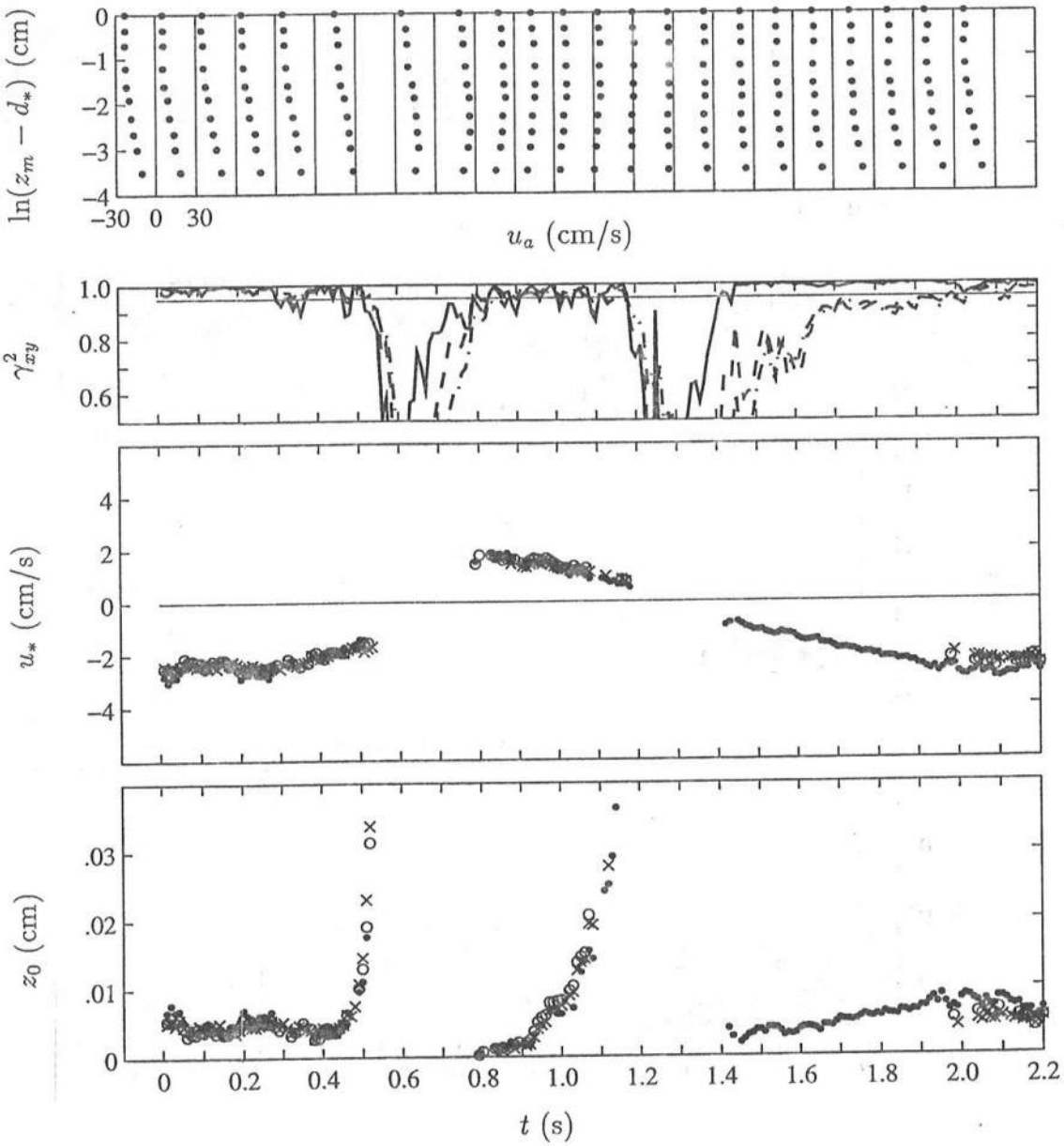

Figure 5.7: Vertical Variations of Phase-Averaged Horizontal Velocity, u_a (•), at 22 Phases (Top); Temporal Variations of Correlation Coefficient Squared, γ^2_{xy}, for $n = 4$ (——), $n = 5$ (– –), and $n = 6$ (–·–), (Second); Shear Velocity, u_*, for $n = 4$ (•), $n = 5$ (○), and $n = 6$ (×), (Third); and Bottom Roughness, z_0, same notation as above (Bottom); for $d_* = 0.10$ cm and for L5, Method A.

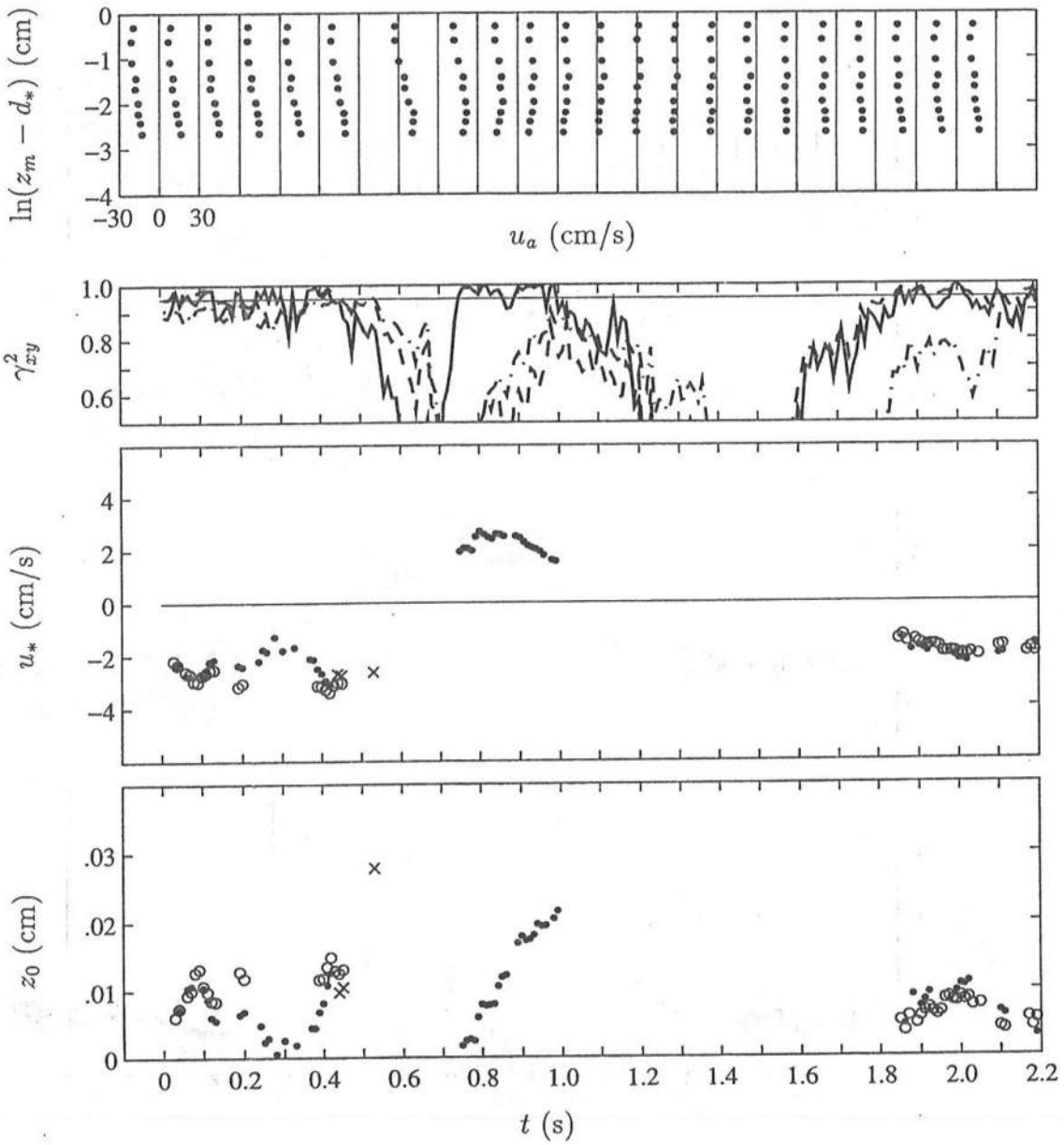

Figure 5.8: Vertical Variations of Phase-Averaged Horizontal Velocity, u_a (•), at 22 Phases (Top); Temporal Variations of Correlation Coefficient Squared, γ^2_{xy}, for $n = 4$ (——), $n = 5$ (– –), and $n = 6$ (–·–), (Second); Shear Velocity, u_*, for $n = 4$ (•), $n = 5$ (○), and $n = 6$ (×), (Third); and Bottom Roughness, z_0, same notation as above (Bottom); for $d_* = 0.06$ cm and for L6, Method A.

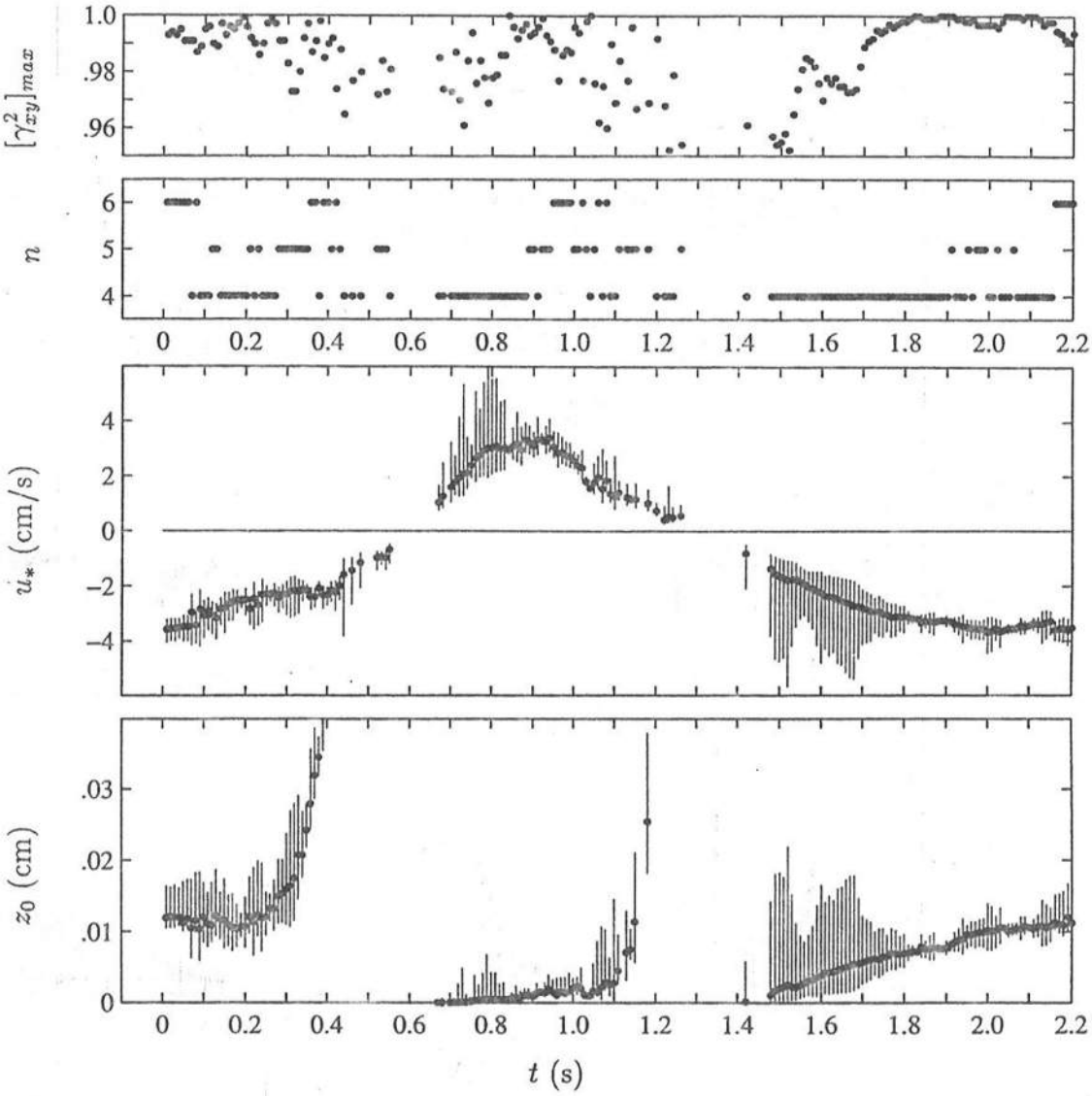

Figure 5.9: Temporal Variations of Maximum Correlation Coefficient Squared, $[\gamma^2_{xy}]_{max}$ (•), (Top); Corresponding n Value (•) (Second); Shear Velocity, u_* (•) with 95% Confidence Interval (——) for adopted $d_* = 0.10$ cm, (Third); and Bottom Roughness, z_0, same notation as above, (Bottom); for L1, Method A.

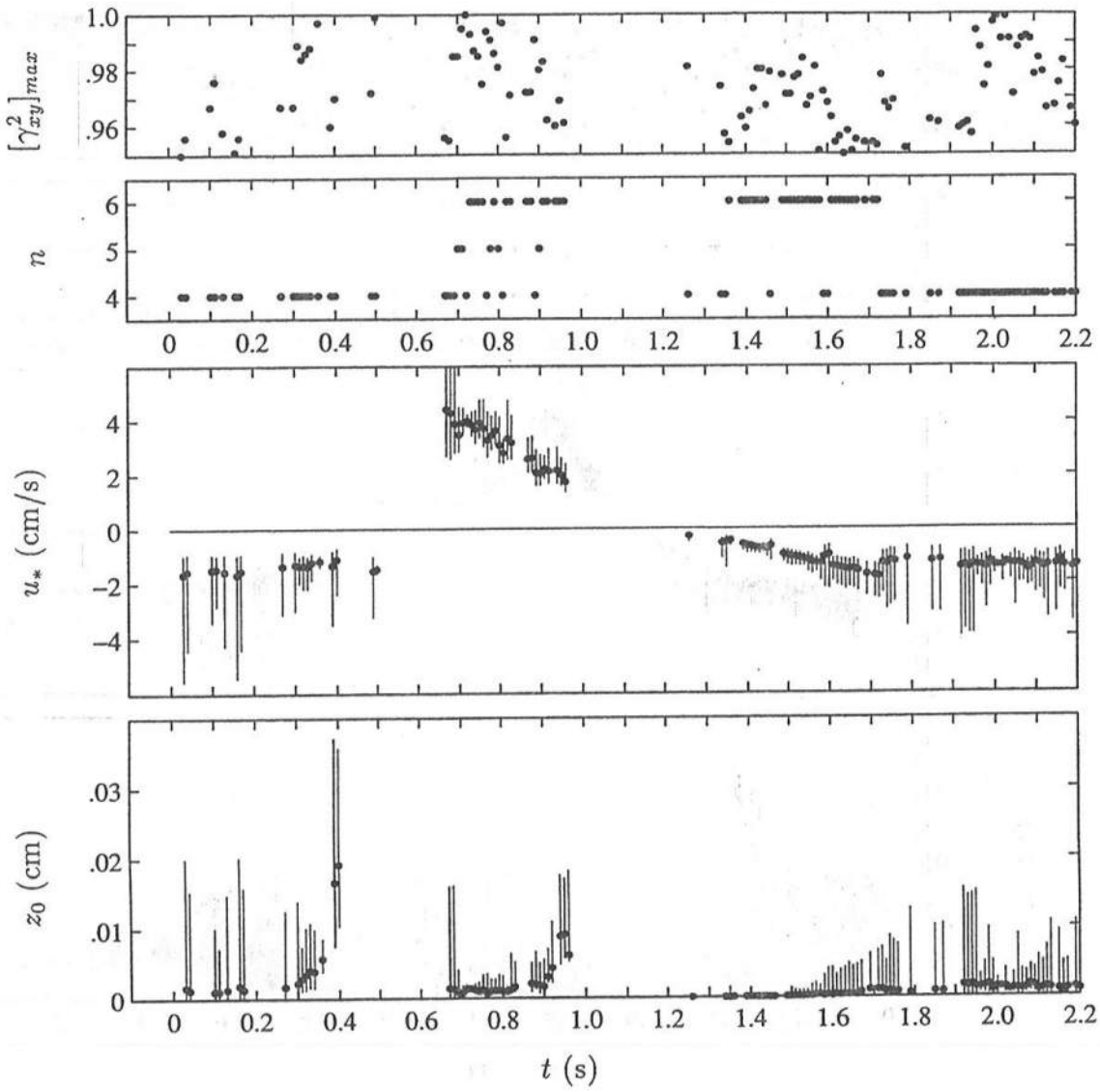

Figure 5.10: Temporal Variations of Maximum Correlation Coefficient Squared, $[\gamma^2_{xy}]_{max}$ (•), (Top); Corresponding n Value (•) (Second); Shear Velocity, u_* (•) with 95% Confidence Interval (——) for adopted $d_* = 0.10$ cm, (Third); and Bottom Roughness, z_0, same notation as above, (Bottom); for L2, Method A.

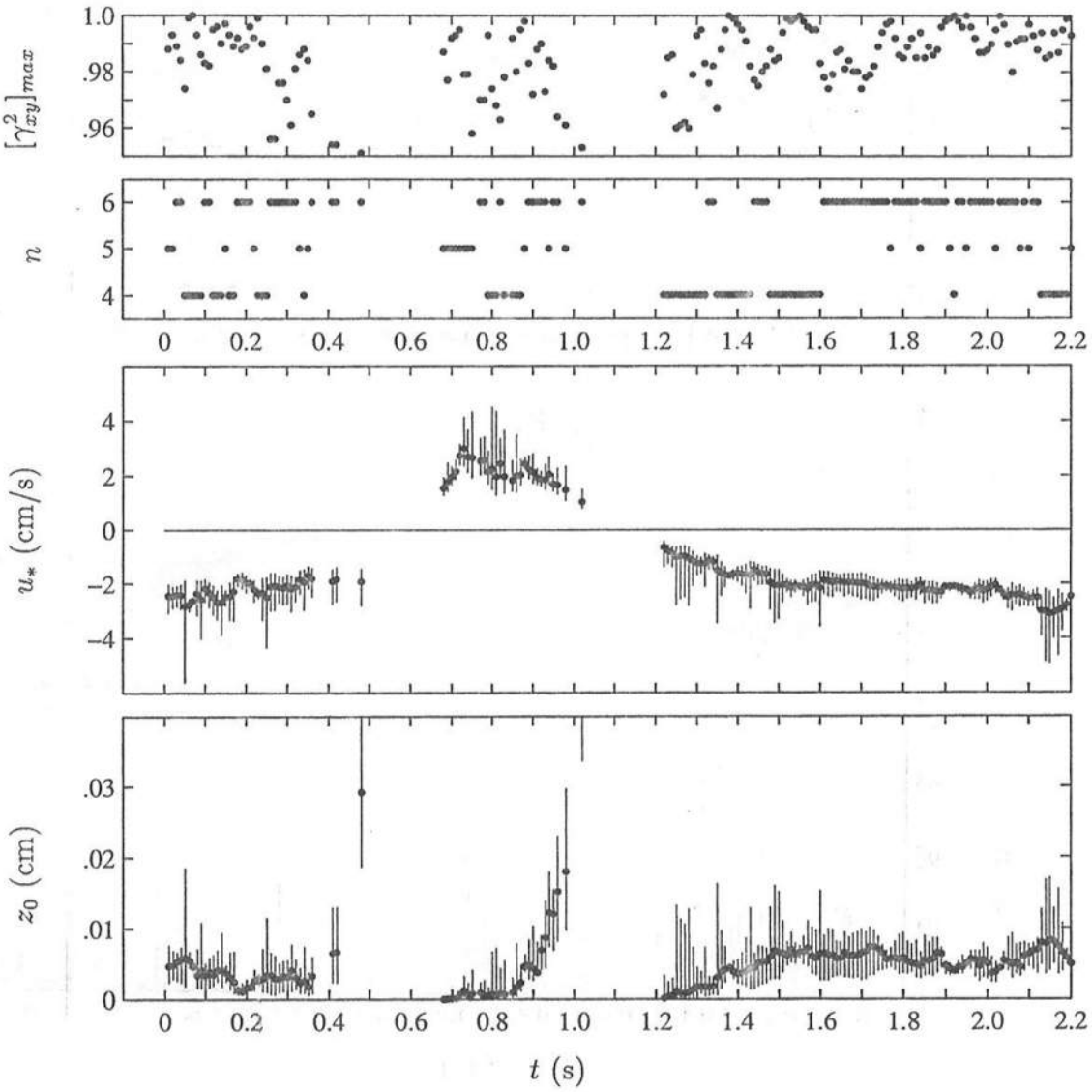

Figure 5.11: Temporal Variations of Maximum Correlation Coefficient Squared, $[\gamma^2_{xy}]_{max}$ (•), (Top); Corresponding n Value (•) (Second); Shear Velocity, u_* (•) with 95% Confidence Interval (——) for adopted $d_* = 0.10$ cm, (Third); and Bottom Roughness, z_0, same notation as above, (Bottom); for L3, Method A.

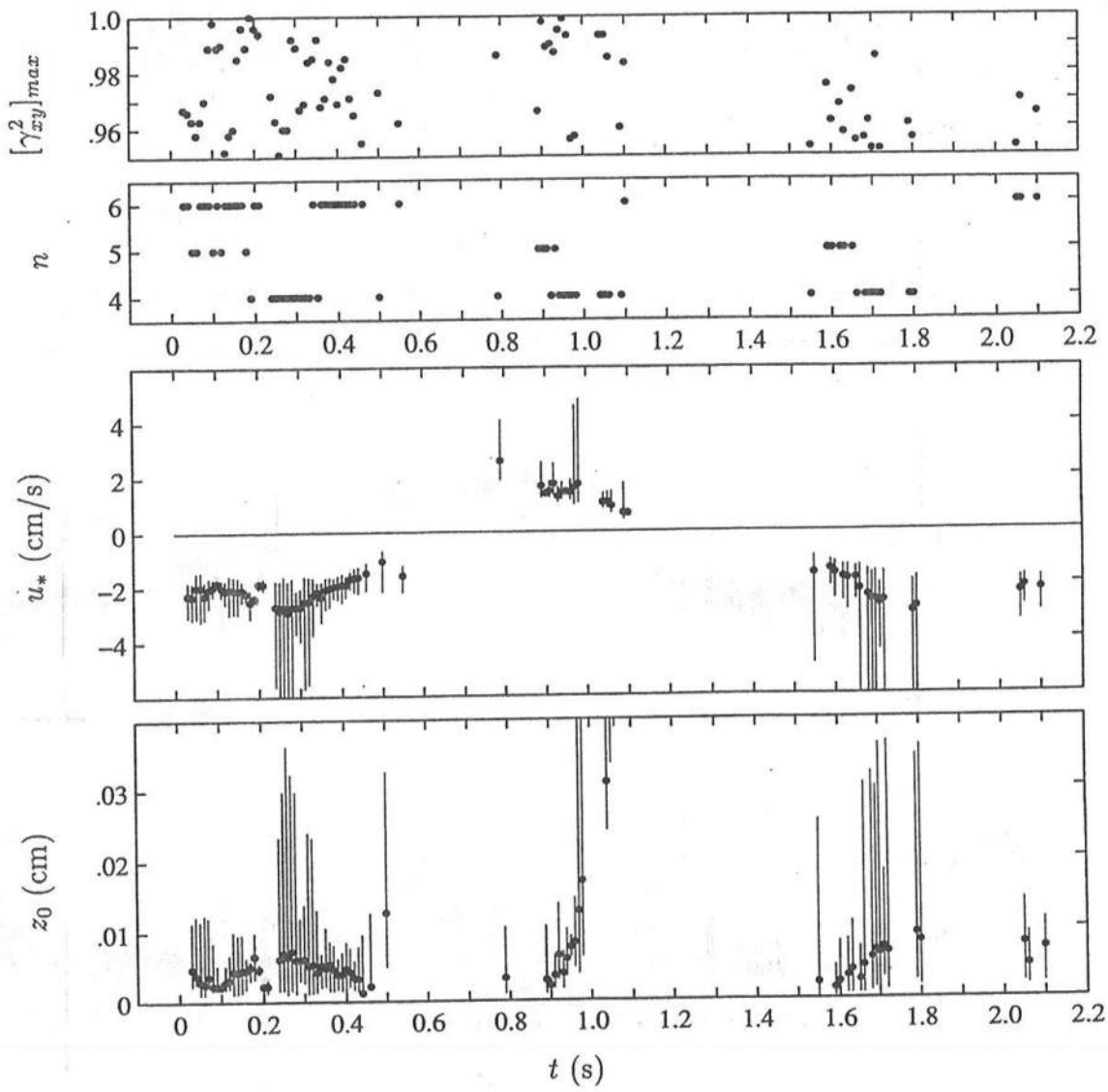

Figure 5.12: Temporal Variations of Maximum Correlation Coefficient Squared, $[\gamma^2_{xy}]_{max}$ (•), (Top); Corresponding n Value (•) (Second); Shear Velocity, u_* (•) with 95% Confidence Interval (——) for adopted $d_* = 0.08$ cm, (Third); and Bottom Roughness, z_0, same notation as above, (Bottom); for L4, Method A.

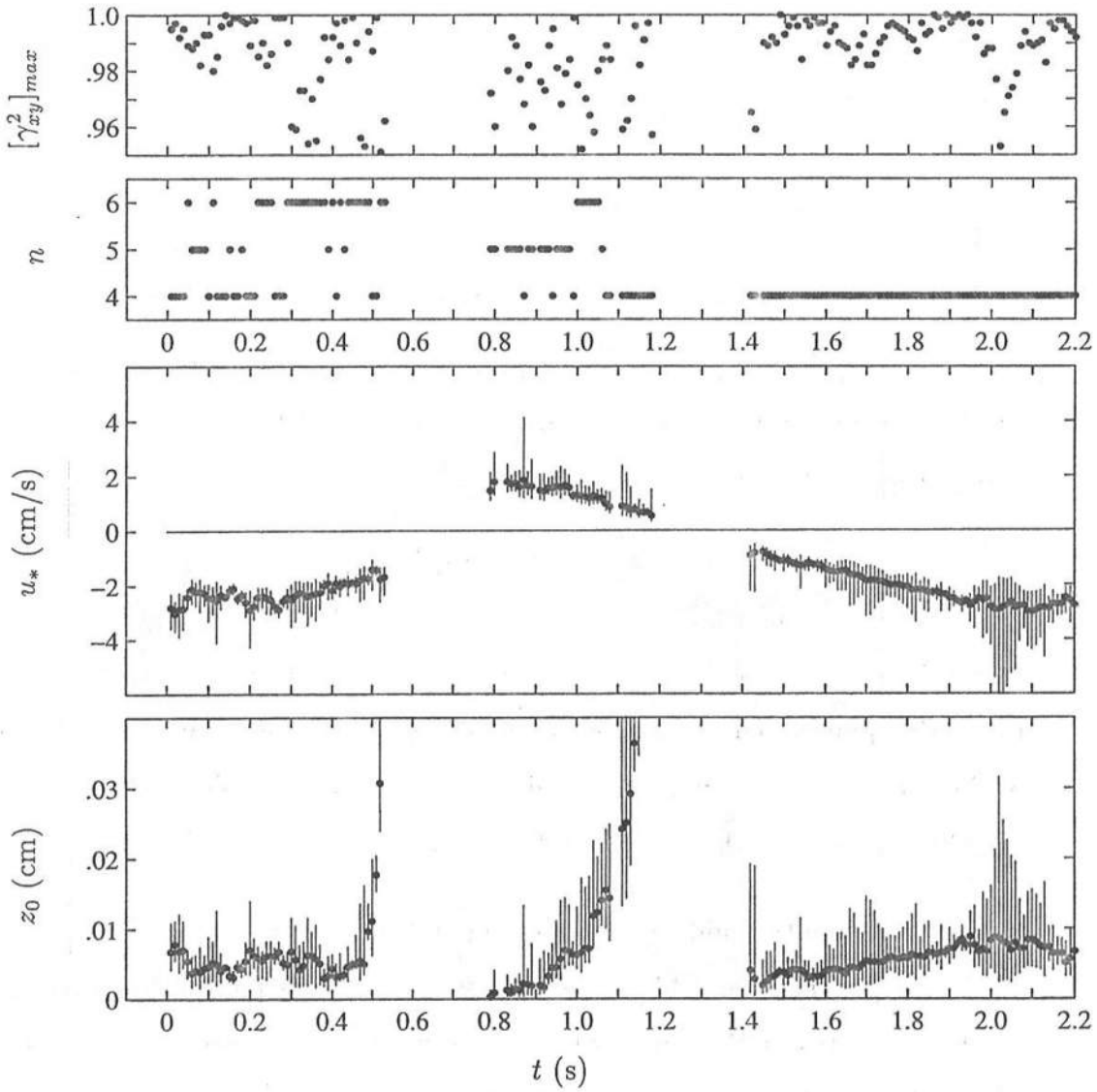

Figure 5.13: Temporal Variations of Maximum Correlation Coefficient Squared, $[\gamma^2_{xy}]_{max}$ (•), (Top); Corresponding n Value (•) (Second); Shear Velocity, u_* (•) with 95% Confidence Interval (——) for adopted $d_* = 0.10$ cm, (Third); and Bottom Roughness, z_0, same notation as above, (Bottom); for L5, Method A.

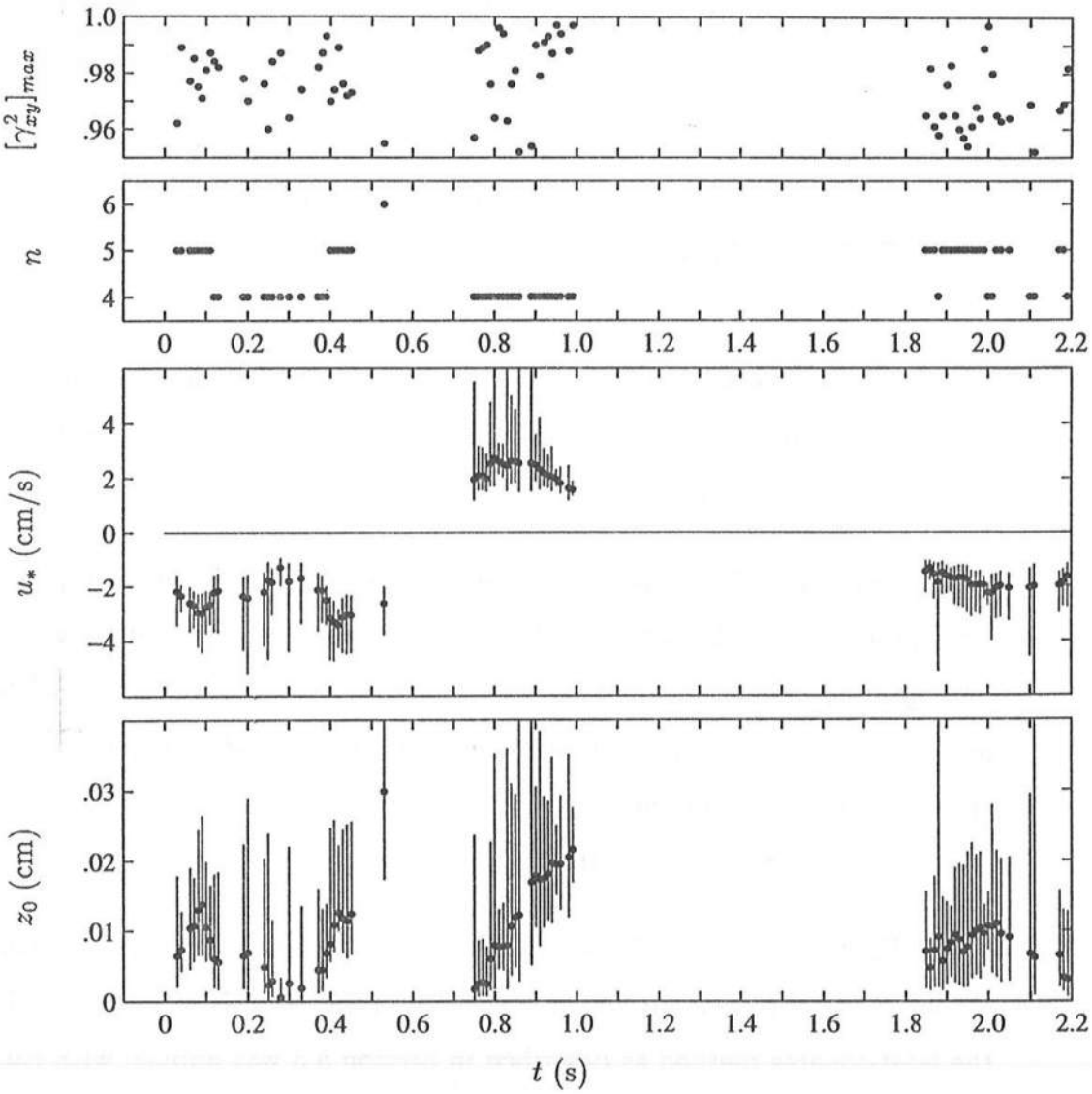

Figure 5.14: Temporal Variations of Maximum Correlation Coefficient Squared, $[\gamma^2_{xy}]_{max}$ (•), (Top); Corresponding n Value (•) (Second); Shear Velocity, u_* (•) with 95% Confidence Interval (——) for adopted $d_* = 0.06$ cm, (Third); and Bottom Roughness, z_0, same notation as above, (Bottom); for L6, Method A.

5.4 Sensitivity to Bottom Displacement

This section discusses the sensitivity of the shear velocity, u_*, and the bottom roughness, z_0, to the displacement height, d_*, introduced in the logarithmic profile given by Eq 5.18. The method used to choose d_* is based on the square of the correlation coefficient, γ_{xy}^2, introduced in Eq 5.27.

The displacement height, d_*, for a given grain size may be estimated following Jackson (1981) as

$$d_* \simeq 0.7 h_r \tag{5.34}$$

where h_r is the length scale of the roughness element. The mean roughness height can be assumed to be the median grain diameter so that $h_r = d_{50} = 0.1$ cm, and this gives $d_* \simeq .07$ cm.

The value of d_* depends on the setup of the laser-Doppler measuring volume above the rough bottom and must be determined separately for each main measuring line and for each of the offset measuring lines using the eight additional measuring points. The procedure to determine the best d_* is based on the square of the correlation coefficient, γ_{xy}^2, and is outlined below. Tables 5.1 to 5.3 indicate the choice of d_* and the sensitivity to $[\gamma_{xy}^2]_{crit}$.

Following the guideline of Jackson (1981) and the uncertainty in positioning the laser, the displacement height was varied in the range $0.06 < d_* < 0.10$ cm and the least-squares method as described in Section 5.3 was applied with each value of d_*. The critical value of γ_{xy}^2 introduced in Eq 5.33 was varied as $[\gamma_{xy}^2]_{crit} =$ 0.95, 0.975, and 0.99 for each d_*. The number of phases, N_γ, out of 220 for which $\gamma_{xy}^2 > [\gamma_{xy}^2]_{crit}$, and the corresponding mean value, $\overline{[\gamma_{xy}^2]_{max}}$, were computed for a given d_* and $[\gamma_{xy}^2]_{crit}$. These values are given in Tables 5.1 to 5.3. For $[\gamma_{xy}^2]_{crit} = 0.99$, the value of N_γ is small for several locations. Therefore, the

seventh and eighth columns of Tables 5.1 to 5.3 are not used for this critical value in determining d_*. For the third through sixth columns for $[\gamma_{xy}^2]_{crit} = 0.95$ and 0.975, the highest values of N_γ and $\overline{[\gamma_{xy}^2]_{max}}$ at each d_* are indicated by boxes. In most cases, the adopted value of d_* is simply the d_* value corresponding to the row with the majority of highest numbers, that is, either 3 out of 4 or 4 out of 4 highest numbers. In the cases of L1 Δx^+, L4 Δx^0, L5 Δx^-, and L5 Δx^+, there was no row with a majority of highest numbers; and in these cases, the middle value $d_* = 0.08$ cm was adopted.

Following Figures 5.9 to 5.14 in the previous section, Figures 5.15 to 5.20 show the temporal variations of the shear velocity and bottom roughness for the adopted d_* including the 95% confidence intervals. Figures 5.15 to 5.20 also show the temporal variations of u_* and z_0 for d_* shifted by 0.02 cm from the adopted value. In most cases, the shear velocity for the shifted d_* are within the 95% confidence interval of the adopted d_*. The bottom roughness estimates are more sensitive to the choice of d_* and are not always within the 95% confidence interval of the adopted d_*. Similar results were obtained for Method B and are not presented for brevity.

Similar to Figure 5.17 for L3 using Method A, Figure 5.21 shows the computed shear velocity and bottom roughness for L3 using Method A* based on the offset line Δx^- as explained in Section 5.3. Since Method A* is essentially the same as Method A, comparison of Figures 5.17 and 5.21 gives additional confidence in the repeatability of the measurements and the analysis method.

Table 5.1: Sensitivity to $[\gamma^2_{xy}]_{crit}$ and Selection of d_* for L1 and L2.

Line No.	d_* (cm)	$[\gamma^2_{xy}]_{crit} = 0.95$ N_γ	$\overline{[\gamma^2_{xy}]_{max}}$	$[\gamma^2_{xy}]_{crit} = 0.975$ N_γ	$\overline{[\gamma^2_{xy}]_{max}}$	$[\gamma^2_{xy}]_{crit} = 0.99$ N_γ	$\overline{[\gamma^2_{xy}]_{max}}$
	.10	177	.9871	146	.9915	100	.9959
L1	.09	175	.9866	139	.9926	103	.9963
n=4,5,6	.08	174	.9857	134	.9931	103	.9962
Δx^0	.07	168	.9859	132	.9930	98	.9962
	.06	160	.9868	132	.9924	96	.9959
	.10	161	.9876	134	.9922	103	.9952
L1	.09	155	.9855	126	.9908	80	.9945
n=4	.08	148	.9840	121	.9890	54	.9949
Δx^-	.07	144	.9823	114	.9875	48	.9945
	.06	141	.9806	107	.9864	38	.9948
	.10	143	.9817	99	.9899	57	.9945
L1	.09	142	.9832	105	.9903	65	.9947
n=4	.08	143	.9833	103	.9910	69	.9949
Δx^+	.07	142	.9835	104	.9908	65	.9952
	.06	141	.9835	104	.9905	68	.9947
	.10	112	.9730	50	.9865	18	.9946
L2	.09	103	.9720	46	.9850	12	.9942
n=4,5,6	.08	97	.9721	40	.9848	10	.9937
Δx^0	.07	98	.9710	36	.9844	8	.9936
	.06	108	.9687	36	.9832	6	.9940
	.10	173	.9768	96	.9858	29	.9934
L2	.09	171	.9753	97	.9839	20	.9941
n=4	.08	166	.9743	85	.9838	13	.9958
Δx^-	.07	159	.9736	74	.9838	16	.9943
	.06	155	.9727	66	.9841	15	.9946
	.10	164	.9894	149	.9923	104	.9962
L2	.09	160	.9901	146	.9927	110	.9961
n=4	.08	159	.9893	141	.9924	104	.9960
Δx^+	.07	159	.9880	132	.9926	103	.9953
	.06	160	.9866	129	.9919	88	.9955

Table 5.2: Sensitivity to $[\gamma_{xy}^2]_{crit}$ and Selection of d_* for L3 and L4.

Line No.	d_* (cm)	$[\gamma_{xy}^2]_{crit} = 0.95$ N_γ	$\overline{[\gamma_{xy}^2]_{max}}$	$[\gamma_{xy}^2]_{crit} = 0.975$ N_γ	$\overline{[\gamma_{xy}^2]_{max}}$	$[\gamma_{xy}^2]_{crit} = 0.99$ N_γ	$\overline{[\gamma_{xy}^2]_{max}}$
	.10	167	.9851	139	.9893	69	.9952
L3	.09	166	.9838	129	.9892	69	.9945
n=4,5,6	.08	164	.9826	121	.9891	63	.9947
Δx^0	.07	163	.9812	116	.9887	55	.9951
	.06	163	.9796	107	.9891	54	.9949
	.10	141	.9753	73	.9854	22	.9935
L3	.09	144	.9735	69	.9845	19	.9937
n=4,5,6	.08	140	.9725	61	.9846	18	.9937
Δx^-	.07	136	.9719	58	.9846	17	.9941
	.06	129	.9720	54	.9849	15	.9949
	.10	79	.9736	39	.9869	18	.9944
L4	.09	80	.9728	34	.9891	18	.9941
n=4,5,6	.08	76	.9739	33	.9893	15	.9946
Δx^0	.07	74	.9743	33	.9888	14	.9949
	.06	72	.9744	35	.9872	14	.9946
	.10	125	.9770	72	.9870	32	.9931
L4	.09	134	.9777	82	.9872	36	.9935
n=4	.08	146	.9770	89	.9872	38	.9943
Δx^-	.07	149	.9777	90	.9879	39	.9952
	.06	147	.9790	90	.9886	40	.9957
	.10	58	.9744	27	.9882	10	.9947
L4	.09	64	.9746	32	.9872	14	.9939
n=4	.08	67	.9749	34	.9875	17	.9933
Δx^+	.07	69	.9748	33	.9883	17	.9932
	.06	69	.9753	33	.9887	14	.9941

Table 5.3: Sensitivity to $[\gamma_{xy}^2]_{crit}$ and Selection of d_* for L5 and L6.

Line No.	d_* (cm)	$[\gamma_{xy}^2]_{crit} = 0.95$ N_γ	$\overline{[\gamma_{xy}^2]_{max}}$	$[\gamma_{xy}^2]_{crit} = 0.975$ N_γ	$\overline{[\gamma_{xy}^2]_{max}}$	$[\gamma_{xy}^2]_{crit} = 0.99$ N_γ	$\overline{[\gamma_{xy}^2]_{max}}$
	.10	166	.9860	135	.9913	86	.9953
L5	.09	162	.9847	128	.9903	75	.9951
n=4,5,6	.08	157	.9836	123	.9890	63	.9948
Δx^0	.07	152	.9827	113	.9886	54	.9946
	.06	150	.9813	110	.9875	49	.9941
	.10	145	.9826	105	.9891	52	.9954
L5	.09	149	.9829	113	.9887	55	.9953
n=4	.08	148	.9830	111	.9894	57	.9952
Δx^-	.07	142	.9841	110	.9897	61	.9949
	.06	141	.9838	108	.9899	62	.9946
	.10	128	.9821	90	.9898	53	.9945
L5	.09	122	.9832	89	.9909	57	.9953
n=4	.08	117	.9839	85	.9918	61	.9952
Δx^+	.07	109	.9853	85	.9914	56	.9957
	.06	106	.9854	83	.9914	52	.9961
	.10	53	.9720	26	.9825	5	.9922
L6	.09	66	.9721	30	.9848	7	.9930
n=4,5,6	.08	70	.9739	37	.9848	8	.9931
Δx^0	.07	74	.9746	39	.9854	9	.9939
	.06	75	.9756	41	.9855	11	.9938

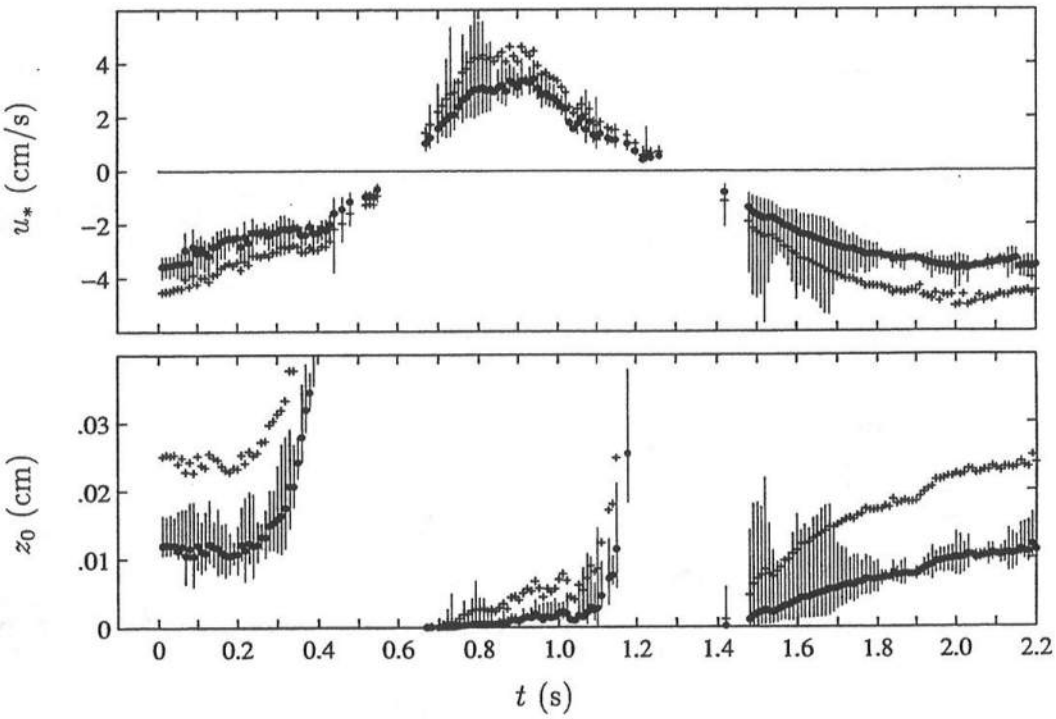

Figure 5.15: Temporal Variations of Shear Velocity, u_* for Adopted $d_* = 0.10$ cm (•) with 95% Confidence Interval (——) and u_* for $d_* = 0.08$ cm (+), (Top); and Bottom Roughness, z_0, same notation as above, (Bottom); for L1, Method A.

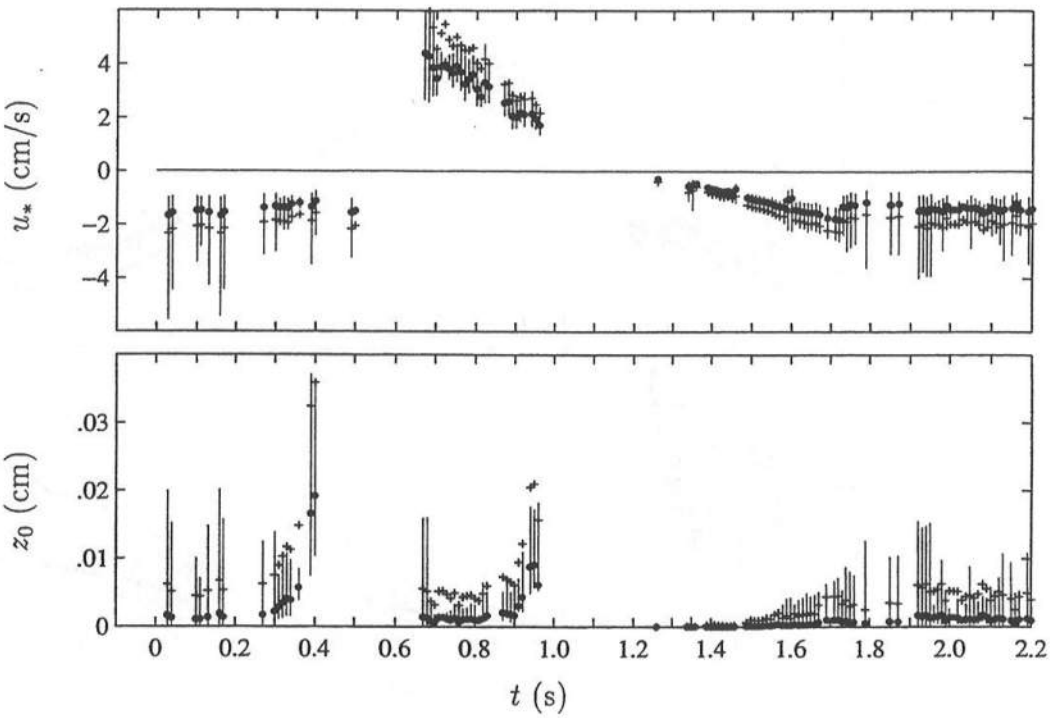

Figure 5.16: Temporal Variations of Shear Velocity, u_* for Adopted $d_* = 0.10$ cm (•) with 95% Confidence Interval (——) and u_* for $d_* = 0.08$ cm (+), (Top); and Bottom Roughness, z_0, same notation as above, (Bottom); for L2, Method A.

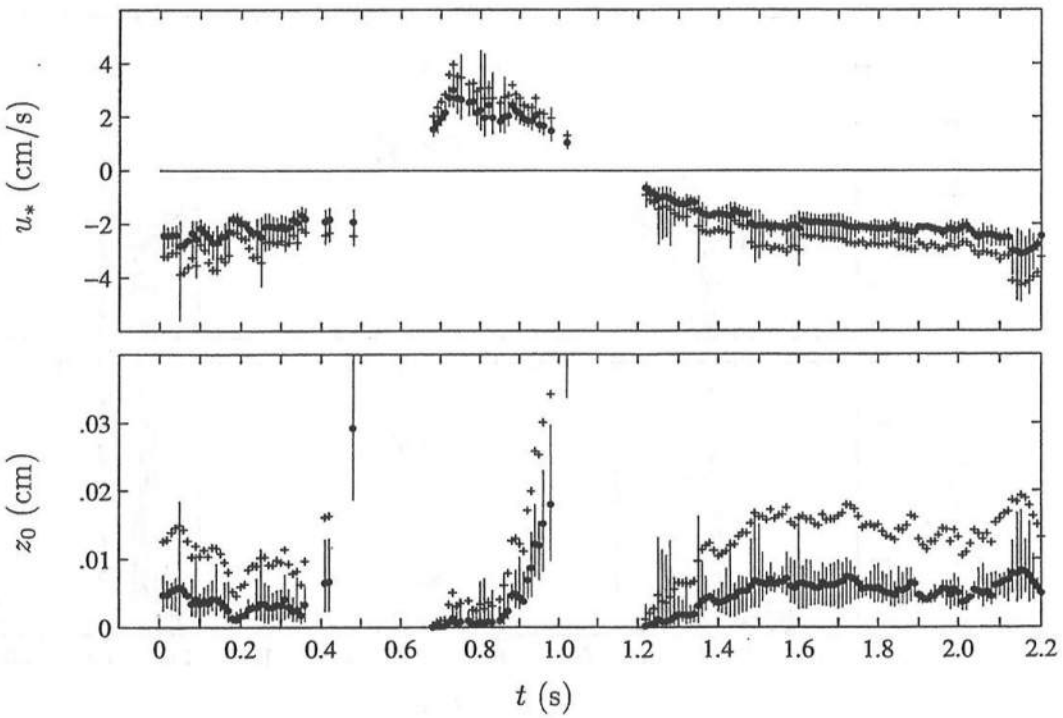

Figure 5.17: Temporal Variations of Shear Velocity, u_* for Adopted $d_* = 0.10$ cm (•) with 95% Confidence Interval (——) and u_* for $d_* = 0.08$ cm (+), (Top); and Bottom Roughness, z_0, same notation as above, (Bottom); for L3, Method A.

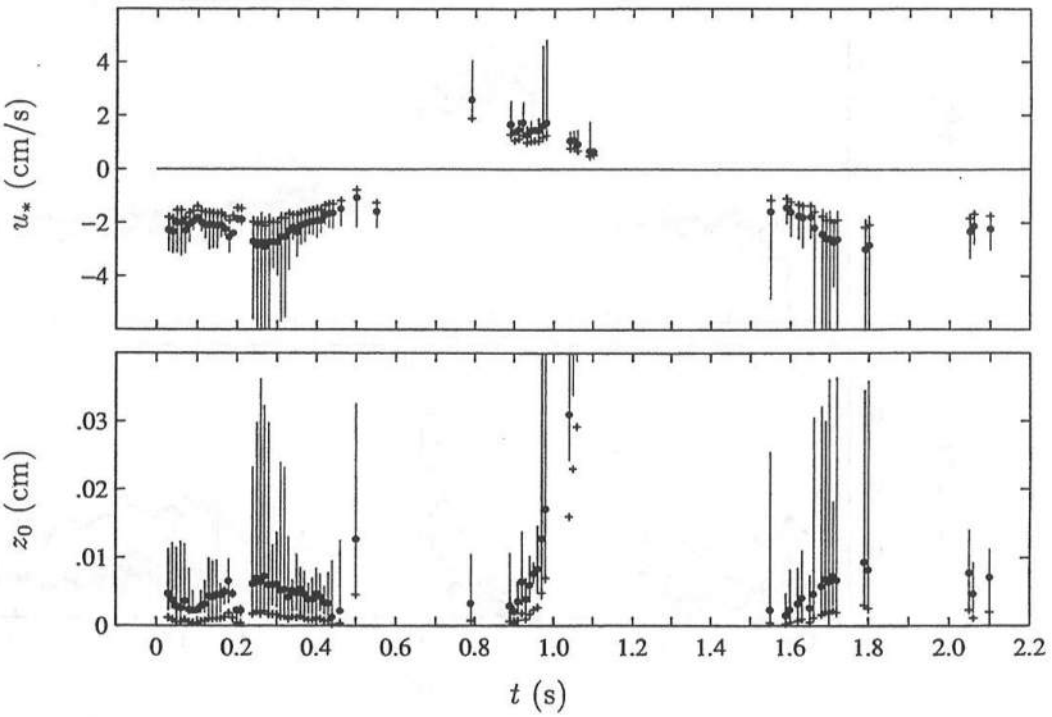

Figure 5.18: Temporal Variations of Shear Velocity, u_* for Adopted $d_* = 0.08$ cm (•) with 95% Confidence Interval (——) and u_* for $d_* = 0.10$ cm (+), (Top); and Bottom Roughness, z_0, same notation as above, (Bottom); for L4, Method A.

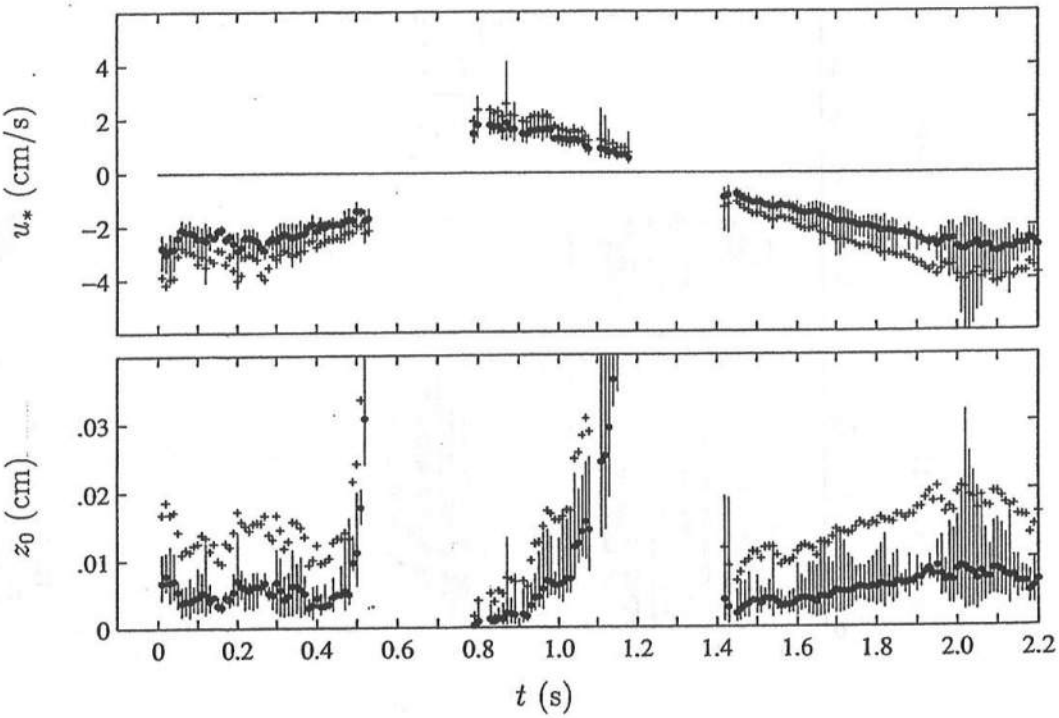

Figure 5.19: Temporal Variations of Shear Velocity, u_* for Adopted $d_* = 0.10$ cm (•) with 95% Confidence Interval (——) and u_* for $d_* = 0.08$ cm (+), (Top); and Bottom Roughness, z_0, same notation as above, (Bottom); for L5, Method A.

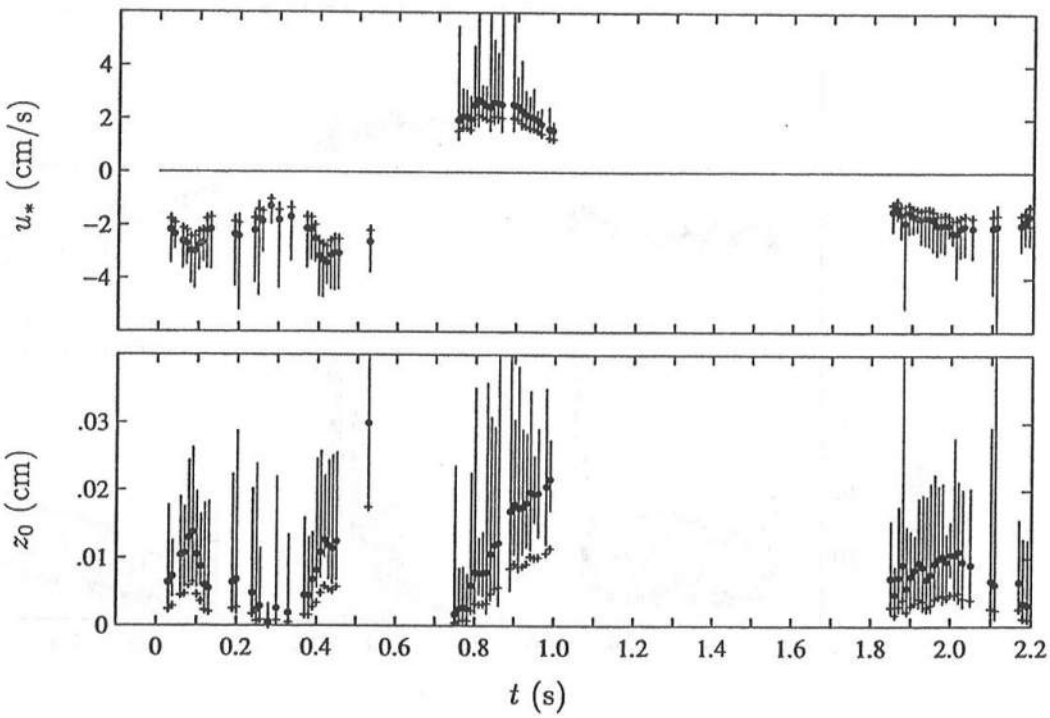

Figure 5.20: Temporal Variations of Shear Velocity, u_* for Adopted $d_* = 0.06$ cm (•) with 95% Confidence Interval (——) and u_* for $d_* = 0.08$ cm (+), (Top); and Bottom Roughness, z_0, same notation as above, (Bottom); for L6, Method A.

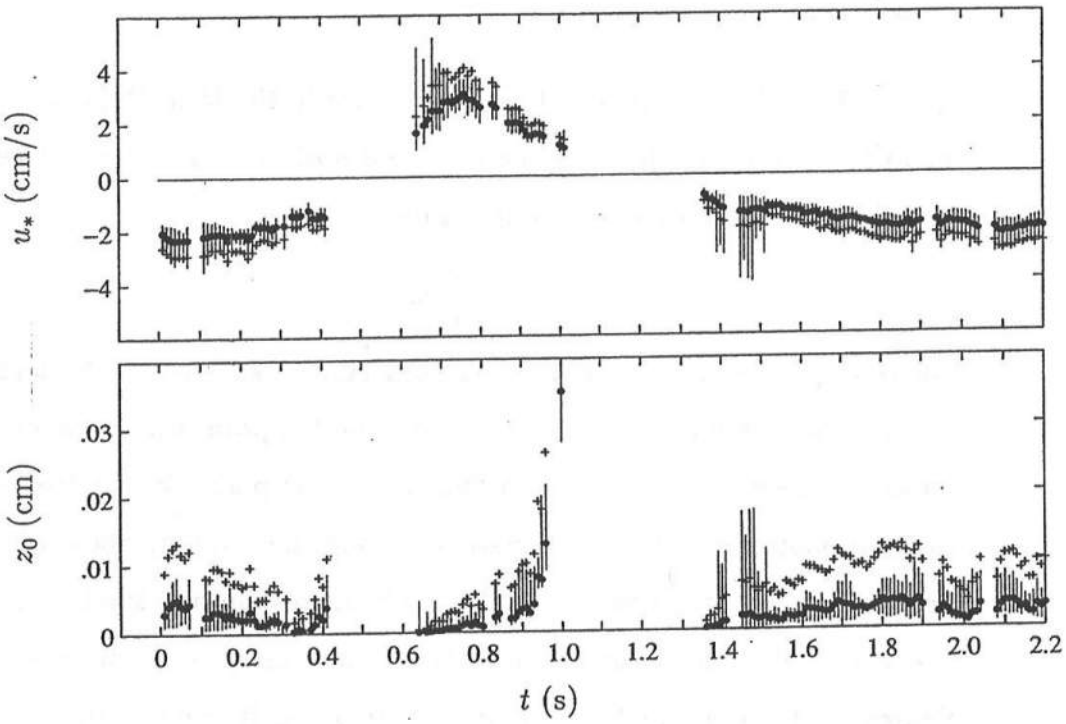

Figure 5.21: Temporal Variations of Shear Velocity, u_* for Adopted $d_* = 0.10$ cm (•) with 95% Confidence Interval (——) and u_* for $d_* = 0.08$ cm (+), (Top); and Bottom Roughness, z_0, same notation as above, (Bottom); for L3, Method A*.

5.5 Near-Bottom Shear Stress Estimates by Turbulent Velocity Covariance Measurements

In this section the shear stress estimates from the turbulent horizontal and vertical velocity covariance measurements near the bottom are presented. Comparisons are made to the bottom shear stress estimates based on the logarithmic velocity procedure from Section 5.3.

Assuming a constant shear stress layer in the logarithmic region (e.g., Yaglom 1979), the covariance of the turbulent horizontal and vertical velocities may be related to the bottom shear stress by

$$\frac{\tau_b}{\rho} \simeq -\sigma_{uw} \tag{5.35}$$

where σ_{uw} is the turbulent velocity covariance measured in the logarithmic velocity region. Figures 5.22 to 5.27 show the temporal variations of the velocity covariance, $-\sigma_{uw}$, at the bottom four measuring points for L1 to L6. These figures are plotted using a combination of solid lines and symbols where the lines are plotted using the data at all of the 220 phases and the symbols are plotted at every fifth phase for clarity. There is a significant amount of noise in all of the figures, particularly for L3 to L6 in the surf zone. It is noted that the magnitude of σ_{uw} is much smaller near the bottom, $\sigma_{uw} \sim 10$ cm^2/s^2, than below trough level under the breaking wave, $\sigma_{uw} \sim 100$ cm^2/s^2 as shown in Figure 4.15. Measurement errors are larger when measuring the smaller quantity, especially the small vertical velocity near the rough bottom. Also, it was noted in Chapter 3 that a pair of burst spectrum analyzers were used to reduce the noise due to reflection from the solid boundary. However, it is unlikely that the BSAs could eliminate the problem completely. For these reasons, the measurements of $-\sigma_{uw}$ near the bottom are interpreted with caution. Nevertheless, Figures 5.22 to 5.27 show that the variation of $-\sigma_{uw}$ at a given phase for the four measuring point elevations is

small, suggesting that the assumption of a constant stress layer might be valid in the logarithmic velocity region. It is important to note that Grant and Madsen (1986) indicated that the approximation of the logarithmic velocity region is valid to a greater extent than the approximation of a constant stress layer.

The bottom shear stress for the oscillatory flow is related to the shear velocity by

$$\frac{\tau_b}{\rho} = |u_*|\, u_* \tag{5.36}$$

where u_* is the shear velocity and was estimated from the logarithmic fit using the least-squares method in Section 5.3. Figures 5.22 to 5.27 compare the bottom shear stress following Eqs 5.36 and 5.35 for L1 to L6. The bottom shear stress estimates from the shear velocity follow from Figures 5.9 to 5.14 of Section 5.3. The bottom shear stress estimated from the turbulent velocity covariance is taken as the average of the velocity covariances at the bottom four points shown in Figures 5.22 to 5.27 and is denoted by $-[\sigma_{uw}]_{ave}$. In general, the bottom shear stress estimates from the velocity covariance are much less than the bottom shear stress estimates from the least-squares method. Sleath (1987) also indicated difficulty in measuring the covariance near a rough bed using a laser-Doppler velocimeter, even in the absence of wave breaking. Considering the noise and unknown confidence interval of the covariance measurements, the bottom shear stress estimated using Eq 5.35 is unreliable in the immediate vicinity of the bottom. The bottom shear stress estimated using Eq 5.36 are used in the following analysis.

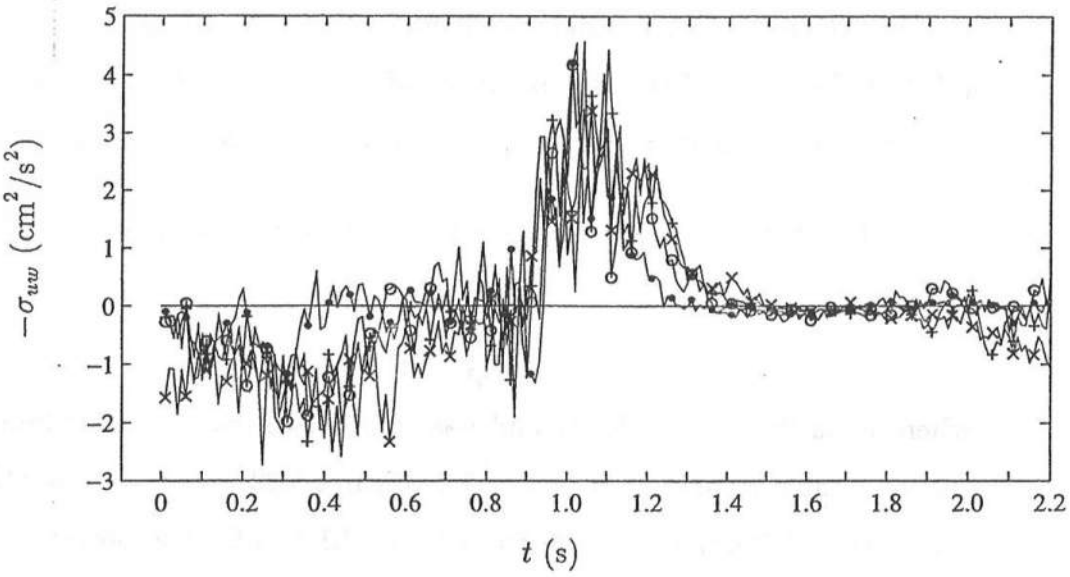

Figure 5.22: Temporal Variations of Measured Bottom Shear Stress, $-\sigma_{uw}$, at Bottom Four Elevations with $z_m = 0.13$ (——•), $z_m = 0.15$ (——○), $z_m = 0.17$ (——+), $z_m = 0.20$ cm (——×) for L1.

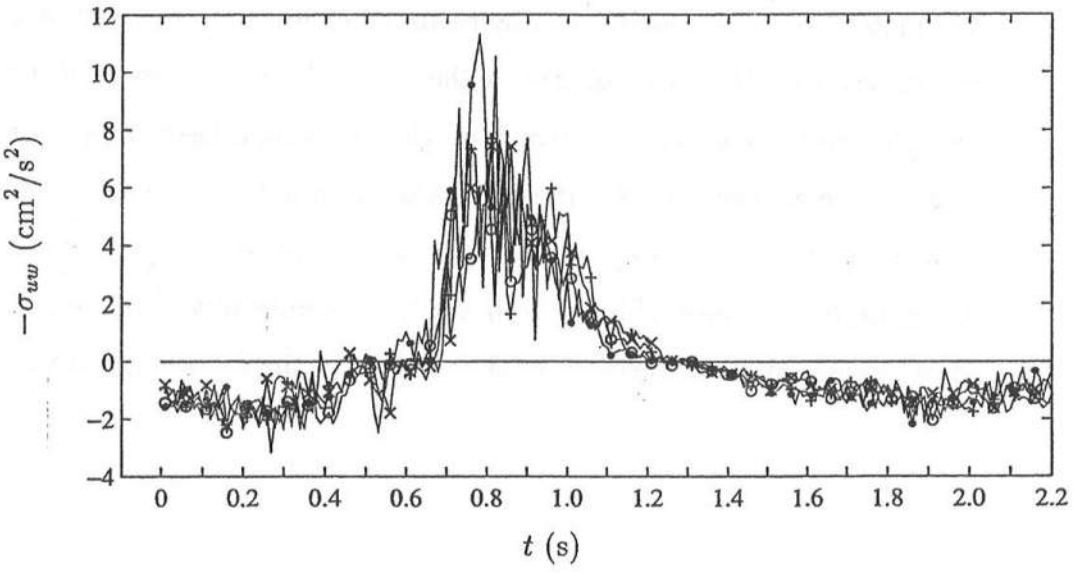

Figure 5.23: Temporal Variations of Measured Bottom Shear Stress, $-\sigma_{uw}$, at Bottom Four Elevations with $z_m = 0.13$ (——•), $z_m = 0.15$ (——○), $z_m = 0.17$ (——+), $z_m = 0.20$ cm (——×) for L2.

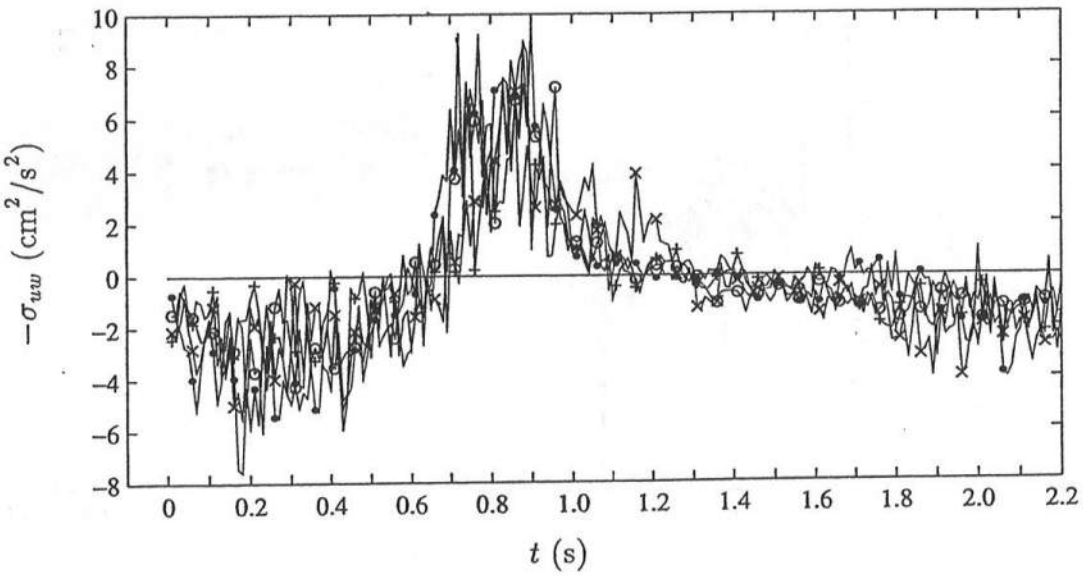

Figure 5.24: Temporal Variations of Measured Bottom Shear Stress, $-\sigma_{uw}$, at Bottom Four Elevations with $z_m = 0.13$ (——•), $z_m = 0.15$ (——○), $z_m = 0.17$ (——+), $z_m = 0.20$ cm (——×) for L3.

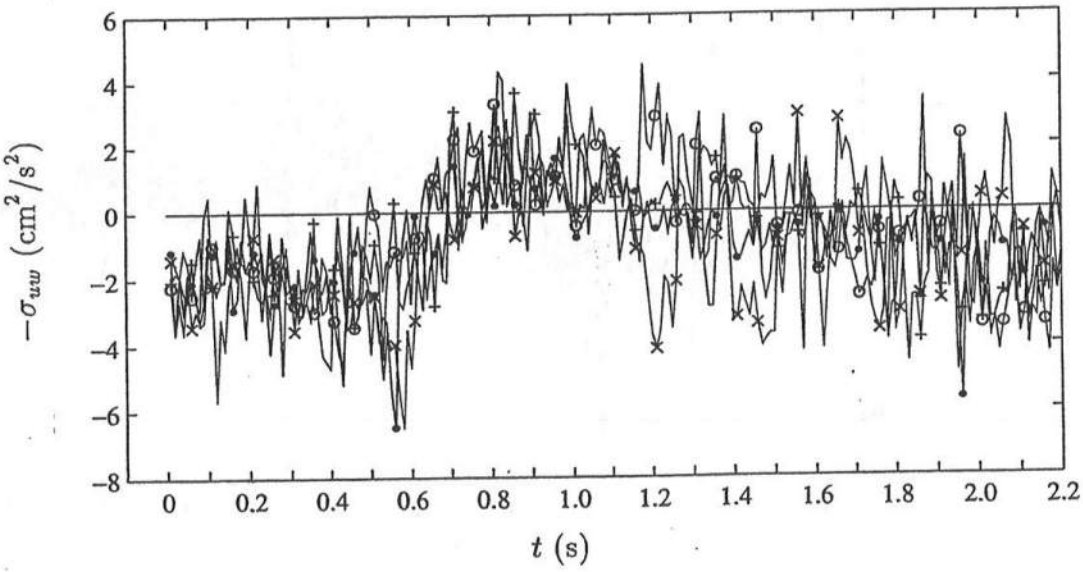

Figure 5.25: Temporal Variations of Measured Bottom Shear Stress, $-\sigma_{uw}$, at Bottom Four Elevations with $z_m = 0.13$ (——•), $z_m = 0.15$ (——○), $z_m = 0.17$ (——+), $z_m = 0.20$ cm (——×) for L4.

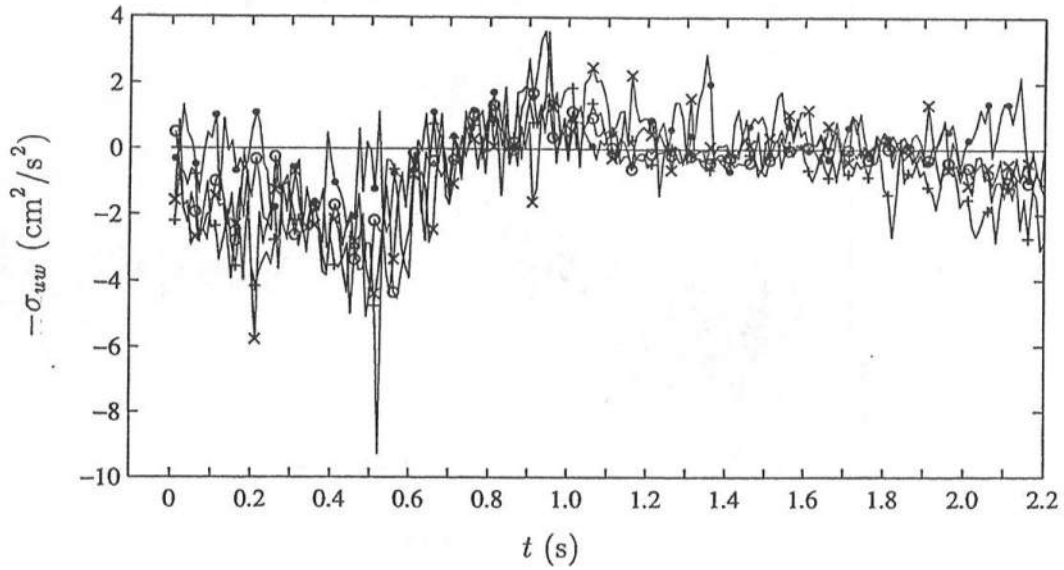

Figure 5.26: Temporal Variations of Measured Bottom Shear Stress, $-\sigma_{uw}$, at Bottom Four Elevations with $z_m = 0.13$ (——•), $z_m = 0.15$ (——○), $z_m = 0.17$ (——+), $z_m = 0.20$ cm (——×) for L5.

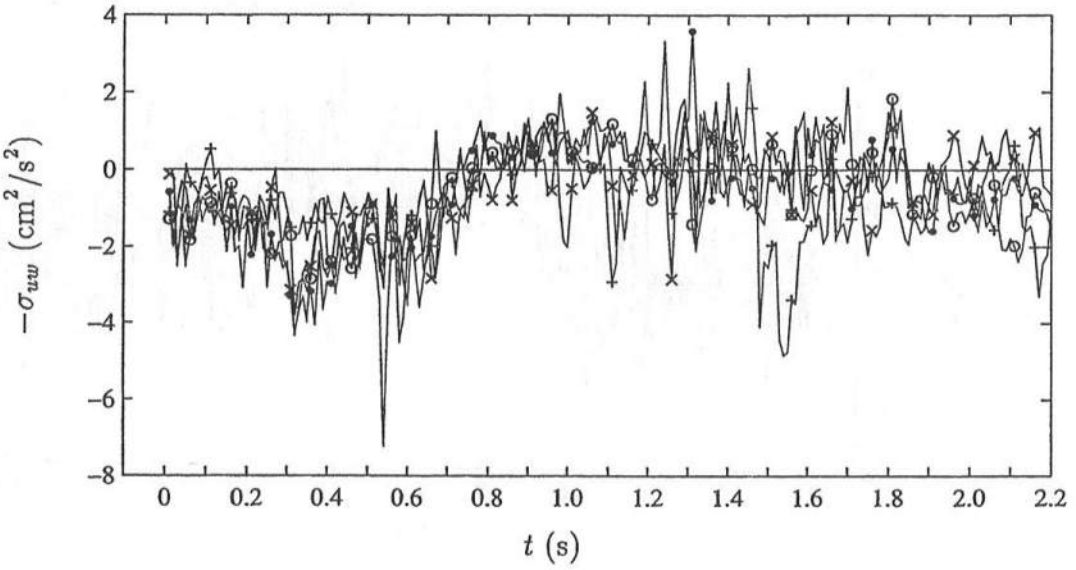

Figure 5.27: Temporal Variations of Measured Bottom Shear Stress, $-\sigma_{uw}$, at Bottom Four Elevations with $z_m = 0.13$ (——•), $z_m = 0.15$ (——○), $z_m = 0.17$ (——+), $z_m = 0.20$ cm (——×) for L6.

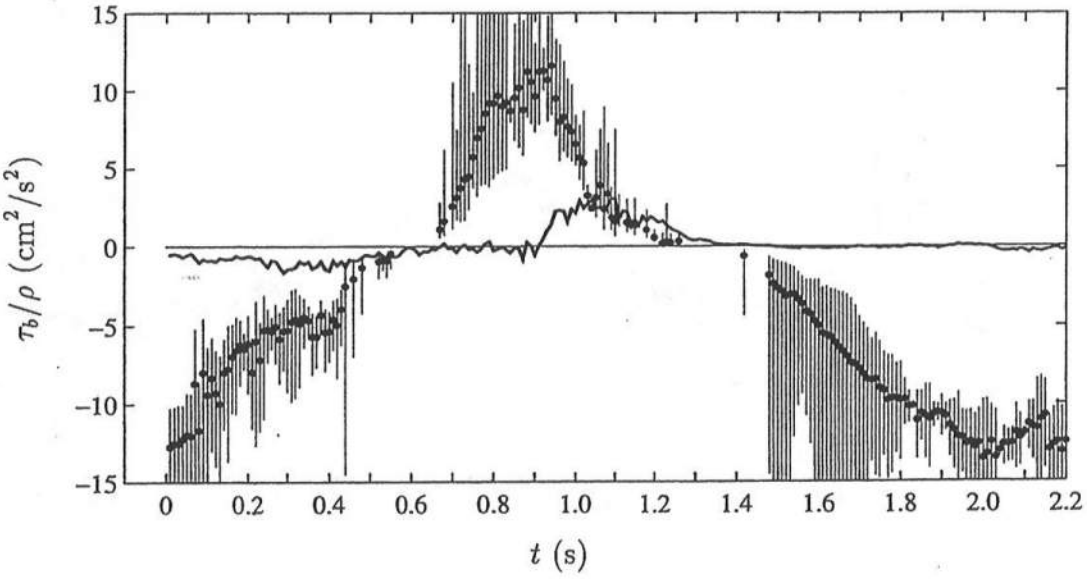

Figure 5.28: Temporal Variations of Bottom Shear Stress, $|u_*|\, u_*$ (•) with 95% Confidence Interval (——), and Shear Stress Averaged for $0.13 \leq z_m \leq 0.20$ cm, $-[\sigma_{uw}]_{ave}$ (——), for L1.

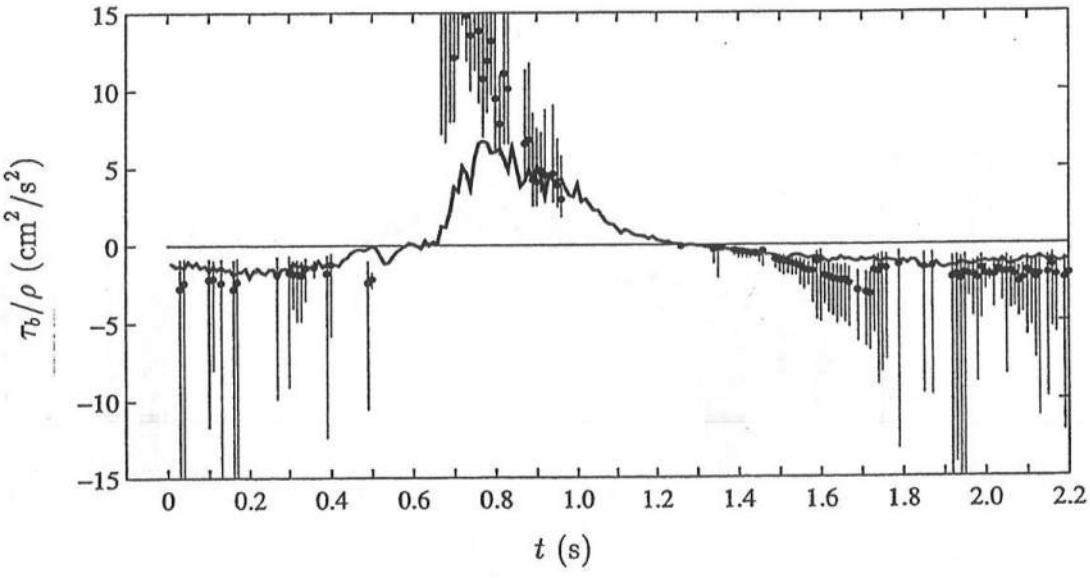

Figure 5.29: Temporal Variations of Bottom Shear Stress, $|u_*|\, u_*$ (•) with 95% Confidence Interval (——), and Shear Stress Averaged for $0.13 \leq z_m \leq 0.20$ cm, $-[\sigma_{uw}]_{ave}$ (——), for L2.

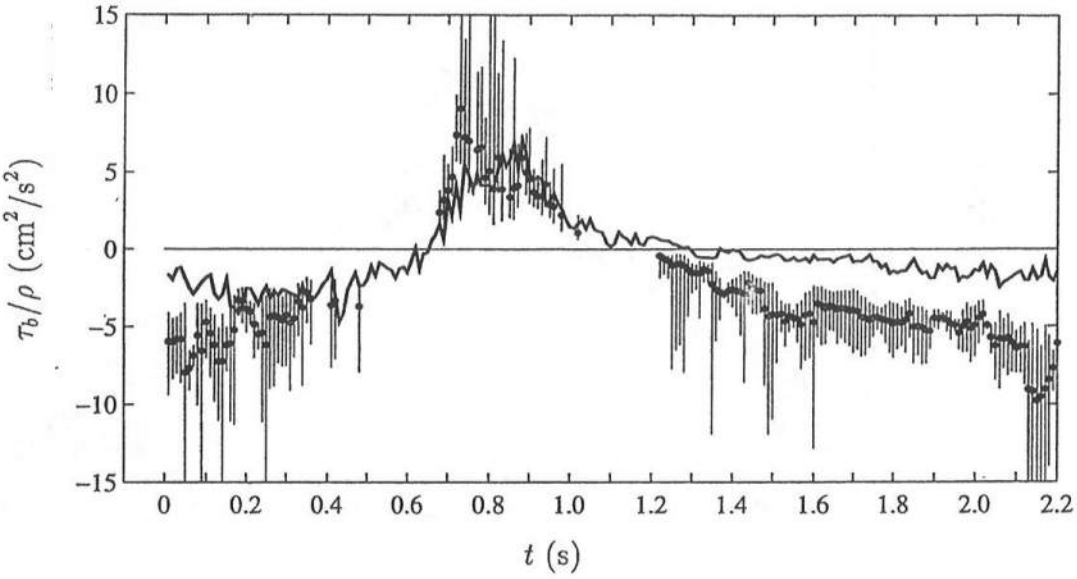

Figure 5.30: Temporal Variations of Bottom Shear Stress, $|u_*|\, u_*$ (•) with 95% Confidence Interval (——), and Shear Stress Averaged for $0.13 \leq z_m \leq 0.20$ cm, $-[\sigma_{uw}]_{ave}$ (——), for L3.

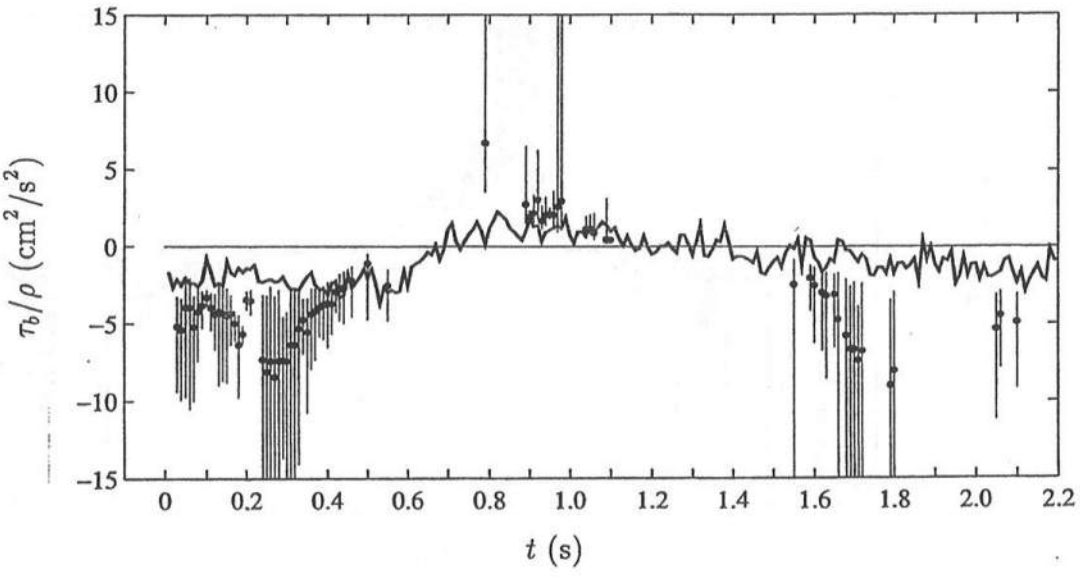

Figure 5.31: Temporal Variations of Bottom Shear Stress, $|u_*|\, u_*$ (•) with 95% Confidence Interval (——), and Shear Stress Averaged for $0.13 \leq z_m \leq 0.20$ cm, $-[\sigma_{uw}]_{ave}$ (——), for L4.

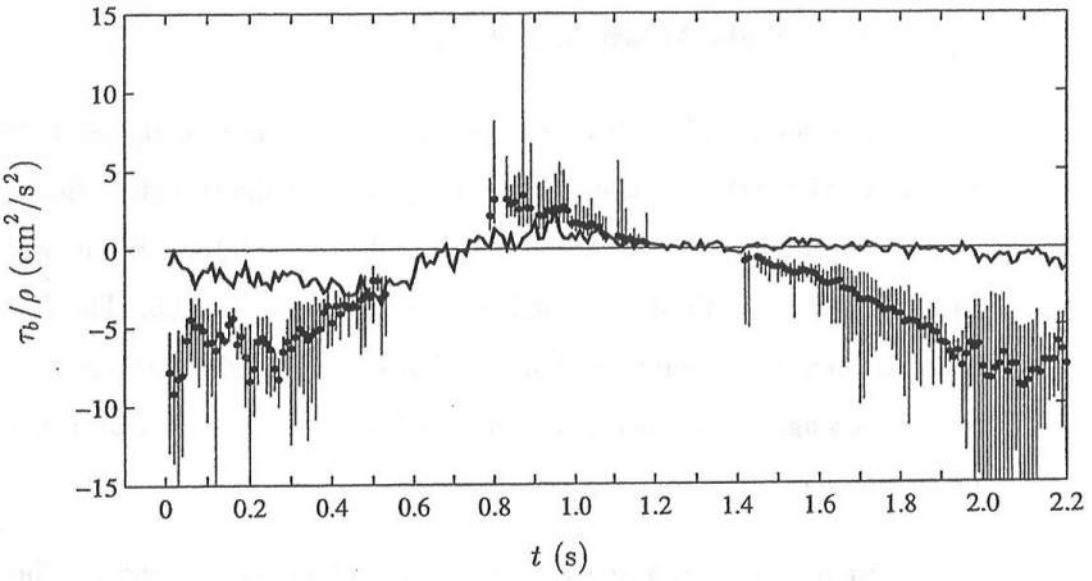

Figure 5.32: Temporal Variations of Bottom Shear Stress, $|u_*|\ u_*$ (•) with 95% Confidence Interval (——), and Shear Stress Averaged for $0.13 \leq z_m \leq 0.20$ cm, $-[\sigma_{uw}]_{ave}$ (——), for L5.

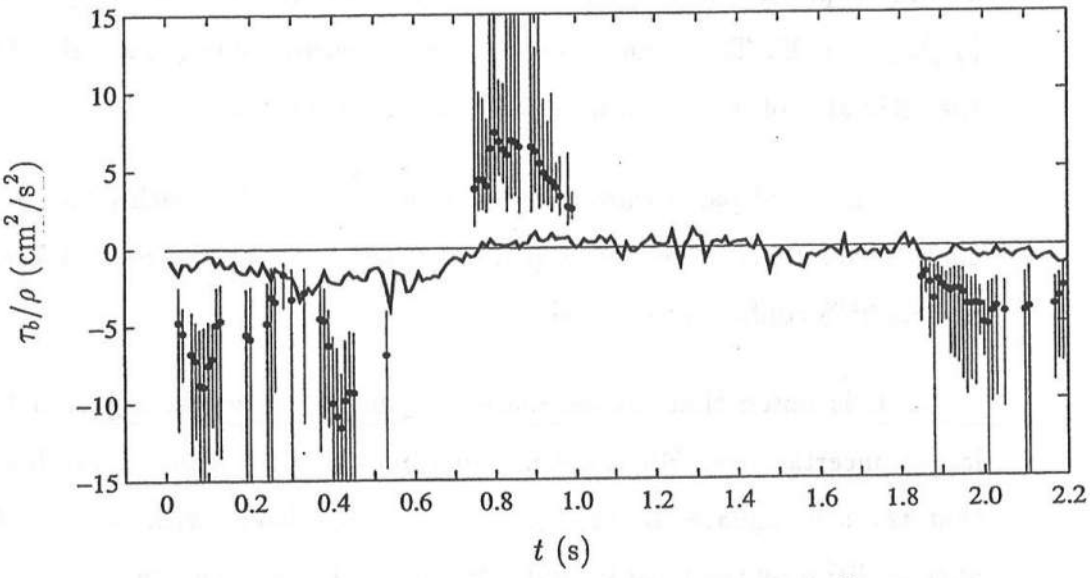

Figure 5.33: Temporal Variations of Bottom Shear Stress, $|u_*|\ u_*$ (•) with 95% Confidence Interval (——), and Shear Stress Averaged for $0.13 \leq z_m \leq 0.20$ cm, $-[\sigma_{uw}]_{ave}$ (——), for L6.

5.6 Estimates of Shear Velocity and Bottom Roughness with Additional Eight Measuring Points

This section discusses the estimates of the shear velocity and bottom roughness using the eight additional measuring points of the two offset lines. The least-squares method applied to these points is denoted Method B and was described in Section 5.3. Method B is applied to L1, L2, L4, and L5. There were no additional measuring points at L6. For L3, the eight additional measuring points were in a single offset measuring line, and the results were shown in Figure 5.21 of Section 5.4.

Figures 5.34 to 5.37 show the results of Method B and can be compared to Figures 5.9, 5.10, 5.12 and 5.13 of Method A. The top panel of Figure 5.34 shows the temporal variation of the maximum correlation coefficient squared, $[\gamma_{xy}^2]_{max}$, for the three lines at a given phase. The maximum correlation coefficient squared is plotted in the range $0.95 < [\gamma_{xy}^2]_{max} < 1.00$ and for many of the phases, $[\gamma_{xy}^2]_{max} > 0.99$. The second panel shows the corresponding Δx value from which the estimates of u_* and z_0 were selected at a given phase.

The third panel shows the value of u_* selected at each phase and its 95% confidence interval. The fourth panel shows the value of z_0 selected at each phase and its 95% confidence interval.

It is noted that the estimate of z_0 for L4 shown in Figure 5.36 contains larger uncertainties. For the remaining lines, L1, L2, and L5, Method B shows that the least-squares method gives results consistent with Method A and are affected little by the local irregularities in the bottom roughness.

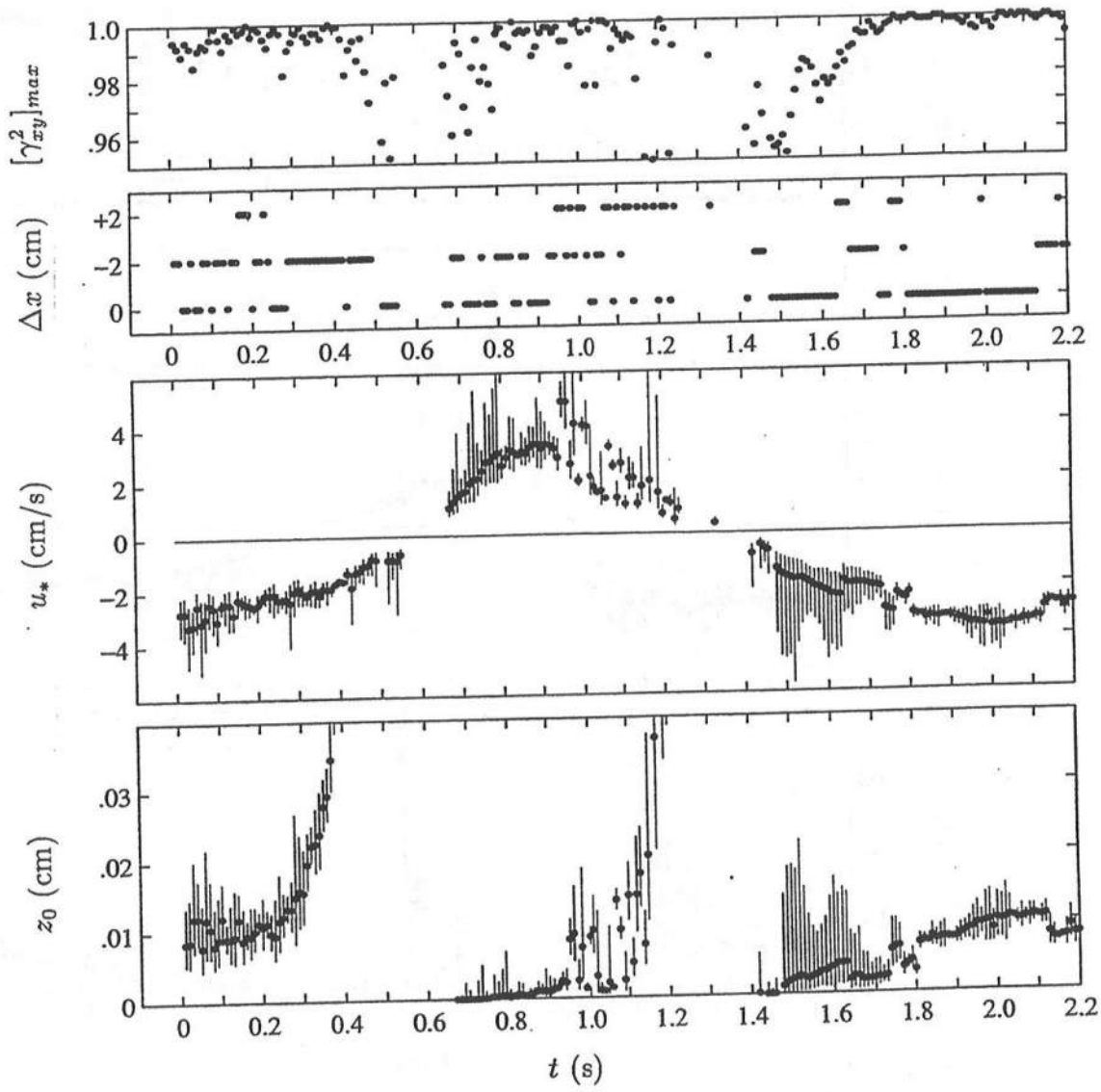

Figure 5.34: Temporal Variations of Maximum Correlation Coefficient Squared, $[\gamma^2_{xy}]_{max}$ (•), (Top); Corresponding Δx Location (•) (Second); Shear Velocity, u_* (•) with 95% Confidence Interval (——), (Third); and Bottom Roughness, z_0 (•) with 95% Confidence Interval (——), (Bottom); and for L1, Method B.

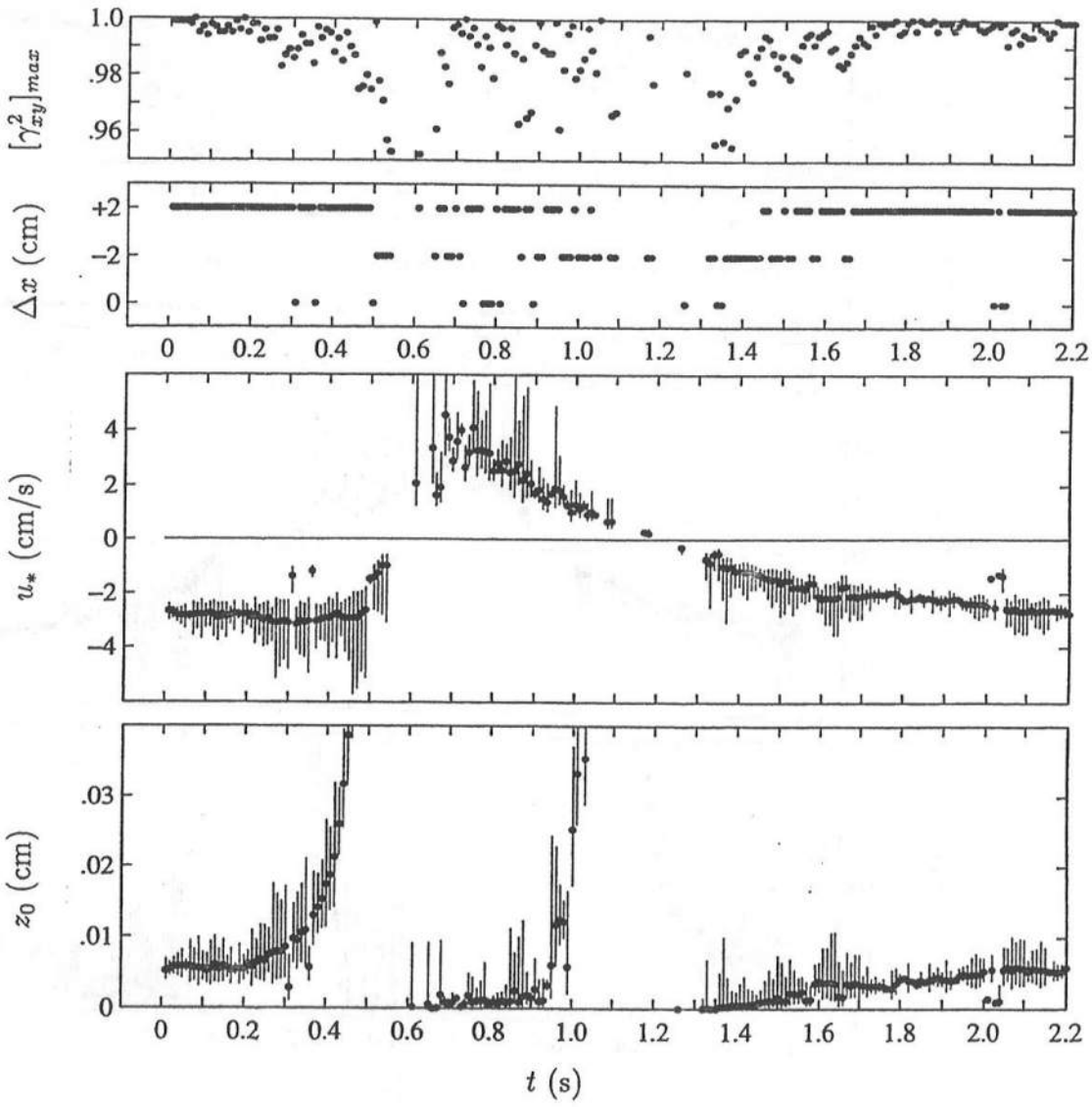

Figure 5.35: Temporal Variations of Maximum Correlation Coefficient Squared, $[\gamma^2_{xy}]_{max}$ (•), (Top); Corresponding Δx Location (•) (Second); Shear Velocity, u_* (•) with 95% Confidence Interval (——), (Third); and Bottom Roughness, z_0 (•) with 95% Confidence Interval (——), (Bottom); and for L2, Method B.

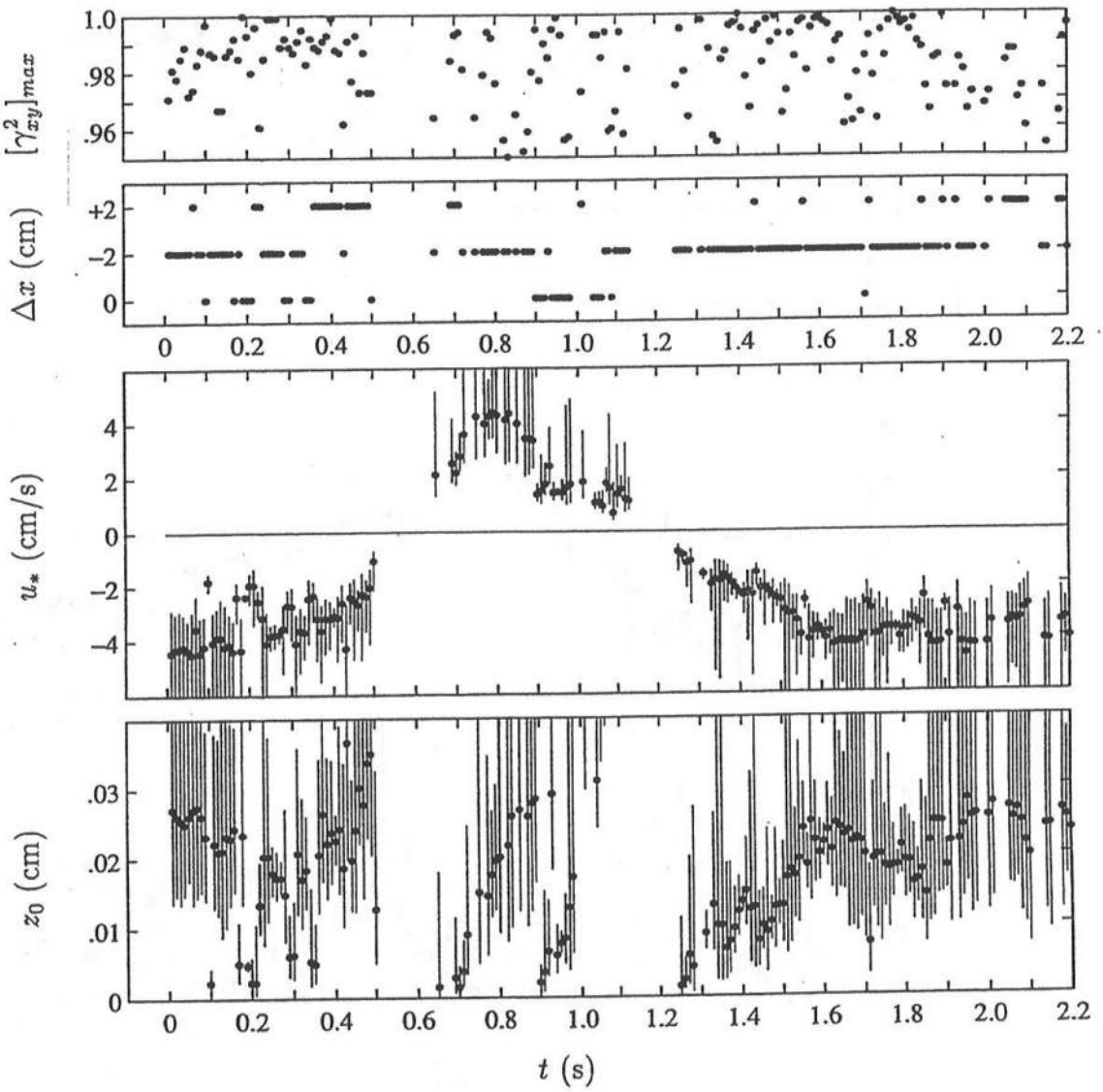

Figure 5.36: Temporal Variations of Maximum Correlation Coefficient Squared, $[\gamma^2_{xy}]_{max}$ (•), (Top); Corresponding Δx Location (•) (Second); Shear Velocity, u_* (•) with 95% Confidence Interval (——), (Third); and Bottom Roughness, z_0 (•) with 95% Confidence Interval (——), (Bottom); and for L4, Method B.

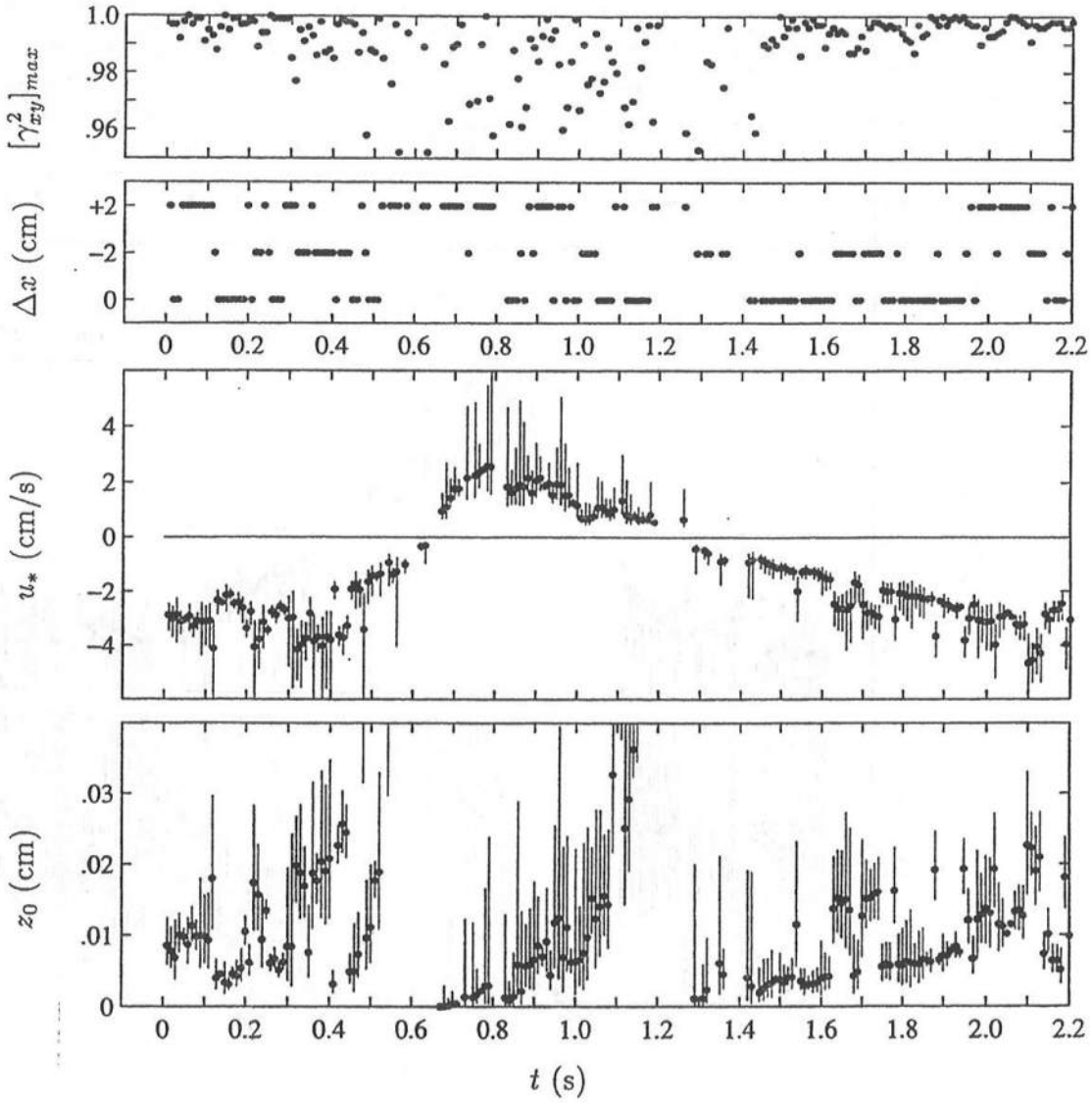

Figure 5.37: Temporal Variations of Maximum Correlation Coefficient Squared, $[\gamma^2_{xy}]_{max}$ (•), (Top); Corresponding Δx Location (•) (Second); Shear Velocity, u_* (•) with 95% Confidence Interval (——), (Third); and Bottom Roughness, z_0 (•) with 95% Confidence Interval (——), (Bottom); and for L5, Method B.

5.7 Boundary Layer Thickness

This section discusses the thickness of the boundary layer. The vertical variations of the horizontal velocity, turbulent kinetic energy, and shear stress estimated from the velocity covariance are shown near the bottom for the range $0 < z_m < 2.1$ cm to infer the boundary layer thickness.

The horizontal velocity profile near the bottom is smooth and continuous, and there is no sharp transition to indicate the exact thickness of the boundary layer. The thickness of the boundary layer depends on the definition. Grant and Madsen (1979) defined the boundary layer thickness, δ, as twice the boundary length scale given as

$$\delta_{GM} = 2\ell = 2\frac{\kappa\,|u_{*cw}|}{\omega}, \tag{5.37}$$

where δ_{GM} is the boundary layer thickness with the subscript GM indicating that it is the definition of Grant and Madsen (1979), ℓ is the boundary layer length scale, $|u_{*cw}|$ is the shear velocity including the effects of waves and currents, κ is the Kármán constant ($\kappa \simeq 0.4$), and ω is the wave frequency. The shear velocity in Eq 5.37 is related to the maximum bottom shear stress as

$$|u_{*cw}| = \left(\frac{|\tau_{b,max}|}{\rho}\right)^{\frac{1}{2}}, \tag{5.38}$$

where $|\tau_{b,max}|$ is the maximum bottom shear stress due to the combined effects of waves and currents

Trowbridge and Madsen (1984a) defined the boundary layer length scale in terms of the absolute value of the time-averaged shear velocity, $\overline{|u_*|}$, to be

$$\ell = \frac{\kappa\overline{|u_*|}}{\omega} \tag{5.39}$$

where

$$\overline{|u_*|} = \overline{\left|\frac{\tau_b}{\rho}\right|}^{\frac{1}{2}}. \tag{5.40}$$

Assuming the boundary layer thickness to be twice the boundary length scale would give

$$\delta_{TM} = 2\frac{\kappa\overline{|u_*|}}{\omega} \tag{5.41}$$

where the subscript TM indicates that the definition of the boundary layer thickness follows from Trowbridge and Madsen (1984a).

Table 5.4 lists the boundary layer thickness following Eqs 5.37 and 5.41. It is noted that $\overline{|u_*|}$ indicated in the table is not a time-average over all of the phases. The third column indicates the number of phases, N_γ, used to compute $\overline{|u_*|}$. The mean boundary layer thickness for the 11 estimates in Table 5.4 using Eqs 5.37 and 5.41, respectively, is

$$\delta_{GM} = 1.08 \text{ cm } (.22) \tag{5.42}$$

$$\delta_{TM} = 0.62 \text{ cm } (.10) \tag{5.43}$$

where the standard deviation is indicated in parentheses. These estimates will be assessed in comparison to the vertical variation of the hydrodynamic quantities.

The time-averaged horizontal velocity, $\overline{u_a}$, is separated from the phase-averaged velocity, u_a to yield the oscillatory component, $\tilde{u}_a$, given by

$$\tilde{u}_a = u_a - \overline{u_a}. \tag{5.44}$$

Similarly, the Reynolds stress estimates and turbulent kinetic energy are separated as

$$\frac{\tilde{\tau}}{\rho} = \frac{\tau}{\rho} - \frac{\overline{\tau}}{\rho} \tag{5.45}$$

and

$$\tilde{k} = k - \overline{k}, \tag{5.46}$$

where $\tau/\rho = -\sigma_{uw}$ and $k = (3/4)(\sigma_u^2 + \sigma_w^2)$ as explained in Section 6.1

Table 5.4: Estimates of Bottom Boundary Layer Thickness for L1 to L6.

Line No.		Method		N_γ	$\lvert u_* \rvert_{max}$ (cm/s)	δ_{GM} (cm)	$\overline{\lvert u_* \rvert}$ (cm/s)	δ_{TM} (cm)
L1	A	n=4,5,6	Δx^0	177	3.68	1.03	2.57	0.72
	B	n=4	$\Delta x^{0,-,+}$	187	4.92	1.38	2.39	0.67
L2	A	n=4,5,6	Δx^0	112	4.42	1.24	1.71	0.48
	B	n=4	$\Delta x^{0,-,+}$	190	4.55	1.27	2.21	0.62
L3	A	n=4,5,6	Δx^0	167	3.13	0.88	2.08	0.58
	A*	n=4,5,6	Δx^-	141	3.08	0.86	1.87	0.52
L4	A	n=4,5,6	Δx^0	76	3.00	0.84	2.00	0.56
	B	n=4	$\Delta x^{0,-,+}$	168	4.66	1.31	3.06	0.86
L5	A	n=4,5,6	Δx^0	166	3.03	0.85	1.97	0.55
	B	n=4	$\Delta x^{0,-,+}$	189	4.66	1.31	2.21	0.62
L6	A	n=4,5,6	Δx^0	75	3.41	0.96	2.20	0.62

Figures 5.38 to 5.43 show the vertical variations of the oscillatory horizontal velocity, $\tilde{u}_a$, for the range $0 < z_m < 2.1$ cm at eleven phases for L1 to L6. The figures also show the time-averaged horizontal velocity, or undertow, $\overline{u_a}$, for the same range. The oscillatory velocities do not vary much outside the bottom boundary layer where both estimates given by Eqs 5.42 and 5.43 seem to be reasonable. The undertow profiles are fairly smooth and continuous across the boundary layer. The modeling of the undertow profiles is beyond the scope of this dissertation, but this data set could be used in developing the bottom boundary conditions for undertow models (e.g., Stive and De Vriend 1994).

Figures 5.44 to 5.49 show the vertical variations of the oscillatory shear stress, $\tilde{\tau}/\rho$, for the range $0 < z_m < 2.1$ cm at eleven phases for L1 to L6. The figures also show the time-averaged shear stress, $\overline{\tau}/\rho$, for the same range. The reliability of the Reynolds stress measurements in the immediate vicinity of the

rough bottom was discussed in Section 5.5. The measurements presented in Figures 5.44 to 5.49 are at a sufficient distance from the bottom and are expected to be less contaminated by the reflection at the boundary. These measurements should be acceptable at least qualitatively. Figures 5.44 and 5.45 for L1 and L2 show that the oscillatory shear stresses approach zero at the upper portion of the bottom boundary layer where the thickness is about 1 cm in a manner similar to the bottom boundary layer for purely oscillatory flow. Figures 5.46 to 5.49 for L3 to L6 show large variations without clear trends in $\tilde{\tau}/\rho$ near the bottom under breaking waves. It is difficult to delineate the bottom boundary in these figures. The time-averaged shear stress does not seem to have a linear variation with depth near the bottom as assumed in analytical solutions for undertow (e.g., Svendsen *et al.* 1987).

Figures 5.50 to 5.55 show the vertical variations of the oscillatory turbulent kinetic energy, $\tilde{k}$, for the range $0 < z_m < 2.1$ cm at eleven phases for L1 to L6. The figures also show the time-averaged turbulent kinetic energy, $\overline{k}$, for the same range. Figures 5.50 and 5.51 for L1 and L2 show that the turbulent kinetic energy is confined mainly to the bottom boundary layer outside the surf zone. The magnitudes of the oscillatory and mean components are similar outside the surf zone. Figures 5.52 to 5.55 for L3 to L6 show that the turbulent kinetic energy is larger in the surf zone and that it varies vertically across the bottom boundary layer whose thickness is difficult to identify. The magnitude of the mean component is larger than the oscillatory component in the surf zone. The vertical variations of the shear stress and turbulent kinetic energy are without a clear separation of the bottom boundary layer, suggesting that the turbulence generated by wave breaking reaches the bottom boundary layer.

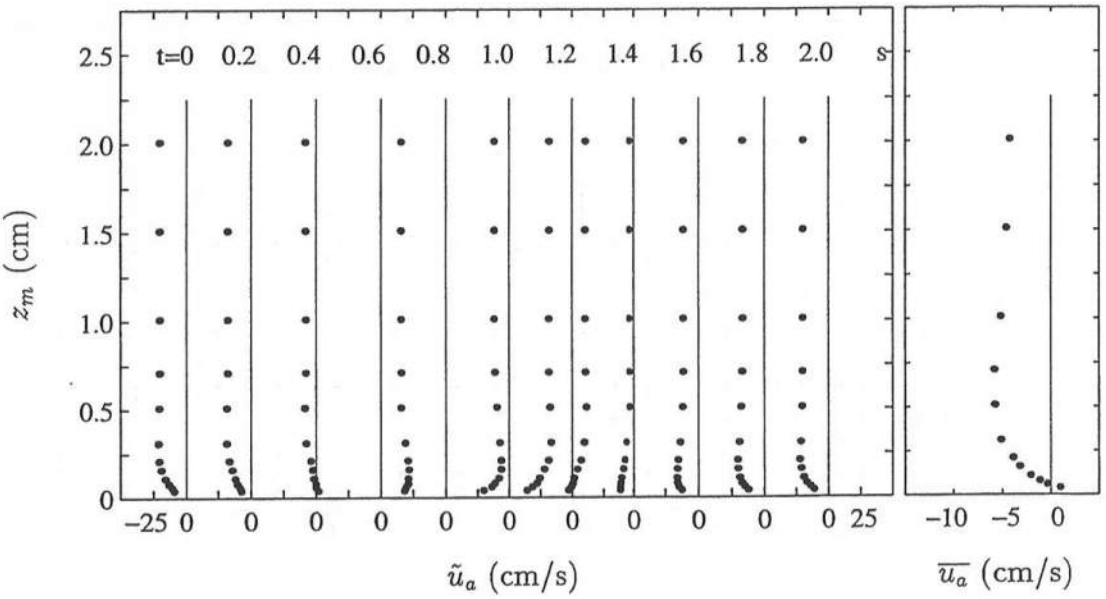

Figure 5.38: Vertical Variations of Oscillatory Component of Horizontal Velocity, $\tilde{u_a}$ (•), at Eleven Phases (Left), and Time-Averaged Horizontal Velocity, $\overline{u_a}$ (•), (Right) for L1.

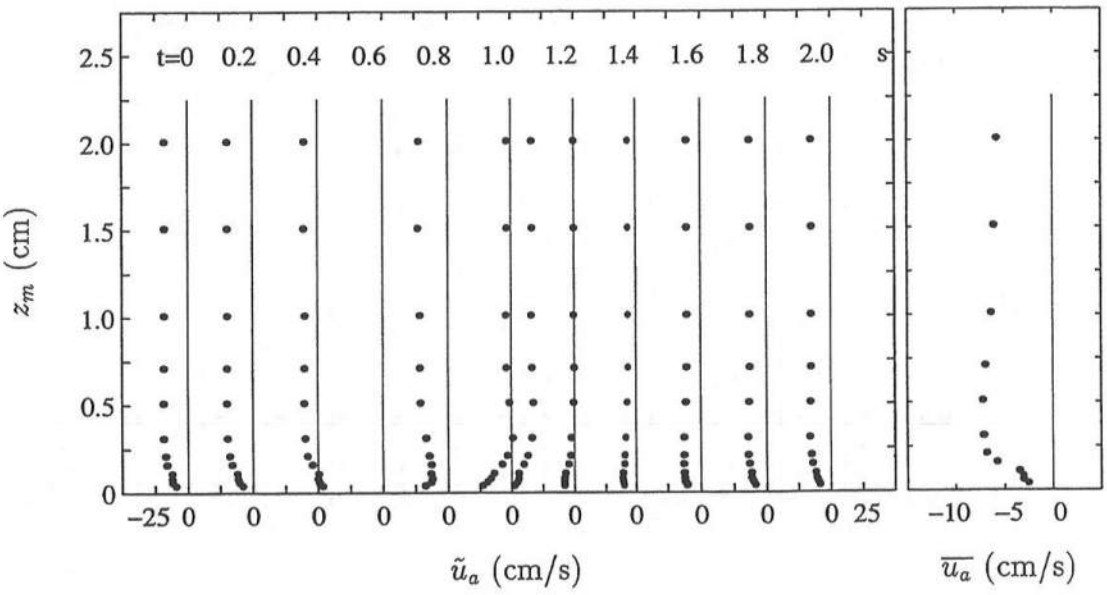

Figure 5.39: Vertical Variations of Oscillatory Component of Horizontal Velocity, $\tilde{u_a}$ (•), at Eleven Phases (Left), and Time-Averaged Horizontal Velocity, $\overline{u_a}$ (•), (Right) for L2.

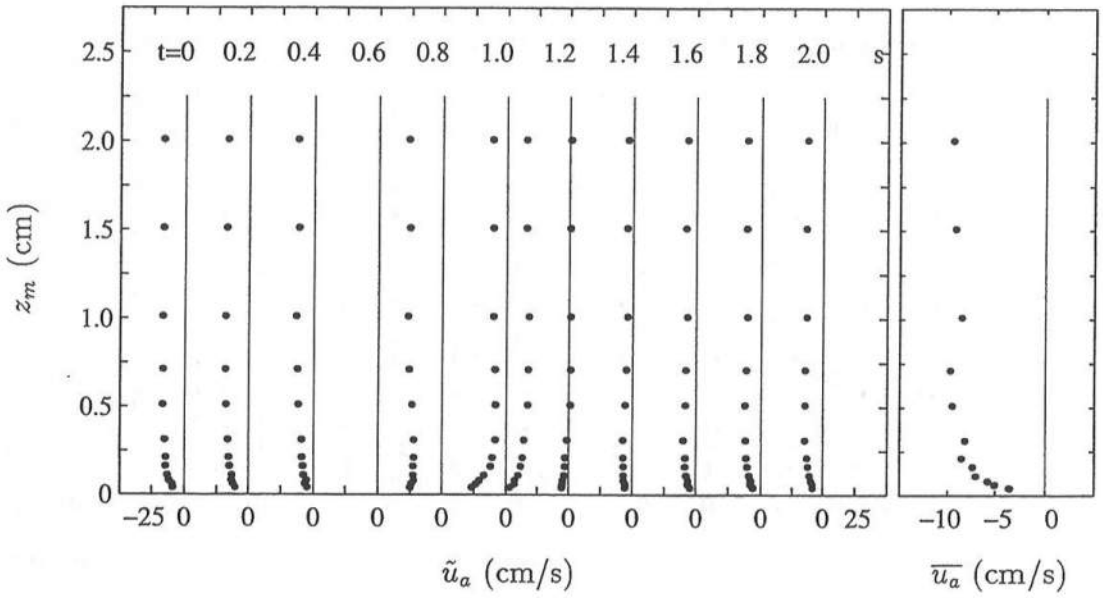

Figure 5.40: Vertical Variations of Oscillatory Component of Horizontal Velocity, $\tilde{u_a}$ (•), at Eleven Phases (Left), and Time-Averaged Horizontal Velocity, $\overline{u_a}$ (•), (Right) for L3.

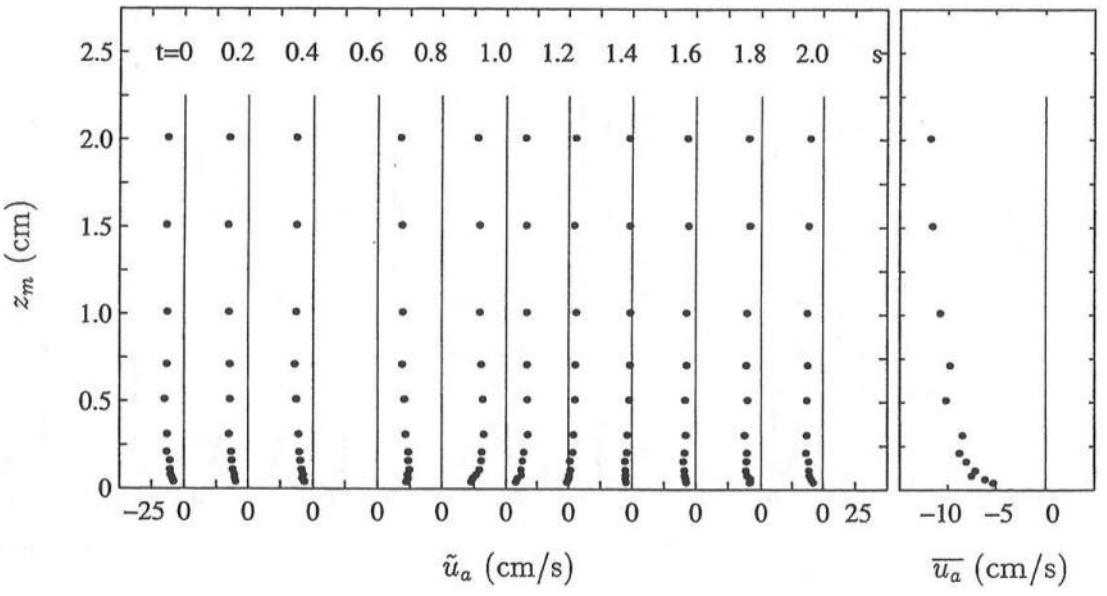

Figure 5.41: Vertical Variations of Oscillatory Component of Horizontal Velocity, $\tilde{u_a}$ (•), at Eleven Phases (Left), and Time-Averaged Horizontal Velocity, $\overline{u_a}$ (•), (Right) for L4.

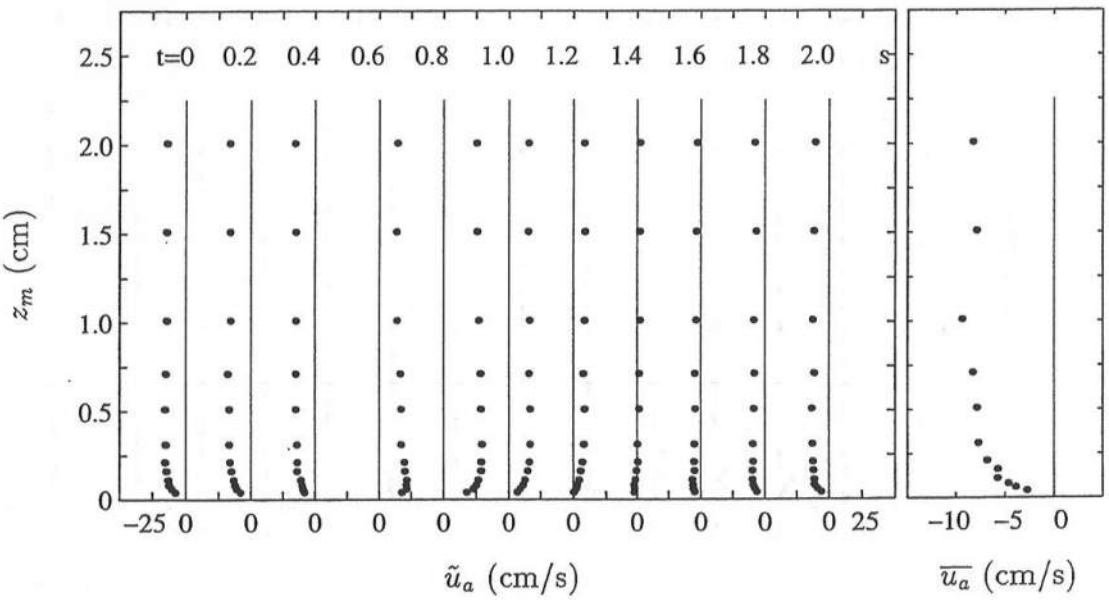

Figure 5.42: Vertical Variations of Oscillatory Component of Horizontal Velocity, $\tilde{u_a}$ (•), at Eleven Phases (Left), and Time-Averaged Horizontal Velocity, $\overline{u_a}$ (•), (Right) for L5.

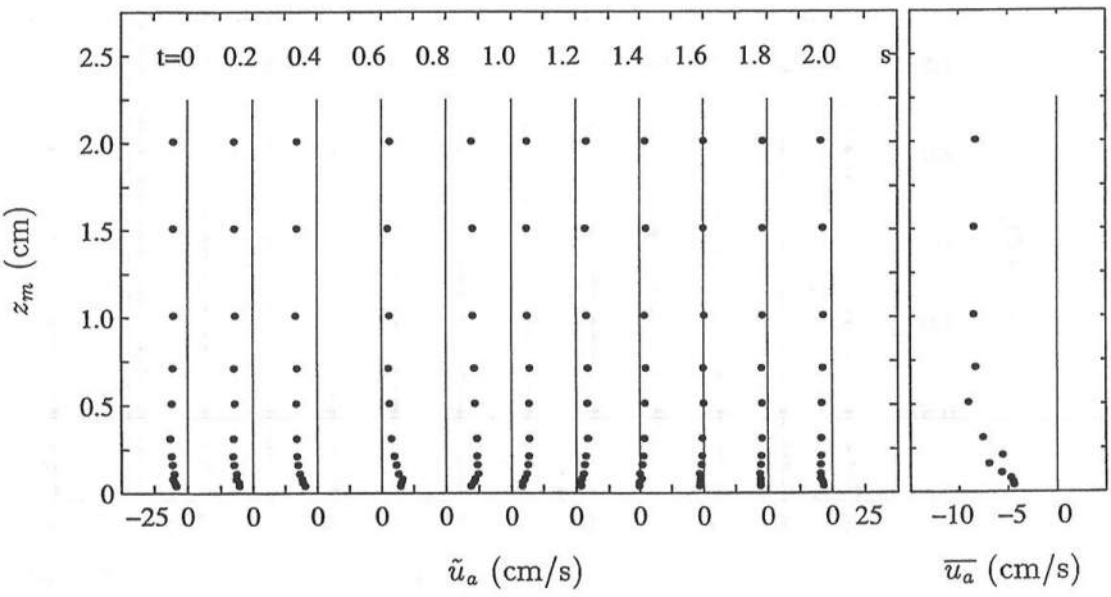

Figure 5.43: Vertical Variations of Oscillatory Component of Horizontal Velocity, $\tilde{u_a}$ (•), at Eleven Phases (Left), and Time-Averaged Horizontal Velocity, $\overline{u_a}$ (•), (Right) for L6.

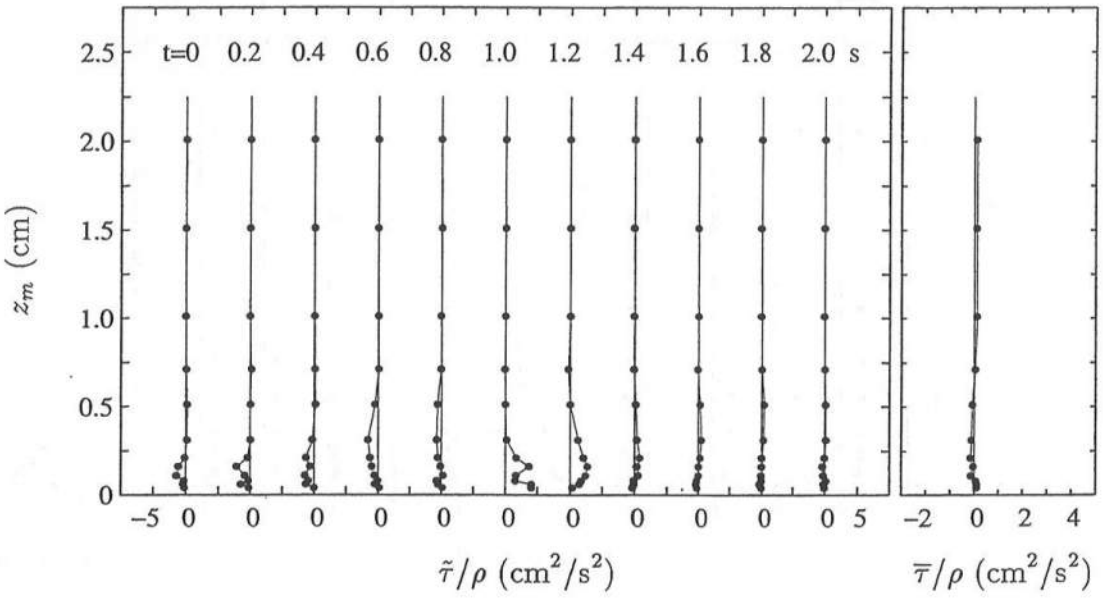

Figure 5.44: Vertical Variations of Oscillatory Component of Shear Stress, $\tilde{\tau}/\rho$ (• ——), at Eleven Phases (Left), and Time-Averaged Shear Stress, $\overline{\tau}/\rho$ (• ——), (Right) for L1.

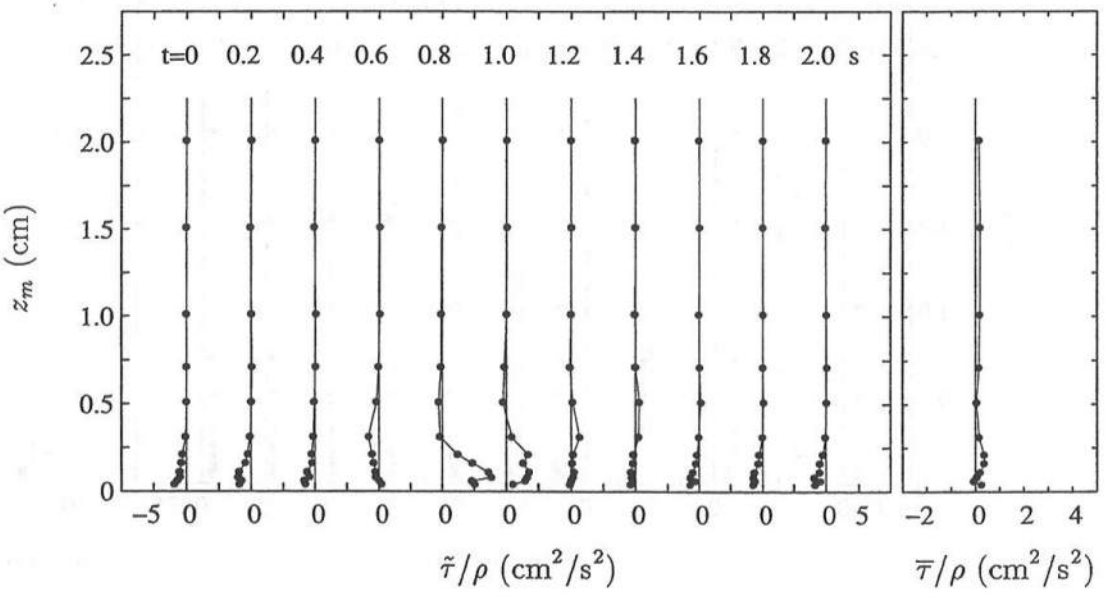

Figure 5.45: Vertical Variations of Oscillatory Component of Shear Stress, $\tilde{\tau}/\rho$ (• ——), at Eleven Phases (Left), and Time-Averaged Shear Stress, $\overline{\tau}/\rho$ (• ——), (Right) for L2.

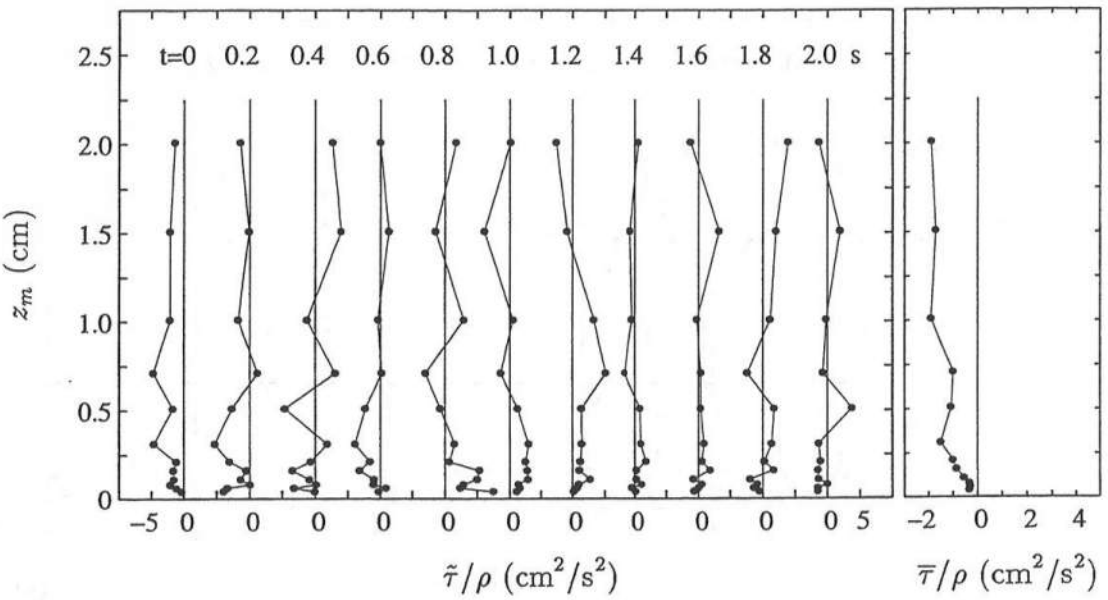

Figure 5.46: Vertical Variations of Oscillatory Component of Shear Stress, $\tilde{\tau}/\rho$ (• ——), at Eleven Phases (Left), and Time-Averaged Shear Stress, $\overline{\tau}/\rho$ (• ——), (Right) for L3.

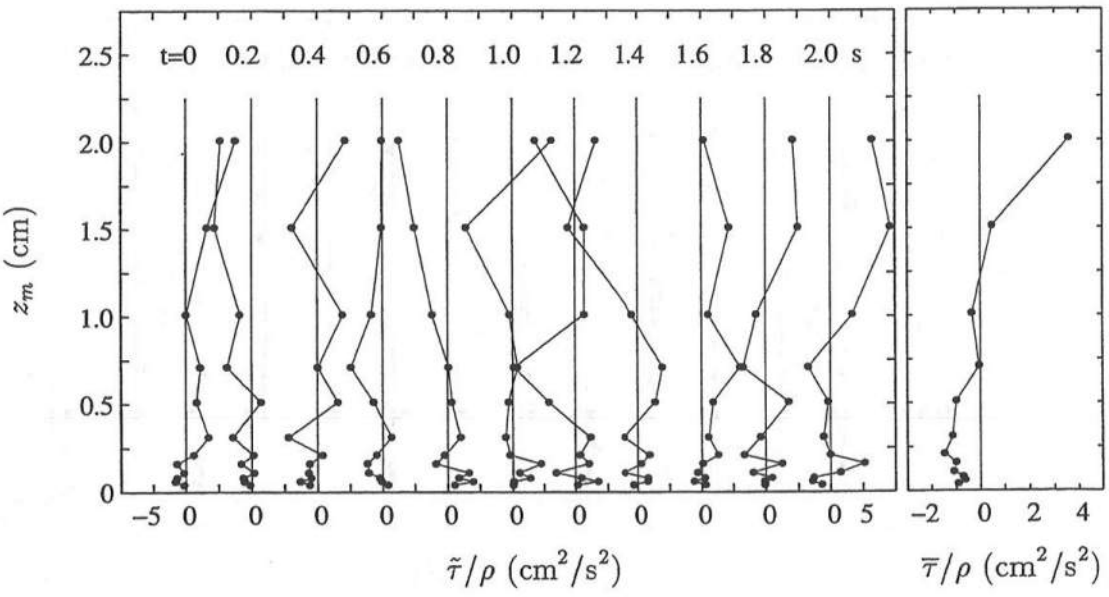

Figure 5.47: Vertical Variations of Oscillatory Component of Shear Stress, $\tilde{\tau}/\rho$ (• ——), at Eleven Phases (Left), and Time-Averaged Shear Stress, $\overline{\tau}/\rho$ (• ——), (Right) for L4.

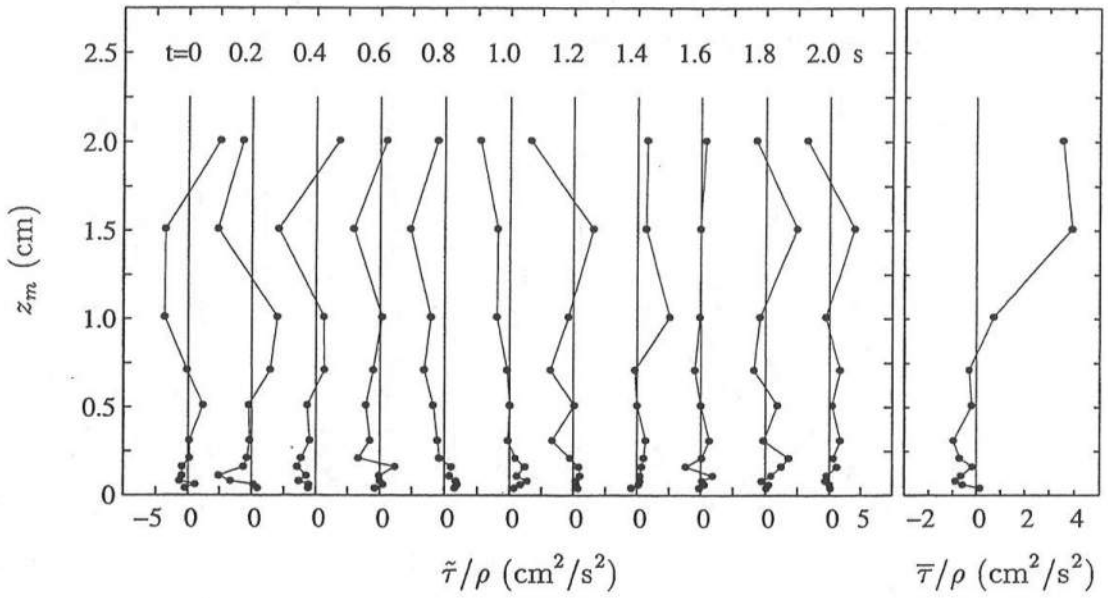

Figure 5.48: Vertical Variations of Oscillatory Component of Shear Stress, $\tilde{\tau}/\rho$ (• ——), at Eleven Phases (Left), and Time-Averaged Shear Stress, $\overline{\tau}/\rho$ (• ——), (Right) for L5.

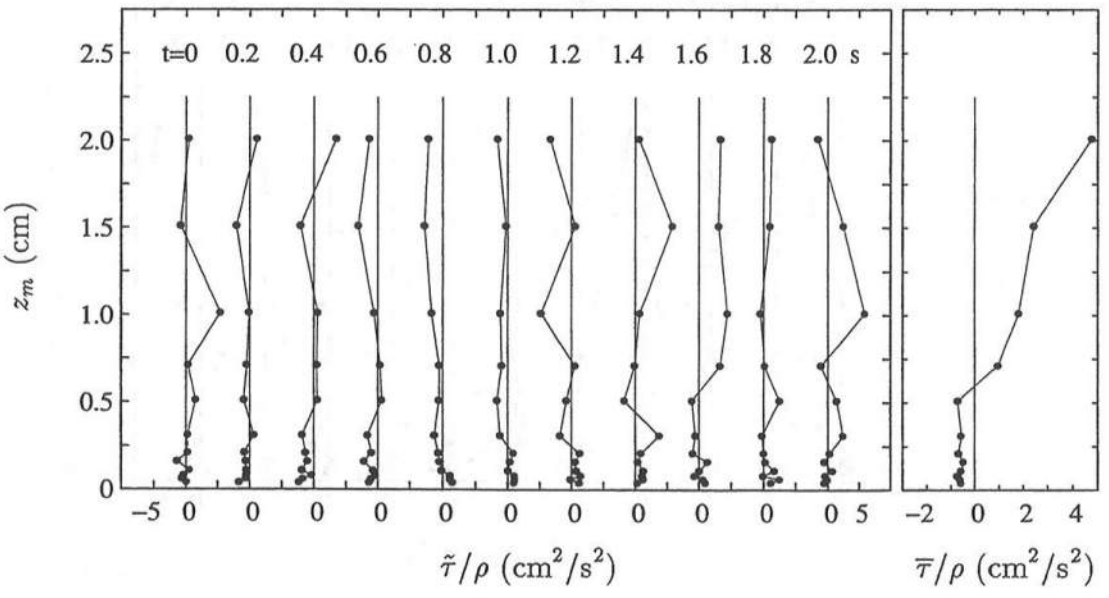

Figure 5.49: Vertical Variations of Oscillatory Component of Shear Stress, $\tilde{\tau}/\rho$ (• ——), at Eleven Phases (Left), and Time-Averaged Shear Stress, $\overline{\tau}/\rho$ (• ——), (Right) for L6.

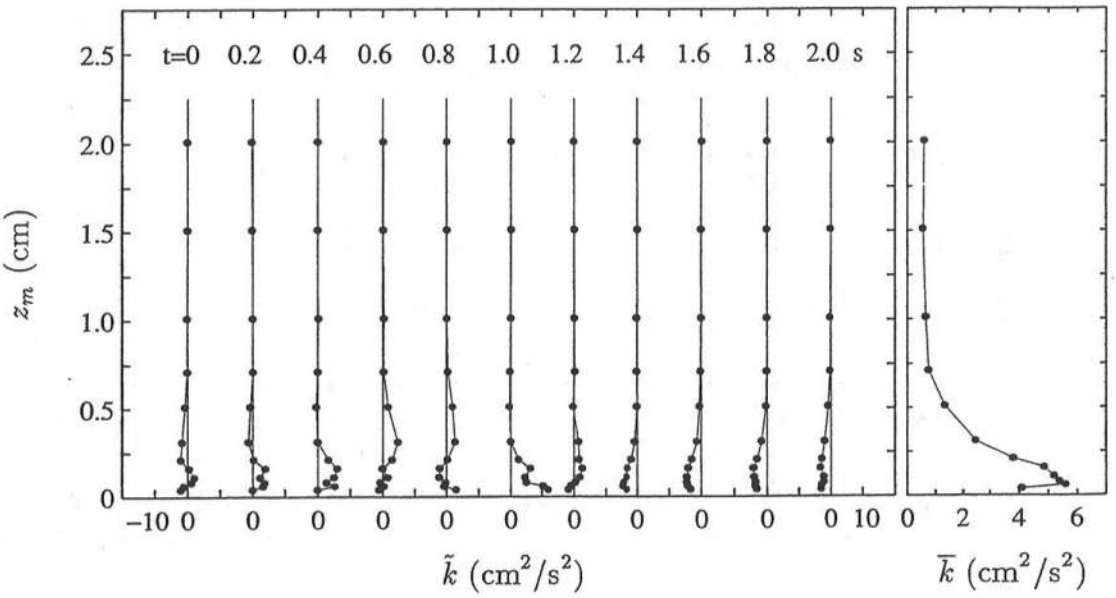

Figure 5.50: Vertical Variations of Oscillatory Component of TKE, $\tilde{k}$ (• ——), at Eleven Phases (Left), and Time-Averaged TKE, $\overline{k}$ (• ——), (Right) for L1.

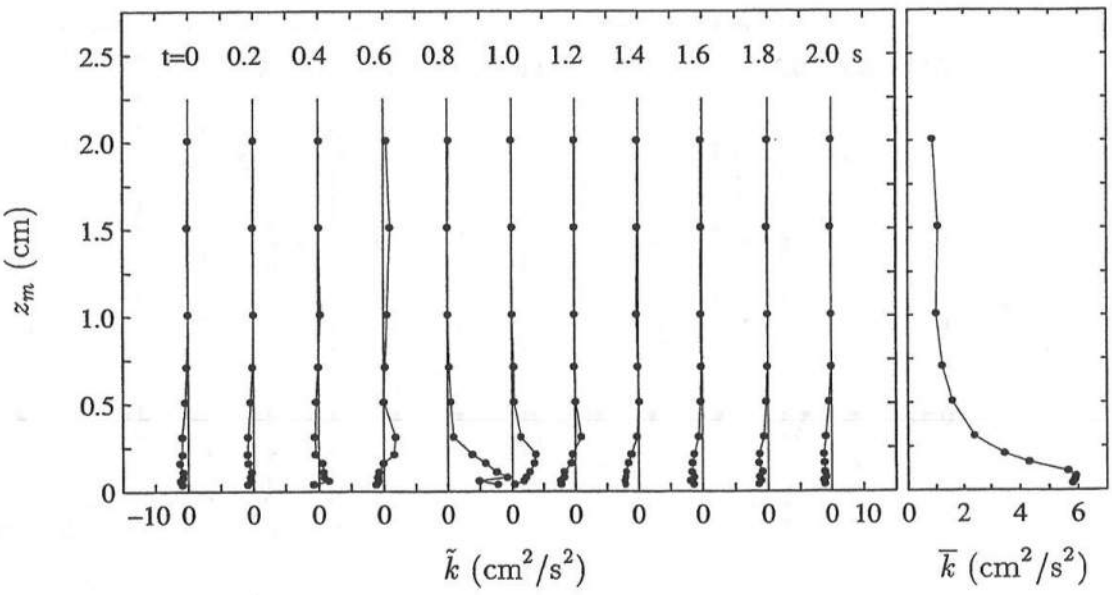

Figure 5.51: Vertical Variations of Oscillatory Component of TKE, $\tilde{k}$ (• ——), at Eleven Phases (Left), and Time-Averaged TKE, $\overline{k}$ (• ——), (Right) for L2.

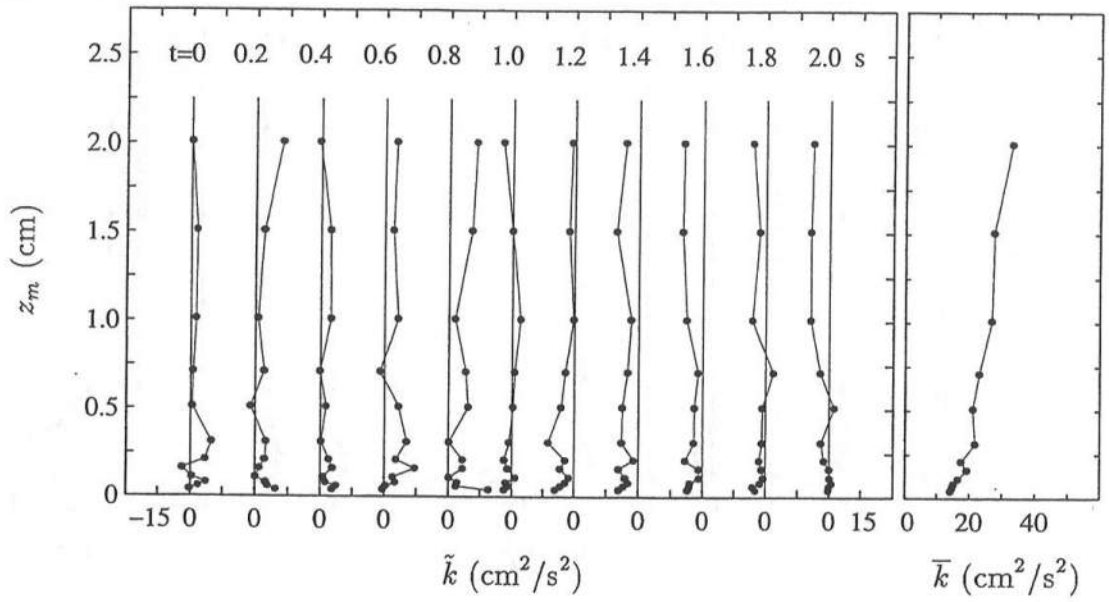

Figure 5.52: Vertical Variations of Oscillatory Component of TKE, $\tilde{k}$ (• ——), at Eleven Phases (Left), and Time-Averaged TKE, $\overline{k}$ (• ——), (Right) for L3.

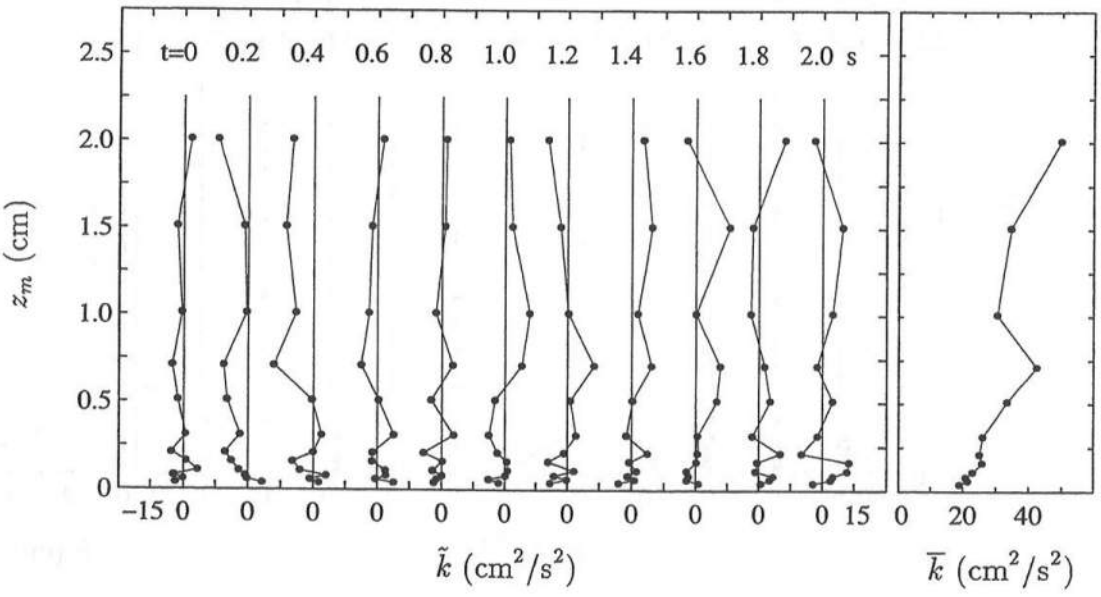

Figure 5.53: Vertical Variations of Oscillatory Component of TKE, $\tilde{k}$ (• ——), at Eleven Phases (Left), and Time-Averaged TKE, $\overline{k}$ (• ——), (Right) for L4.

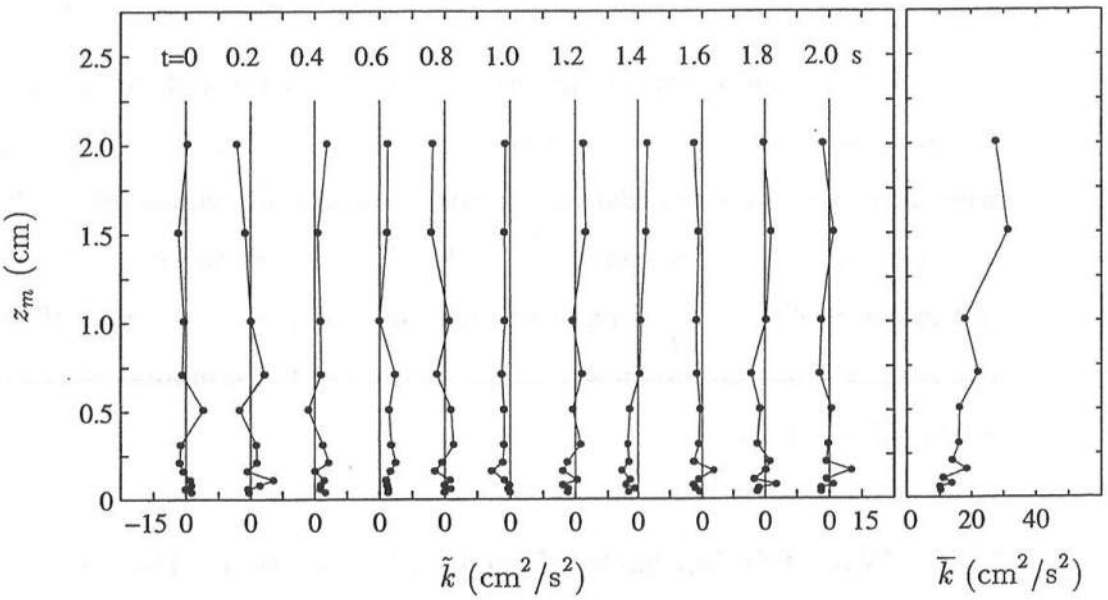

Figure 5.54: Vertical Variations of Oscillatory Component of TKE, $\tilde{k}$ (• ——), at Eleven Phases (Left), and Time-Averaged TKE, $\overline{k}$ (• ——), (Right) for L5.

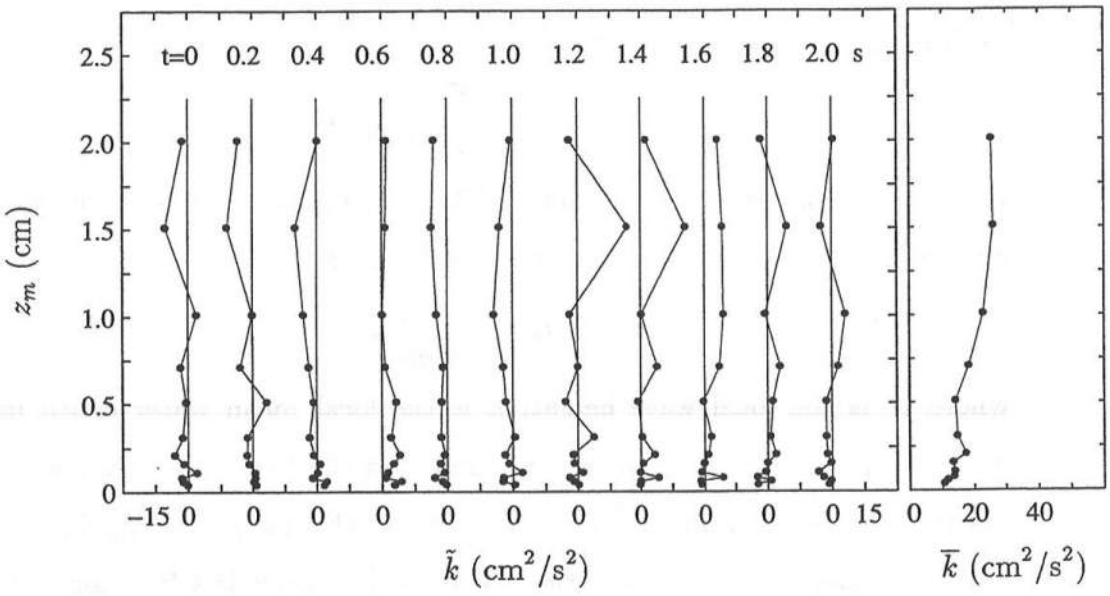

Figure 5.55: Vertical Variations of Oscillatory Component of TKE, $\tilde{k}$ (• ——), at Eleven Phases (Left), and Time-Averaged TKE, $\overline{k}$ (• ——), (Right) for L6.

5.8 Bottom Friction Factor and Bottom Roughness

This section discusses the bottom friction factor and bottom roughness. The purpose of this section is to determine to what extent boundary layer theories developed for sinusoidal flows under non-breaking waves are applicable to boundary layers under breaking waves. The first subsection introduces the theory and makes preliminary comparisons based on linear wave theory with the data. The second subsection discusses the predictions of the temporal variation of the bottom shear stress.

5.8.1 Wave Friction Factor Based on Linear Wave Theory

Following Jonsson (1966) and Jonsson and Carlsen (1976), the temporal variation of the bottom shear stress for sinusoidal flow is given by

$$\tau_b(t) = \rho \, |u_*| \, u_* = \frac{1}{2} \rho f_w U_b{}^2 \, |\sin \omega t| \sin \omega t \tag{5.47}$$

or in terms of the shear velocity

$$u_* = \sqrt{\frac{f_w}{2}} U_b \sin \omega t \tag{5.48}$$

where f_w is the wave friction factor. The near-bottom orbital velocity, U_b, may be estimated by linear wave theory and is given by

$$U_b = \frac{H\omega}{2 \sinh k\overline{h}} \tag{5.49}$$

where H is the local wave height; $\overline{h}$ is the local mean water depth including wave setup or setdown, $\overline{h} = d + \overline{\eta_a}$; and k is the local wave number from the linear dispersion relation, $\omega^2 = gk \tanh k\overline{h}$, in which ω is the angular frequency, $\omega = 2\pi/T$ and T is the wave period. The friction factor is a function of the wave Reynolds number, RE, and the relative roughness, A_b/k_s, expressed as

$$f_w = f_w \left(\frac{U_b A_b}{\nu}, \frac{A_b}{k_s} \right) \tag{5.50}$$

Table 5.5: Wave Friction Factor Parameters for L1 to L6

Line No.	d (cm)	$\overline{\eta_a}$ (cm)	$\overline{h}$ (cm)	$k\overline{h}$	H (cm)	A_b (cm)	U_b (cm/s)	$RE = \frac{U_b A_b}{\nu}$ ($\times 10^{-4}$)
L1	28.00	-0.30	27.70	0.499	13.22	12.71	36.30	4.9
L2	21.14	-0.44	20.70	0.427	17.10	19.42	55.47	11.4
L3	17.71	-0.05	17.66	0.393	12.71	15.77	45.04	7.5
L4	14.29	0.20	14.48	0.354	8.24	11.40	32.55	3.9
L5	10.86	0.75	11.61	0.316	7.08	11.02	31.49	3.7
L6	7.43	1.13	8.56	0.270	5.05	9.23	26.37	2.6

where A_b is the excursion amplitude,

$$A_b = \frac{H}{2 \sinh k\overline{h}} \tag{5.51}$$

and k_s is the Nikuradse sand roughness. The Nikuradse sand roughness is given by

$$k_s = 30\, z_0 \tag{5.52}$$

for fully turbulent flow. It is noted that k_s has been related to the grain diameter (e.g., Kamphuis 1975; Sleath 1987) and may be written as

$$k_s \simeq 2\, d_{50} \tag{5.53}$$

Table 5.5 lists the parameters for the wave friction for L1 to L6 where the wave period is $T = 2.2$ s.

The bottom roughness, z_0, estimated from the least-squares fit of the logarithmic velocity region can be used to estimate k_s. Figure 5.56 shows the cross-shore variation of the mean bottom roughness, $\overline{z_0}$, for L1 to L6 following Figures 5.9 to 5.14 for Method A, Figure 5.21 for Method A*, and Figures 5.34 to 5.37 for Method B. It is noted that the mean is not a time average in the strict

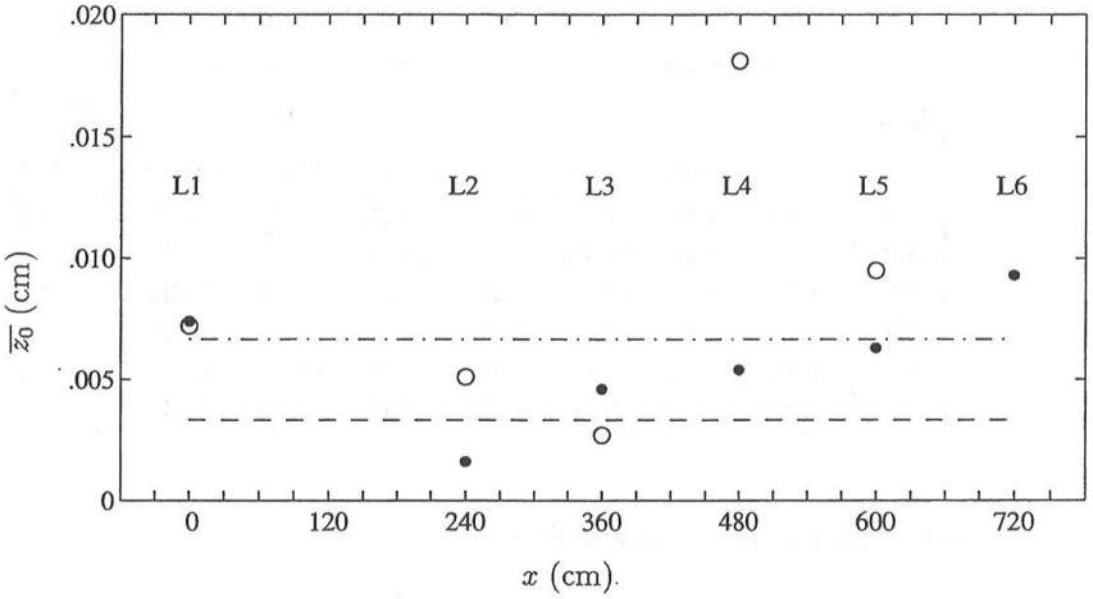

Figure 5.56: Cross-shore Variation of Bottom Roughness. Mean Bottom Roughness $\overline{z_0}$ for Method A (•) and Method B and A* (o). Estimated $z_0 = d_{50}/30$ (– –) and $z_0 = 2\,d_{50}/30$ (–·–).

sense since not all of the phases were included. The use of $\overline{z_0}$ is based on the fact that the estimated z_0 showed large variations at phases of flow reversal as discussed in Section 5.3. The lines indicate a bottom roughness computed from the grain size assuming fully turbulent flow, where $z_0 = d_{50}/30$ is the dashed line and $z_0 = 2\,d_{50}/30$ is the dash-dotted line. The data point at L4 marked by an open circle corresponds to the large bottom roughness variations in Figure 5.36 and should be discarded. Although the remaining points show some scatter, two points can be made. As a first approximation, the bottom roughness can be considered constant across the surf zone. The simple relation of $z_0 = 2\,d_{50}/30$ gives a reasonable approximation of the bottom roughness. Second, the bottom roughness in the surf zone appears to increase slightly with increasing distance shoreward although more data sets would be required to ascertain this trend.

Table 5.6: Relative Roughness and Wave Friction Factor from Linear Theory for L1 to L6.

Line No.		$\overline{z_0}$ (cm)	$k_s = 30\,\overline{z_0}$ A_b/k_s	f_w	$k_s = 30\,(\overline{z_0}/2)$ A_b/k_s (cm)	f_w	$k_s = 30\,(2\,\overline{z_0})$ A_b/k_s (cm)	f_w	$k_s = 2\,d_{50}$ A_b/k_s	f_w
L1	A	.0074	57.2	.028	114.8	.021	28.6	.039	63.5	.026
	B	.0072	58.8	.027	117.7	.020	29.4	.038		
L2	A	.0016	404.6	.013	809.3	.010	208.9	.016	97.1	.022
	B	.0051	126.9	.020	259.0	.015	64.1	.026		
L3	A	.0046	114.3	.021	228.5	.016	56.5	.028	78.8	.024
	A*	.0027	194.7	.017	404.3	.013	99.2	.022		
L4	A	.0054	70.3	.025	140.7	.019	35.2	.035	57.0	.028
	B	.0181	21.0	.045	41.7	.032	10.5	.068		
L5	A	.0063	58.3	.028	114.8	.021	28.9	.038	55.1	.028
	B	.0095	38.7	.033	78.2	.024	19.3	.048		
L6	A	.0093	33.1	.036	65.5	.026	16.5	.052	46.2	.031

Table 5.6 lists the mean bottom roughness, $\overline{z_0}$, shown in Figure 5.56 for L1 to L6. The third column lists the relative roughness, A_b/k_s, using the mean bottom roughness, $\overline{z_0}$, assuming fully turbulent flow. The ninth column lists the relative roughness estimate based on $k_s = 2\,d_{50}$.

Figure 5.57 shows the relative roughness, A_b/k_s with $k_s = 30\,\overline{z_0}$ in Table 5.6 verses the Reynolds number RE in Table 5.5. This figure is made following Jonsson (1966) and indicates three regimes: laminar, transitional, and rough turbulent. All points are in the rough turbulent regime except for L2A and L3A*. It is noted that turbulence generated by wave breaking is not accounted for in Figure 5.57.

A semi-theoretical expression for the wave friction factor was derived by Jonsson (1966) assuming fully rough turbulent flow to relate the friction factor to

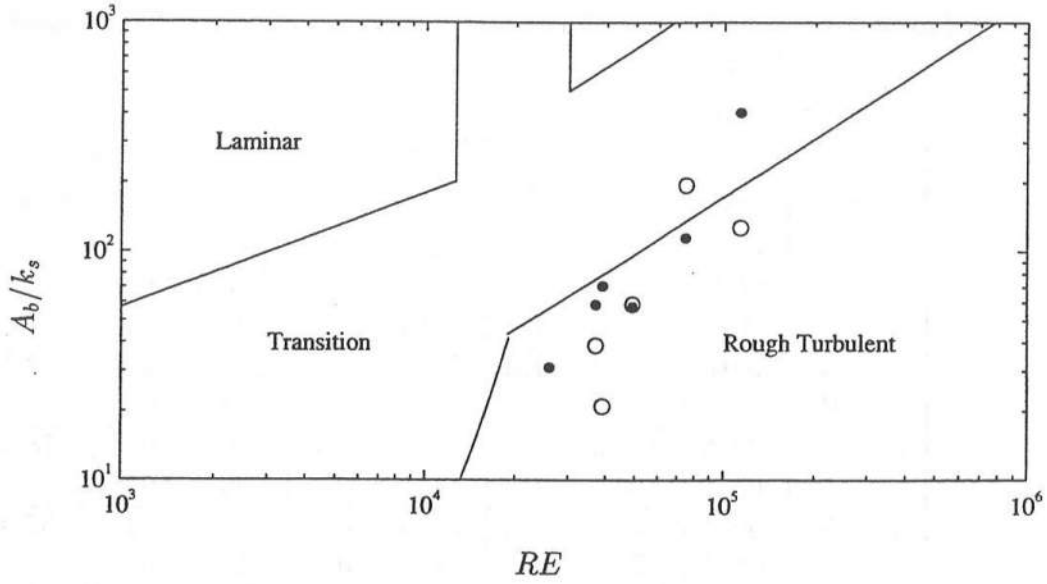

Figure 5.57: Relative Roughness Verses Reynolds Number Following Jonsson (1966) for Method A (•) and Method B (○).

the relative roughness. This expression is given as

$$\frac{1}{4\sqrt{f_w}} + \log \frac{1}{4\sqrt{f_w}} = \log\left(\frac{A_b}{k_s}\right) - 0.08 \tag{5.54}$$

where log denotes the base 10 logarithm and the constant -0.08 was determined empirically. The fourth column of Table 5.6 lists f_w calculated using Eq 5.54 and the relative roughness from the third column. The sensitivity of the computed friction factor to the relative roughness is listed in the sixth and eight columns where k_s is estimated $k_s = 30\,(\overline{z_0}/2)$ and $k_s = 30\,(2\,\overline{z_0})$, respectively. Table 5.6 indicates that the friction factor based on $\overline{z_0} = 2\,d_{50}$ mostly falls within the values of the friction factor based on $z_0 = 0.5\,\overline{z_0}$ and $z_0 = 2\,\overline{z_0}$ which may be a realistic range considering the scatter of z_0 at different phases.

5.8.2 Friction Factor Based on Quadratic Friction Equation

The temporal variation of the bottom shear stress may be expressed using the velocity measured just above the bottom boundary layer in the quadratic form (e.g., Grant and Madsen 1979)

$$\tau_b(t) = \frac{1}{2}\rho f_w \left|u_b\right| u_b \tag{5.55}$$

where u_b is the time-varying velocity immediately outside the bottom boundary layer. Eq 5.55 neglects the phase shift between the bottom shear stress and the velocity immediately outside the boundary layer. The bottom shear stress and the shear velocity, u_*, are related by

$$\tau_b(t) = \rho \left|u_*\right| u_* \tag{5.56}$$

The friction factor, f_w, which is assumed constant, may be estimated by a least-squares fit using Eqs 5.55 and 5.56 together with the measured temporal variations of $u_b(t)$ and $u_*(t)$. This procedure can be shown to yield

$$f_w = \frac{\sum_{j=1}^{J} \left(\left|u_*\right| u_*\right)_j \left(\left|u_b\right| u_b\right)_j}{\frac{1}{2}\sum_{j=1}^{J} \left(u_b\right)_j^4} \tag{5.57}$$

where u_* is the shear velocity presented in Figures 5.9 to 5.14 for Method A, Figure 5.21 for Method A*, and Figures 5.34 to 5.37 for Method B; J is the number of phases over the wave period as indicated in the third column of Table 5.4; and u_b is the velocity just above the boundary layer. The friction factor, f_w, may be regarded as the measured friction factor based on the quadratic friction equation, Eq 5.55.

Table 5.7 lists the fitted friction factors for L1 to L6 following Eq 5.57. The second column lists the friction factor computed with u_b at $z_m = 1.6$ cm. A sensitivity analysis indicated that f_w varied by less than 3% when computed with

Table 5.7: Friction Factors Fitted using Shear Velocity and Near Bottom Velocity for L1 to L6

Line No.		$u = u_b$		$u = u_{mid}$	
		f_w	ϵ^2	f_w	ϵ^2
L1	A	.025	12.89	.018	21.09
	B	.024	11.80	.018	17.02
L2	A	.014	3.96	.014	2.78
	B	.016	10.49	.013	12.88
L3	A	.017	2.95	.016	2.85
	A*	.014	0.57	.013	1.71
L4	A	.016	3.41	.018	4.17
	B	.046	30.85	.053	37.47
L5	A	.026	2.86	.027	4.00
	B	.040	9.90	.042	11.89
L6	A	.028	7.47	.031	7.68

u_b at $z_m = 1.1$ and 2.1 cm. The third column indicates the least-squared error, ϵ^2, for the least-squares fit. It is noted that L4, Method B, has a large error and should be discarded. This is consistent with the discussion of the bottom roughness in the previous subsection and shown in Figure 5.56. Collectively, Methods A, A*, and B yield consistent values of f_w.

Comparisons will be made with a depth-integrated, time-dependent numerical model in Chapter 7. The numerical model includes bottom friction in a form similar to Eq 5.55 except that the depth-averaged velocity is used instead of the velocity above the bottom boundary layer. For comparisons with this model, the least-squares fit using Eq 5.57 was repeated with u_b replaced by an approximate mid-depth velocity, u_{mid}. The mid-depth elevations are given in Chapter 7. The fourth column of Table 5.7 shows the fitted friction factor using the approximate mid-depth velocity, and the fifth column shows the least-squared error. As

expected, L4, Method B, has a large error and should be discarded.

The fitted friction factors in the second column of Table 5.7 and the relative roughness in the third column of Table 5.6 are plotted in Figure 5.58. The data of Jonsson and Carlsen (1976) and Sleath (1987) are included, and it is noted that both data sets were obtained using an oscillating water tunnel with rough bottoms. The data of Jonsson and Carlsen (1976) were reduced by a logarithmic fit, and the data of Sleath (1987) were reduced by the momentum integral method. The solid curve is Eq 5.54 from Jonsson (1966), and the dashed curve is the equation of Kamphius (1975) given by

$$\frac{1}{4\sqrt{f_w}} + \log \frac{1}{4\sqrt{f_w}} = \frac{3}{4} \log \left(\frac{A_b}{k_s} \right) - 0.35 \tag{5.58}$$

where the coefficients 3/4 and -0.35 were determined empirically. Figure 5.58 shows that the data lie near the two curves with the scatter expected from previous studies where the review paper by Soulsby *et al.* (1993) is given as an additional reference.

Figure 5.59 compares the cross-shore variation of the friction factor computed using linear wave theory in Section 5.8.1 and using the least-squares fit in this subsection. In the figure, the friction factors estimated for Method A are indicated with solid circles, and the friction factors estimated for Method B are indicated with open circles. The circles with the vertical lines indicating the uncertainty of the measured bottom roughness are for the friction factors estimated using linear wave theory from Table 5.6. The center data point is from the fourth column with $k_s = 30\,\overline{z_0}$, and the minimum and maximum indicated by the line are from the sixth column with $k_s = 30\,(\overline{z_0}/2)$ and eighth column with $k_s = 30\,(2\,\overline{z_0})$, respectively. The circles without the vertical lines are for the estimates from the least-squares fit in Eq 5.57 and are listed in the second column of Table 5.7. The data of L4, Method B, are excluded from this figure. Although the figure contains

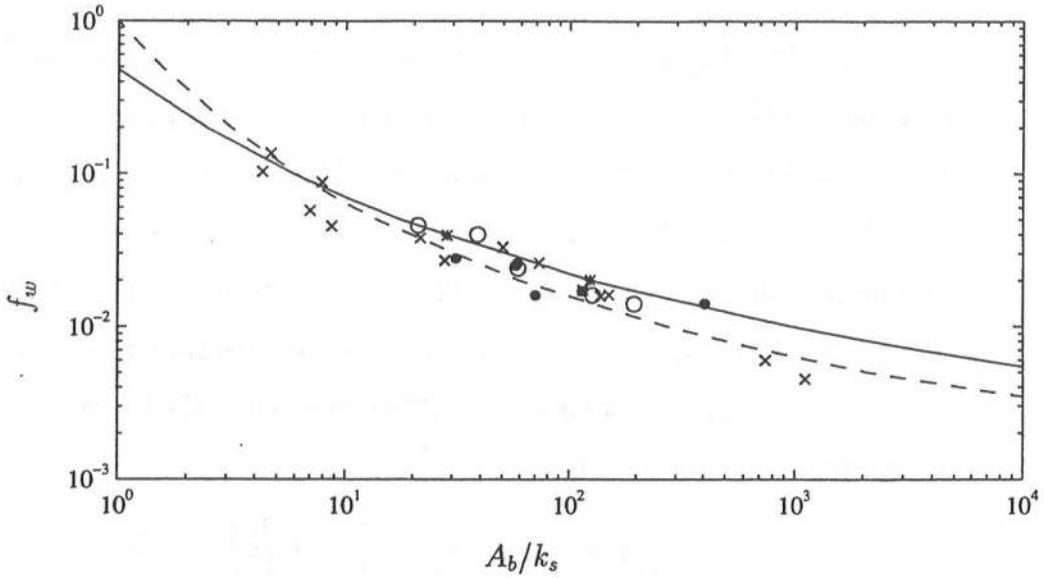

Figure 5.58: Friction Factor Verses Relative Roughness with Method A (•), Method B (○), Jonsson and Carlsen (1976) (∗), Sleath (1987) (×), Jonsson (1966) (——), and Kamphius (1975) (– –).

some scatter, several points can be made. First, comparisons of the data between Method A and Method B show a reasonable consistency and indicate that the results were not contaminated by irregularities in the bottom roughness or uncertainties in determining the position of the laser-Doppler measuring volume. Second, as a first approximation, the friction factor may be assumed constant across the surf zone. Third, Jonsson's equation, Eq 5.54, based on linear wave theory (circles with the lines) gives a fairly good estimate of the measured wave friction factor based on the quadratic friction equation, Eq 5.55, although Eq 5.54 appears to slightly overpredict the measured value in the inner surf zone.

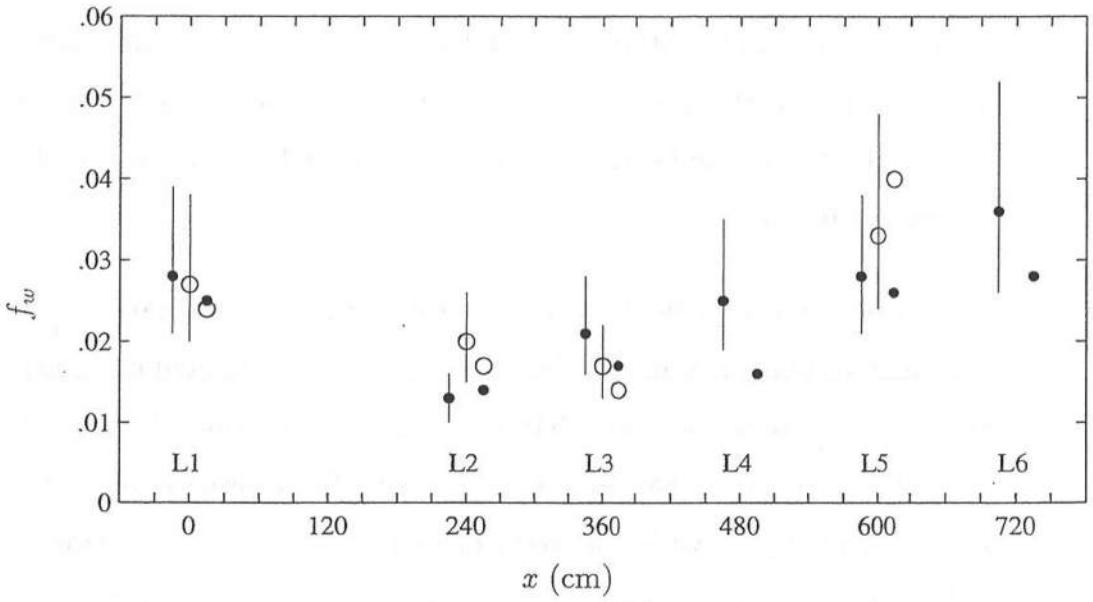

Figure 5.59: Cross-shore Variation of Friction Factor with f_w from Table 5.6 with Method A (• ——) and Method B (○ ——); and with f_w from Table 5.7 with Method A (•) and Method B (○).

5.8.3 Temporal Variation of Bottom Shear Stress Estimates

This subsection discusses how well the quadratic friction equation, Eq 5.55, predicts the measured temporal variation of the bottom shear stress. Figures 5.60 to 5.70 show the measured bottom shear stress estimates, $\tau_b/\rho = |u_*|u_*$, described in Section 5.3, and are indicated in the figures by the solid circles with the 95% confidence intervals. The bottom shear stress estimates indicated by the solid curve are computed using the quadratic friction equation, Eq 5.55, together with the fitted friction factor in the second column of Table 5.7 and the measured horizontal velocity at $z_m = 1.6$ cm above the boundary layer. The envelope is computed using the values of $2f_w$ and $f_w/2$ in the quadratic friction equation.

The measured bottom shear stresses for Method A and Method B are plotted in separate figures on the same page. Comparisons of Method A and

Method B show that the temporal variations of the shear stresses are fairly similar at each measuring line within the confidence intervals of about two, indicating that the bottom shear stress based on the logarithmic velocity profile was not affected by irregularities in the bottom. An exception is at L4, where results for Method B were not reliable.

Comparisons of the measured bottom shear stress indicated by solid circles with light vertical lines and the bottom shear stress estimated using Eq 5.55 with constant friction factor show that the temporal variation of the bottom shear stress in the surf zone can be estimated using the measured velocity above the bottom boundary to within a factor of two. The phase shift between $\tau_b(t)$ and $u_b(t)$ neglected in Eq 5.55 appears to be negligible in these figures.

Estimating the temporal variation of the bottom shear stress using Eq 5.55 requires the prediction of the temporal variation of the horizontal velocity just above the bottom boundary layer, $u_b(t)$, which is far from sinusoidal. A numerical model will be presented in the Chapter 7 and its ability in predicting the temporal variation of the bottom shear stress is discussed.

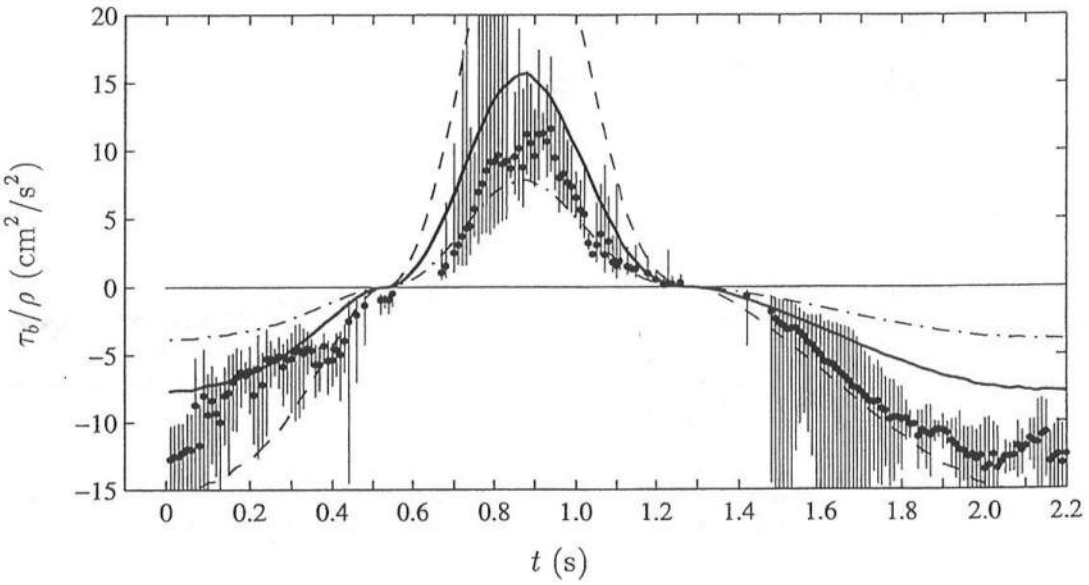

Figure 5.60: Temporal Variation of τ_b. Computed from u_* (•) with 95% Confidence Limits (——). Using Fitted f_w (——), $f_w/2$ (– –), 2 f_w (–· –), for L1, Method A.

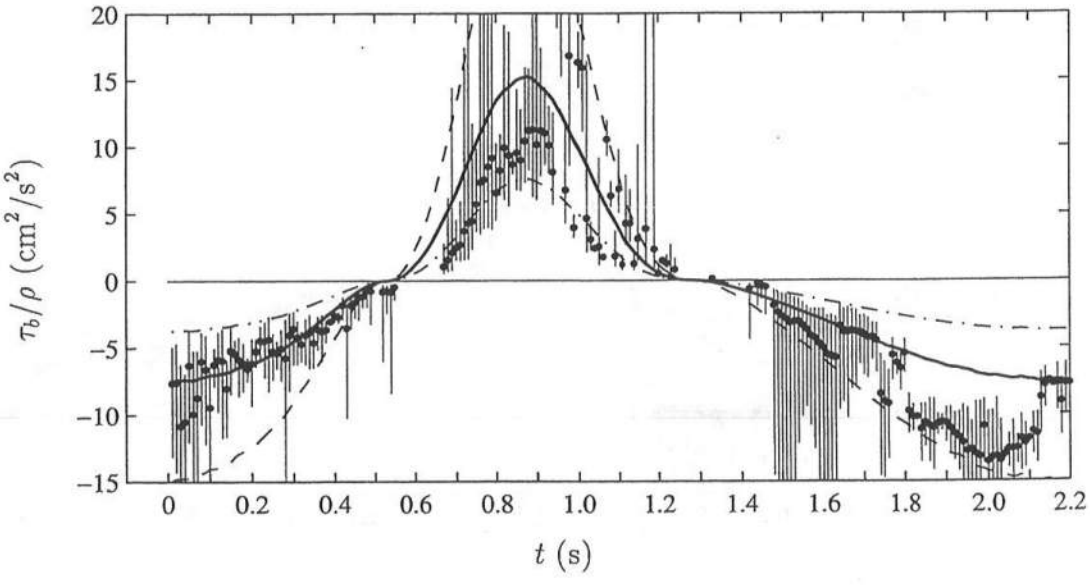

Figure 5.61: Temporal Variation of τ_b. Computed from u_* (•) with 95% Confidence Limits (——). Using Fitted f_w (——), $f_w/2$ (– –), 2 f_w (–· –), for L1, Method B.

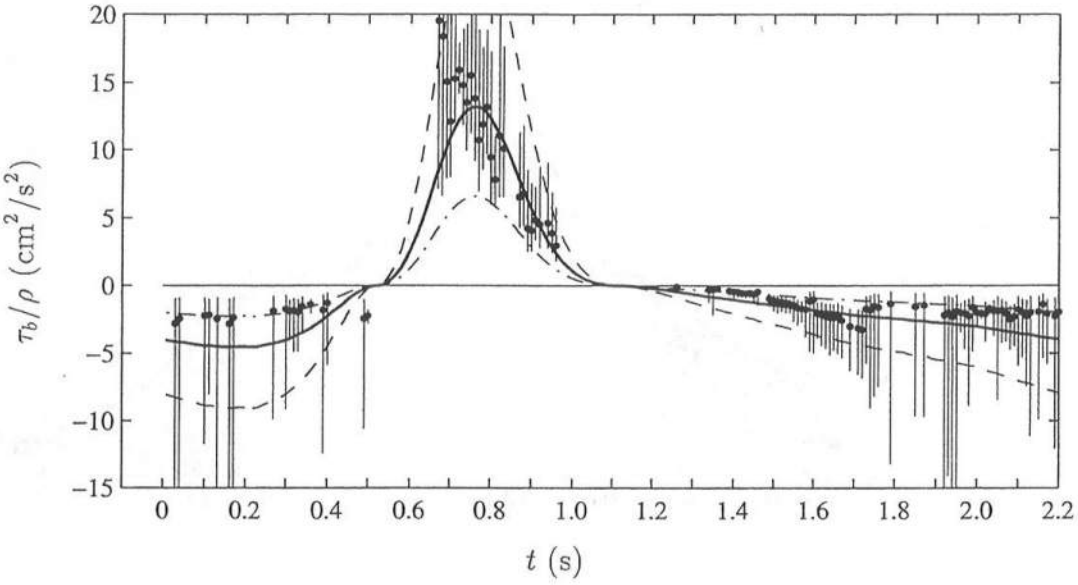

Figure 5.62: Temporal Variation of τ_b. Computed from u_* (•) with 95% Confidence Limits (——). Using Fitted f_w (——), $f_w/2$ (– –), 2 f_w (–· –), for L2, Method A.

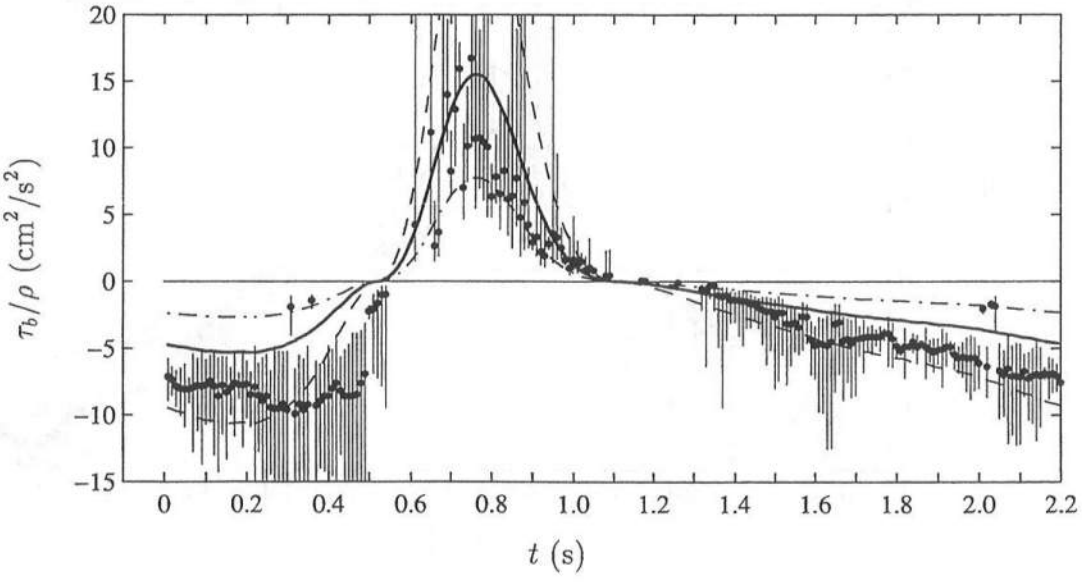

Figure 5.63: Temporal Variation of τ_b. Computed from u_* (•) with 95% Confidence Limits (——). Using Fitted f_w (——), $f_w/2$ (– –), 2 f_w (–· –), for L2, Method B.

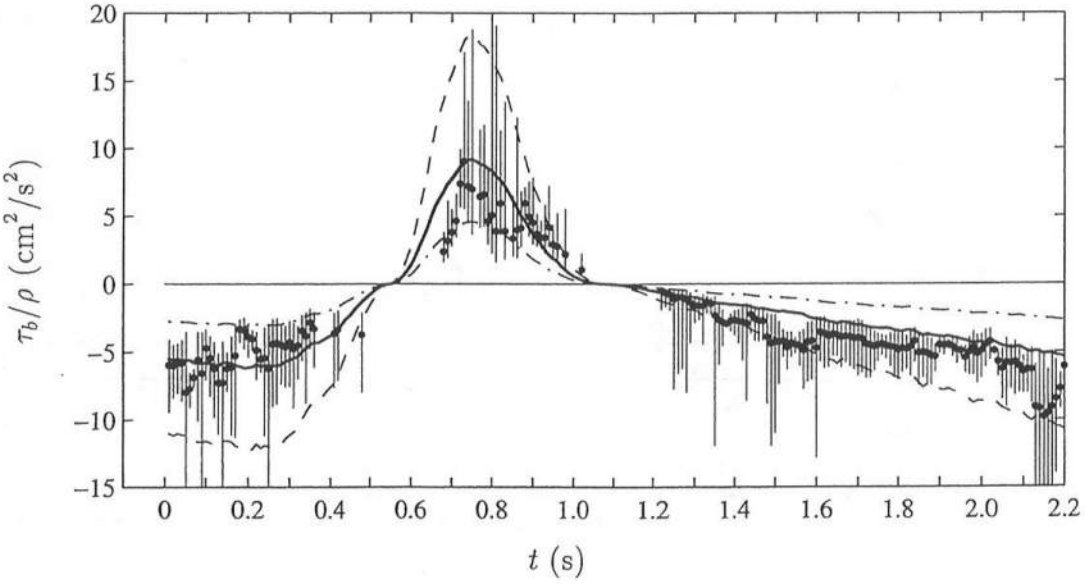

Figure 5.64: Temporal Variation of τ_b. Computed from u_* (•) with 95% Confidence Limits (——). Using Fitted f_w (——), $f_w/2$ (– –), 2 f_w (– – –), for L3, Method A.

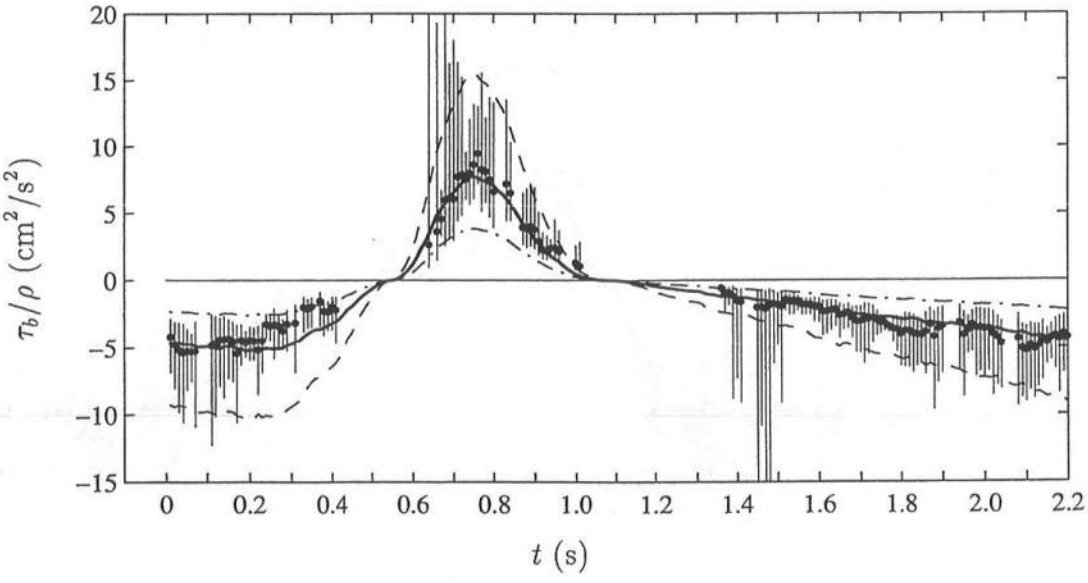

Figure 5.65: Temporal Variation of τ_b. Computed from u_* (•) with 95% Confidence Limits (——). Using Fitted f_w (——), $f_w/2$ (– –), 2 f_w (– – –), for L3, Method A*.

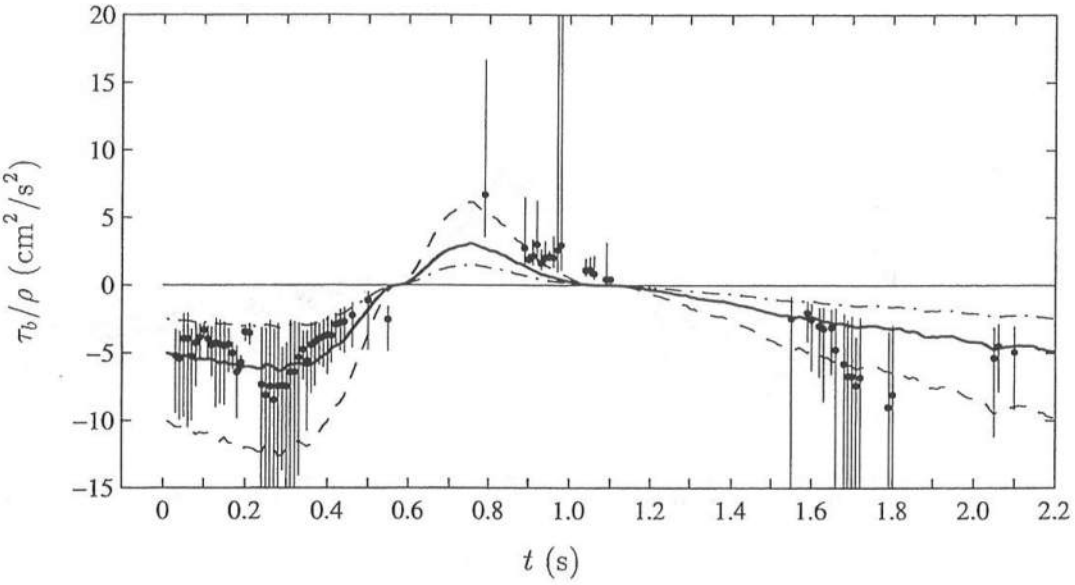

Figure 5.66: Temporal Variation of τ_b. Computed from u_* (•) with 95% Confidence Limits (——). Using Fitted f_w (——), $f_w/2$ (– –), 2 f_w (– – –), for L4, Method A.

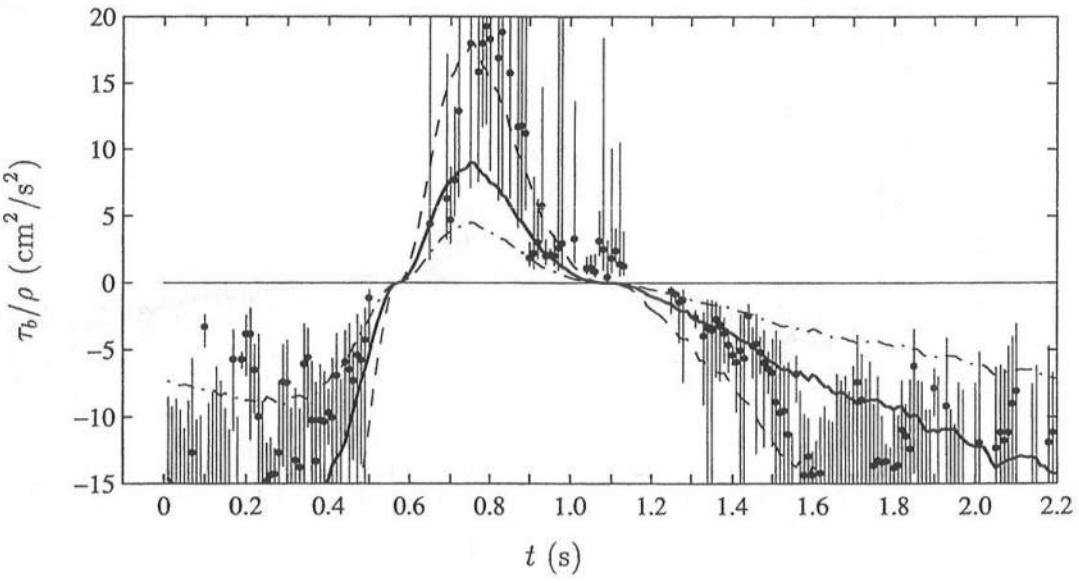

Figure 5.67: Temporal Variation of τ_b. Computed from u_* (•) with 95% Confidence Limits (——). Using Fitted f_w (——), $f_w/2$ (– –), 2 f_w (– – –), for L4, Method B.

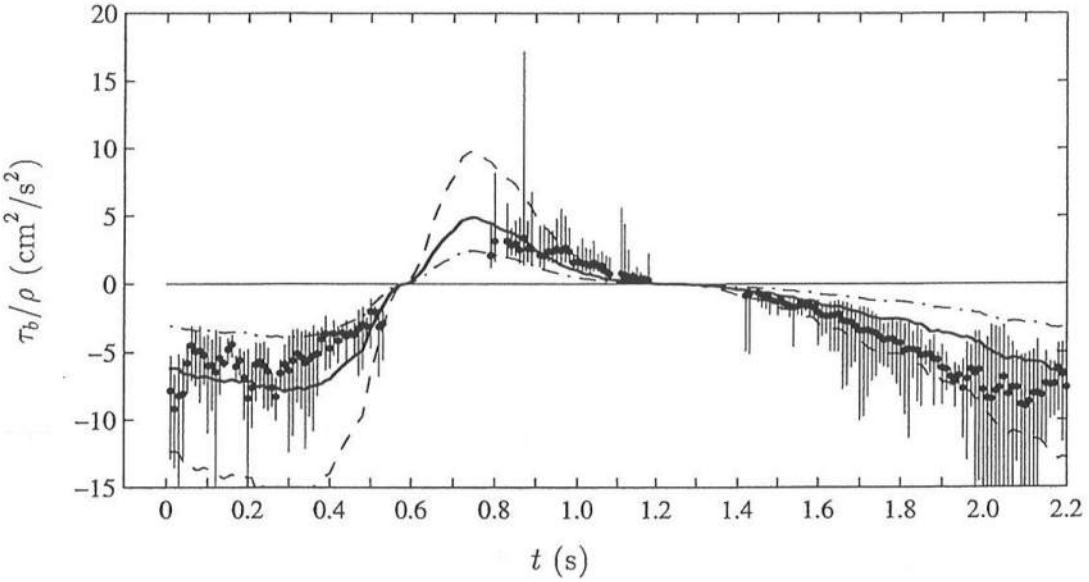

Figure 5.68: Temporal Variation of τ_b. Computed from u_* (•) with 95% Confidence Limits (——). Using Fitted f_w (——), $f_w/2$ (– –), 2 f_w (– – –), for L5, Method A.

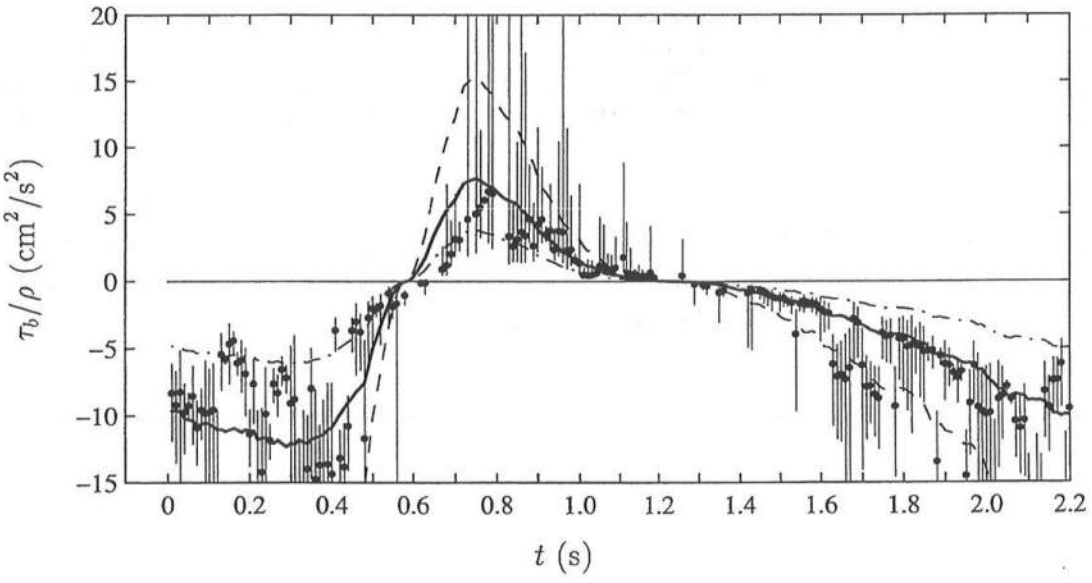

Figure 5.69: Temporal Variation of τ_b. Computed from u_* (•) with 95% Confidence Limits (——). Using Fitted f_w (——), $f_w/2$ (– –), 2 f_w (– – –), for L5, Method B.

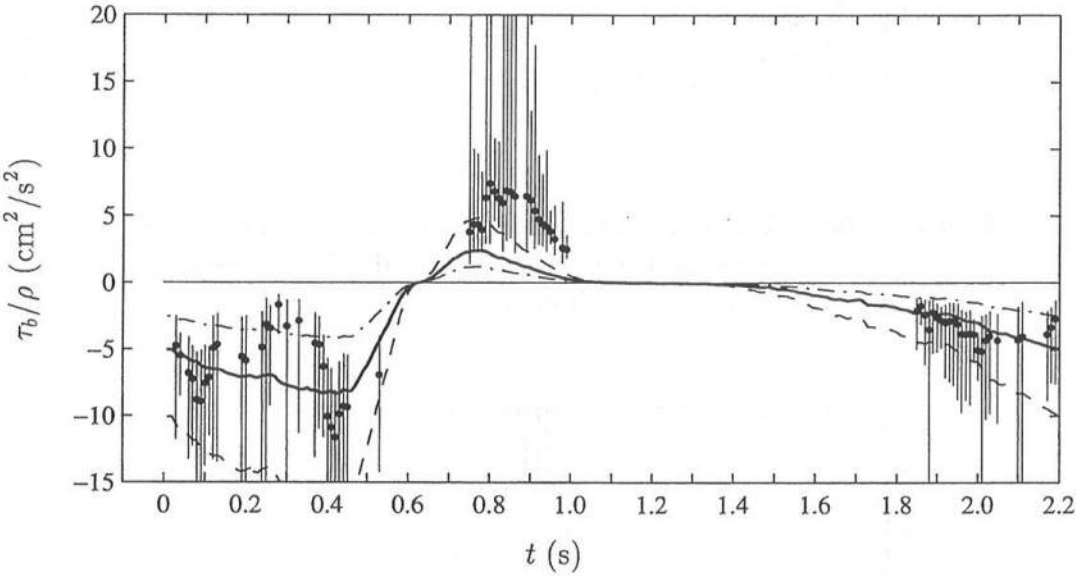

Figure 5.70: Temporal Variation of τ_b. Computed from u_* (•) with 95% Confidence Limits (——). Using Fitted f_w (——), $f_w/2$ (– –), 2 f_w (–· –), for L6, Method A.

Chapter 6

WAVE GENERATED TURBULENCE

This chapter discusses the turbulence generated by wave breaking. In Section 6.1, the estimate of the turbulent kinetic energy from measurements in two-dimensions is considered. In Section 6.2, the assumption of an approximate local equilibrium of turbulence is reviewed from Chapter 2. It is noted that in this section, several equations are repeated from Chapter 2 for convenience. In Section 6.3, the dissipation coefficient, C_d, from the transport equation of turbulent kinetic energy is estimated from the data. In Section 6.4, the temporal variation of the mixing length coefficient, C_ℓ, is computed, and a time-averaged mixing length coefficient, $\overline{C_\ell}$, is estimated. Additionally, the vertical and temporal variations of the eddy viscosity are presented using the calibrated values of C_d and $\overline{C_\ell}$. In Section 6.5, the assumption of an approximate local equilibrium of turbulence is assessed using the calibrated coefficients. Most of the findings of this chapter appear in Cox *et al.* (1994a).

6.1 Approximation of Turbulent Kinetic Energy from Measurements in Two Dimensions

Recalling from Chapter 2, the dimensional turbulent shear stresses may be written in tensor notation as (e.g., Rodi 1980)

$$\tau_{ij} = \rho \left[\nu_t \left(\frac{\partial u_i}{\partial x_j} + \frac{\partial u_j}{\partial x_i} \right) - \frac{2}{3} k \delta_{ij} \right] \tag{6.1}$$

where use is made of the repeated indices, $i = 1, 2, 3$; τ_{ij} is the turbulent stress; δ_{ij} is the Kronecker delta; ν_t is the kinematic viscosity; ρ is the fluid density; and k is the turbulent kinetic energy. The turbulent kinetic energy, k, is defined in terms of the normal stresses as

$$k = -\frac{1}{2\rho} \left(\tau_{11} + \tau_{22} + \tau_{33} \right). \tag{6.2}$$

Assuming that Reynolds averaging is the same as the phase averaging used here, the normal stresses may be expressed in terms of the measured variances

$$\tau_{11} = -\rho \sigma_u^2 \ ; \ \tau_{22} = -\rho \sigma_w^2 \ ; \ \tau_{33} = -\rho \sigma_v^2, \tag{6.3}$$

and the phase-averaged quantities from the previous chapters may be expressed

$$\eta = \eta_a \ ; \ u = u_a \ ; \ w = w_a. \tag{6.4}$$

It is noted that σ_v^2 was not measured for this experiment. From Eq 6.1, the normal stresses may be written as

$$\tau_{11} = \rho \left[2\nu_t \frac{\partial u_1}{\partial x_1} - \frac{2}{3} k \right] \tag{6.5}$$

$$\tau_{22} = \rho \left[2\nu_t \frac{\partial u_2}{\partial x_2} - \frac{2}{3} k \right] \tag{6.6}$$

$$\tau_{33} = \rho \left[2\nu_t \frac{\partial u_3}{\partial x_3} - \frac{2}{3} k \right]. \tag{6.7}$$

Using the continuity equation, the sum of the normal stresses is given as

$$\tau_{11} + \tau_{22} + \tau_{33} = -2\rho k \tag{6.8}$$

Including the definitions from Eq 6.3, the standard definition of k is given as

$$k = \frac{1}{2}\left(\sigma_u^2 + \sigma_w^2 + \sigma_v^2\right). \tag{6.9}$$

For an idealized two-dimensional turbulent flow, $\partial u_3/\partial x_3 = 0$ so that Eq 6.7 yields

$$\tau_{33} = -\frac{2}{3}\rho k. \tag{6.10}$$

Using $\tau_{33} = -\rho\sigma_v^2$, Eq 6.10 becomes

$$\sigma_v^2 = \frac{2}{3}k. \tag{6.11}$$

This reduces Eq 6.9 to

$$k = -\frac{3}{4\rho}\left(\tau_{11} + \tau_{22}\right) = \frac{3}{4}\left(\sigma_u^2 + \sigma_w^2\right). \tag{6.12}$$

The use of Eq 6.11 results in

$$\frac{\sigma_v^2}{2k} = \frac{1}{3} \tag{6.13}$$

corresponding to homogeneous isotropic turbulence. For steady turbulent flow, the ratios of the normal stresses to the turbulent kinetic energy have been tabulated by Svendsen (1987) and are given in Table 6.1. This table indicates that

$$0.21 \leq \frac{\sigma_v^2}{2k} < \frac{1}{3}, \tag{6.14}$$

so that σ_v^2 may be overestimated slightly for this dissertation. It is desirable to measure this quantity directly in future experiments.

Having measured σ_u^2 and σ_w^2 directly, it is of interest to determine whether the ratio of vertical to horizontal variance is constant over a wave period. This relation may be expressed as

$$\sigma_w^2 = C_w\sigma_u^2 \tag{6.15}$$

where $C_w(x,z)$ is an empirical constant and assumed to be independent of time. Using the least-squares method to solve for C_w, it can be shown that

$$C_w = \frac{\sum_{j=1}^{J}(\sigma_w^2)_j(\sigma_u^2)_j}{\sum_{j=1}^{J}(\sigma_u^2)_j^2} \tag{6.16}$$

where $J = 220$ is the number of phases.

Figure 6.1 shows the cross-shore variation of C_w for L1 to L6. The values lie in the range $0.06 \leq C_w \leq 0.86$ whereas the range for the types of flows listed in Table 6.1 is $0.16 \leq C_w \leq 1.00$. It is noted that for L1 and L2 above the bottom boundary layer, the values of σ_u^2 and σ_w^2 are nearly zero. For L3 to L6, C_w is fairly constant over depth until the lower portion of the water column where it decreases linearly to a small value because of the presence of the bottom.

Figure 6.2 shows the temporal variations of $C_w\sigma_u^2$ and σ_w^2 for the five representative vertical elevations for L2. The representative elevations were shown in Figure 4.6 and listed in Table 4.2. The lower curves for L2e show that it is appropriate to assume that C_w is constant over a wave period in the boundary layer outside the surf zone. Figure 6.3 shows the temporal variations of $C_w\sigma_u^2$ and σ_w^2 for the five vertical elevations for L4. This figure also shows that C_w can be considered constant over a wave period at a given x and z location for spilling waves in the surf zone. The values for scaling the turbulent stresses in the surf zone, gH_r/σ, are given in the captions for completeness and are discussed in the next section.

Table 6.1: Steady Turbulent Flow Tabulated by Svendsen (1987).

	$\frac{\sigma_u^2}{2k}$	$\frac{\sigma_w^2}{2k}$	$\frac{\sigma_w^2}{\sigma_u^2}$	$\frac{\sigma_v^2}{2k}$
Plane wake	0.42	0.32	0.76	0.26
Plane mixing layer	0.467	0.267	0.57	0.267
Boundary layer				
inner region	0.62	0.10	0.16	0.28
outer region	0.45	0.23	0.51	0.32
Plane jet	0.42	0.30	0.71	0.29
Open channel				
midstream	0.58	0.20	0.34	0.22
near bottom	0.62	0.17	0.27	0.21
Homogeneous				
isotropic turbulence	0.33	0.33	1.00	0.33

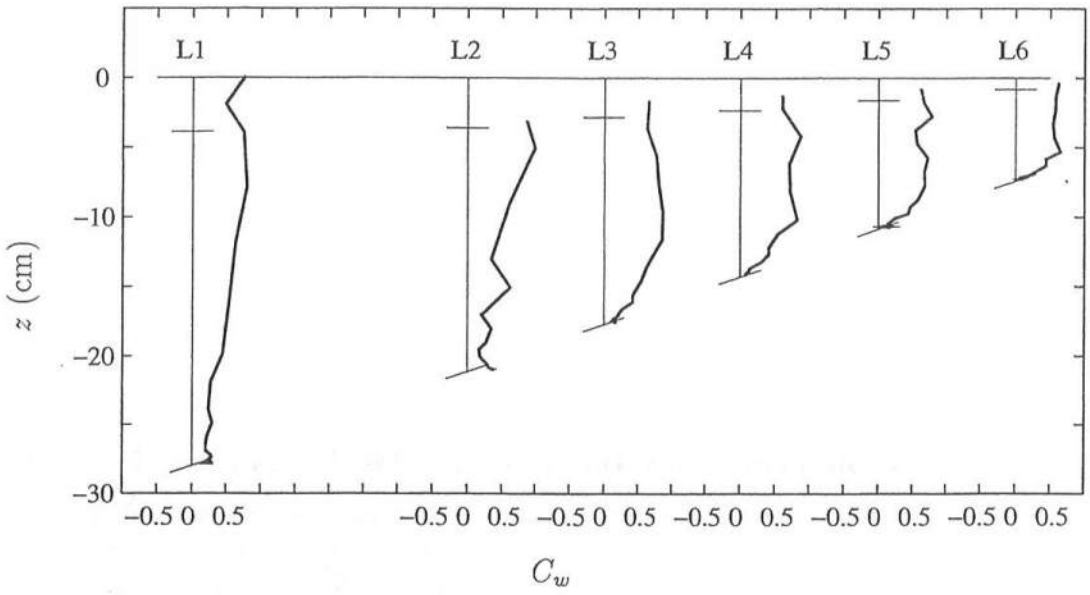

Figure 6.1: Cross-Shore Variation of C_w for L1 to L6.

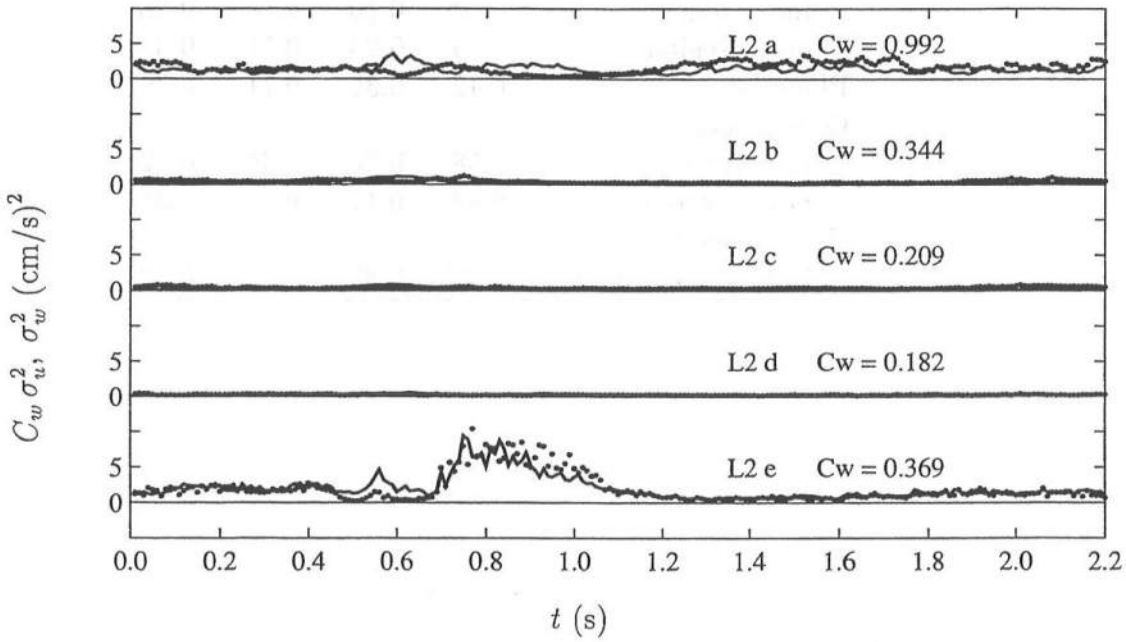

Figure 6.2: Temporal Variations of Horizontal Variance, $C_w\sigma_u^2$ (——), and Vertical Variance, σ_w^2 (•), for Five Vertical Elevations for L2 with $gH_r/\sigma = 1007$ (cm/s)^2.

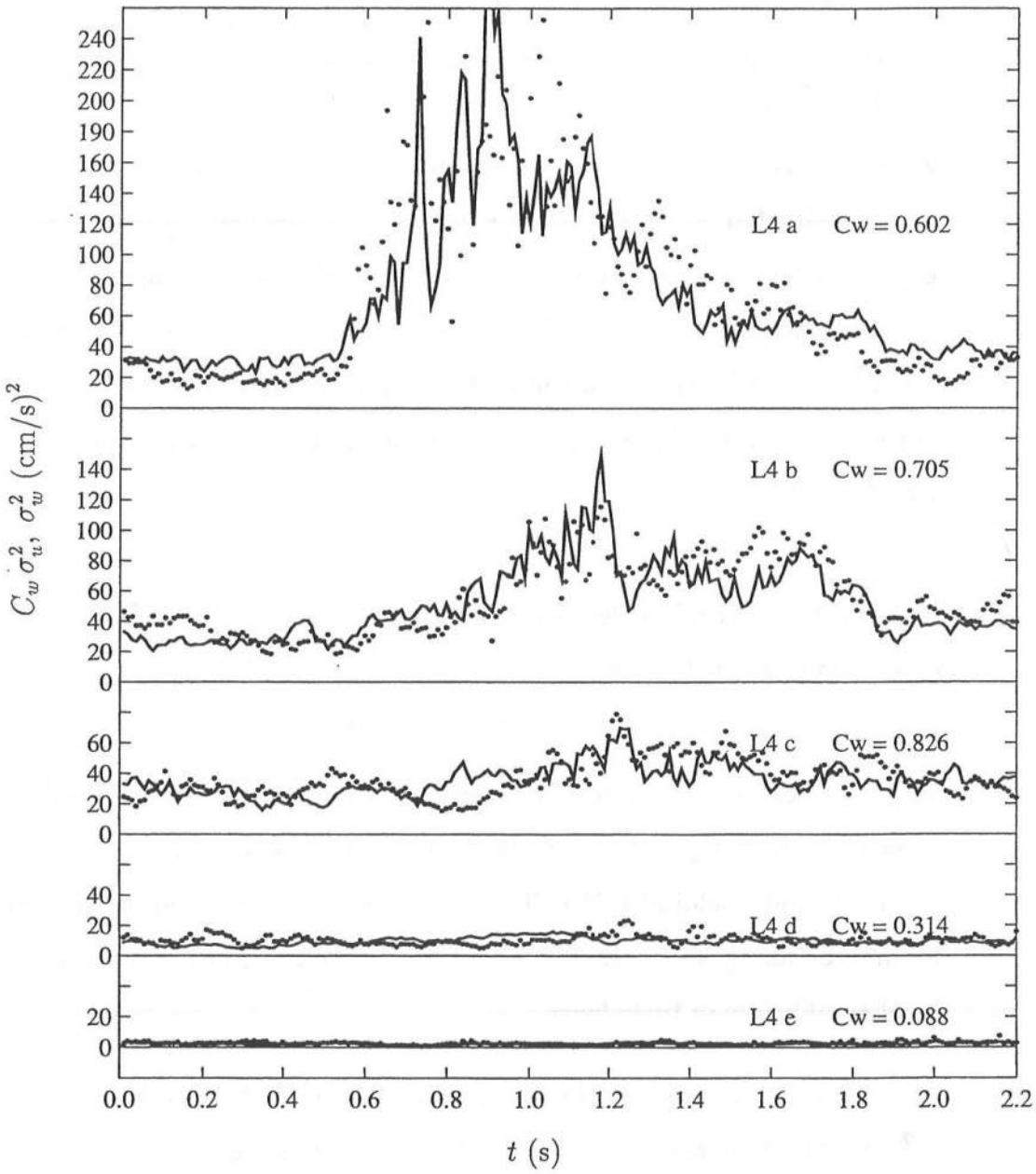

Figure 6.3: Temporal Variations of Horizontal Variance, $C_w\sigma_u^2$ (——), and Vertical Variance, σ_w^2 (•), for Five Vertical Elevations for L4 with $gH_r/\sigma = 337$ (cm/s)^2.

6.2 Approximate Local Equilibrium of Turbulence

Recalling from Chapter 2, the transport equation of turbulent kinetic energy, k, may be written as (e.g., ASCE 1988)

$$\frac{\partial k}{\partial t} + u_j \frac{\partial k}{\partial x_j} = \nu_t \left(\frac{\partial u_i}{\partial x_j} + \frac{\partial u_j}{\partial x_i} \right) \frac{\partial u_i}{\partial x_j} + \frac{\partial}{\partial x_j} \left(\frac{\nu_t}{\sigma_k} \frac{\partial k}{\partial x_j} \right) - C_d^{3/4} \frac{(k)^{3/2}}{\ell}, \qquad (6.17)$$

where use is made of the repeated indices, $i = 1, 2$; t is time, $x_1 = x$ is the onshore directed horizontal coordinate; $x_2 = z$ is the vertical coordinate, positive upward with $z = 0$ at the still water level (SWL); $u_1 = u$ and $u_2 = w$ are the horizontal and vertical velocities; and σ_k is an empirical constant associated with the diffusion of k. The turbulent eddy viscosity, ν_t, may be expressed as a product of the turbulent length scale, ℓ_t, and a turbulent velocity scale, typically $\sqrt{k}$, (e.g., ASCE 1988)

$$\nu_t = \ell_t \sqrt{k}. \qquad (6.18)$$

The turbulent length scale may be written as $\ell_t = C_d^{1/4} \ell$ so that Eq 6.18 may be expressed (e.g., ASCE 1988)

$$\nu_t = C_d^{1/4} \ell \sqrt{k}, \qquad (6.19)$$

where ℓ is the turbulent mixing length, and C_d is an empirical coefficient. The typical values of C_d and σ_k for *steady* turbulent flow are $C_d \simeq 0.08$ and $\sigma_k \simeq 1.0$ (Launder and Spalding 1972). The value of C_d is determined in the next section for non-breaking and breaking waves under the assumption of an approximate local equilibrium of turbulence.

The equation for the dissipation rate of k might be used to estimate the turbulence length scale (k-ϵ model) but this equation is more empirical than Eq 6.17 and gives only slightly better results for the case of bed shear stress calculations

outside the surf zone (Fredsøe and Deigaard 1992). Alternatively, the mixing length ℓ in Eq 6.19 may be specified simply as

$$\ell = \begin{cases} \kappa(z - z_b) & \text{for } z < \left(\overline{C_\ell} h/\kappa + z_b\right) \\ \\ \overline{C_\ell}\, h & \text{for } z \geq \left(\overline{C_\ell} h/\kappa + z_b\right) \end{cases} \tag{6.20}$$

where κ is the Kármán constant ($\kappa \simeq 0.4$); z_b is the bottom elevation; h is the instantaneous water depth; and $\overline{C_\ell}$ is an empirical coefficient related to the eddy size. $\overline{C_\ell}$ is written with an overbar to show that it is time-invariant and to differentiate it from C_ℓ used later. Eq 6.20 is similar to that used by Deigaard *et al.* (1986) for their analysis of suspended sediment in the surf zone. Their formulation was in terms of the turbulent length scale in which use was made of $\overline{C_\ell} \sim O(0.1)$ and the mean water depth, $\overline{h}$, instead of the instantaneous depth, h. The use of h should be more appropriate in the swash zone in light of the limited field data of Flick and George (1990). Svendsen (1987) suggested a larger $\overline{C_\ell}$ by a factor of 2 to 3 for his qualitative analysis of surf zone turbulence. The coefficient for the *unsteady* flow, C_ℓ , and the time-averaged value, $\overline{C_\ell}$, will be determined in Section 6.4.

The dimensionless variables are introduced following Kobayashi and Wurjanto (1992):

$$t' = \frac{t}{T_r};\quad x' = \frac{x}{T_r\sqrt{gH_r}};\quad z' = \frac{z}{H_r};\quad u' = \frac{u}{\sqrt{gH_r}};\quad w' = \frac{w}{H_r/T_r} \tag{6.21}$$

$$p' = \frac{p}{\rho g H_r};\quad \nu_t' = \frac{\nu_t}{{H_r}^2/T_r};\quad k' = \frac{k}{gH_r/\sigma};\quad \ell' = \frac{\ell}{H_r/\sqrt{\sigma}};\quad \sigma = \frac{T_r\sqrt{gH_r}}{H_r} \tag{6.22}$$

where the primes indicate dimensionless quantities, T_r and H_r are the characteristic wave period and height of the shallow water waves, and σ is the ratio between the horizontal and vertical length scales. The order of magnitude of k, ℓ, and ν_t is estimated such that the resulting normalized quantities k', ℓ', and ν_t' are of order unity or less.

Substitution of Eqs 6.21 and 6.22 into Eq 6.17 under the assumption of $\sigma^2 \gg 1$ yields

$$\sigma^{-1}\left(\frac{\partial k'}{\partial t'} + u'\frac{\partial k'}{\partial x'} + w'\frac{\partial k'}{\partial z'}\right) = \tau'\frac{\partial u'}{\partial z'} + \sigma^{-1}\frac{\partial}{\partial z'}\left(\frac{\nu_t'}{\sigma_k}\frac{\partial k'}{\partial z'}\right) - C_d^{3/4}\frac{k'^{3/2}}{\ell'} \qquad (6.23)$$

where the first and third terms on the right-hand-side are the production and dissipation terms, respectively. For their analysis of suspended sediment in the surf zone, Deigaard *et al.* (1986) used Eq 6.23 in which the advection terms were neglected and the production of k' was estimated empirically. Eq 6.23 indicates that the production and dissipation of k' are dominant under the assumption of $\sigma^2 \gg 1$. This is qualitatively consistent with the findings of Svendsen (1987) who concluded that only a very small portion of the energy loss in the breaker (2–6% for the cases considered) was dissipated below trough level.

Considering the empirical nature of Eq 6.23 with the coefficients σ_k and C_d as well as the uncertainty of the free surface boundary condition of k' even for steady turbulent flow (Rodi 1980), Eq 6.23 may be simplified further by neglecting the terms of the order σ^{-1}, and the resulting equation is expressed in dimensional form as

$$\frac{\tau}{\rho}\frac{\partial u}{\partial z} \simeq C_d^{3/4}\frac{k^{3/2}}{\ell} \qquad (6.24)$$

which implies the local equilibrium of turbulence. Substitution of $\tau/\rho = \nu_t \partial u/\partial z$ and Eq 6.19 into Eq 6.24 yields

$$k = \frac{|\tau|}{\rho\sqrt{C_d}} \qquad (6.25)$$

and

$$\nu_t = \ell^2\left|\frac{\partial u}{\partial z}\right|. \qquad (6.26)$$

With these assumptions, Eq 6.25 is used to determine the appropriate value of C_d in Section 6.3. Eq 6.26 corresponds to the standard mixing length model (ASCE 1988) and is used with Eq 6.19 to determine C_ℓ and $\overline{C_\ell}$ in Eq 6.20 in Section 6.4.

The degree of the local equilibrium of turbulence is assessed using Eq 6.24 with the calibrated coefficients C_d and $\overline{C_\ell}$ in Section 6.5.

The normalization parameters for the turbulent quantities, k, ℓ and ν_t, in Eq 6.22 are given in Table 6.2 with the range of values for the measured data. The range is found by taking the minimum and maximum values for the phase-averaged quantities between the trough level and the bottom boundary layer which is defined as 1 cm above the impermeable bottom and consistent with the results in Section 5.7. The ranges given in parentheses are for the bottom boundary layer. Table 6.2 shows that $k/(gH_r/\sigma)$, $\ell/(H_r/\sqrt{\sigma})$, and $\nu_t/({H_r}^2/T_r)$ are indeed of the order unity for L3 to L6 in the surf zone. These quantities are less than unity for L1 and L2 outside the surf zone.

For completeness, the normalization parameters for the steady and turbulent quantities for L1 to L6 are given in Table 6.3 where H_r is the local wave height, T_r is the wave period $T_r = 2.2$ s, and σ is the ratio of the horizontal length scales to vertical length scales as defined in Eq 6.22.

Table 6.2: Range of k, ℓ and ν_t and Normalization Quantities for L1 to L6.

Line No.	k (cm^2/s^2)	gH_r/σ (cm^2/s^2)	ℓ (cm)	$H_r/\sqrt{\sigma}$ (cm)	ν_t (cm^2/s)	${H_r}^2/T_r$ (cm^2/s)
L1	0.2 – 2.8	684	0.60 – 1.20	3.04	0.11 – 0.61	79.4
	(0.3 – 18.8)		(0.01 – 0.40)		(0.00 – 0.27)	
L2	0.4 – 3.8	1007	0.60 – 1.91	4.19	0.17 – 1.03	132.9
	(0.4 – 35.9)		(0.01 – 0.40)		(0.01 – 0.28)	
L3	14.4 – 297	645	0.60 – 3.23	2.89	0.65 – 18.4	73.4
	(4.9 – 45.6)		(0.01 – 0.40)		(0.01 – 0.76)	
L4	20.7 – 559	337	0.61 – 4.26	1.68	0.81 – 34.8	30.9
	(6.8 – 65.7)		(0.02 – 0.41)		(0.01 – 0.68)	
L5	17.4 – 206	268	0.60 – 2.64	1.39	0.97 – 12.9	22.8
	(4.1 – 35.6)		(0.01 – 0.40)		(0.01 – 0.60)	
L6	13.9 – 179	162	0.61 – 2.00	0.91	0.81 – 11.1	11.6
	(4.4 – 76.7)		(0.02 – 0.41)		(0.02 – 0.83)	

Table 6.3: Normalization Parameters for Steady and Turbulent Quantities for L1 to L6.

Line No.	H_r (cm)	$\sqrt{gH_r}$ (cm/s)	$\frac{H_r}{T_r}$ (cm/s)	$\frac{{H_r}^2}{T_r}$ (cm^2/s)	σ	$\frac{gH_r}{\sigma}$ (cm^2/s^2)	$\frac{H_r}{\sqrt{\sigma}}$ (cm)
L1	13.22	113.9	6.01	79.4	18.95	684	3.04
L2	17.10	129.5	7.77	132.9	16.66	1007	4.19
L3	12.71	111.7	5.78	73.4	19.33	645	2.89
L4	8.24	89.9	3.75	30.9	24.00	337	1.68
L5	7.08	83.3	3.22	22.8	25.90	268	1.39
L6	5.05	70.4	2.30	11.6	30.66	162	0.91

6.3 Estimation of Dissipation Coefficient

To calibrate the dissipation coefficient, C_d, a least-squares error method is used similar to that used to find C_w in Section 6.1. Making use of Eq 6.25 with $|\tau|/\rho = |\sigma_{uw}|$ and assuming that C_d is a function of x and z only, the least-squares equation can be shown to be

$$\sqrt{C_d} = \frac{\sum_{j=1}^{J} |\sigma_{uw}|_j k_j}{\sum_{j=1}^{J} k_j^2} \tag{6.27}$$

where $j = 220$ is the number of phases.

Figure 6.4 shows the cross-shore variation of C_d for L1 to L6 using Eq 6.27. The vertical variation of C_d is distinctly different for the three regions: L1 and L2 seaward of breaking, L3 in the transition region, and L4 to L6 in the inner surf zone. For L1 and L2, $C_d \simeq 0.06$ in the bottom boundary layer whereas $C_d = 0.08$ has been used for oscillatory flows (e.g., Deigaard *et al.* 1991). For L3, the magnitude of C_d is small over the water column. For L4 to L6, there is considerable scatter in C_d, but it does not appear to vary with depth except in the lower portion where it decreases to a small value.

Figure 6.4 shows the cross-shore variation of C_d in detail for L4 to L6. An average value of the dissipation coefficient, $[C_d]_{ave}$, was computed for L4 to L6 using only those measuring point elevations for which C_d did not appear to vary with depth. The average value for L4 to L6 is given by

$$[C_d]_{ave} \simeq 0.053 \ \ (0.020) \tag{6.28}$$

where the standard deviation is given in parentheses. Figure 6.5 shows the measuring point elevations used to estimate $[C_d]_{ave}$ and are indicated with a solid circle. The thick vertical line indicates $[C_d]_{ave} = 0.053$ and is plotted over the range of depths for which C_d did not appear to vary with depth. The thin dashed lines are this average $\pm$ one standard deviation.

Figure 6.6 shows the temporal variations of $\sqrt{C_d}k$ and $|\sigma_{uw}|$ for the five vertical elevations for L2. Like C_w in Figure 6.2, the lower curve shows that it is appropriate to assume that C_d is constant over a wave period in the boundary layer outside the surf zone. Figure 6.7 shows the temporal variations of $\sqrt{C_d}k$ and $|\sigma_{uw}|$ for the five vertical elevations for L4. This figure shows that C_d is relatively constant over a wave period in the surf zone as well.

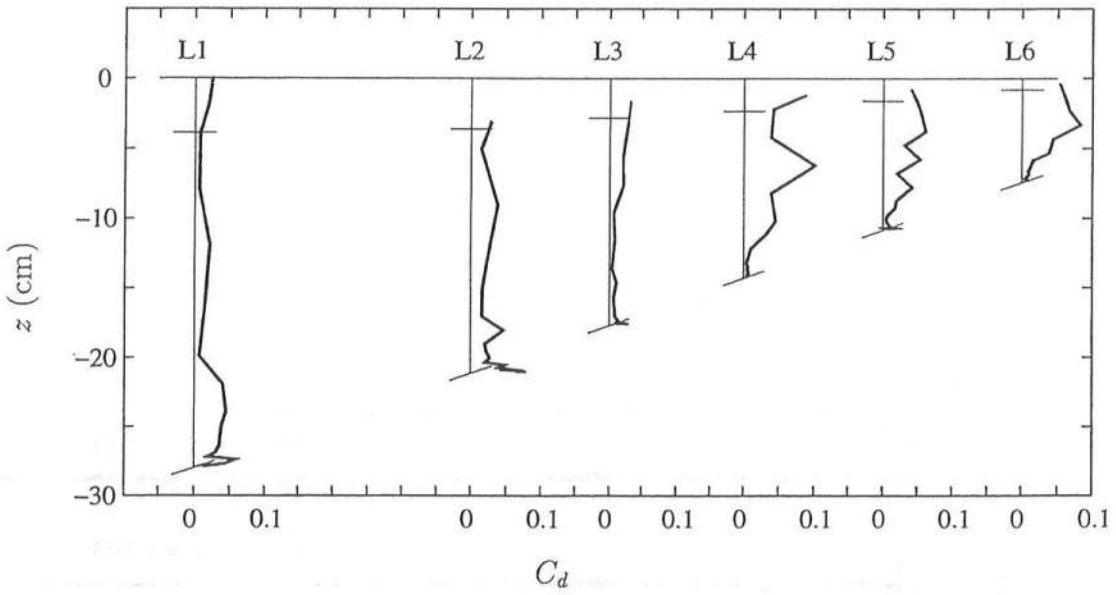

Figure 6.4: Cross-Shore Variation of C_d for L1 to L6.

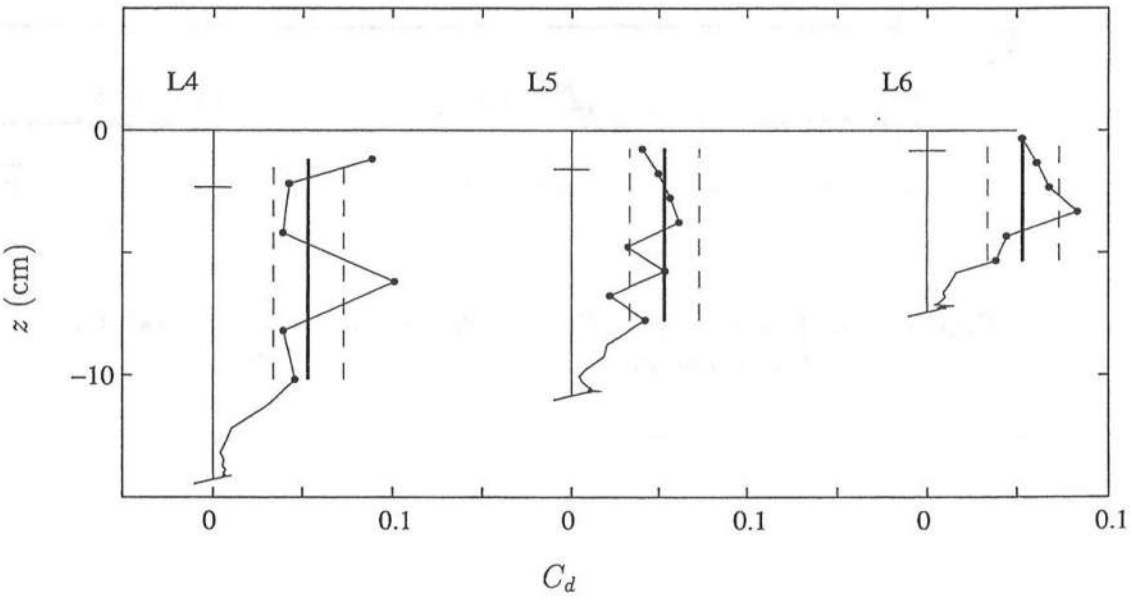

Figure 6.5: Cross-Shore Variation of C_d in Detail with Values Used to Compute $[C_d]_{ave}$ (•); and $[C_d]_{ave} = 0.053$ (——) with Standard Deviation $C_d = 0.053 \pm 0.020$ (– –) for L4 to L6.

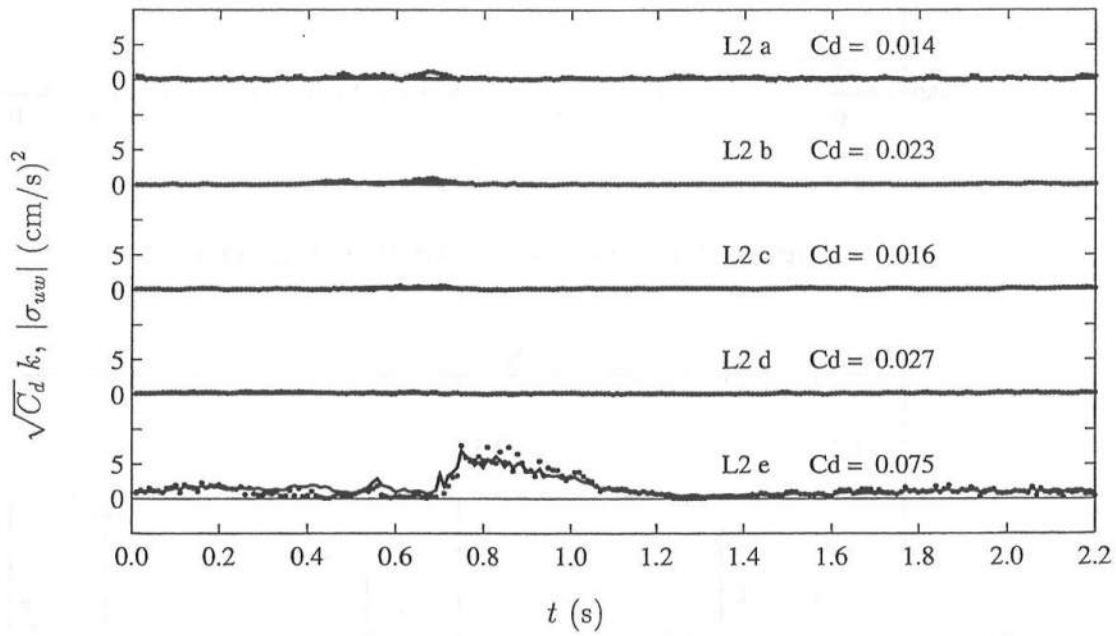

Figure 6.6: Temporal Variations of $\sqrt{C_d}\,k$ (——), and $|\sigma_{uw}|$ (•), for Five Vertical Elevations for L2 with $gH_r/\sigma = 1007$ $(\mathrm{cm/s})^2$.

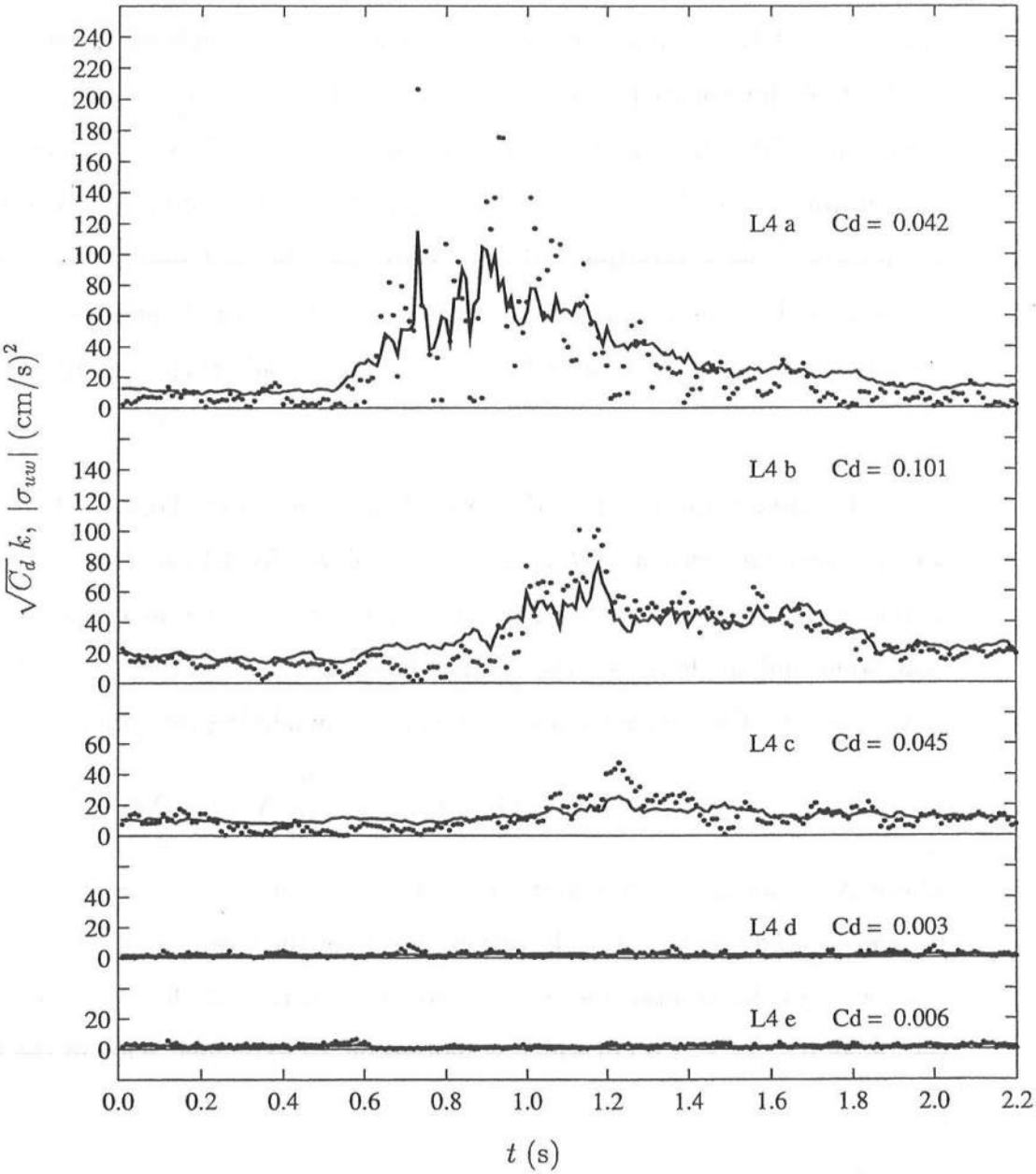

Figure 6.7: Temporal Variations of $\sqrt{C_d}\,k$ (——), for Five Vertical Elevations for L4 with $gH_r/\sigma = 337\ (\mathrm{cm/s})^2$.

6.4 Estimation of Mixing Length and Eddy Viscosity

The mixing length, ℓ, and the eddy viscosity, ν_t, are estimated in this section using Eqs 6.19 and 6.26 and the calibrated coefficient, C_d. The vertical gradient of the horizontal velocity, $\partial u/\partial z$, in Eq 6.26 is computed using IMSL subroutines DCSIEZ and DDERIV without smoothing (Visual Numerics 1991). The subroutine DCSIEZ computes the value of the cubic spline interpolant for the given data. The subroutine DDERIV computes the first derivative of the data using the cubic spline from the subroutine DCSIEZ. Double precision is used for both subroutines. It is restated that for the Reynolds averaging assumed here, $u \simeq u_a$.

Figure 6.8 and 6.9 show the vertical variations of the horizontal velocity, u, and the vertical derivative, $\partial u/\partial z$, at eleven phases for L1 and L4. The direction of the light line connected to each data point indicates the tangent computed at that point and the length of the line is related to the magnitude of the derivative at that point. The tangent lines are drawn by connecting two points

$$[u(x,z,t),\, z] \quad \text{and} \quad [u(x,z,t) + \frac{\partial u}{\partial z}\Delta z,\, z + \Delta z] \tag{6.29}$$

where Δz is an arbitrary scalar with $\Delta z = 2.0$ and 1.0 for the upper panels of Figures 6.8 and 6.9, respectively, and $\Delta z = 0.2$ for the lower panels of both figures. The two light horizontal lines in the lower right corner of the top panel indicate the range $0 < z_m < 2.0$ cm which is plotted on an expanded scale in the bottom panel.

Both the upper and lower panels of Figure 6.8 show that the velocity profile is fairly smooth and continuous and that the derivatives can be estimated reasonably well outside the surf zone. Figure 6.9 for L4 in the surf zone shows in the upper panel that the velocity profiles are less smooth and that the derivatives

contain more noise than for L1 shown in Figure 6.8. Similarly in the bottom boundary layer shown in the lower panel, the derivatives contain more noise than for L1. Similar results were obtained for L2, L3, L5 and L6 and are not shown for brevity.

Eqs 6.26 and 6.19 with the calibrated values of C_d are used to determine C_ℓ in Eq 6.20. For this procedure, an error term is computed for a range of C_ℓ values by summing the absolute value of the difference of Eqs 6.26 and 6.19 over the water column at each of the 220 phases. The error term is given as

$$Err(j) = \frac{1}{I}\sum_{i=1}^{I} \frac{|a-b|_i}{b_i}, \quad j = 1, 2, \ldots, 220 \tag{6.30}$$

where

$$a = \ell^2 \left|\frac{\partial u}{\partial z}\right| \tag{6.31}$$

and

$$b = C_d^{1/4} \ell \sqrt{k} \tag{6.32}$$

and the index i refers to points in the vertical measuring line. The error term, Err, is dimensionless and $Err = 1.0$ corresponds to a relative error of 100%. The quantity in Eq 6.32 was used to normalize the error estimate since the quantity in Eq 6.31 is likely to contain more noise due to the derivative on the horizontal velocity. The ranges of C_ℓ were $0.01 \leq C_\ell \leq 0.20$ for L1 and L2 and $0.05 \leq C_\ell \leq 0.45$ for L3 to L6. The value of C_ℓ that gave the least error in Eq 6.30 was adopted at that phase.

Figures 6.10 to 6.15 show the temporal variations of the error estimates and the adopted value of C_ℓ at each of the 220 phases for L1 to L6. It is noted that the C_ℓ values for which the error term exceeds unity, i.e. $Err > 1.0$, are marked with a plus in the figures are not used to compute $\overline{C_\ell}$. These figures show the amount of scatter expected for the calibrated C_ℓ and indicates that there is

a slight variation over the wave period. The time-average values, $\overline{C_\ell}$, are listed in Table 6.4 where the standard deviations are given in parentheses. The overall values for the three regimes are

$$C_\ell \simeq \begin{cases} 0.04 \quad (0.03) & \text{outside the surf zone} \\ 0.12 \quad (0.07) & \text{in the transition region} \\ 0.18 \quad (0.09) & \text{for the inner surf zone} \end{cases} \tag{6.33}$$

where the value for outside the surf zone is the average of L1 and L2 from Table 6.4, the value in the transition zone is simply L3 from Table 6.4, and the value for the inner surf zone is the average of L4, L5 and L6. The corresponding averages of the standard deviations are given in parentheses.

Table 6.4: Time-Averaged Mixing Length Coefficient for L1 to L6.

Line No.	$\overline{C_\ell}$	
L1	0.032	(0.021)
L2	0.055	(0.041)
L3	0.117	(0.065)
L4	0.211	(0.105)
L5	0.162	(0.081)
L6	0.172	(0.089)

The next two figures show how well the relation

$$\ell \left| \frac{\partial u}{\partial z} \right| \simeq C_d^{1/4} \sqrt{k} \tag{6.34}$$

used to determine $\overline{C_\ell}$ is satisfied. Figure 6.16 shows the vertical variations of $\ell |\partial u/\partial z|$ and $C_d^{1/4}\sqrt{k}$ at 11 phases for L1. The light vertical lines in the upper panel indicate the extent of the water column at the given phase. The two light horizontal lines in the lower left corner of the top panel indicate the range $0 <$

$z_m < 2.0$ cm which is plotted on an expanded scale in the bottom panel. The agreement is fair considering that k is a small quantity in the boundary layer seaward of breaking. Figure 6.16 also shows reasonable agreement in the middle portion of the water column, but there is some disagreement under the wave crest at $t \simeq 0.8$ s. Figure 6.17 shows that Eq 6.34 is satisfied reasonably well below trough level for L4 except near the surface roller at $t \simeq 0.6$–0.8 s. It is noted that the scale in the upper panel of Figure 6.17 is an order of magnitude larger than the scale in the upper panel of Figure 6.16. The lower panel of Figure 6.17 shows that Eq 6.34 is reasonably well satisfied in the bottom boundary layer for L4, and it is noted that the scale in this panel is the same as the lower panel of Figure 6.16. The figures for L2, L3, L5 and L6 were similar and are omitted for brevity.

Figures 6.18 and 6.19 show the vertical and temporal variations of the eddy viscosity, ν_t, given in Eq 6.19 computed using the calibrated values of C_d and $\overline{C_\ell}$ for L1 and L4, respectively. The light vertical lines in the upper figure indicate the extent of the water column at the given phase. The two light horizontal lines in the lower left corner of the top panel indicate the range $0 < z_m < 2.0$ cm which is plotted on an expanded scale in the bottom panel. The figures show that ν_t at a given phase increases gradually from the bottom until about the middle of the water column where it is more or less constant over depth. Also, it is reasonable to assume that ν_t is time-invariant except near trough level with the passing of the bore. It is noted that the scales in both the upper and lower panels of Figure 6.19 are an order of magnitude larger than the scales in Figure 6.18. The figures for L2, L3, L5 and L6 were similar and are omitted for brevity.

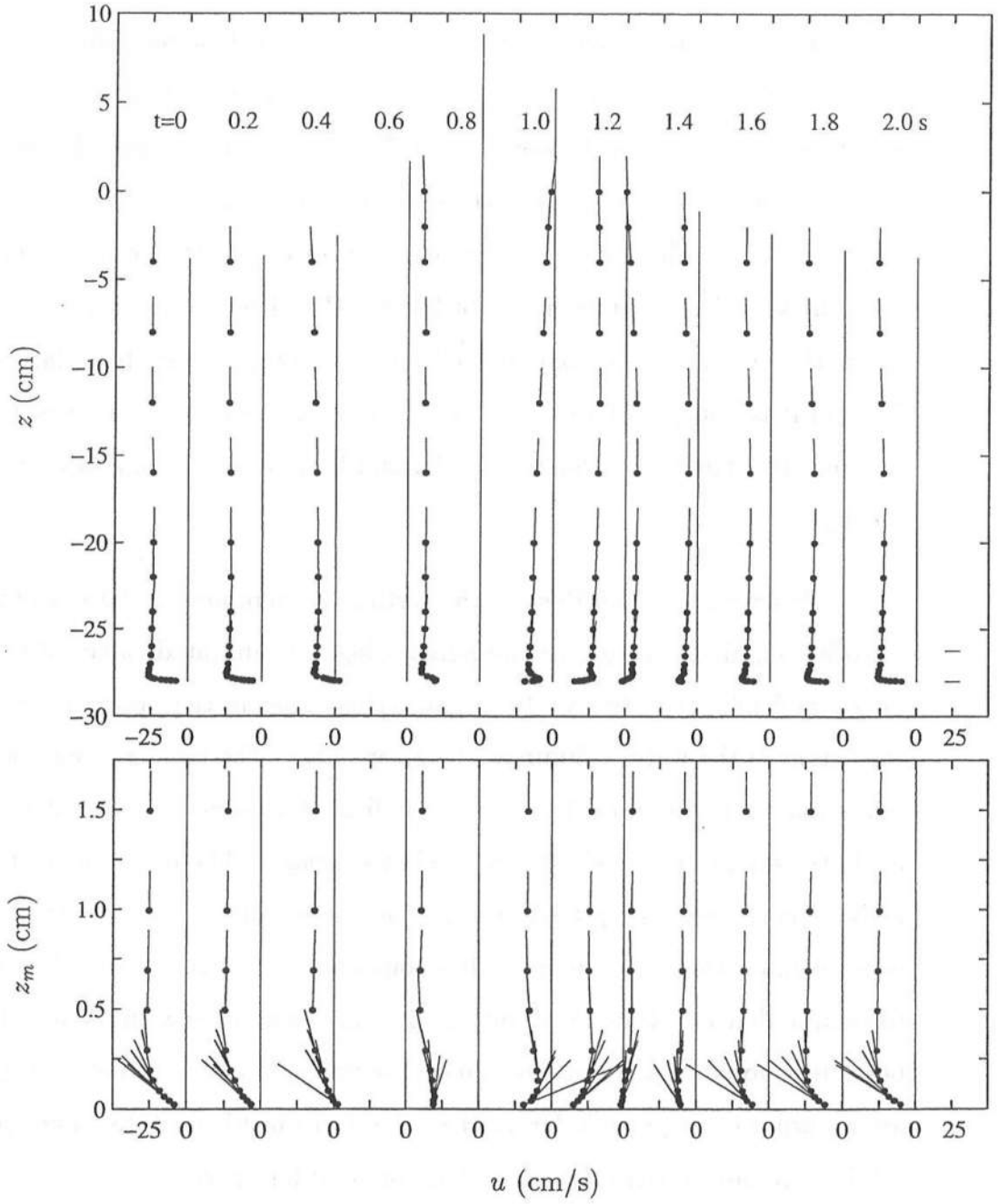

Figure 6.8: Vertical Variations of Horizontal Velocity, $u(\bullet)$, and Vertical Derivative $\partial u/\partial z(——)$ at Eleven Phases for L1 (Top) with Detail of Bottom Boundary Layer (Bottom) and $\sqrt{gH_r} = 113.9$ cm/s.

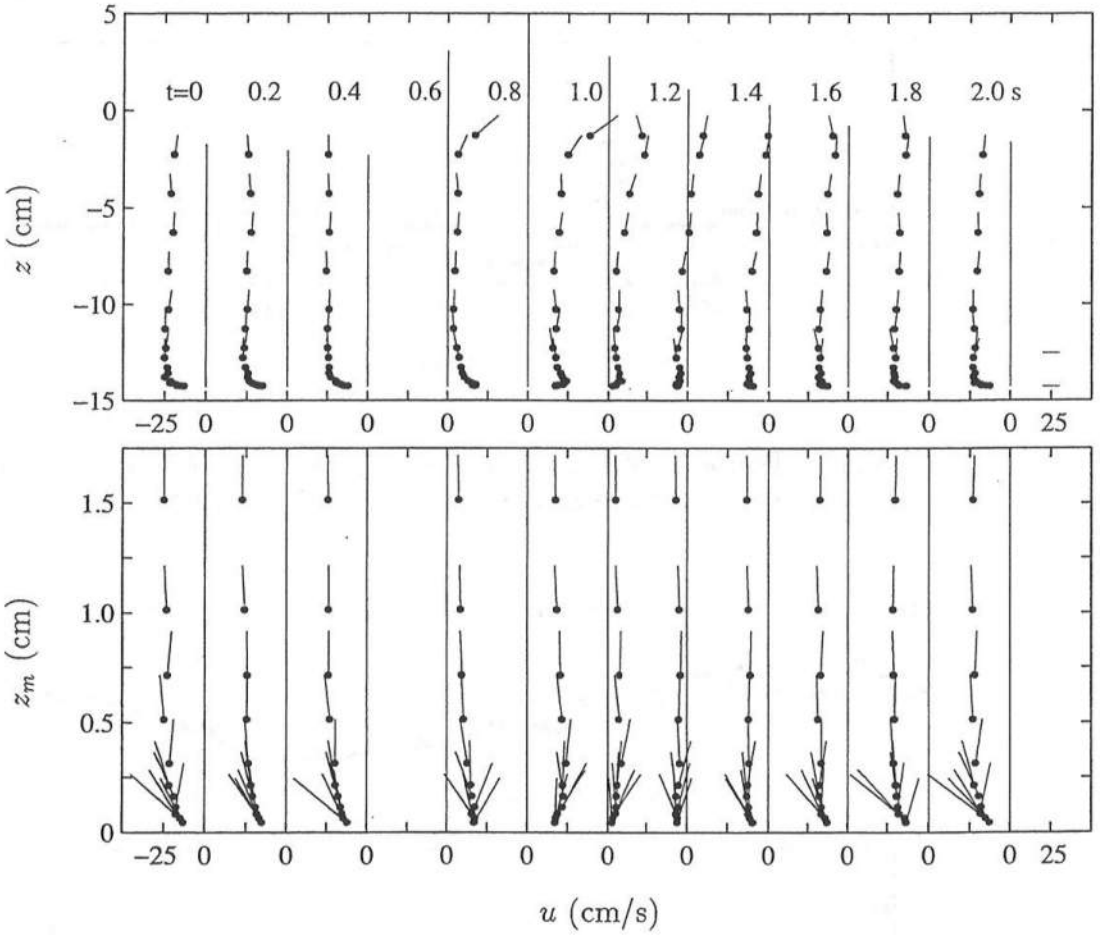

Figure 6.9: Vertical Variations of Horizontal Velocity, $u(\bullet)$, and Vertical Derivative $\partial u/\partial z(——)$ at Eleven Phases for L4 (Top) with Detail of Bottom Boundary Layer (Bottom) and $\sqrt{gH_r} = 89.9$ cm/s.

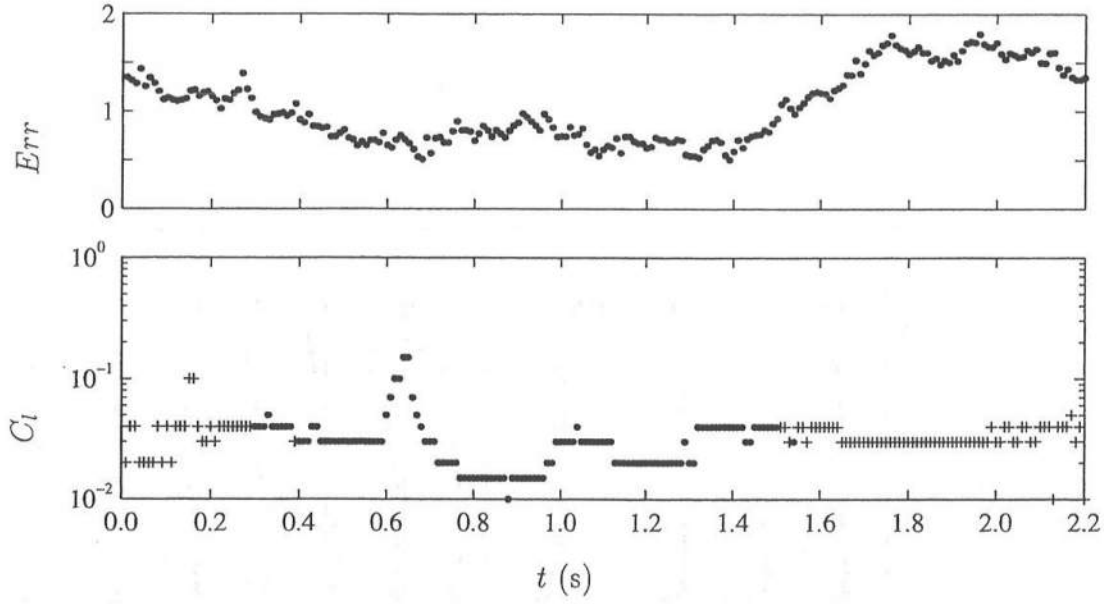

Figure 6.10: Temporal Variations of Error Estimate in Adopted C_ℓ (Top) and Adopted C_ℓ (Bottom) for L1 with $\overline{C_\ell} = .0364$.

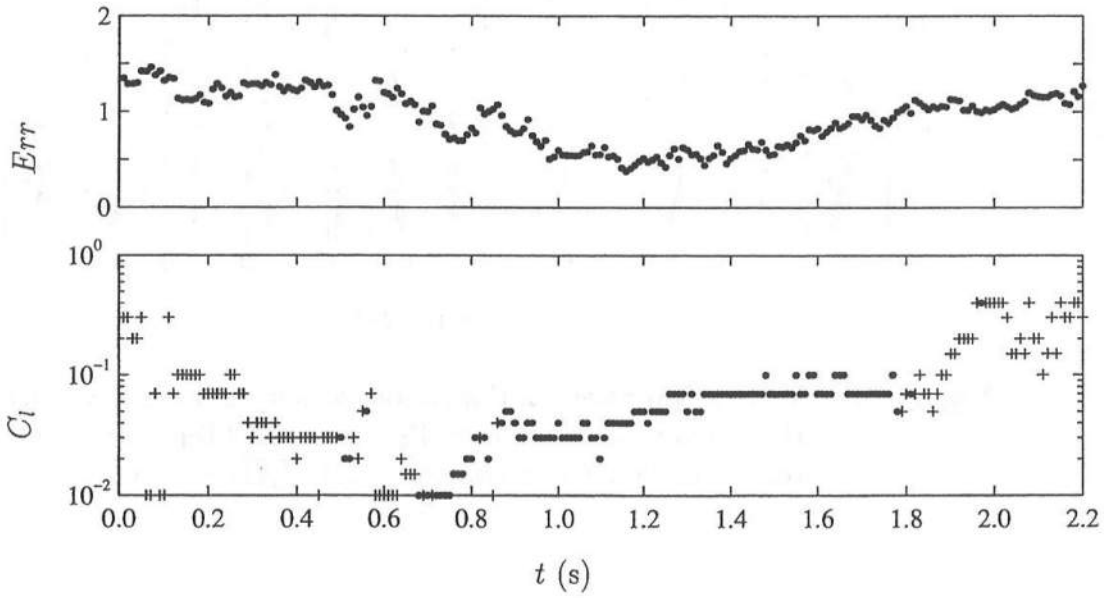

Figure 6.11: Temporal Variations of Error Estimate in Adopted C_ℓ (Top) and Adopted C_ℓ (Bottom) for L2 with $\overline{C_\ell} = .0705$.

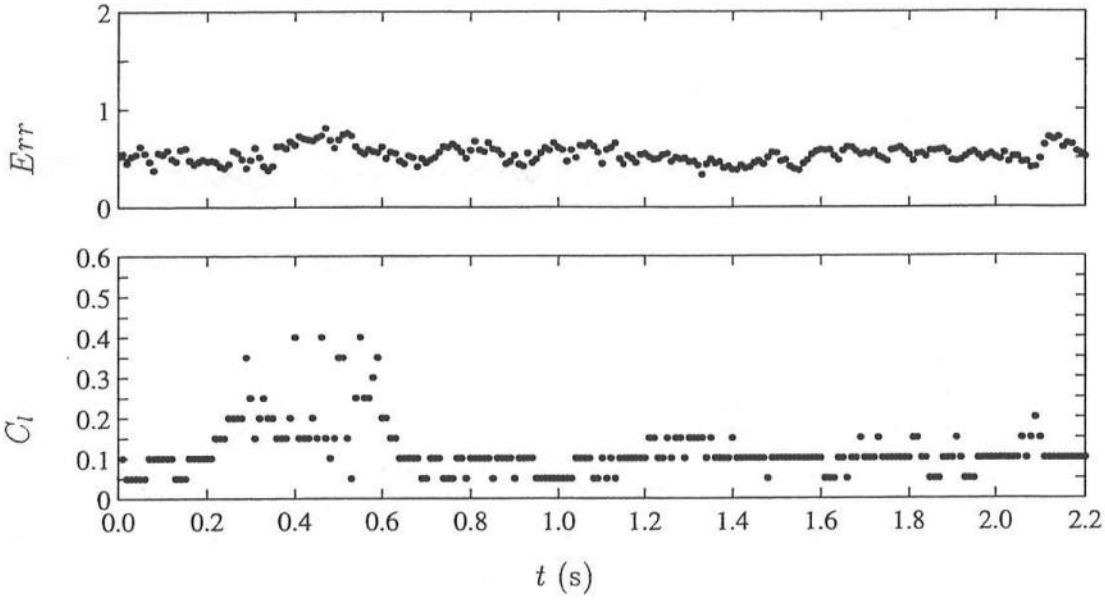

Figure 6.12: Temporal Variations of Error Estimate in Adopted C_ℓ (Top) and Adopted C_ℓ (Bottom) for L3 with $\overline{C_\ell} = .1498$.

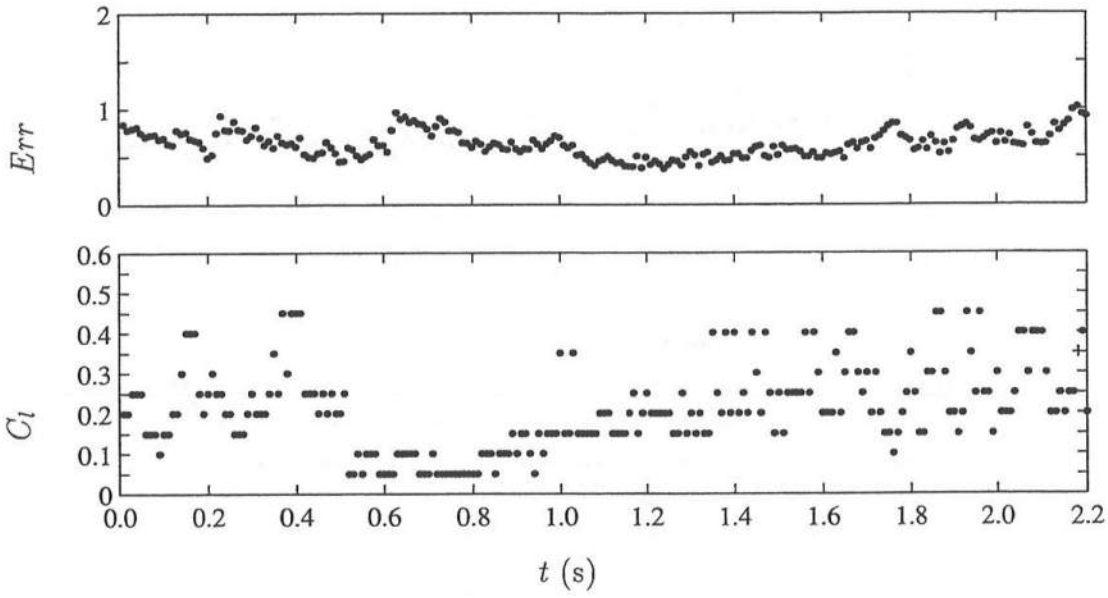

Figure 6.13: Temporal Variations of Error Estimate in Adopted C_ℓ (Top) and Adopted C_ℓ (Bottom) for L4 with $\overline{C_\ell} = .2357$.

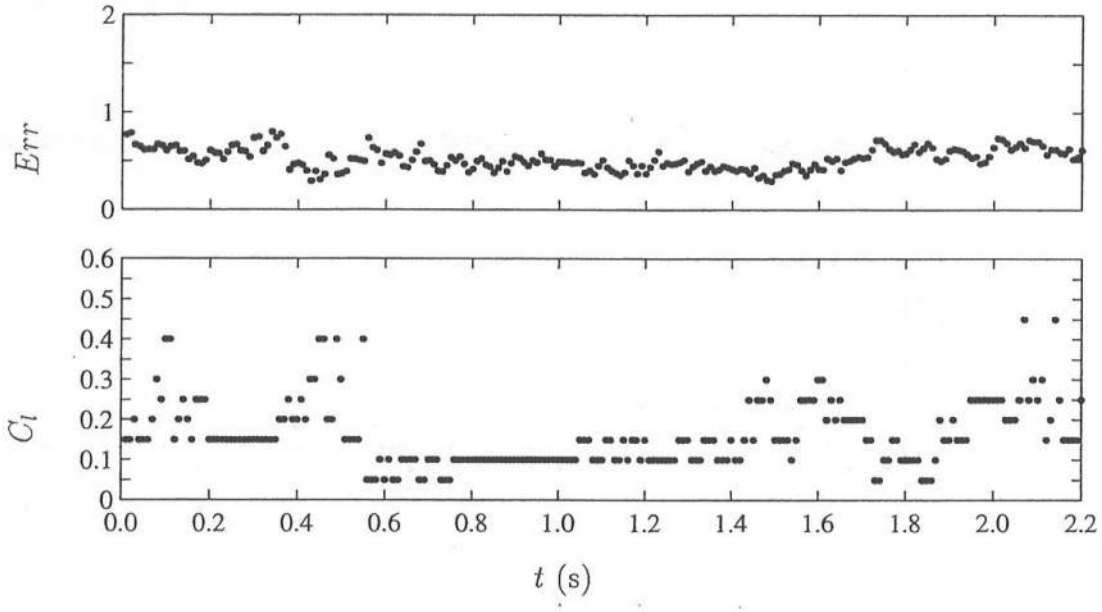

Figure 6.14: Temporal Variations of Error Estimate in Adopted C_ℓ (Top) and Adopted C_ℓ (Bottom) for L5 with $\overline{C_\ell} = .2136$.

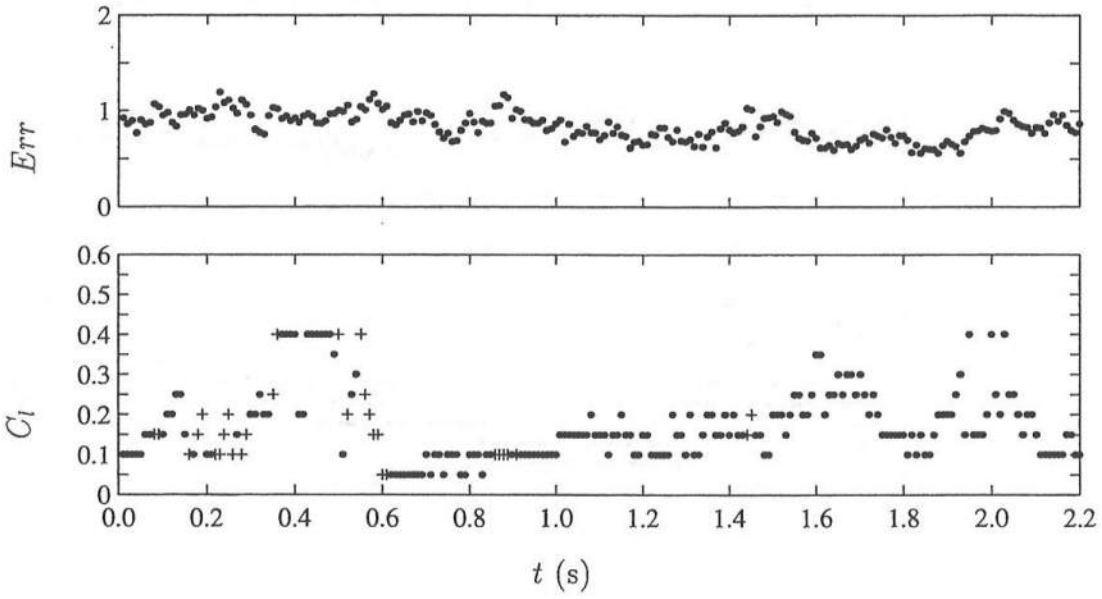

Figure 6.15: Temporal Variations of Error Estimate in Adopted C_ℓ (Top) and Adopted C_ℓ (Bottom) for L6 with $\overline{C_\ell} = .1891$.

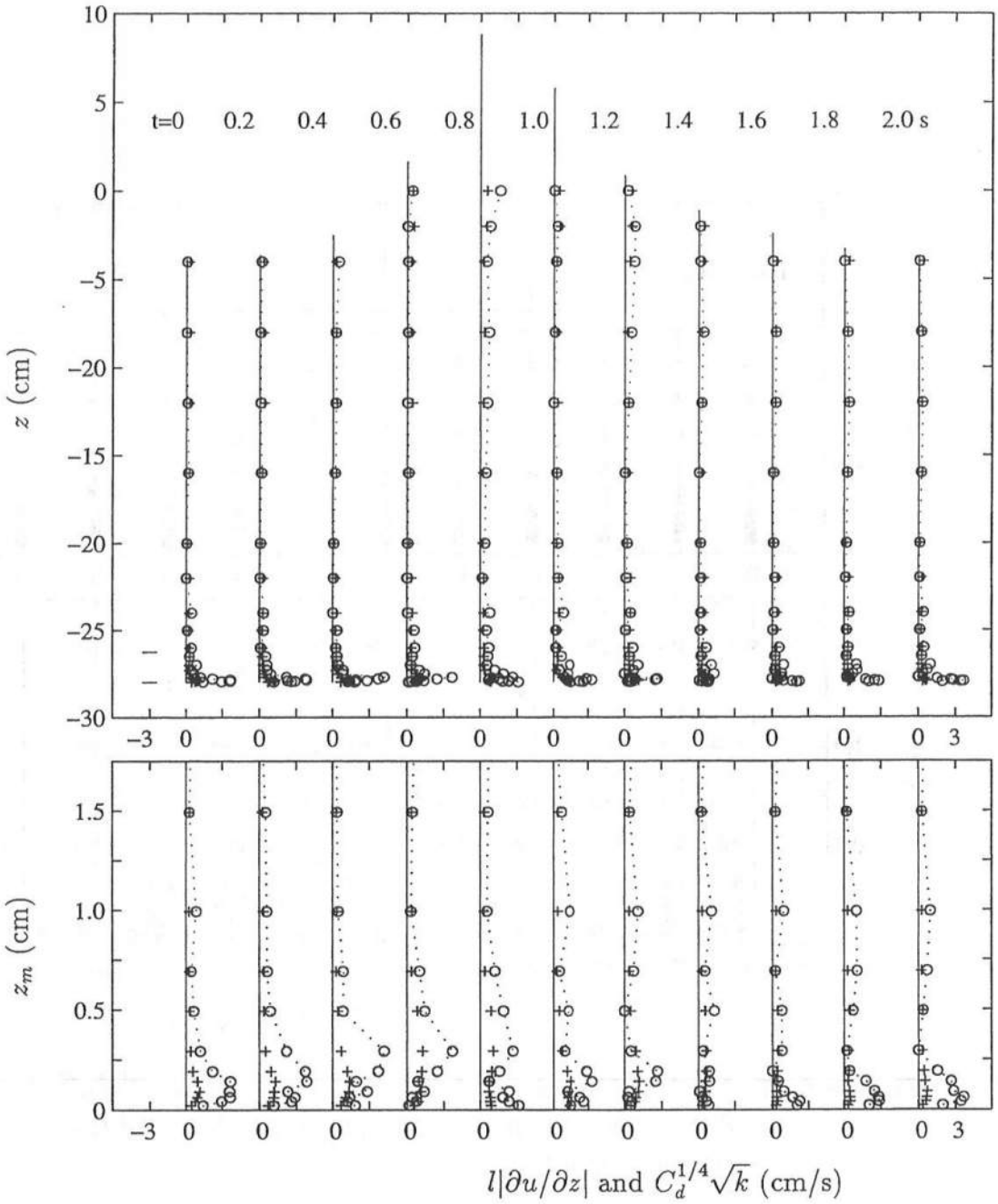

Figure 6.16: Vertical Variations of $\ell|\partial u/\partial z|$ (o ····) and $C_d^{1/4}\sqrt{k}$ (+) at 11 Phases for L1 with $\overline{C_\ell} = .032$ (Top) with Detail of Bottom Boundary Layer (Bottom).

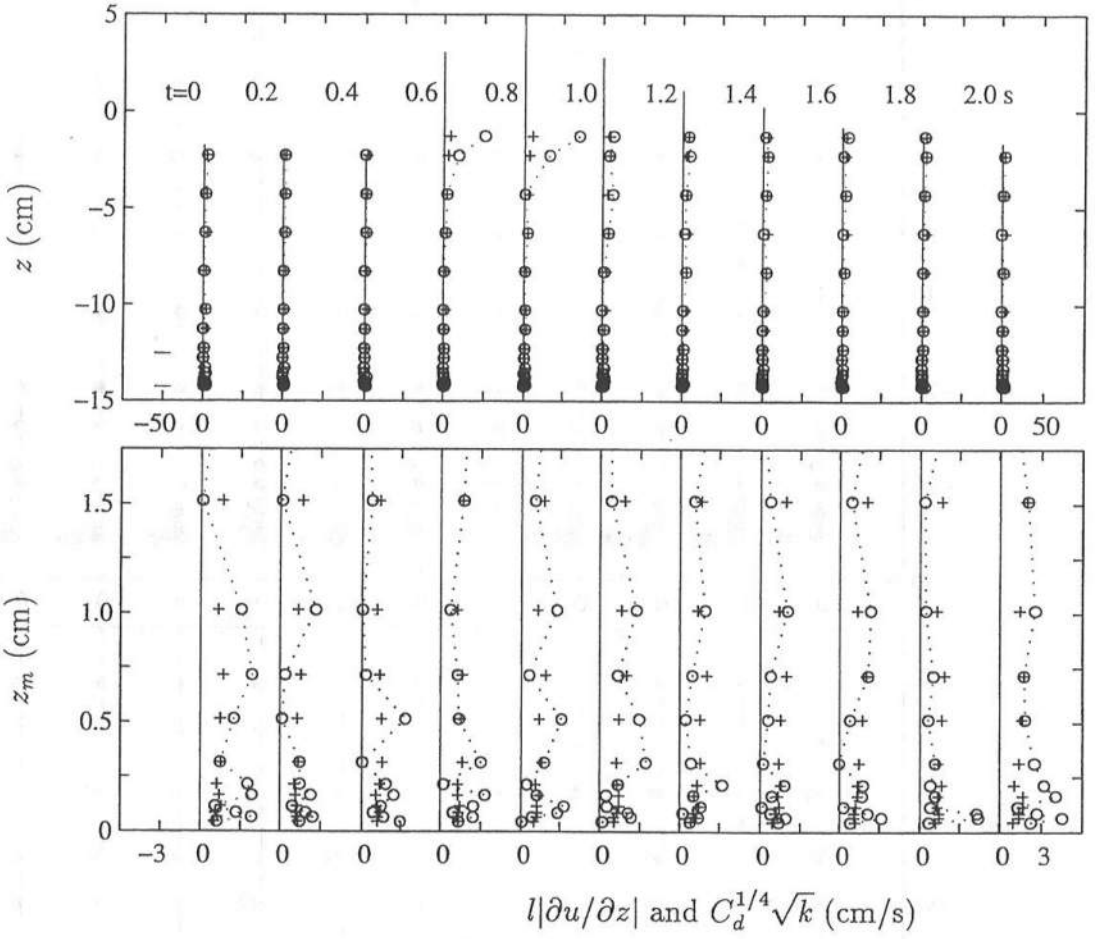

Figure 6.17: Vertical Variations of $\ell|\partial u/\partial z|$ (o ····) and $C_d^{1/4}\sqrt{k}$ (+) at 11 Phases for L4 with $\overline{C_\ell} = .211$ (Top) with Detail of Bottom Boundary Layer (Bottom).

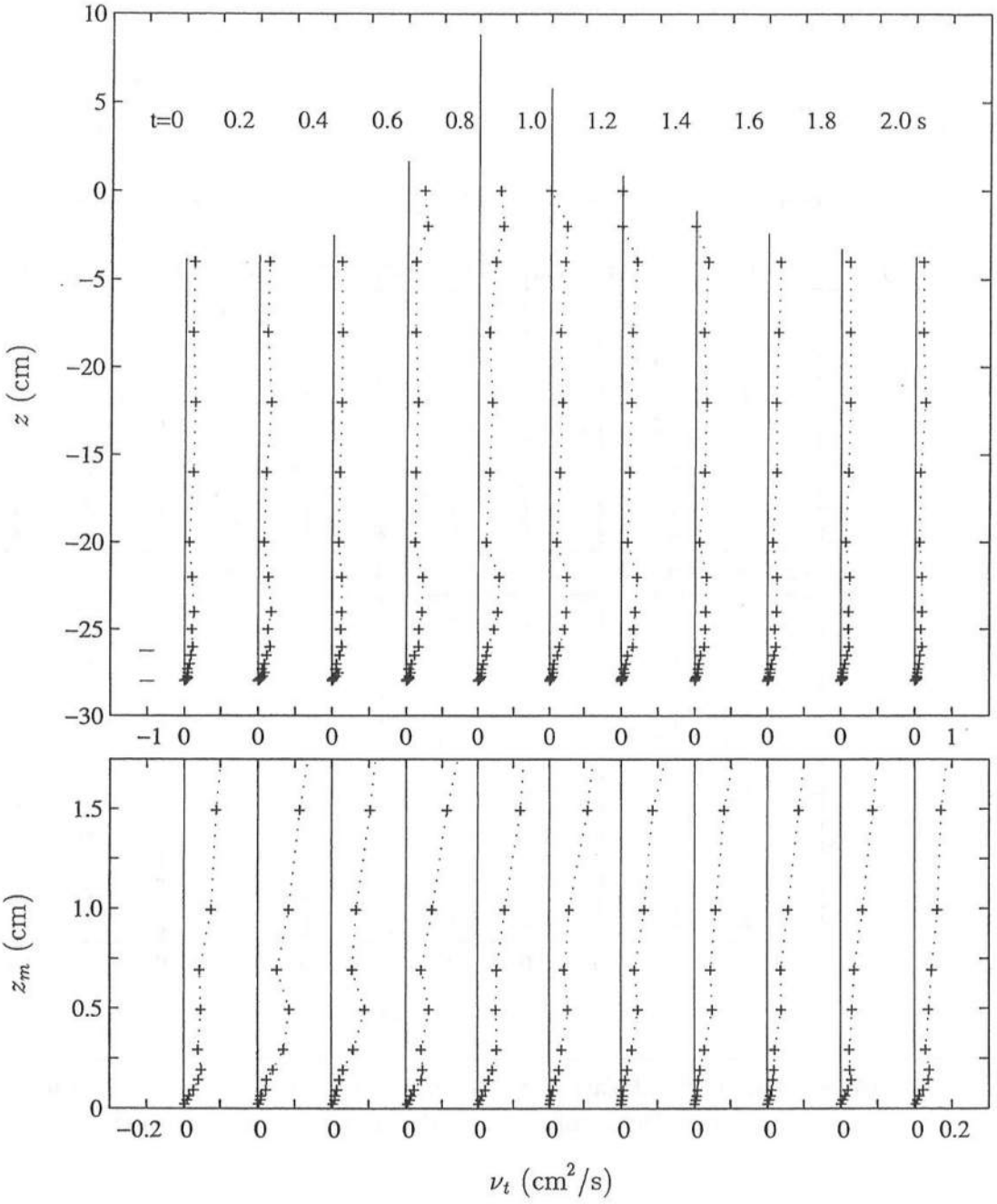

Figure 6.18: Vertical Variations of Eddy Viscosity, ν_t, at 11 Phases for L1 (Top) with Detail of Bottom Boundary Layer (Bottom).

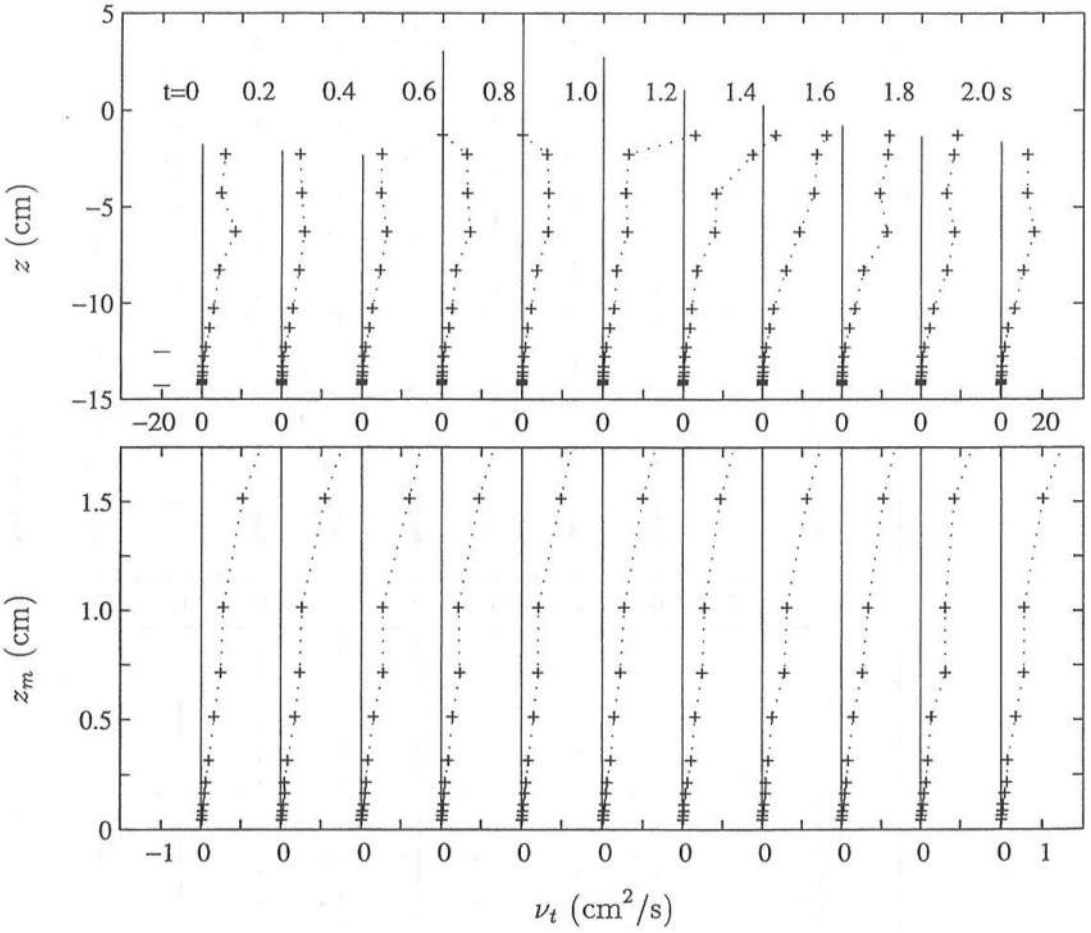

Figure 6.19: Vertical Variations of Eddy Viscosity, ν_t, at 11 Phases for L4 (Top) with Detail of Bottom Boundary Layer (Bottom).

6.5 Assessment of Local Equilibrium of Turbulence Approximation

In this section, the approximation of the local equilibrium of turbulence is assessed using the calibrated coefficients.

Figures 6.20 to 6.25 show the temporal variations of the dissipation term, $C_d^{3/4}(k^{3/2}/\ell)$, and the production term, $(\tau/\rho)(\partial u/\partial z)$, using the calibrated coefficients, C_d and $\overline{C_\ell}$, for L1 to L6. The units for the contours in these figures are $\mathrm{cm}^2/\mathrm{s}^3$. Superposed on these contours is the phase-averaged free surface displacement, η_a, and standard deviation envelope, $\eta_a \pm \sigma_\eta$. It is noted that a smoothing procedure was applied to the contours and is described below.

Figures 6.20 and 6.21 for L1 and L2 show that both the dissipation and production terms are small in the absence of wave breaking. Figures 6.22 for L3 shows that the local equilibrium of turbulence approximation is not valid in the transition region and that the magnitude of the production term under the wave crest is larger than the dissipation term. Figures 6.23 to 6.25 for L4, L5 and L6 show that the production and dissipation terms are roughly of the same magnitude under the wave crest and that the local equilibrium of turbulence approximation may be a reasonable assumption for spilling waves in the inner surf zone.

Smoothing was used for the contour figures in this section since the contour lines of the unsmoothed values were difficult to discern in black and white. Since the temporal resolution was much greater than the vertical resolution, approximately 220 points in t by 20 points in z, the smoothing was applied first by a running average in time and then by an average in both space and time. The first running average was a seven point scheme where the value at a given phase was the average of that value with the three nearest points on each side. This is

expressed as

$$(a_j)_{sm} = \frac{1}{7}(a_{j-3} + a_{j-2} + a_{j-1} + a_j + a_{j+1} + a_{j+2} + a_{j+3}) \tag{6.35}$$

where $(a_j)_{sm}$ is the resulting smoothed value at the jth phase and all of the coefficients on the right-hand-side of Eq 6.35 are unity. The second running average in z and t was similar to Eq 6.35 except that five points were used in two dimensions with weighted coefficients given by

$$\begin{vmatrix} 1 & 1 & 1 & 1 & 1 \\ 1 & 5 & 5 & 5 & 1 \\ 1 & 5 & 13 & 5 & 1 \\ 1 & 5 & 5 & 5 & 1 \\ 1 & 1 & 1 & 1 & 1 \end{vmatrix} \tag{6.36}$$

The effect of this smoothing verses the unsmoothed data can be seen by comparing Figures 6.23 and 6.26. Figure 6.26 shows the temporal variation of the dissipation term $C_d^{3/4}(k^{3/2}/\ell)$ and the production term $(\tau/\rho)(\partial u/\partial z)$ for L4 similar to Figures 6.23 except that Figures 6.26 is plotted without smoothing. For the upper panel of Figures 6.26, the contour lines can be seen easily. For the lower panel, it is difficult to distinguish the contour lines. A comparison of Figures 6.23 and 6.26 indicates that the smoothing procedure retains the essential information of the unsmoothed data. Comparisons between the smoothed and unsmoothed figures for the other measuring lines as well as for the figures discussed below were similar to those of Figures 6.23 and 6.26 and are omitted for brevity.

Figures 6.27 to 6.32 each show the temporal variations of two additional terms of the dimensional equivalent of Eq 6.23 for L1 to L6. The terms shown in the upper and lower panels are

$$w\frac{\partial k}{\partial z} \quad \text{and} \quad \frac{\partial k}{\partial t} \tag{6.37}$$

where the contours are in units of cm^2/s^3. For both the upper and lower panels of Figures 6.27 to 6.32, the two-step smoothing procedure was applied as described above. It is noted that the term $u(\partial k/\partial z)$ in the dimensional equivalent of Eq 6.23 could not be computed for this data set. Also, the diffusion term

$$\frac{\partial}{\partial z}\left(\frac{\nu_t}{\sigma_k}\frac{\partial k}{\partial z}\right) \tag{6.38}$$

was estimated, but the results had large uncertainties, especially for L3 to L6 in the surf zone, due to the two derivatives in z.

The upper panels of Figures 6.27 and 6.28 for L1 and L2 indicate that the magnitude of $w(\partial k/\partial z)$ is small outside the surf zone. The lower panels of these two figures show that there is considerable noise in the $\partial k/\partial t$ term, even outside the surf zone where the turbulent kinetic energy is small. The problem of noise can also be inferred from Figure 4.15 which shows the temporal variations of σ_u^2 and σ_w^2 at the five representative measuring point elevations for L4. The upper panel of Figures 6.29 for L3 in the transition region shows that the advection term $w(\partial k/\partial z)$ under the wave crest is larger than the dissipation term and of the same magnitude as the production term in Figure 6.22.

Comparing the production and dissipation terms in Figure 6.23 with the advection term, $w(\partial k/\partial z)$, in Figure 6.30 for L4 shows that the magnitude of the advection term is less than the production and dissipation terms under the wave crest near trough level for $t \simeq 0.8$ s. The advection term is larger in the middle of the water column with the passing of the wave crest at $t \simeq 1.0$ s. The upper panels of Figures 6.31 and 6.32 for L5 and L6 also show that the advection term may be of the same magnitude as the production and dissipation terms for some of the phases. As a whole, the figures indicate that the local equilibrium of turbulence is a reasonable assumption for spilling waves in the inner surf zone.

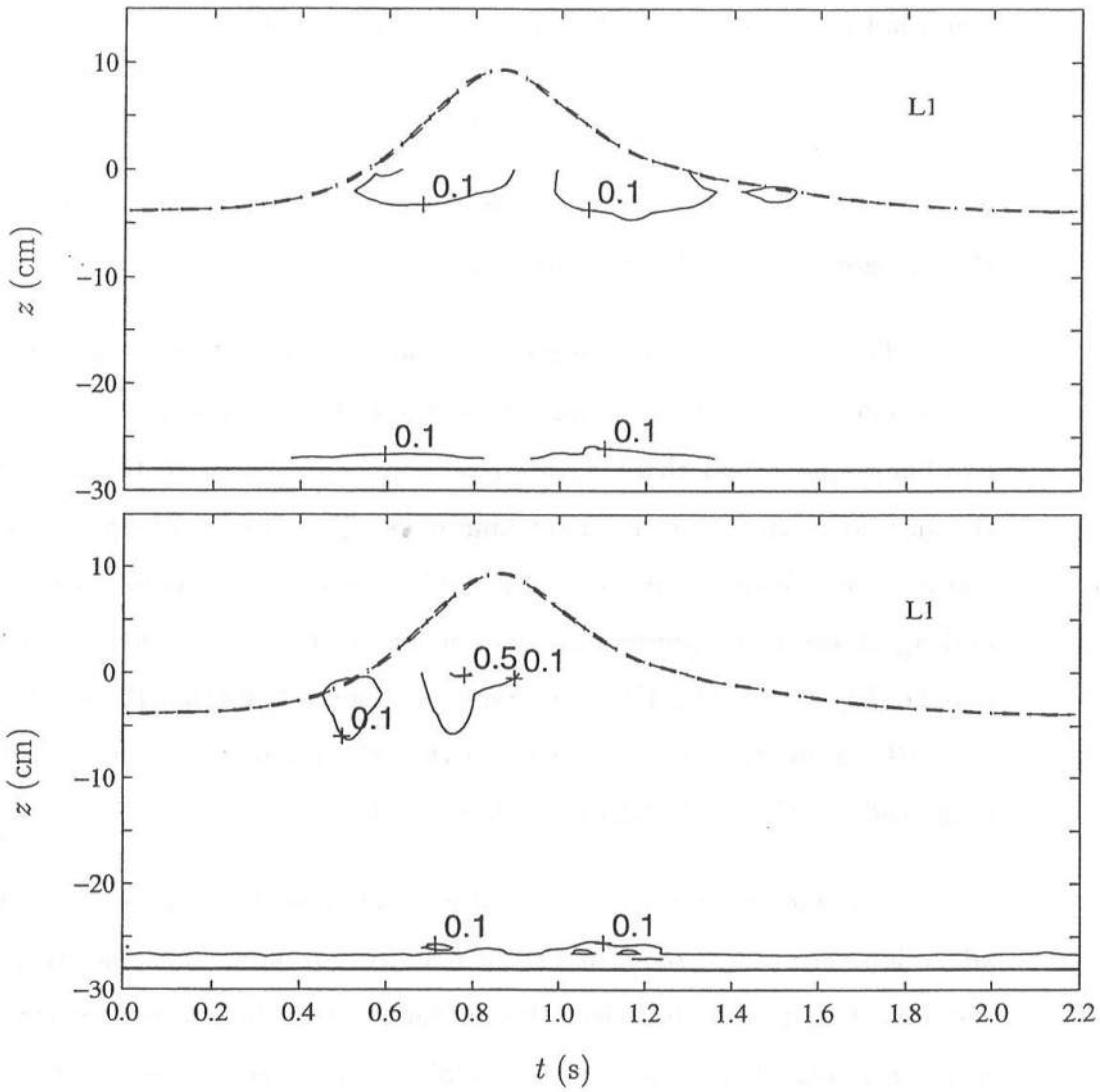

Figure 6.20: Contour Plot of Temporal Variation of Dissipation Term, $C_d^{3/4}(k^{3/2}/\ell)$ (Top) and Production Term, $(\tau/\rho)(\partial u/\partial z)$ (Bottom) using Calibrated C_d and $\overline{C_\ell}$ for L1. Contours in units of $\mathrm{cm}^2/\mathrm{s}^3$. Free Surface Elevation, η_a (– –), Standard Deviation Envelope, $\eta_a \pm \sigma_\eta$ (–·–) and Depth Below SWL, $z = -d$ (——).

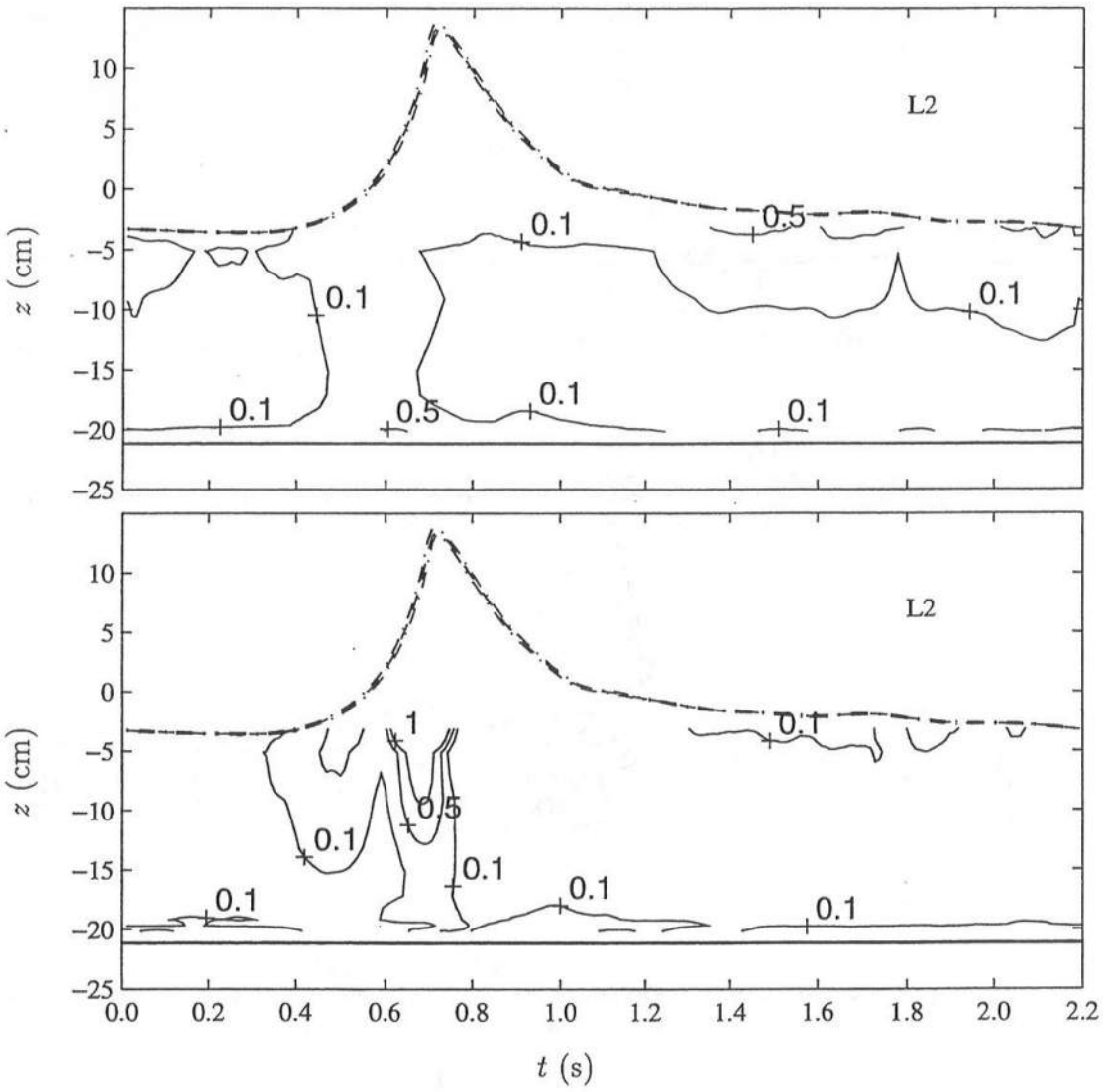

Figure 6.21: Contour Plot of Temporal Variation of Dissipation Term, $C_d^{3/4}(k^{3/2}/\ell)$ (Top) and Production Term, $(\tau/\rho)(\partial u/\partial z)$ (Bottom) using Calibrated C_d and $\overline{C_\ell}$ for L2. Contours in units of $\mathrm{cm}^2/\mathrm{s}^3$. Free Surface Elevation, η_a (– –), Standard Deviation Envelope, $\eta_a \pm \sigma_\eta$ (–·–) and Depth Below SWL, $z = -d$ (——).

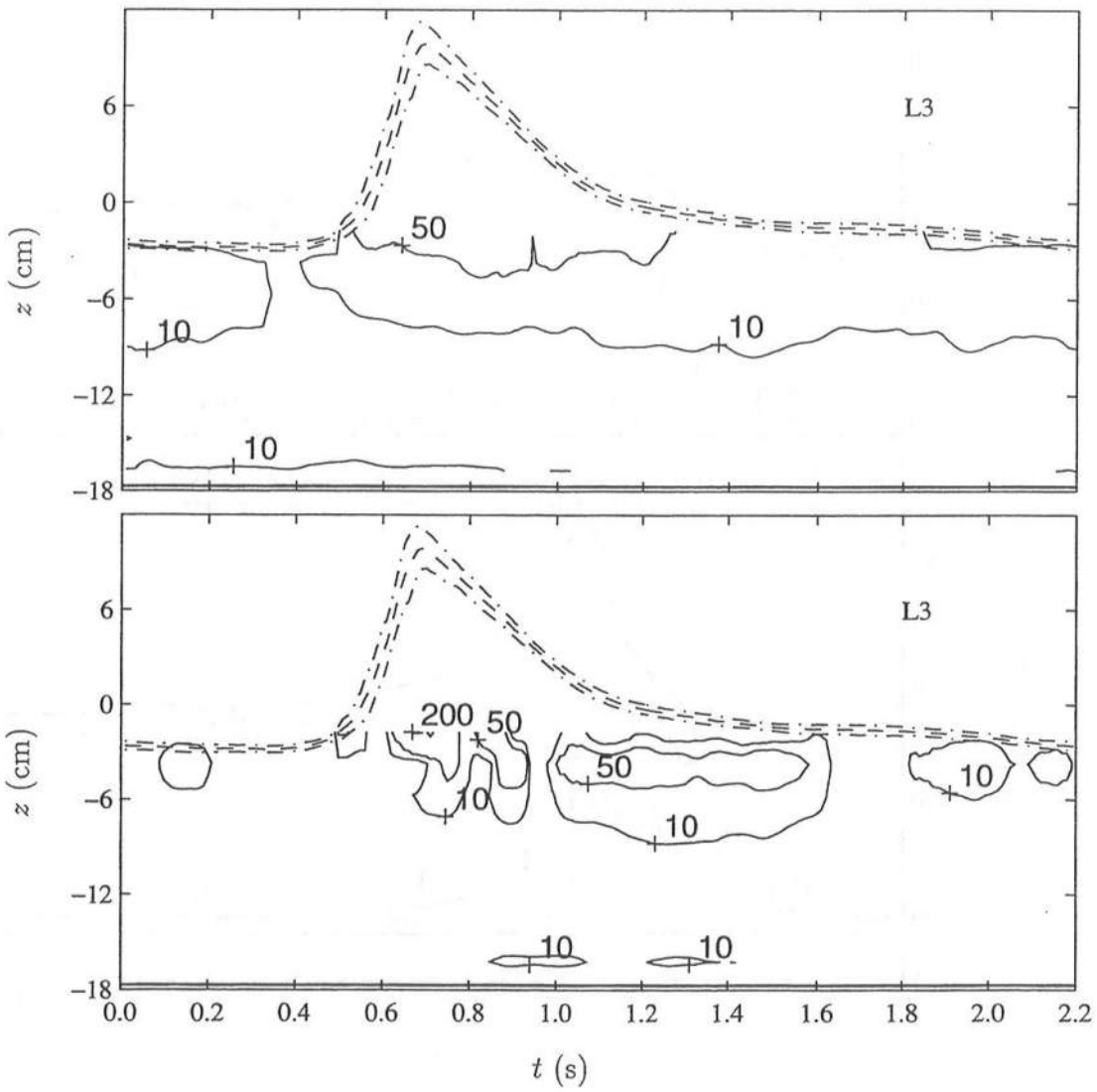

Figure 6.22: Contour Plot of Temporal Variation of Dissipation Term, $C_d^{3/4}(k^{3/2}/\ell)$ (Top) and Production Term, $(\tau/\rho)(\partial u/\partial z)$ (Bottom) using Calibrated C_d and $\overline{C_\ell}$ for L3. Contours in units of $\mathrm{cm}^2/\mathrm{s}^3$. Free Surface Elevation, η_a (– –), Standard Deviation Envelope, $\eta_a \pm \sigma_\eta$ (–·–) and Depth Below SWL, $z = -d$ (——).

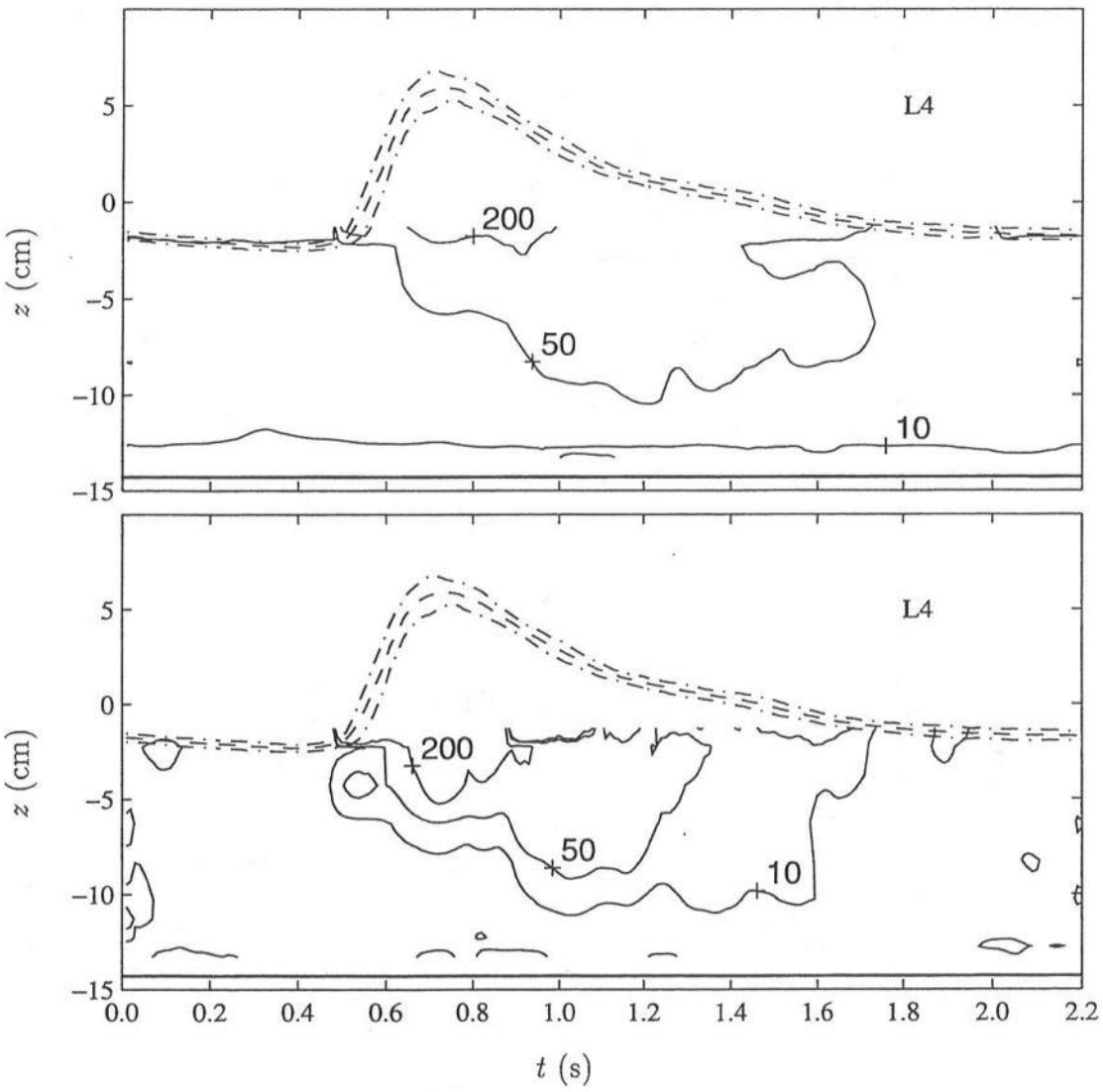

Figure 6.23: Contour Plot of Temporal Variation of Dissipation Term, $C_d^{3/4}(k^{3/2}/\ell)$ (Top) and Production Term, $(\tau/\rho)(\partial u/\partial z)$ (Bottom) using Calibrated C_d and $\overline{C_\ell}$ for L4. Contours in units of $\mathrm{cm}^2/\mathrm{s}^3$. Free Surface Elevation, η_a (– –), Standard Deviation Envelope, $\eta_a \pm \sigma_\eta$ (–·–) and Depth Below SWL, $z = -d$ (——).

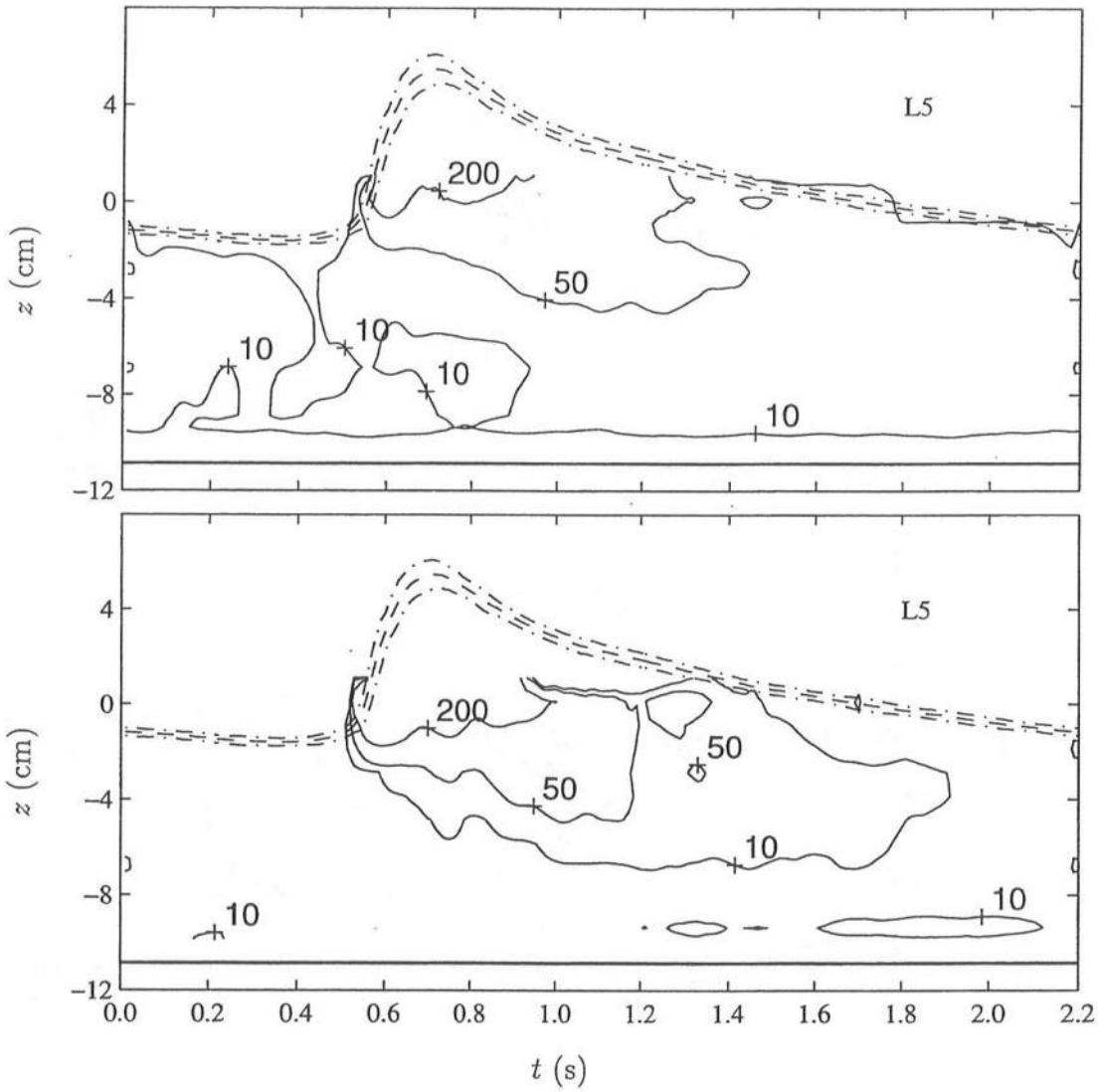

Figure 6.24: Contour Plot of Temporal Variation of Dissipation Term, $C_d^{3/4}(k^{3/2}/\ell)$ (Top) and Production Term, $(\tau/\rho)(\partial u/\partial z)$ (Bottom) using Calibrated C_d and $\overline{C_\ell}$ for L5. Contours in units of $\mathrm{cm}^2/\mathrm{s}^3$. Free Surface Elevation, η_a (– –), Standard Deviation Envelope, $\eta_a \pm \sigma_\eta$ (–·–) and Depth Below SWL, $z = -d$ (——).

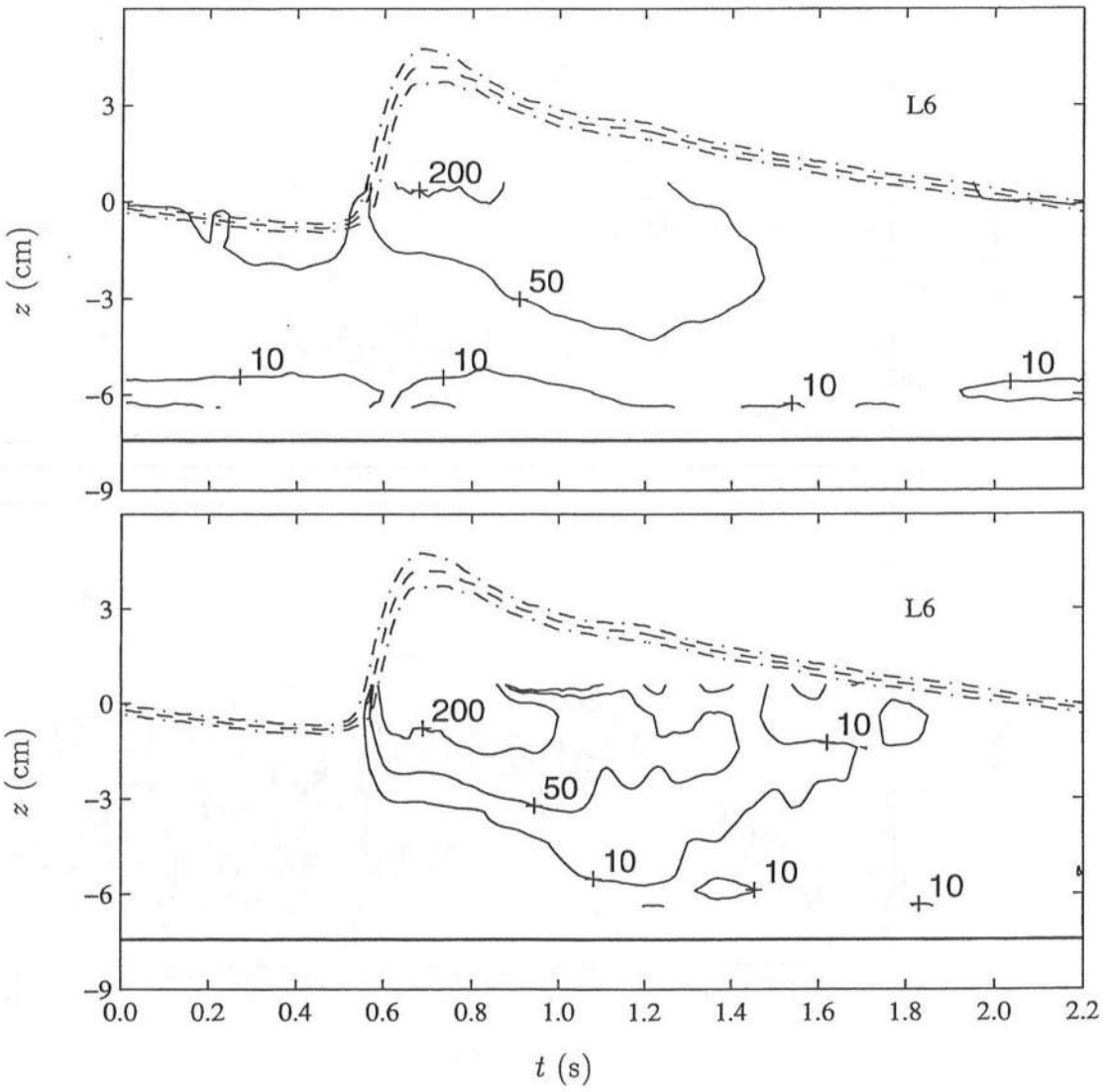

Figure 6.25: Contour Plot of Temporal Variation of Dissipation Term, $C_d^{3/4}(k^{3/2}/\ell)$ (Top) and Production Term, $(\tau/\rho)(\partial u/\partial z)$ (Bottom) using Calibrated C_d and $\overline{C_\ell}$ for L6. Contours in units of $\mathrm{cm}^2/\mathrm{s}^3$. Free Surface Elevation, η_a (– –), Standard Deviation Envelope, $\eta_a \pm \sigma_\eta$ (–·–) and Depth Below SWL, $z = -d$ (——).

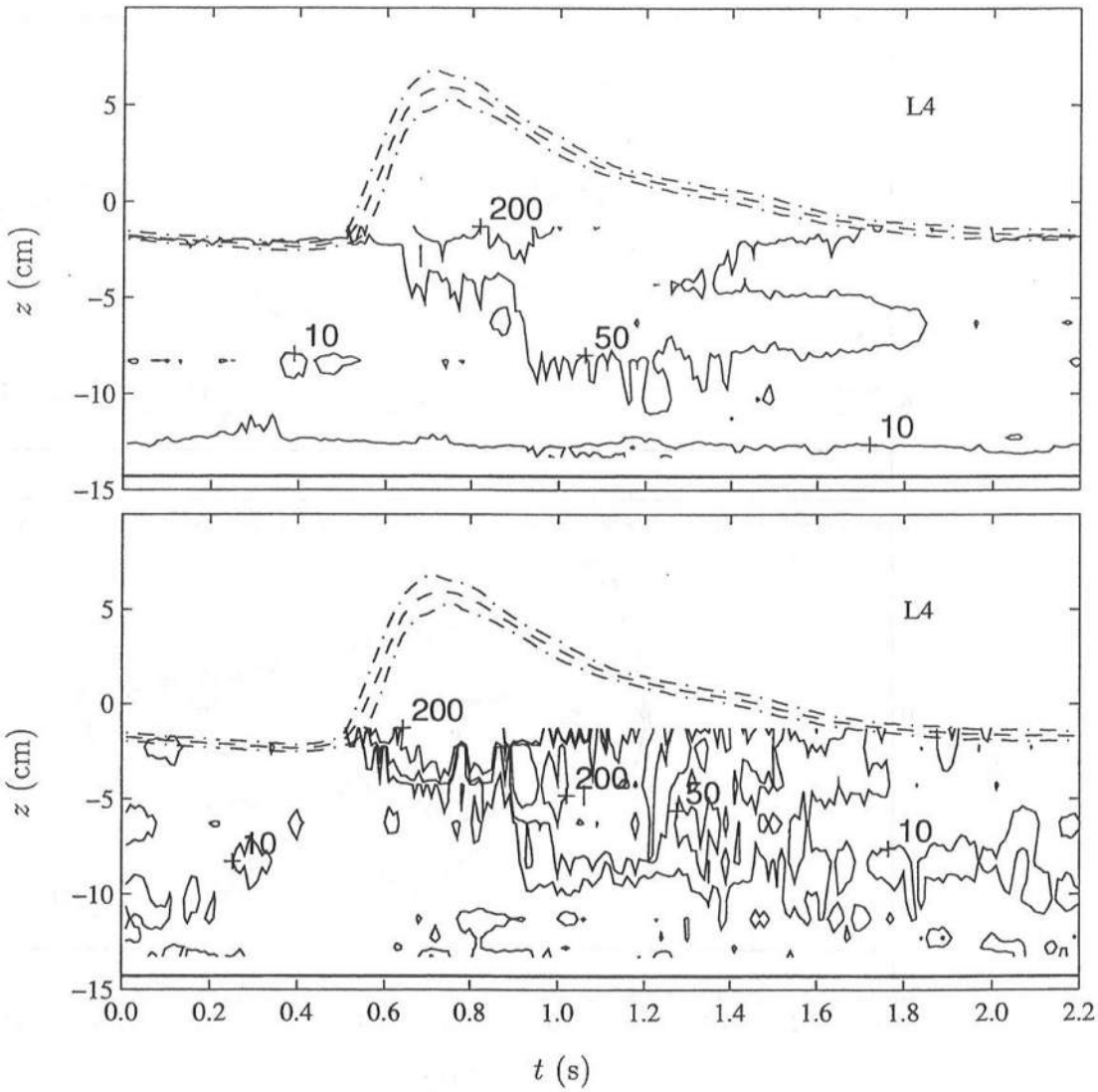

Figure 6.26: Contour Plot of Temporal Variation of Dissipation Term, $C_d^{3/4}(k^{3/2}/\ell)$ (Top) and Production Term, $(\tau/\rho)(\partial u/\partial z)$ (Bottom) using Calibrated C_d and $\overline{C_\ell}$ for L6. Without Smoothing. Contours in units of $\mathrm{cm}^2/\mathrm{s}^3$. Free Surface Elevation, η_a (– –), Standard Deviation Envelope, $\eta_a \pm \sigma_\eta$ (–·–) and Depth Below SWL, $z = -d$ (——).

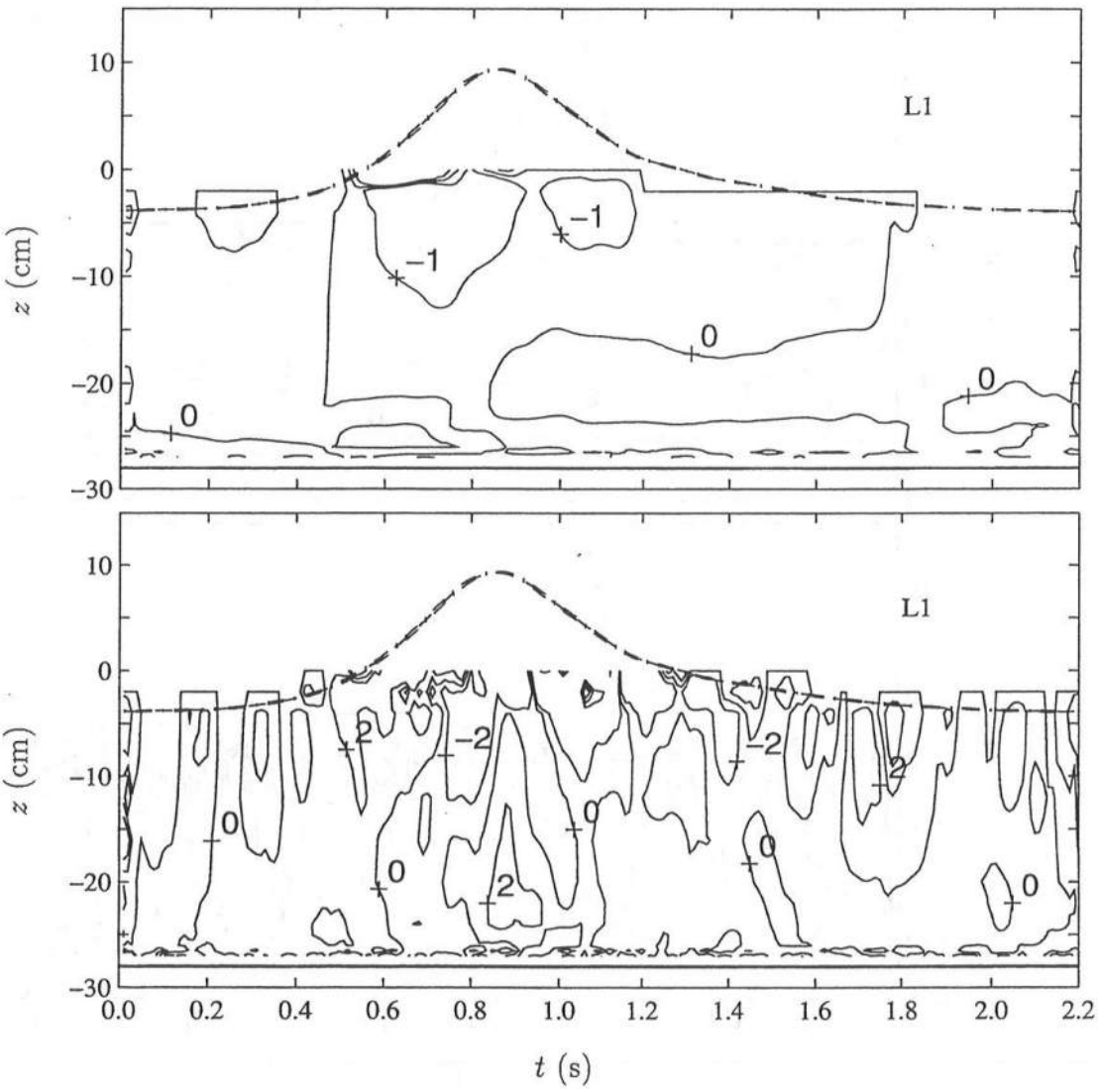

Figure 6.27: Contour Plot of Temporal Variation of $w(\partial k/\partial z)$ (Top) and $\partial k/\partial t$ (Bottom) with η_a (– –) and $\eta_a \pm \sigma_\eta$ (–·–) for L1. Contours in units of $\mathrm{cm}^2/\mathrm{s}^3$.

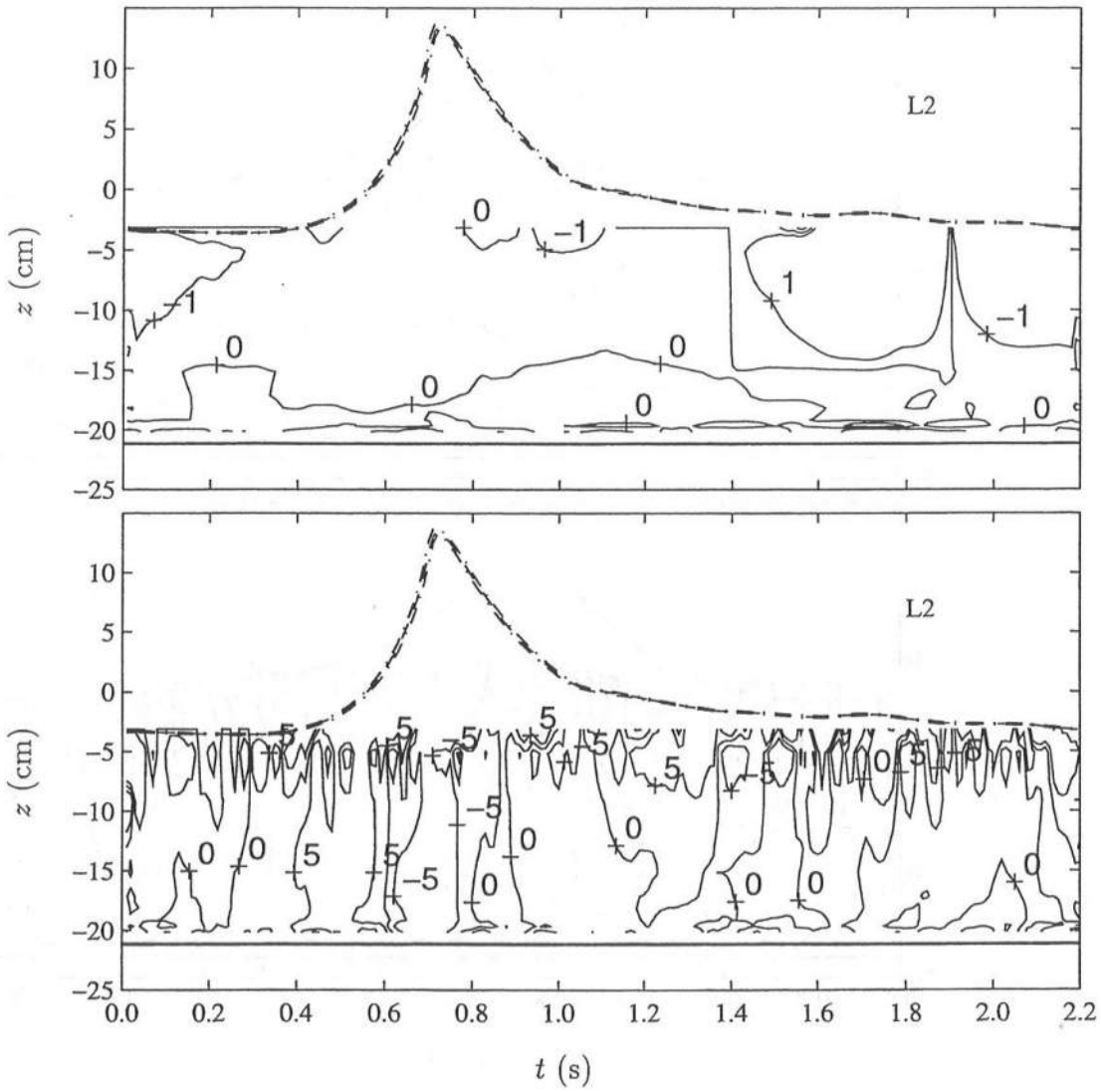

Figure 6.28: Contour Plot of Temporal Variation of $w(\partial k/\partial z)$ (Top) and $\partial k/\partial t$ (Bottom) with η_a (– –) and $\eta_a \pm \sigma_\eta$ (–·–) for L2. Contours in units of $\mathrm{cm}^2/\mathrm{s}^3$.

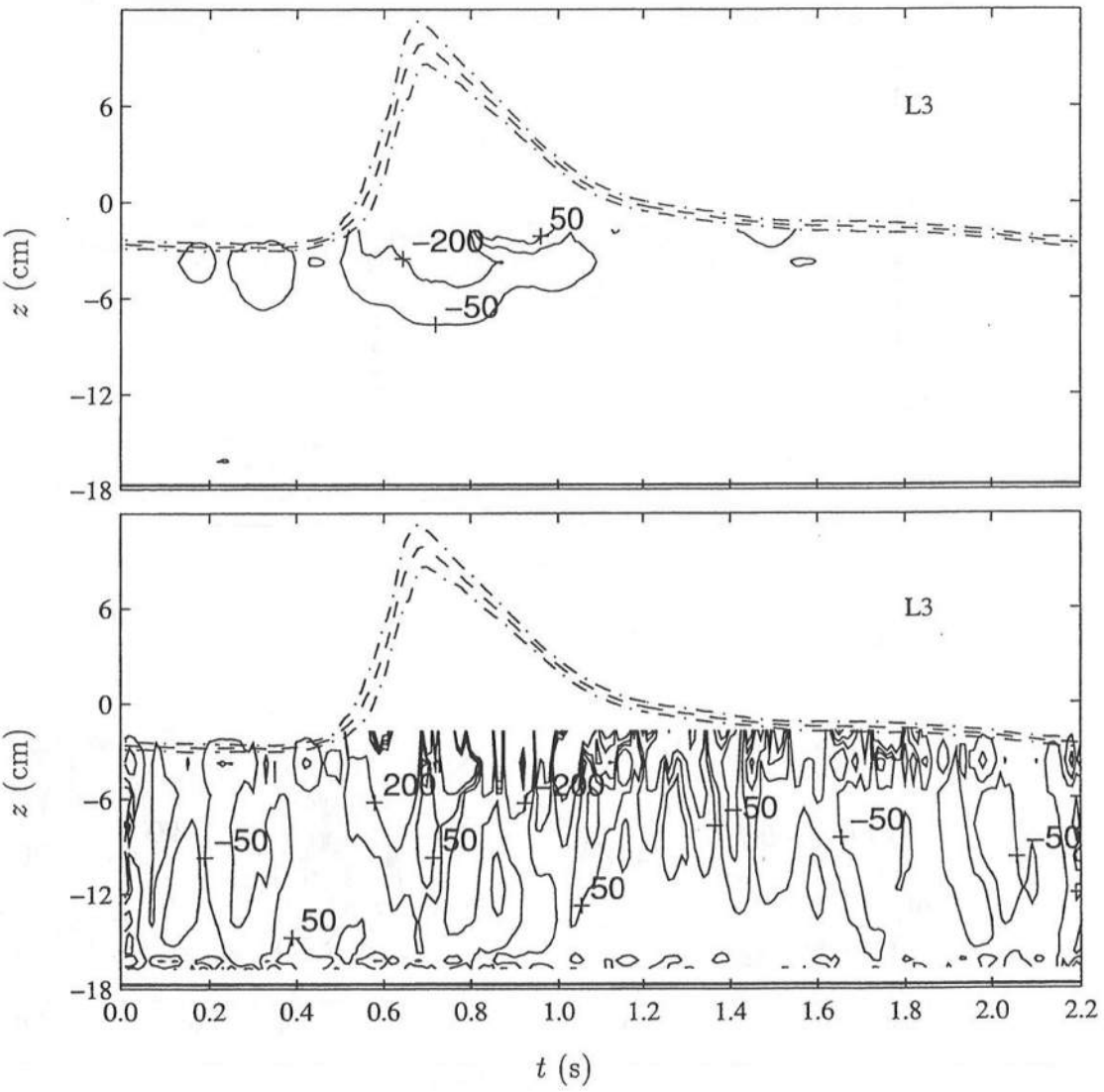

Figure 6.29: Contour Plot of Temporal Variation of $w(\partial k/\partial z)$ (Top) and $\partial k/\partial t$ (Bottom) with η_a (– –) and $\eta_a \pm \sigma_\eta$ (–·–) for L3. Contours in units of $\mathrm{cm}^2/\mathrm{s}^3$.

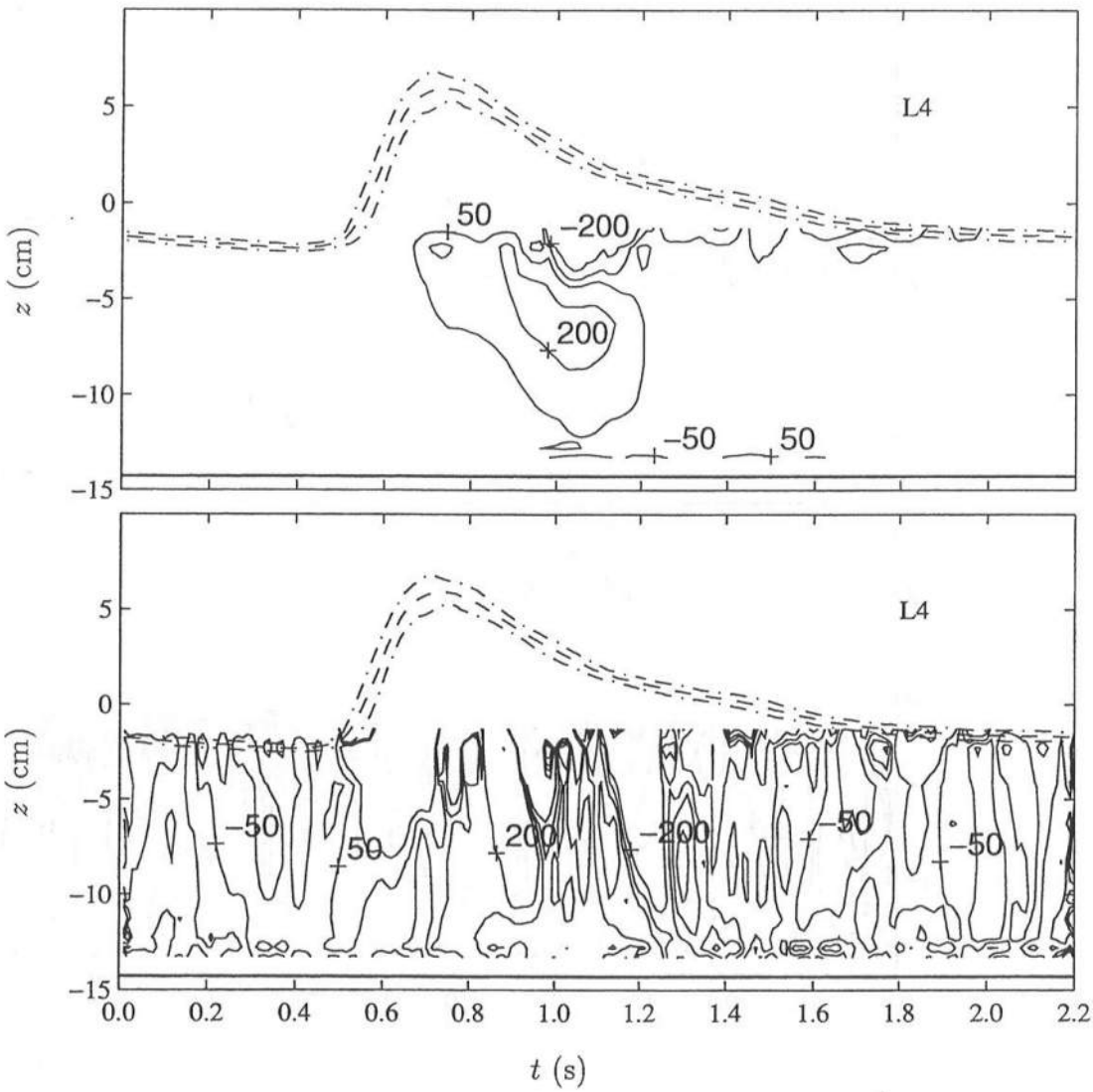

Figure 6.30: Contour Plot of Temporal Variation of $w(\partial k/\partial z)$ (Top) and $\partial k/\partial t$ (Bottom) with η_a (– –) and $\eta_a \pm \sigma_\eta$ (–·–) for L4. Contours in units of $\mathrm{cm}^2/\mathrm{s}^3$.

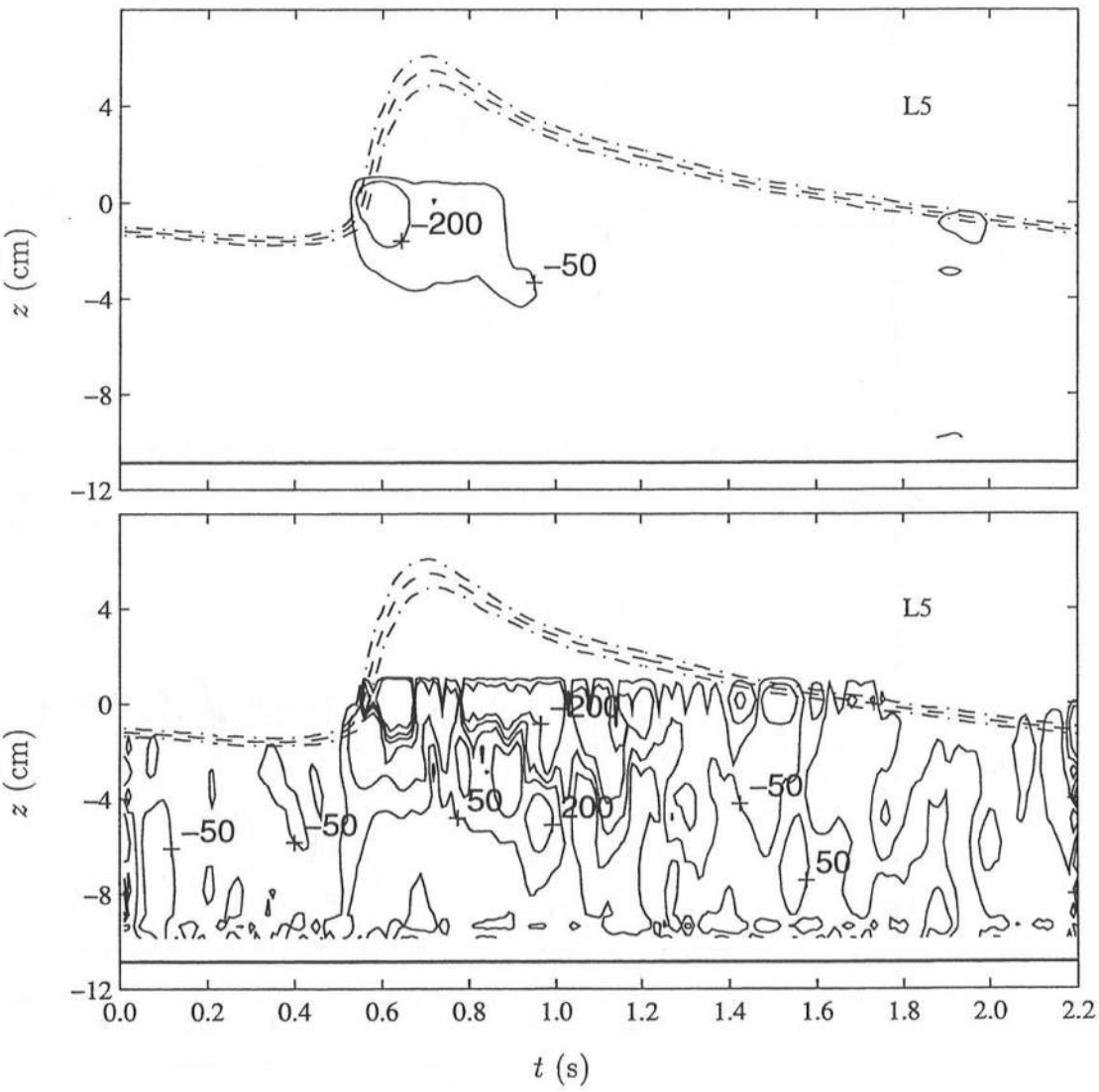

Figure 6.31: Contour Plot of Temporal Variation of $w(\partial k/\partial z)$ (Top) and $\partial k/\partial t$ (Bottom) with η_a (– –) and $\eta_a \pm \sigma_\eta$ (–·–) for L5. Contours in units of $\mathrm{cm}^2/\mathrm{s}^3$.

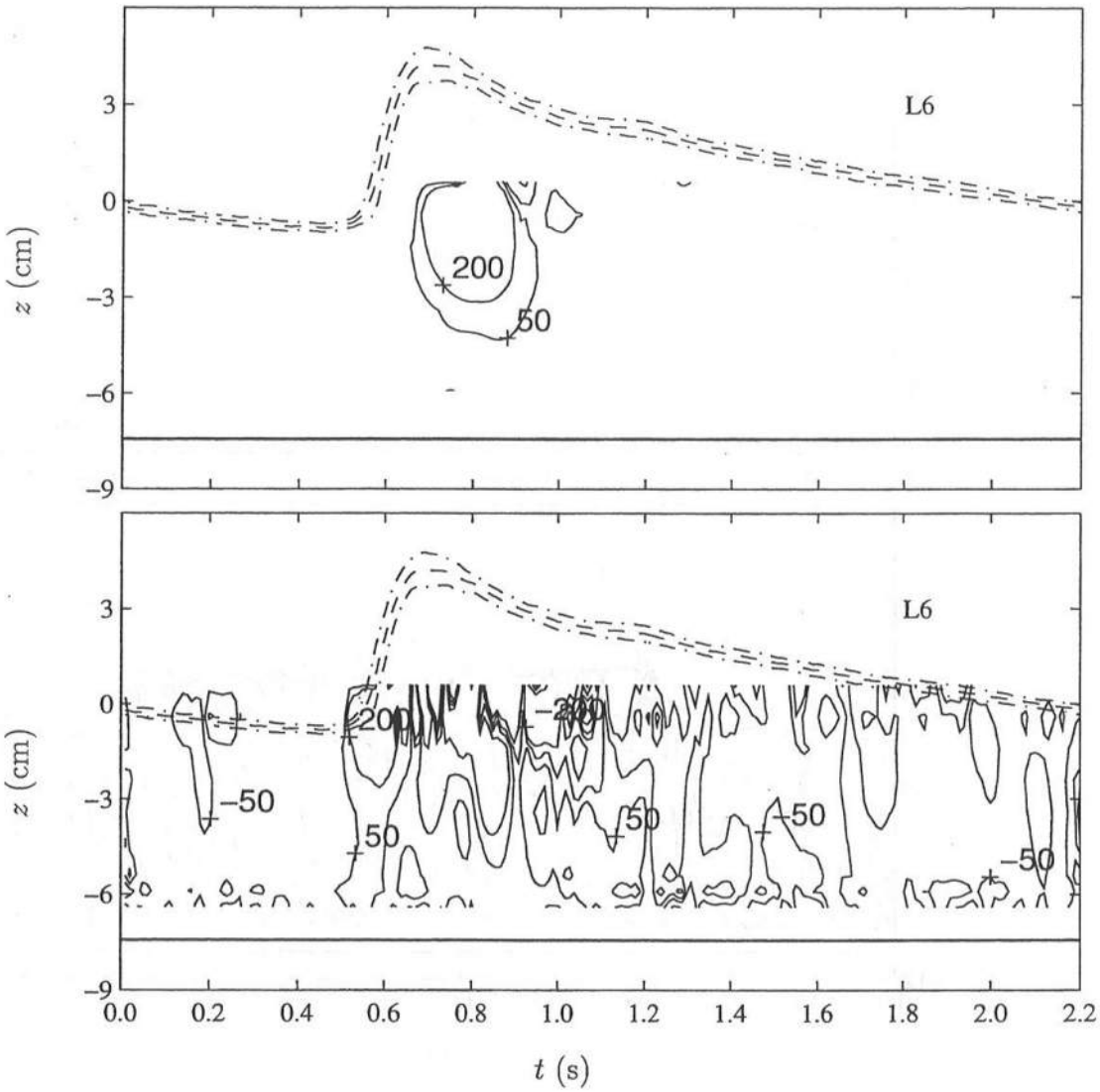

Figure 6.32: Contour Plot of Temporal Variation of $w(\partial k/\partial z)$ (Top) and $\partial k/\partial t$ (Bottom) with η_a (– –) and $\eta_a \pm \sigma_\eta$ (–·–) for L6. Contours in units of $\mathrm{cm}^2/\mathrm{s}^3$.

Chapter 7

COMPARISONS WITH ONE-DIMENSIONAL MODEL

In this chapter, comparisons are made at the six measuring lines between the measured and computed free surface elevations, between the measured horizontal velocity profile and the computed depth-averaged horizontal velocity, and between the measured vertical velocity and the vertical velocity estimated from the computed horizontal velocity gradient together with the continuity equation. This chapter is organized as follows. Section 7.1 briefly describes the one-dimensional numerical model. Section 7.2 gives the input specifications and methodology for the comparisons. Section 7.3 discusses the transitional effects due to the initial condition of no wave action in the numerical model. Section 7.4 compares the phase-averaged free surface elevations and standard deviations. Section 7.5 compares the horizontal and vertical velocities. Section 7.6 compares the measured bottom shear stress from Chapter 5 with the shear stress estimated from the computed depth-averaged horizontal velocity. Section 7.7 summarizes this chapter.

7.1 Description of One-Dimensional Numerical Model

The one-dimensional numerical model, discussed in Chapter 2, is summarized in this section. Kobayashi *et al.* (1989) developed a numerical model based on the shallow water wave equations including the effects of bottom friction. This

is probably the simplest one-dimensional, time-dependent model for predicting the nonlinear wave characteristics in the surf and swash zones in a unified manner. Kobayashi and Wurjanto (1992) showed that their extended model could predict available field data on shoreline oscillations fairly well, provided that the incident wave train including the low frequency motion is known. Cox *et al.* (1994b) modified the seaward boundary to allow input of the measured free surface, eliminating the uncertainty associated with the separation of incident and reflected waves using linear theory. They compared the computed free surface oscillations with laboratory measurements of prototype scale in the surf and swash zone and found good agreement. Further, they highlighted the importance of time-domain models over conventional time-averaged models in estimating the swash zone dynamics for predictive sediment transport models.

The two-dimensional coordinate system is defined as follows: x is the horizontal coordinate, positive landward with $x = 0$ at the seaward boundary (SB) of the computational domain; z is the vertical coordinate, positive upward with $z = 0$ at the still water level (SWL). The instantaneous free surface is located at $z = \eta$, and the instantaneous depth is denoted by h. The seabed is located at $z = \eta - h$, and the local angle of the bed slope is θ. Assuming the vertical pressure distribution to be approximately hydrostatic, the governing equations for mass and x-momentum integrated from the fixed seabed to the free surface may be expressed as (Kobayashi *et al.* 1989)

$$\frac{\partial h}{\partial t} + \frac{\partial}{\partial x}(hU) = 0 \tag{7.1}$$

$$\frac{\partial}{\partial t}(hU) + \frac{\partial}{\partial x}(hU^2) = -gh\frac{\partial \eta}{\partial x} - \frac{\tau_b}{\rho} \tag{7.2}$$

where t is time, U is the depth-averaged horizontal velocity, τ_b is the bottom shear stress, ρ is the fluid density which is assumed constant, and g is the gravitational

acceleration. The bottom shear stress may be expressed as

$$\tau_b = \frac{1}{2}\rho f |U| U \tag{7.3}$$

where f is the constant bottom friction factor. The following dimensionless variables are introduced:

$$t' = \frac{t}{T_r} \; ; \; x' = \frac{x}{T_r\sqrt{gH_r}} \; ; \; U' = \frac{U}{\sqrt{gH_r}} \; ; \; z' = \frac{z}{H_r} \; ; \; \eta' = \frac{\eta}{H_r} \tag{7.4}$$

$$\theta' = (2\pi)^{1/2}\xi \; ; \; \xi = \frac{\sigma \tan\theta}{(2\pi)^{1/2}} \; ; \; f' = \frac{1}{2}\sigma f \; ; \; \sigma = \frac{T_r\sqrt{gH_r}}{H_r} \tag{7.5}$$

where T_r and H_r are the reference wave period and wave height, θ' is the normalized gradient of the slope, ξ is the surf similarity parameter for the uniform slope considered hereafter, f' is the normalized friction factor, and σ is the ratio of the horizontal and vertical length scales where $\sigma^2 >> 1$ is assumed in the model. Primes indicate dimensionless variables.

Substitution of (7.4) and (7.5) into (7.1) and (7.2) yields

$$\frac{\partial h'}{\partial t'} + \frac{\partial}{\partial x'}(h'U') = 0 \tag{7.6}$$

$$\frac{\partial}{\partial t'}(h'U') + \frac{\partial}{\partial x'}(h'U'^2 + \frac{1}{2}h'^2) = -\theta' h' - f' |U'| U' \tag{7.7}$$

which are solved numerically in the time domain to obtain the variations of h' and U' with respect to t' and x' for given θ', f', and initial and boundary conditions. For the computations, the computer program RBREAK2 (Kobayashi and Poff 1994) is used which incorporated the modification of the seaward boundary condition (Cox *et al.* 1994b).

7.2 Input Specifications and Reflected Waves

Six cases were used to evaluate the capabilities and limitations of the numerical model. Three options were of interest: specification of the bottom friction

factor, the location of the seaward boundary, and the specification of the input time series at the seaward boundary. Two values of the friction factor were used. For Cases 1, 2, 3 and 4, $f = 0.015$ which corresponds to the calibration of the numerical model with runup data on a gently sloping natural beach (Raubenheimer *et al.* 1995). For Cases 5 and 6, $f = 0.05$ which corresponds to previous comparisons with laboratory data (e.g., Cox *et al.* 1994b). Two locations were used for the seaward boundary. For Cases 1, 2 and 5, the seaward boundary was at L1 which was seaward of the break point. For Cases 3, 4, and 6, the seaward boundary was at L3 which was well inside the surf zone. Last, two conditions were used on the seaward boundary which is denoted by IWAVE following Kobayashi and Poff (1994). For Cases 1 and 3, IWAVE=2 which indicates that the incident wave train was specified as the input time series. For Cases 2, 4, 5 and 6, IWAVE=3 which indicates that the total free surface oscillation, i.e., incident plus reflected wave trains, was specified as the input time series. It is noted that the input time series corresponds to the measured free surface oscillations. These six cases are listed in Table 7.1 where SB denotes the location of the seaward boundary, IWAVE is the condition of the input time series at the seaward boundary, H_r is the reference wave height, and T_r is the reference wave period.

Table 7.1: Six Cases for Three Computational Options.

Case	f	SB	IWAVE	H_r (cm)	T_r (s)
1	0.015	L1	2	13.22	2.2
2	0.015	L1	3	13.22	2.2
3	0.015	L3	2	12.71	2.2
4	0.015	L3	3	12.71	2.2
5	0.050	L1	3	13.22	2.2
6	0.050	L3	3	12.71	2.2

Figures 7.1 and 7.2 show the temporal variation of the input time series

at L1 for Cases 1, 2 and 5, and at L3 for Cases 3, 4 and 6, respectively. The time axis is normalized by the reference wave period, $T_r = 2.2$ s, to indicate that the number of waves for the computations was 300. These input time series were constructed from the measured free surface elevations by repeating the measured time series containing 50 waves six times to give a total of 300 waves. The computed free surface elevations and depth-averaged velocity were stored at the nodes corresponding to the wave gage locations for direct comparison with the measurements. In addition, the depth-averaged velocity was stored at the two adjacent nodes at each wave gage so that the vertical velocity could be computed by the continuity equation as described later. The storage rate of the computations was consistent with the 100 Hz sampling rate of the data. The runup time series and other statistics were also stored for each case. To eliminate the transitional effects associated with the start of the model based on the initial condition of zero wave action in the computation domain, the computation was started at time $t' = -250$, and the stored time series were truncated for $-250 < t' < 0$. The remaining 50 waves were phase-averaged for comparison with the measurements in the same way as the data analyses in Chapter 4.

The input time series shown in Figures 7.1 and 7.2 are made from the measured free surfaces elevations at L1 and L3 and include both the incident and reflected wave trains. For Cases 1 and 3, however, the seaward boundary condition was IWAVE=2 which assumes that only the *incident* time series is specified. For these cases, it was assumed that the reflection from the 1:35 slope was small so that the total (measured) time series was approximately the same as the assumed incident time series. Hence, the same time series were used for IWAVE=2 and IWAVE=3, and no attempt was made to separate the incident and reflected waves from the measured time series (e.g., Cox 1989) since the error of the separation method was likely to be about the same order of magnitude as the reflection

coefficient. The computed reflected time series is discussed at the end of this section. It is noted that the entire input time series are shown in Figures 7.1 and 7.2 and that to plot each data point is beyond the resolution of most laser printers. Hence, Figures 7.1 and 7.2 may appear non-periodic over 50 waves. Nevertheless, Figure 7.1 shows that there is almost no variation in the wave crests of the input wave trains seaward of the break point; and Figure 7.2 shows that there is considerable variation in the wave crests of the input wave trains due to wave breaking.

The input and output quantities of the numerical model are typically normalized quantities, but the comparisons with the measurements are dimensional to be consistent with the previous chapters. For Cases 1, 2 and 5 with the seaward boundary at L1, the reference wave height was $H_r = 13.22$ cm. For Cases 3, 4 and 6, with the seaward boundary at L3, the reference wave height was $H_r = 12.71$ cm, as listed in Table 7.1 in this section. The cross-shore variation of the measured wave heights were listed in Table 4.1.

Comparisons are made with the vertical velocity estimated from the computed depth-averaged horizontal velocity, U, with the continuity equation

$$\frac{\partial w}{\partial z} + \frac{\partial u}{\partial x} = 0, \tag{7.8}$$

where u and w are the depth-varying horizontal and vertical velocities. Assuming that

$$\frac{\partial u}{\partial x} \simeq \frac{\partial U}{\partial x}, \tag{7.9}$$

the approximate vertical velocity is estimated using Eq 7.8

$$W = -\int_0^{z_m} \frac{\partial U}{\partial x} dz \; = \; -\frac{\partial U}{\partial x} z_m, \tag{7.10}$$

in which z_m is the distance from the bottom where $w = 0$ due to the no-slip boundary condition. The notation W is used to indicate the vertical velocity

calculated from the depth-averaged velocity U which is independent of z. The horizontal derivative in Eq 7.10 is approximated by a 3-point, central difference of the computed velocities stored at the adjacent nodes as follows

$$\frac{\partial U}{\partial x} \simeq \frac{1}{2\Delta x}\left(A\,U_{i-1} + B\,U_i + C\,U_{i+1}\right) \tag{7.11}$$

where the subscript i indicates the node corresponding the wave gage position; $A = -1$, $B = 0$, and $C = 1$ are constants; and $\Delta x = 4.00$ cm is the constant node spacing used in the computations. The estimated derivative using Eq 7.11 has a truncation error of $O(\Delta x^2)$ (Fletcher 1991). At the seaward boundary, Eq 7.11 is not applicable; and the derivative is approximated by a 3-point, one-sided difference given by

$$\frac{\partial U}{\partial x} \simeq \frac{1}{2\Delta x}\left(A\,U_1 + B\,U_2 + C\,U_3\right) \tag{7.12}$$

where the subscript $i = 1$ is the first node at the seaward boundary, and $A = -3$, $B = 4$, and $C = -1$ are constants. The estimated derivative using Eq 7.12 has a truncation error of $O(\Delta x^2)$ (Fletcher 1991). It is noted that there is no smoothing of the derivatives estimated by Eqs 7.11 and 7.12 in the computation of Eq 7.10.

Table 7.2 lists the computed reflection coefficient for the six cases. The reflection coefficient, r, is defined for regular waves as (e.g., Kobayashi and Poff 1994)

$$r = \frac{[\eta_{m,refl}]_{max} - [\eta_{m,refl}]_{min}}{H_r} \tag{7.13}$$

where $[\eta_{m,refl}]_{max}$ and $[\eta_{m,refl}]_{min}$ are the maximum and minimum values of the dimensional reflected wave time series at the seaward boundary and H_r is the reference wave height at the seaward boundary. Table 7.2 indicates that the reflection is small for Cases 1, 2, and 5. The computed reflection coefficient for Cases 3, 4, and 6 with the seaward boundary at L3 are larger because the superposition of incident and reflected waves assumed in the numerical model

may be less accurate inside the surf zone. A rigorous assessment of the capability of this numerical model in predicting the reflected time series is beyond the scope of this dissertation.

Table 7.2: Computed Reflection Coefficient for Six Cases.

Case	r
1	0.014
2	0.015
3	0.034
4	0.051
5	0.013
6	0.026

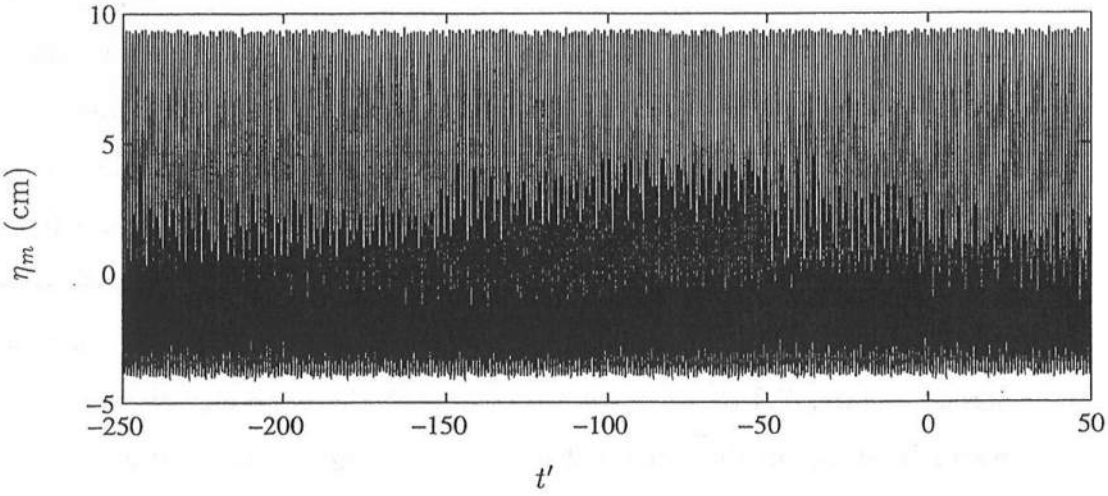

Figure 7.1: Input Time Series at L1 for Cases 1, 2, and 5.

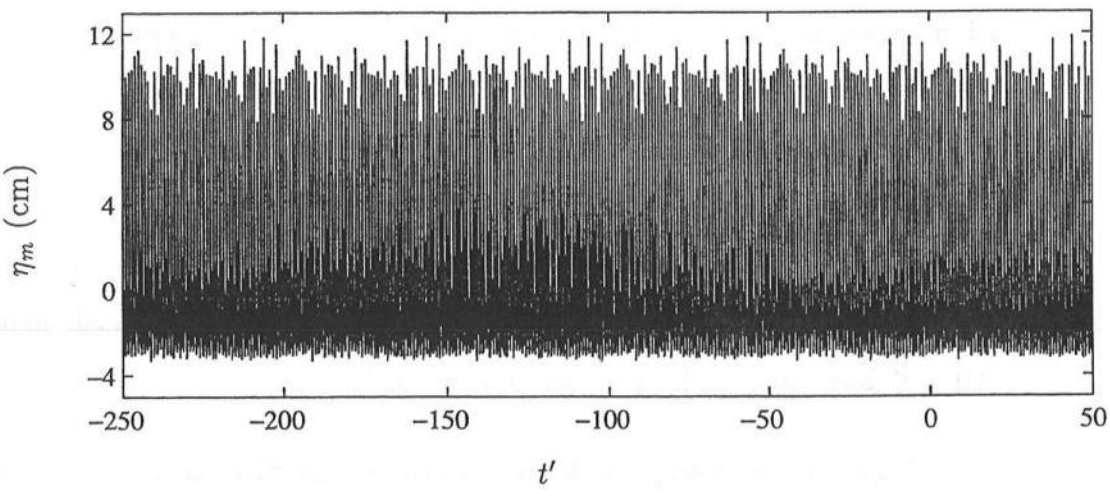

Figure 7.2: Input Time Series at L3 for Cases 3, 4, and 6.

7.3 Transitional Effects

Although the runup was not measured in this experiment, the computed runup elevations above the SWL, Z_c, are plotted in this section to illustrate the transitional effects on the computed time series. Since the slope is mild, the the transitional effects are amplified in the runup time series. Also, the model's sensitivity to the input options, i.e., the friction factor, irregularities in the input signal due to the location of the seaward boundary, and the specification of the seaward boundary condition can be assessed qualitatively using the runup time series. Figures 7.3 to 7.8 show the computed shoreline elevations above the still water level, Z_c, in the range $-250 < t' < 50$, where $t' = -250$ is the start of the computation, for Cases 1 to 6. It is noted that the computed runup is defined at the location of the instantaneous water depth $\delta_r = 5.0$ mm where δ_r is the physical water depth related to the height of a wire runup meter to measure the water line oscillations on a slope (e.g, Cox 1989).

Figure 7.3 for Case 1 with IWAVE=2 shows that the duration of the transition region is short, approximately $-250 < t' < -200$. The variation of the runup crests for $-200 < t'$ is about 2% of the incident wave height, and the variation of the maximum runup to minimum rundown height (termed swash height hereafter) is approximately 5% of the incident wave height. Figure 7.4 for Case 2 with IWAVE=3 shows a much longer transition region, approximately $-250 < t' < -50$. The variation of the runup crests and swash heights for $-50 < t'$, however, is about the same as Case 1.

Figure 7.5 for Case 3 with the seaward boundary at L3 inside the surf zone shows a much larger variability in the runup crests due to the larger variation in the input time series. The transition region is approximately $-250 < t' < -200$, similar to Case 1. There is a much higher variation in the runup crest, about 12%

of the incident wave height. Figure 7.6 for Case 4 also with the seaward boundary at L3 but with IWAVE=3 shows a transition region of about $-250 < t' < -150$. There is also a large variation in the runup crests, about 17% of the incident wave height.

Figure 7.7 for Case 5 with $f = 0.05$ shows the effect of increasing the friction factor when compared to Figure 7.4 for Case 2. Figure 7.7 shows that the transition region is substantially reduced by the increase in the friction factor and that the variation of the runup crest is somewhat reduced. Figure 7.8 for Case 6 with $f = 0.05$ and the seaward boundary at L3 shows the same effect of increasing the friction factor when compared to Figure 7.6 for Case 4.

It is noted that the runup is more sensitive to the effects of the input options, particularly the friction factor. The differences between the measured and computed free surface elevations at the six measuring lines is less as will be shown in Section 7.4. From this section it is concluded that truncating the computed time series for $-250 < t' < 0$ eliminates the transitional effects on the computed time series for the six cases considered.

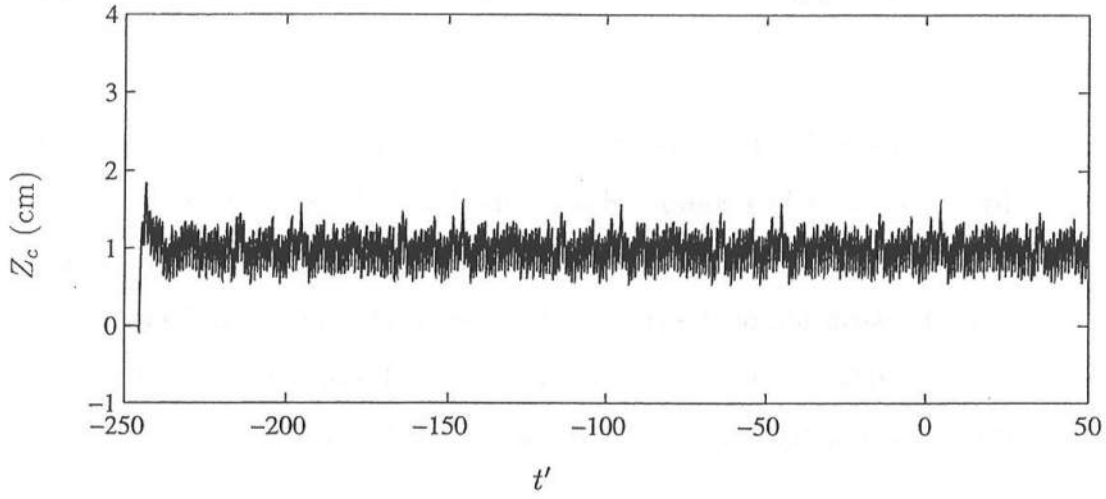

Figure 7.3: Runup Time Series for Case 1: $f = 0.015$, SB at L1, IWAVE=2.

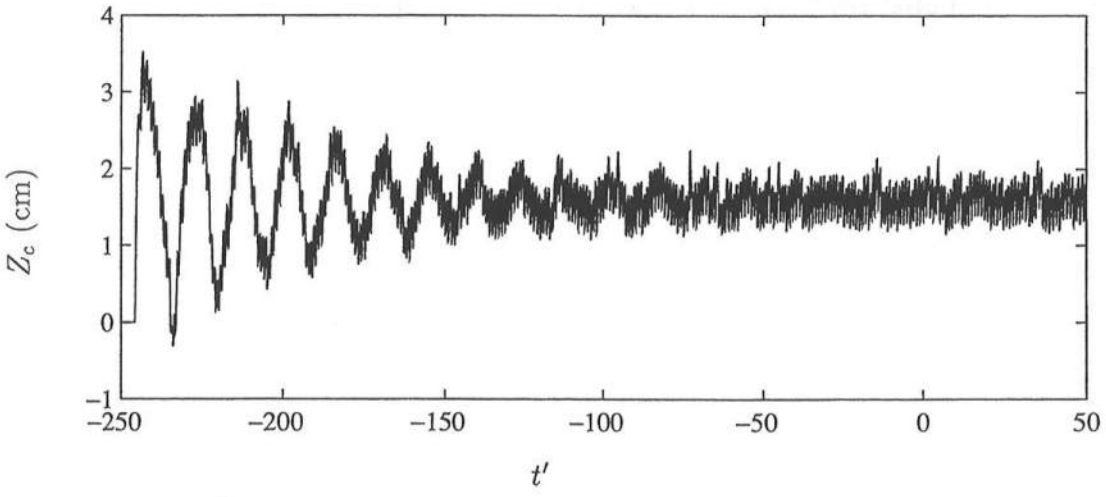

Figure 7.4: Runup Time Series for Case 2: $f = 0.015$, SB at L1, IWAVE=3.

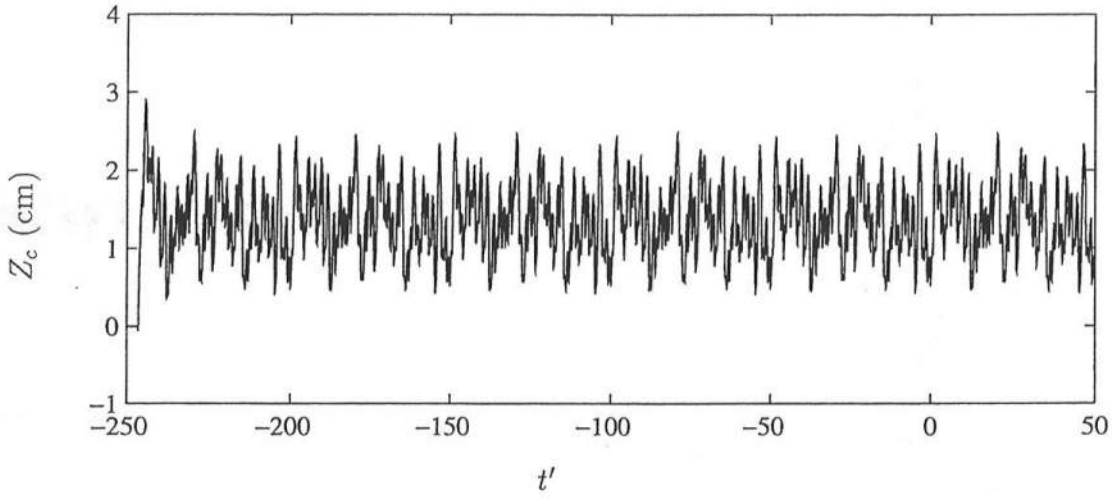

Figure 7.5: Runup Time Series for Case 3: $f = 0.015$, SB at L3, IWAVE=2.

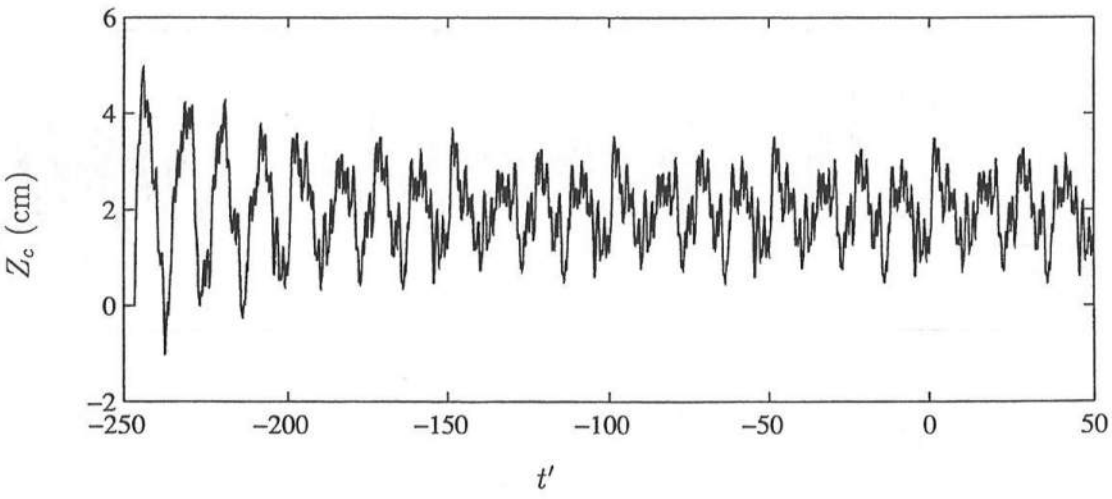

Figure 7.6: Runup Time Series for Case 4: $f = 0.015$, SB at L3, IWAVE=3.

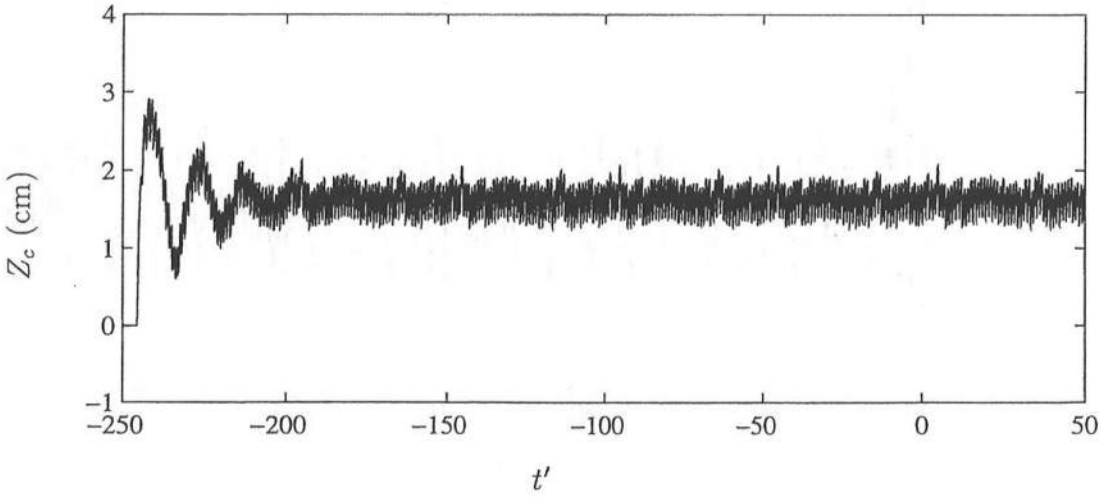

Figure 7.7: Runup Time Series for Case 5: $f = 0.05$, SB at L1, IWAVE=3.

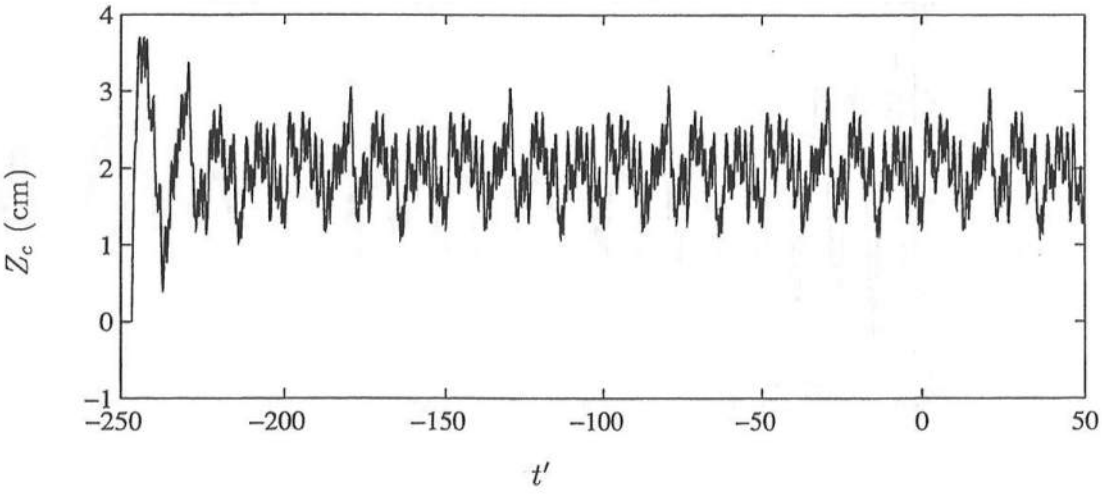

Figure 7.8: Runup Time Series for Case 6: $f = 0.05$, SB at L3, IWAVE=3.

7.4 Free Surface Comparisons

In this section, comparisons are made of the measured and computed free surface elevations to evaluate the model's capability in predicting the wave profile across the surf zone. In Section 7.4.1, measured and computed comparisons are made with the instantaneous free surface elevations for the last 10 of 50 waves for the six cases. In Section 7.4.2, comparisons are made of the phase-averaged free surface elevations to show the predictive capability of the model and to show the model's sensitivity to the three input options.

7.4.1 Instantaneous Free Surface Comparisons

Figures 7.9 to 7.14 show the temporal variations of the measured and computed instantaneous free surface elevations, η_m and η_c, for the last 10 waves for Cases 1 to 6 where the m subscript denotes measured values and the c subscript denotes computed values. Figure 7.9 for Case 1 with IWAVE=2 shows an initial discrepancy between the measured free surface elevation specified as the incident wave train as input and the total computed free surface elevation at L1. This small discrepancy results mostly from an overestimation of the setdown at the seaward boundary. Comparisons at L2 show that the model does not correctly predict the shape of the wave profile at the onset of breaking. It also does not predict the irregularity of wave breaking at L3 in the transition region. For L4 to L6 in the inner surf zone, the model does predict the saw-tooth profile and phases reasonably well.

Figure 7.10 for Case 2 with IWAVE=3 shows no discrepancy in the measured and computed free surface elevations at L1, because the measured free surface elevation specified as input is the total free surface elevation. The variations

the wave profiles across the surf zone for L2 to L6 are similar to Figure 7.9 for Case 1.

Figure 7.11 for Case 3 with IWAVE=2 shows the discrepancy at the seaward boundary at L3 similar to Figure 7.9 for Case 1. As expected, the wave profiles are predicted more accurately in the surf zone since the model has been initiated after breaking. Also, there is less error in the phase than with Case 1 and Case 2 where the seaward boundary was at L1. Figure 7.12 for Case 4 with IWAVE=3 shows the exact match at the seaward boundary at L3 as in Figure 7.10 for L1. The free surface profiles are well predicted and similar to Figure 7.11.

Figure 7.13 for Case 5 with $f = 0.05$ is similar to Figure 7.10 for Case 2 with $f = 0.015$. Direct comparisons are made of the phase-averaged free surface elevations for Cases 2 and 5 in the next section to show that computed free surface elevations are not sensitive to the friction factor in this range. Last, Figure 7.14 for Case 6 with $f = 0.05$ is similar to Figure 7.12 for Case 4 with $f = 0.015$. As a result, the bottom friction factor in the range of $0.015 \leq f \leq 0.05$ yields essentially the same free surface elevations at the measuring lines L1 to L6.

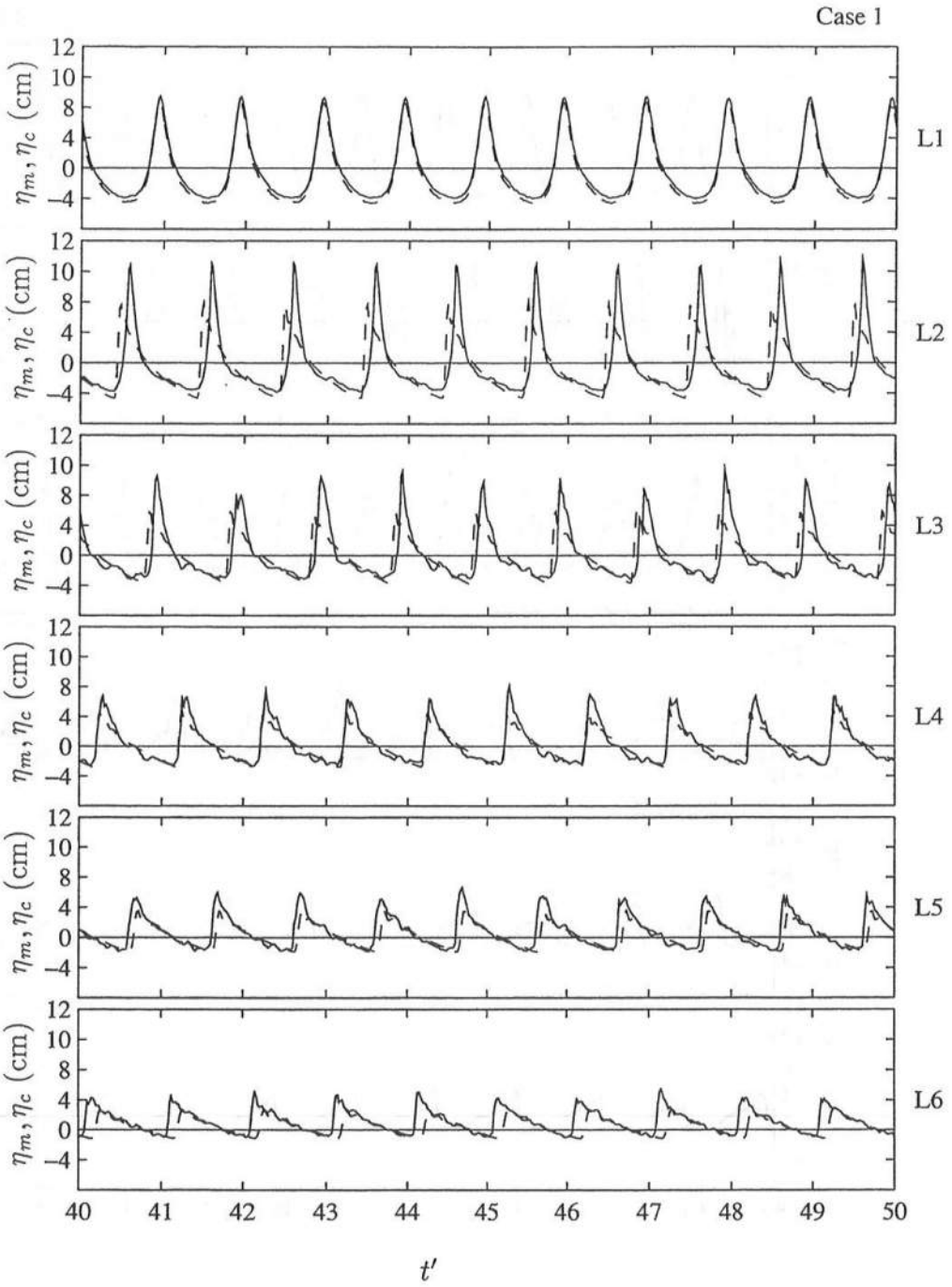

Figure 7.9: Temporal Variations of Free Surface Elevation: Measured, η_m(——), and Computed, η_c(– –), for Last 10 Waves of Case 1, L1 to L6.

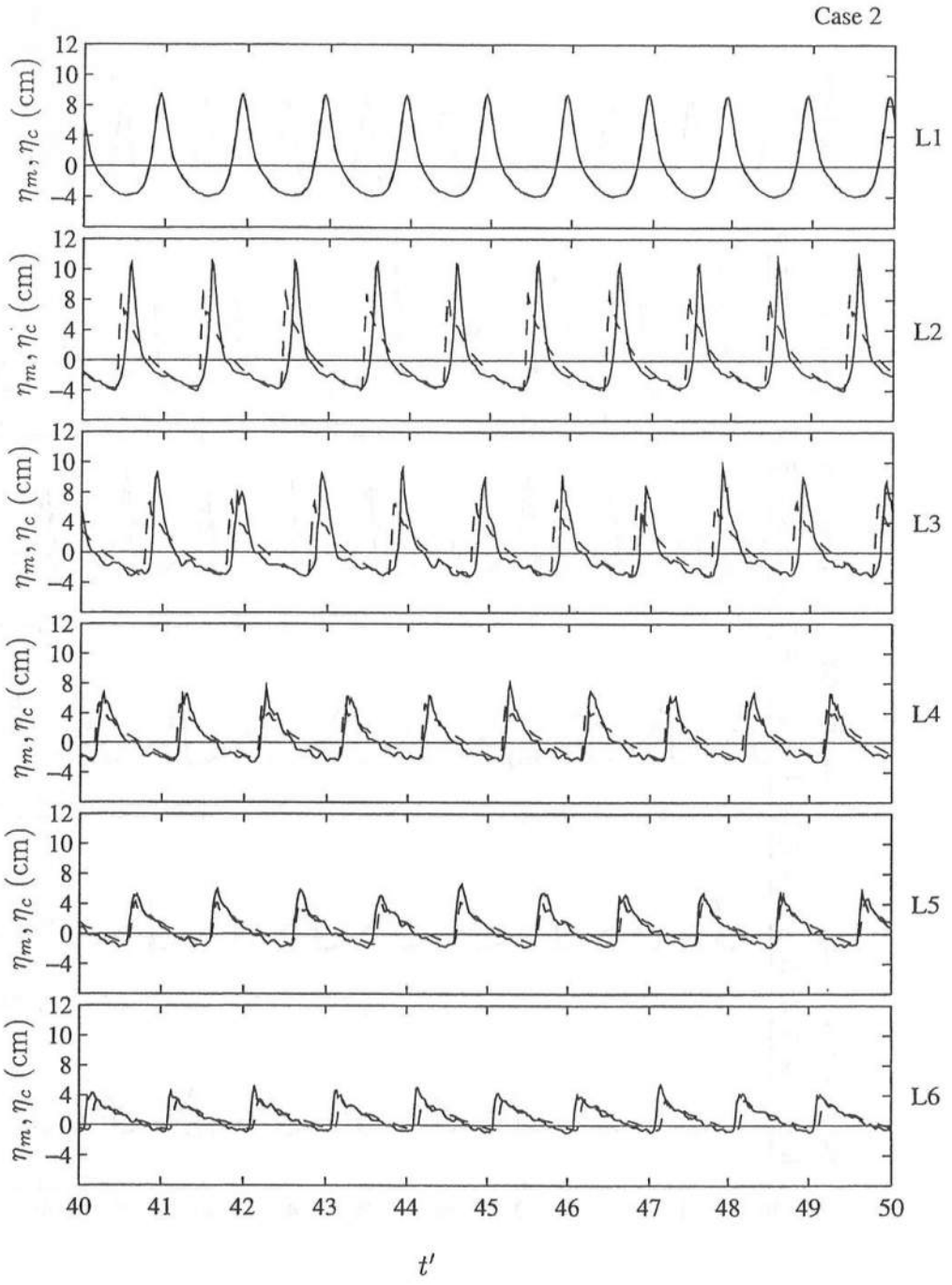

Figure 7.10: Temporal Variations of Free Surface Elevation: Measured, η_m(——), and Computed, η_c(– –), for Last 10 Waves of Case 2, L1 to L6.

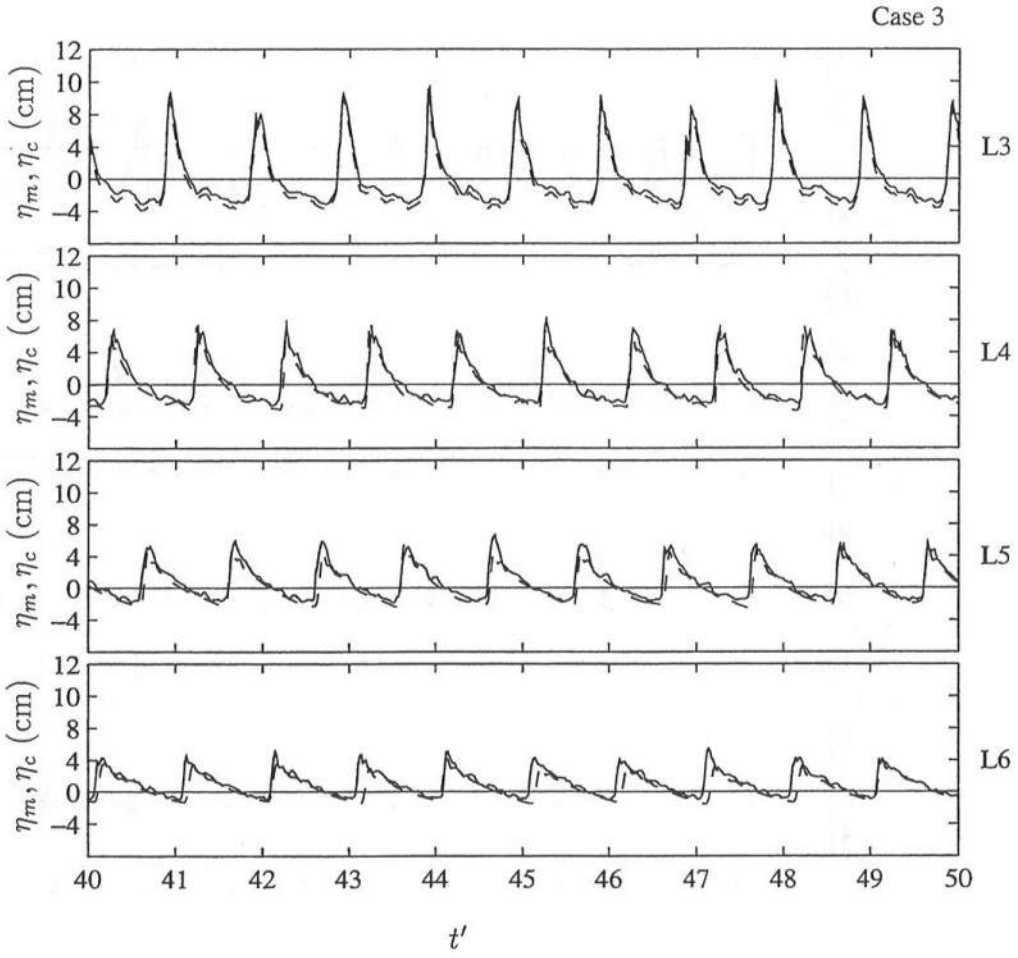

Figure 7.11: Temporal Variations of Free Surface Elevation: Measured, η_m(——), and Computed, η_c(– –), for Last 10 Waves of Case 3, L3 to L6.

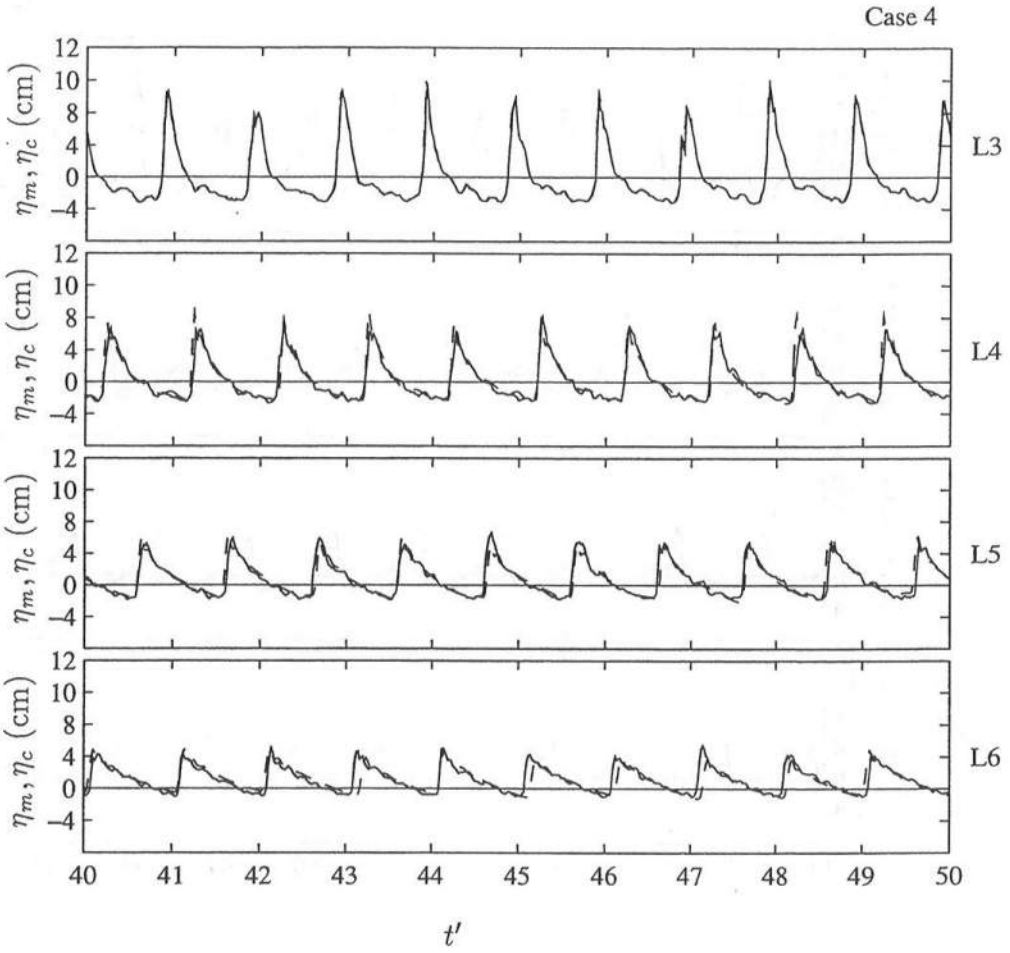

Figure 7.12: Temporal Variations of Free Surface Elevation: Measured, η_m(——), and Computed, η_c(– –), for Last 10 Waves of Case 4, L3 to L6.

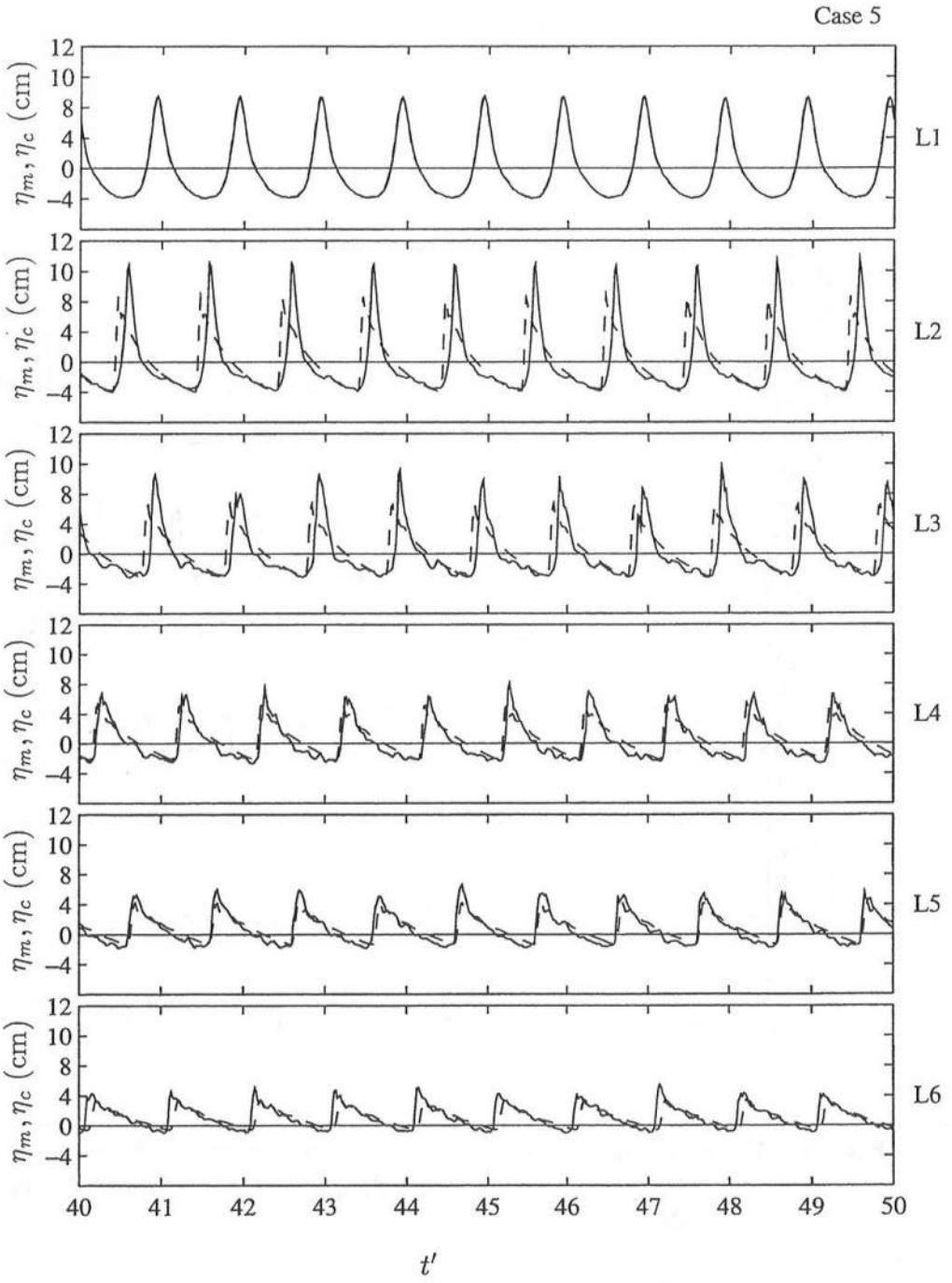

Figure 7.13: Temporal Variations of Free Surface Elevation: Measured, η_m(——), and Computed, η_c(– –), for Last 10 Waves of Case 5, L1 to L6.

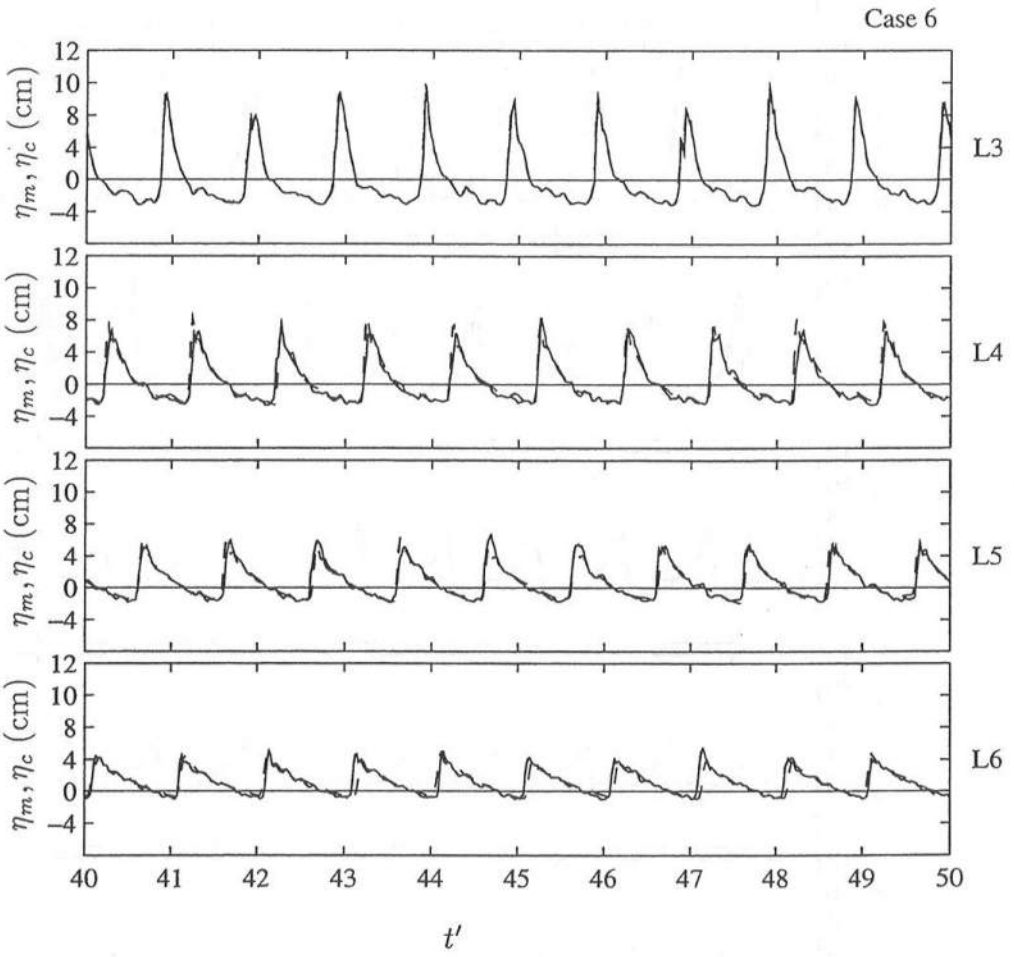

Figure 7.14: Temporal Variations of Free Surface Elevation: Measured, η_m(——), and Computed, η_c(– –), for Last 10 Waves of Case 6, L3 to L6.

7.4.2 Phase-Averaged Free Surface Comparisons

Figures 7.15 to 7.24 are comparisons of the measured phase-averaged free surface elevations, η_a, the computed phase-averaged free surface elevations, η_{ac}, the standard deviation of the measured phase-averaged free surface elevations, σ_η, and the standard deviation of the computed phase-averaged free surface elevations, σ_{η_c}, for the six cases considered. In these figures, the phases have been adjusted so that the zero-upcrossing of the free surface elevation at each of the measuring lines is at $t = T_r/4$ to be consistent with the earlier chapters.

Figure 7.15 shows the temporal variations of η_a and η_{ac} for Case 1 with IWAVE=2 and Case 2 with IWAVE=3 for L1 to L6. At L1 there is the slight discrepancy between η_a and η_{ac} for Case 1 resulting from an overestimation of the setdown of the seaward boundary. Similar to Figures 7.9 and 7.10, Figure 7.15 shows that the model does not predict the wave profile at the onset of breaking at L2 or in the transition region at L3. In the inner surf zone, however, the bore profile is predicted reasonably well, but there is some error in the predicted phase. There is a small difference in the phases between Case 1 and Case 2.

Figure 7.16 shows the temporal variations of σ_η and σ_{η_c} for Case 1 and Case 2 for L1 to L6. At L1, all three curves show that the standard deviation is small. As noted in Chapter 4, σ_η increases with the onset of wave breaking at L2 and is concentrated near the wave tip of the wave crest where the aeration starts. At L3, σ_η is maximum and is fairly confined to the bore region. Across the inner surf zone from L4 to L6, σ_η decreases. For the computed cases, σ_{η_c} does not follow these trends. The small deviation specified at the seaward boundary becomes concentrated on the wave front and does not vary much across the surf zone from L2 to L6.

Figure 7.17 shows the temporal variations of η_a and η_{ac} for Case 2 with $f = 0.015$ and Case 5 with $f = 0.05$. The similarity of the two computed curves shows that the computed free surface elevations are not sensitive to the friction factor in this range. Figure 7.18 shows the temporal variations of σ_η and σ_{η_c} for Case 2 and Case 5 and also indicates that the results are not sensitive to f.

Figure 7.19 shows the temporal variations of η_a and η_{ac} for Case 3 with IWAVE=2 and Case 4 with IWAVE=3 for L3 to L6. The improved agreement between η_a and η_{ac} is expected since the model is initiated inside the surf zone. The saw-tooth wave profile is well predicted and there is less discrepancy in the phases between the measured and computed curves. Similar to Figure 7.15, there is a small difference in the phases of the wave fronts between Case 3 and Case 4.

Figure 7.20 shows the temporal variations of σ_η and σ_{η_c} for Case 3 and Case 4. At L3, all three curves show that the standard deviation is large due to wave breaking. Similar to Figures 7.16 and 7.18 for the computed cases, this variation becomes concentrated on the wave front at L4 and does not decrease much across the surf zone from L4 to L6.

Figure 7.21 for η_a and η_{ac} and Figure 7.22 for σ_η and σ_{η_c} show that the computed results for Case 4 and Case 6 are not sensitive to f, similar to Figure 7.17 and Figure 7.18 for Case 2 and Case 5. Figure 7.22 shows a somewhat greater sensitivity of σ_{η_c} to f, but the difference of σ_{η_c} for Case 4 and Case 6 is small compared to the incident wave height.

The final comparisons in this section are for Case 2 and Case 4 to show the effect of the location of the seaward boundary on the computed wave profile. For Case 2, the model is initiated at L1 seaward of breaking; and for Case 4, the model is initiated at L3 in the surf zone. Figure 7.23 shows that both cases predict the

wave profile well in the inner surf zone for L4 to L6. As expected, the discrepancy in the phase is larger for Case 2. Figure 7.24 shows that the variability specified at the seaward boundary is propagated through the model domain at the wave front with little change across the surf zone.

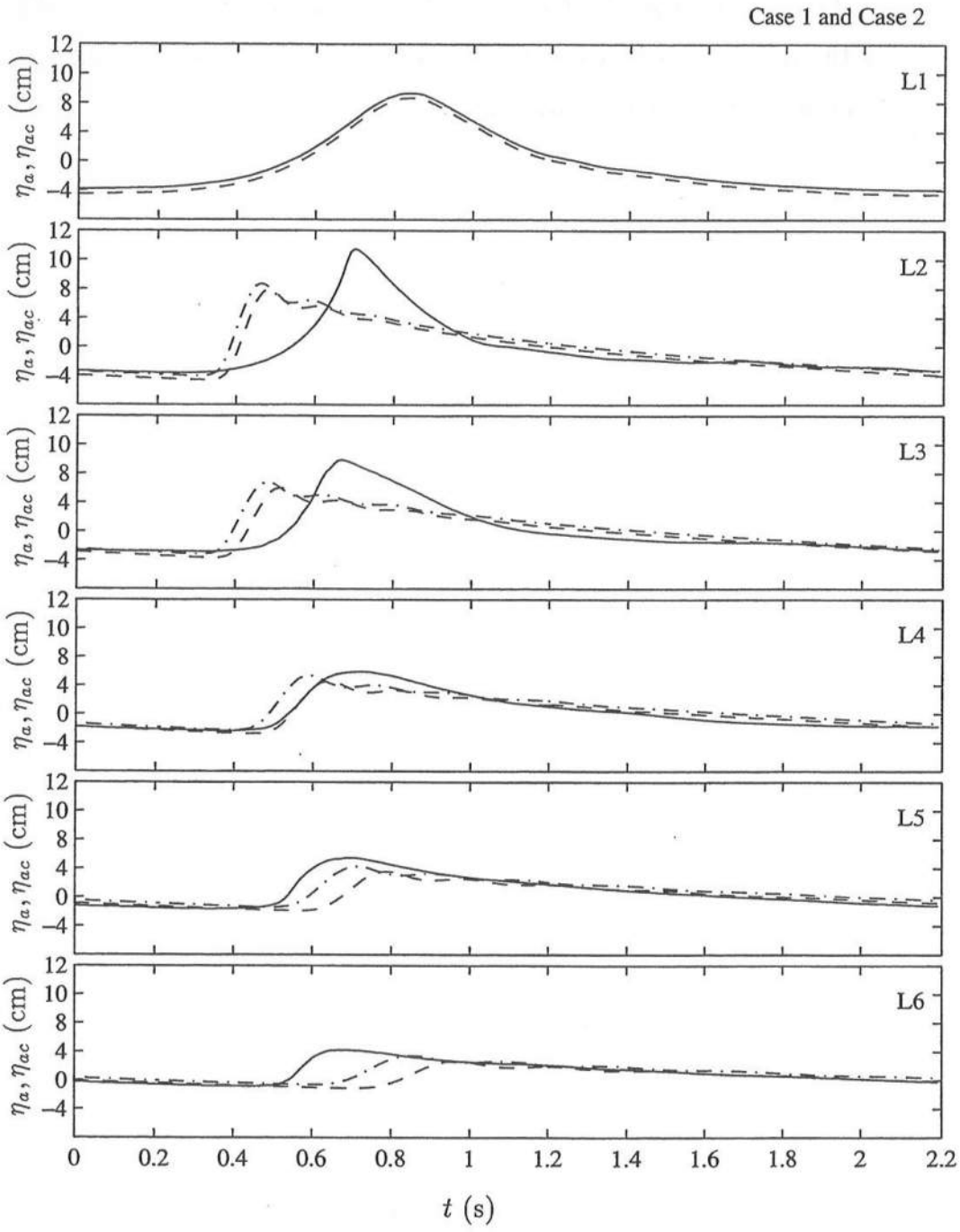

Figure 7.15: Temporal Variations of Phase-Averaged Free Surface Elevation: Measured, η_a(——), and Computed, η_{ac}, with Case 1 (– –) and Case 2 (–·–) for L1 to L6.

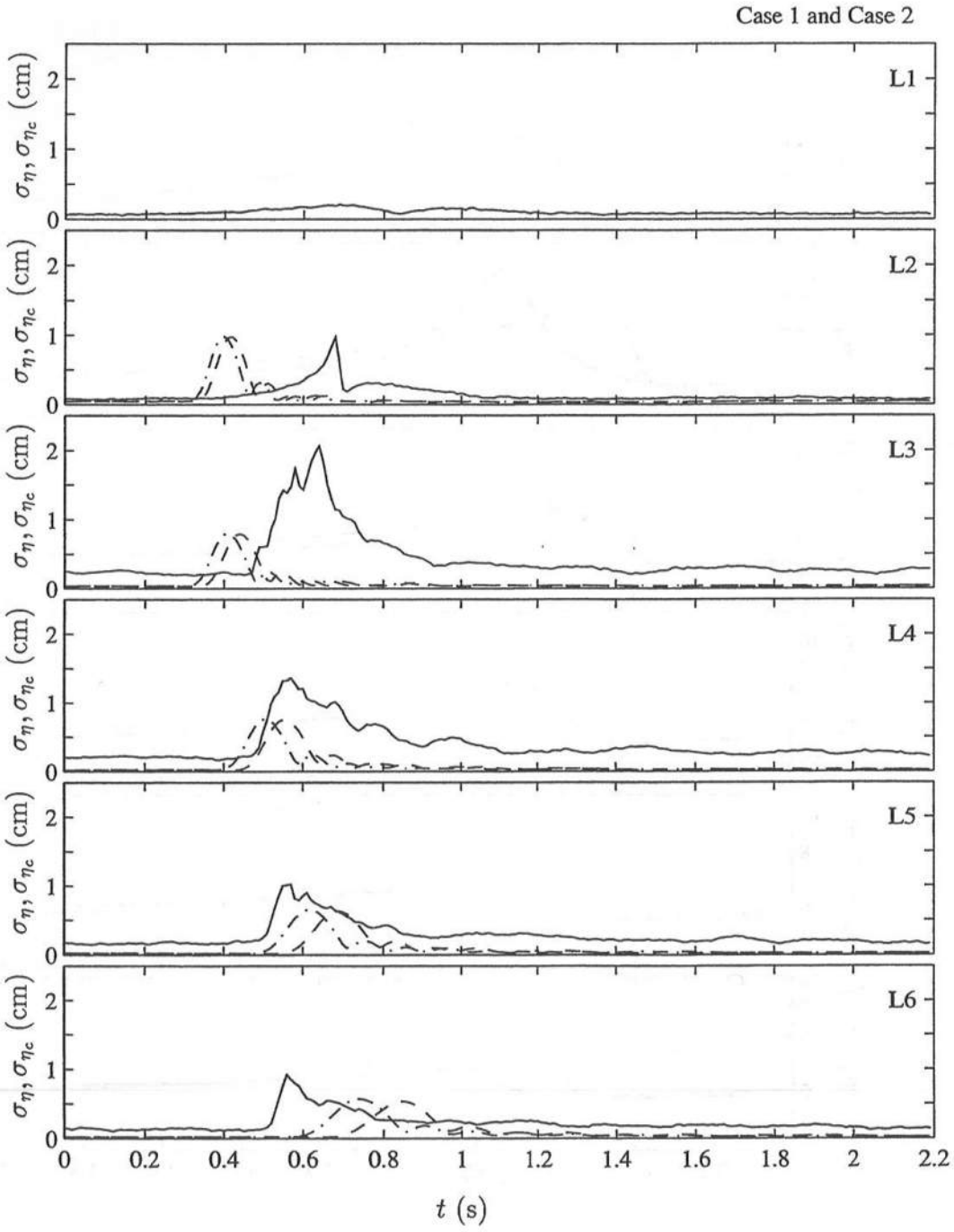

Figure 7.16: Temporal Variations of Standard Deviation of Phase-Averaged Free Surface Elevation: Measured, σ_η(——), and Computed, σ_{η_c}, with Case 1 (– –) and Case 2 (–·–) for L1 to L6.

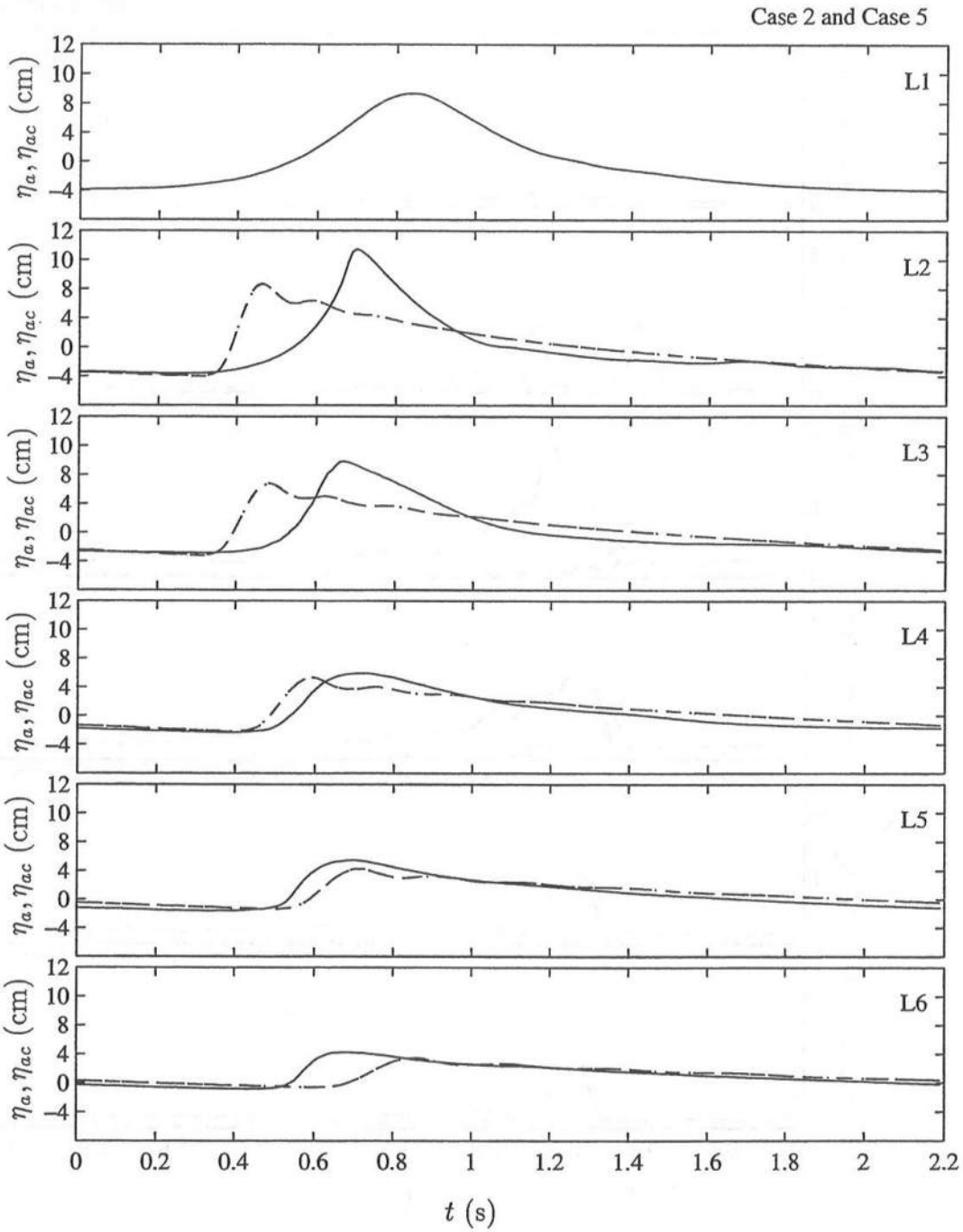

Figure 7.17: Temporal Variations of Phase-Averaged Free Surface Elevation: Measured, η_a(——), and Computed, η_{ac}, with Case 2 (– –) and Case 5 (–·–) for L1 to L6.

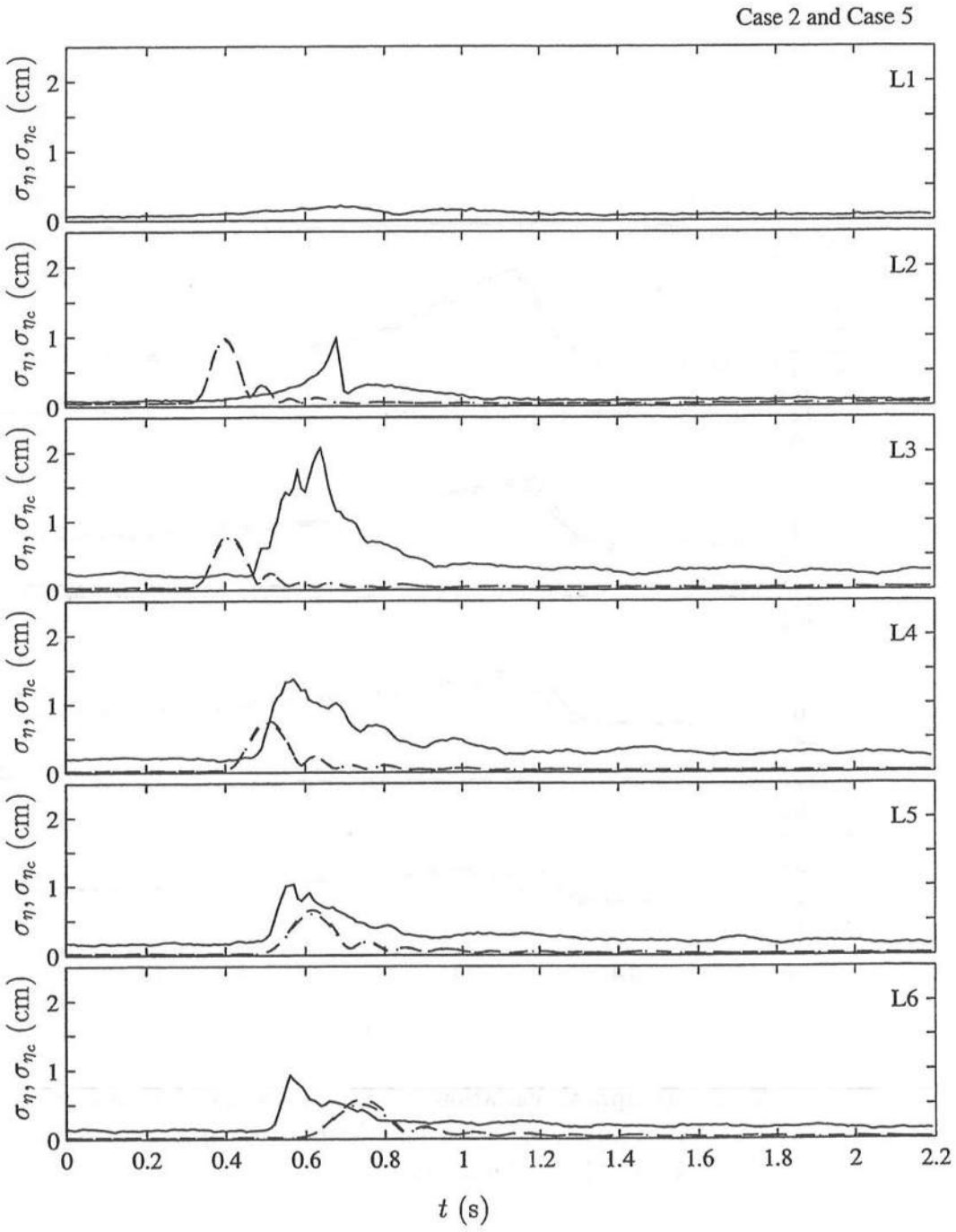

Figure 7.18: Temporal Variations of Standard Deviation of Phase-Averaged Free Surface Elevation: Measured, σ_η(——), and Computed, σ_{η_c}, with Case 2 (– –) and Case 5 (–·–) for L1 to L6.

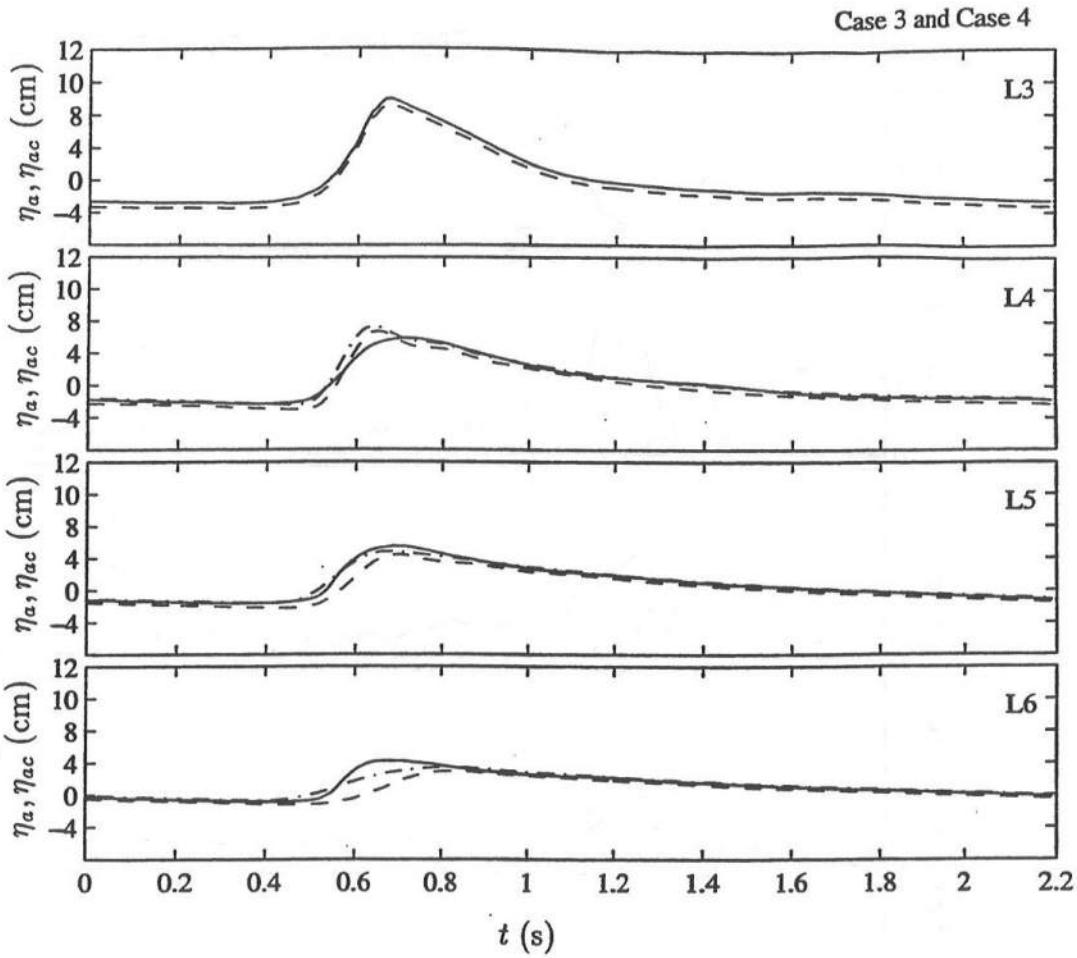

Figure 7.19: Temporal Variations of Phase-Averaged Free Surface Elevation: Measured, η_a(——), and Computed, η_{ac}, with Case 3 (– –) and Case 4 (–·–) for L3 to L6.

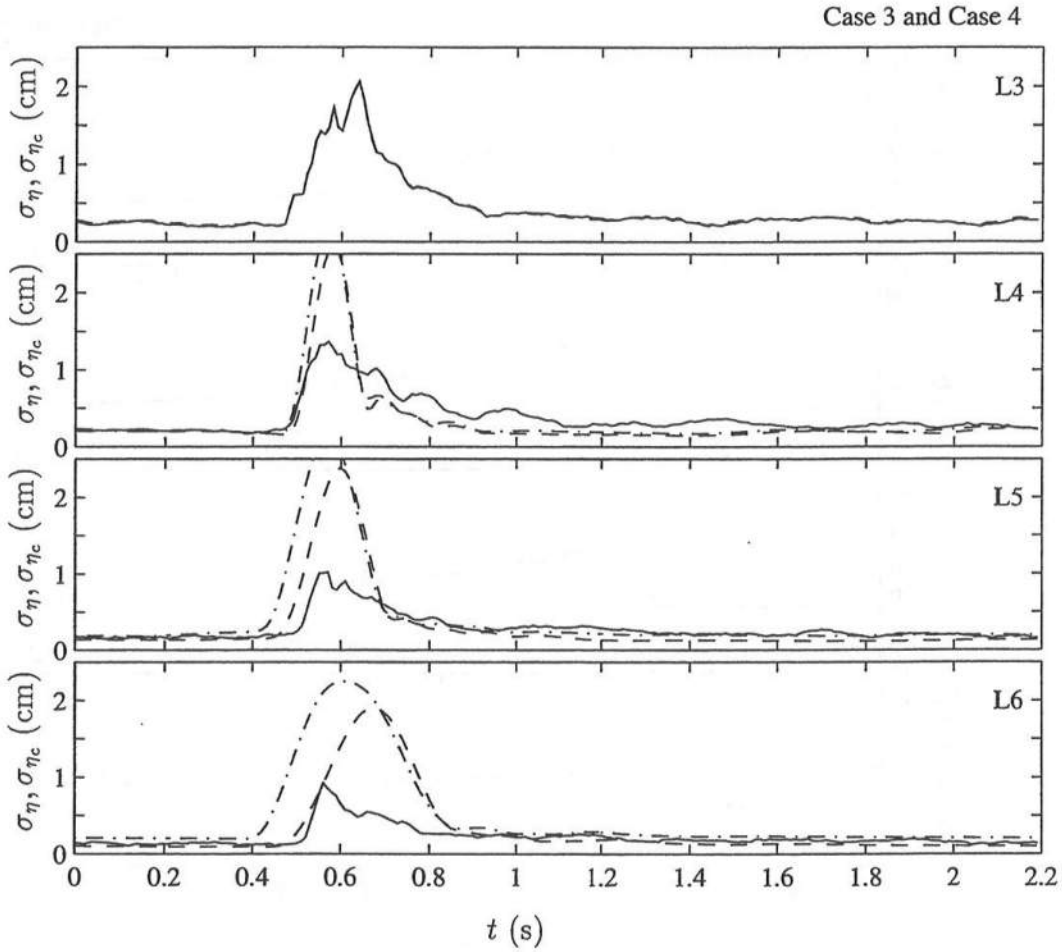

Figure 7.20: Temporal Variations of Standard Deviation of Phase-Averaged Free Surface Elevation: Measured, σ_η(——), and Computed, σ_{η_c}, with Case 3 (– –) and Case 4 (–·–) for L3 to L6.

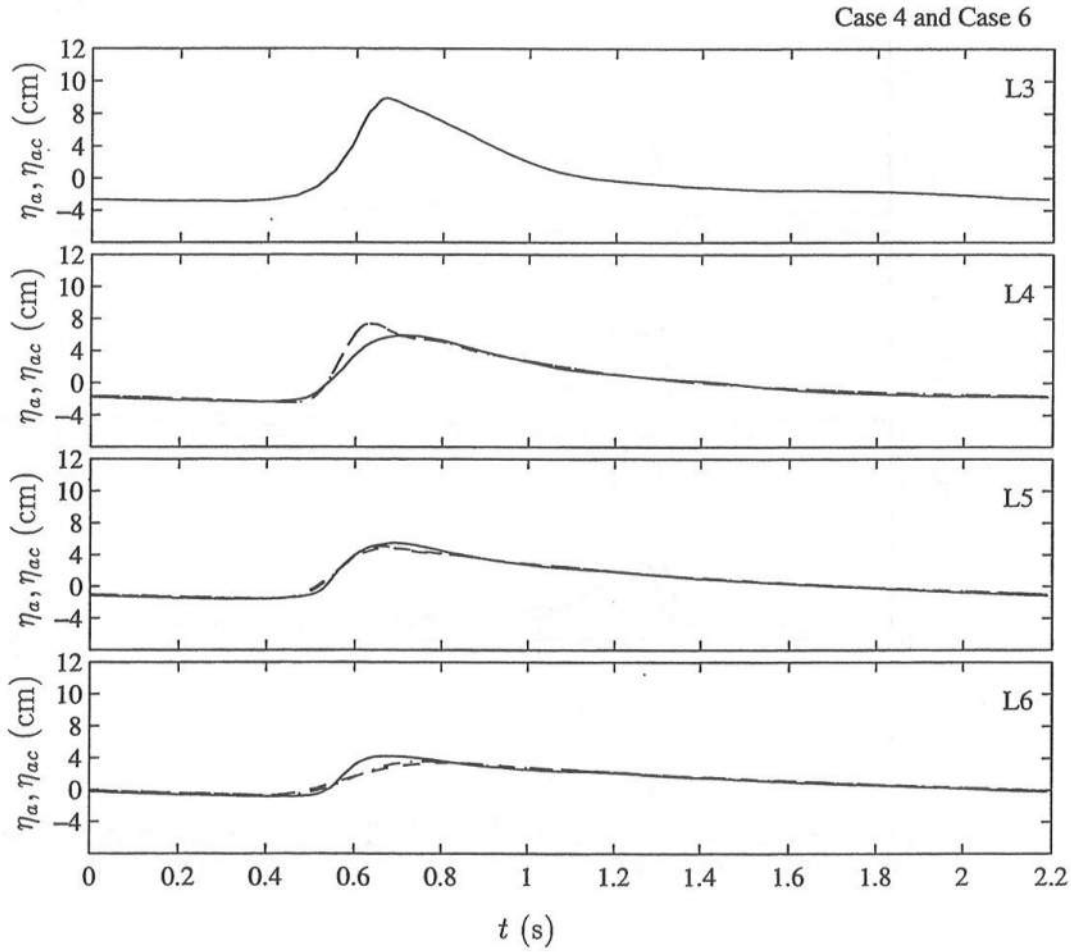

Figure 7.21: Temporal Variations of Phase-Averaged Free Surface Elevation: Measured, η_a(——), and Computed, η_{ac}, with Case 4 (– –) and Case 6 (–·–) for L3 to L6.

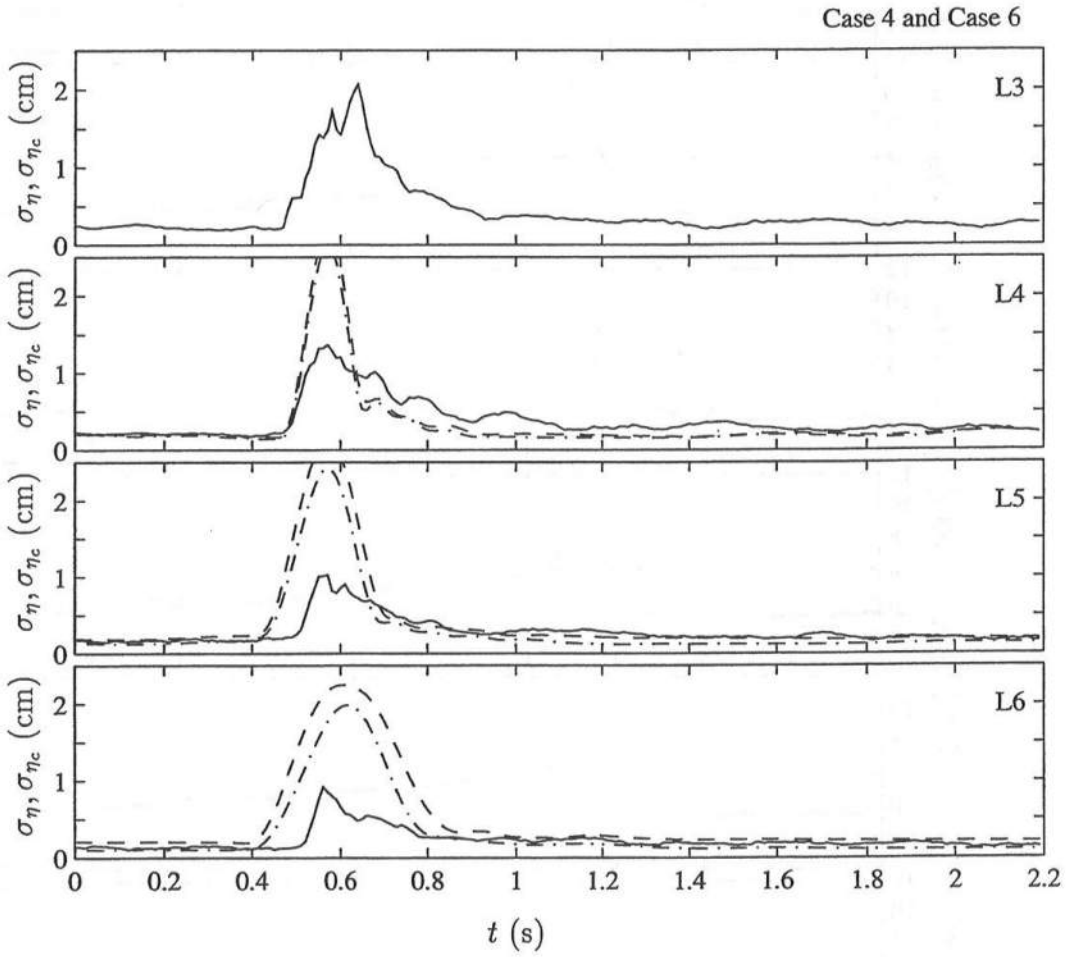

Figure 7.22: Temporal Variations of Standard Deviation of Phase-Averaged Free Surface Elevation: Measured, σ_η(——), and Computed, σ_{η_c}, with Case 4 (– –) and Case 6 (–·–) for L3 to L6.

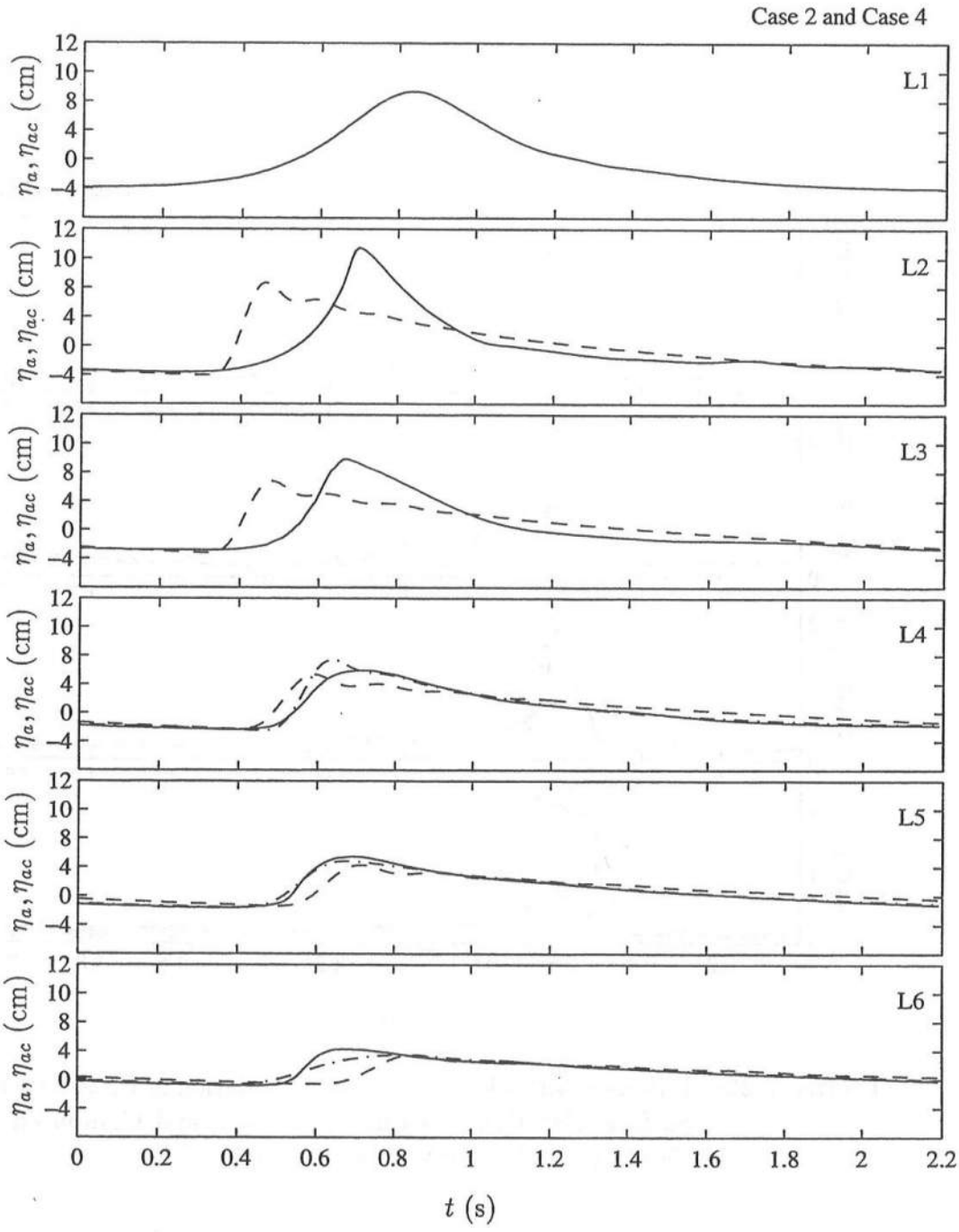

Figure 7.23: Temporal Variations of Phase-Averaged Free Surface Elevation: Measured, η_a(——), and Computed, η_{ac}, with Case 2 (– –) for L1 to L6 and Case 4 (–·–) for L3 to L6.

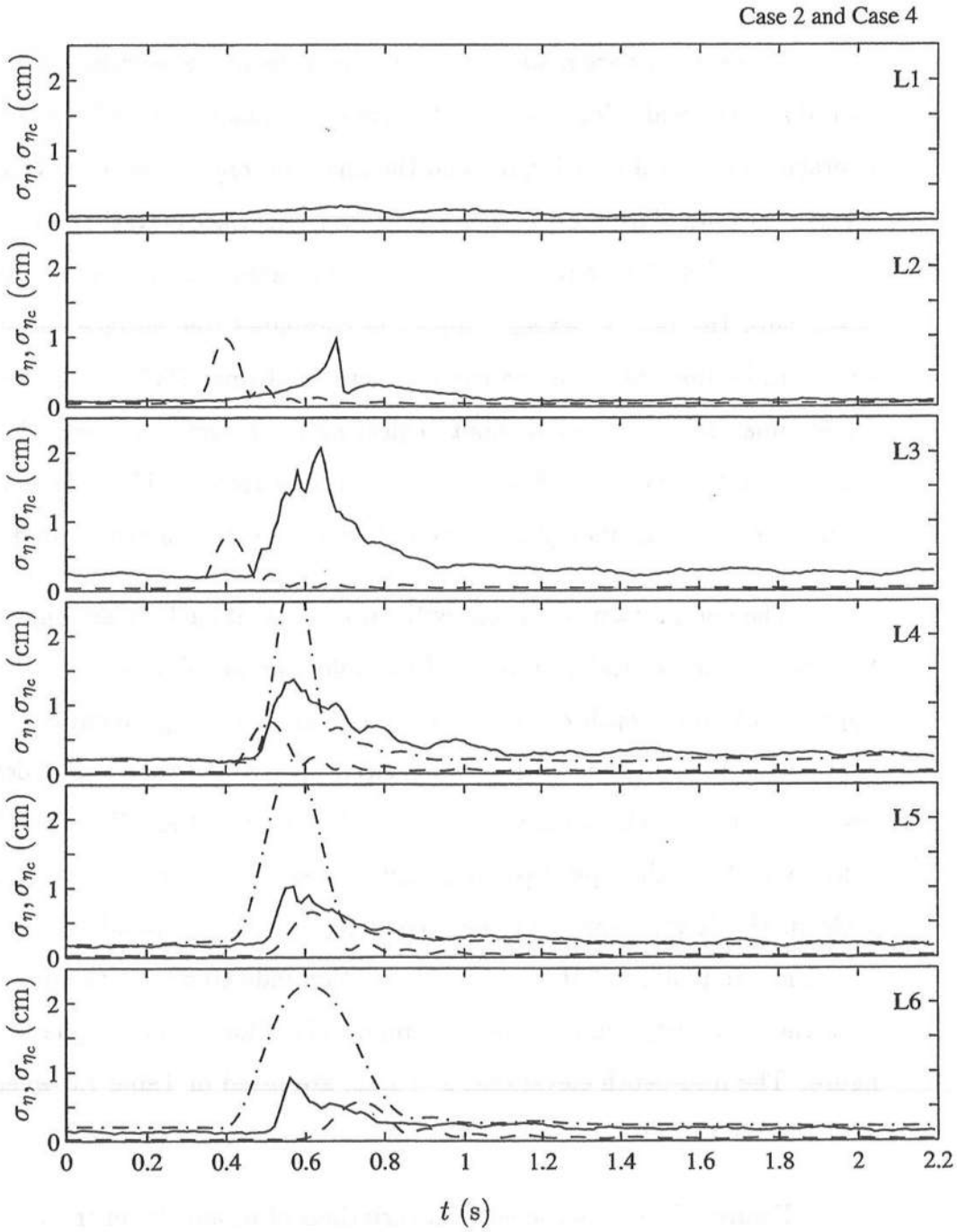

Figure 7.24: Temporal Variations of Standard Deviation of Phase-Averaged Free Surface Elevation: Measured, σ_η(——), and Computed, σ_{η_c}, with Case 2 (– –) for L3 to L6 and Case 4 (–·–) for L3 to L6.

7.5 Velocity Comparisons

Comparisons are made in this section of the phase-averaged measured horizontal and vertical velocities, u_a and w_a, and the phase-averaged computed depth-averaged horizontal velocity, U_a, and the phase-averaged computed vertical velocity, W_a, estimated from Eq 7.10. As with the free surface elevations of the previous section, the first 250 computed waves are truncated, and the phase averages are made with the last 50 waves. Since the computed free surface elevations were shown to be insensitive to the friction factor and since IWAVE=3 uses the measured time series as input without neglecting the reflected waves, only two cases with $f = 0.015$ and IWAVE=3 are shown in this section. These cases are Case 2 with the seaward boundary at L1 and Case 4 with the seaward boundary at L3.

The comparisons are made with two figures at each measuring line. In the first figure, the vertical variations of the velocities are shown at six phases. The approximate mid-depth elevation below trough level, z_{mid}, mentioned briefly in Section 5.8.2 is indicated with an open circle. It is noted that z_{mid} is defined with respect to the z-axis, positive upward with $z = 0$ at the SWL. The horizontal velocity scale in the upper panel is three times larger than the vertical velocity scale in the lower panel. In the second figure, the temporal variations of the velocities are plotted at the mid-depth location indicated from the previous figure with the open circles indicating the temporal location of the six phases from that figure. The mid-depth elevations, $z = z_{mid}$, are listed in Table 7.3 where d is the depth below the SWL.

Figure 7.25 shows the vertical variations of u_a and U_a in the top panel and w_a and W_a in the lower panel for six phases for Case 2 at L1. The measured and computed free surface elevations, η_a and η_{ac}, from Figure 7.15 are also shown at the six phases. The computed depth-averaged horizontal velocity gives a good

Table 7.3: Mid-Depth Locations for Comparison of Measured and Computed Velocities for L1 to L6.

Line No.	d (cm)	z_{mid} (cm)
L1	28.00	-16.00
L2	21.14	-13.14
L3	17.71	-9.71
L4	14.29	-6.29
L5	10.86	-5.86
L6	7.43	-3.43

approximation of the measured horizontal velocity except in the bottom boundary layer for the six phases shown. The profile of the measured vertical velocity at the seaward boundary varies linearly with depth to a zero bottom velocity. The computed vertical velocity estimated from the continuity equation gives a good approximation of the measured profile at L1. Figure 7.26 shows the temporal variations of the horizontal and vertical velocities at the mid-depth location. There is exact agreement of η_a and η_{ac} and good agreement between u_a and U_a and between w_a and W_a over the wave period.

At L2, Figure 7.27 shows good agreement between u_a and U_a at five of the six phases plotted and a large discrepancy at $t = 2T/6$. From Figure 7.28 it can be seen that this discrepancy is related to the poor prediction of the wave profile at breaking. The agreement between w_a and W_a in Figure 7.27 is good at four of the six phases with a very large discrepancy at $t = T/6$ and a smaller discrepancy with the incorrect sign at $t = 2T/6$. Both discrepancies are related to the spatial derivatives on U used in Eq 7.10. From Figure 7.28, it can be seen that the large discrepancy at $t = T/6$ is related to the steepness of the wave front and that the

sign error in the discrepancy at $t = 2T/6$ is related to the small, high-frequency oscillations on the back of the computed wave crest. The numerical high-frequency oscillations are amplified in the spatial derivatives on U.

At L3, Figures 7.29 and 7.30 show results similar to L2 and reflect the inability of the model to correctly predict the wave profile in the transition region. At L4, Figures 7.31 and 7.32 show that the agreement between u_a and U_a improves in the inner surf zone. It is interesting to note that u_a is fairly constant over depth for the six phases except above trough level for $t = 2T/6$ and below the mid-depth elevation for $t = 3T/6$ where the measured profile is presumably affected by the undertow. The profile of the measured vertical velocity, which is small relative to the horizontal velocity, does not vary linearly as at L1, possibly due to eddies generated by wave breaking. The computed vertical velocities can not reproduce the measured profile well in the inner surf zone.

At L5 and L6, the discrepancy in the phases between the measured and computed wave profiles leads to the poor prediction of the measured velocities at the six phases in Figures 7.33 and 7.35. Figures 7.34 and 7.36, however, show that aside from the phase discrepancy, the measured horizontal velocity at the mid-depth location is reasonably well predicted. The oscillations on the back of the wave crest lead to poor agreement of the vertical velocity.

Figures 7.37 to 7.44 show the comparisons for Case 4 where the model is initiated at L3 inside the surf zone. Figure 7.37 shows that the measured horizontal profile is predicted fairly well at five of the six phases. At $t = 2T/6$, the model overpredicts the horizontal velocity. A possible explanation is that at the crest of a breaking wave, the depth-averaged velocity may overpredict the local horizontal velocity below trough level because of the large horizontal velocity above the wave trough. It is noted that there may be some ambiguity in the upper

panel in distinguishing between U_a at $t = 2T/6$ and U_a at $t = 3T/6$. Reading from left to right, $U_a \simeq 58$ cm/s at $t = 2T/6$ is first, and $U_a \simeq 0$ cm/s at $t = 3T/6$ is second. In the lower panel, the vertical velocity profile is also not well predicted at $t = 2T/6$. Figure 7.38 shows a reasonable agreement among the velocities at the mid-depth elevation at the seaward boundary although the agreement is not as good as Case 2 shown in Figure 7.26.

At L4 to L6 in the inner surf zone, Figures 7.39, 7.41, and 7.43 show that the measured horizontal velocity profile is represented fairy well by the computed horizontal velocity at most of the phases except near the wave crest. Figures 7.40, 7.42, and 7.44 show that the phase errors in the predicted quantities are small but that U_a overpredicts u_a at the mid-depth elevation. As in Case 2, the computed vertical velocities can not reproduce well the measured profile in the surf zone for Figures 7.39, 7.41, and 7.43. Also, Figures 7.40 and 7.42 show that the spatial derivatives on U_a give poor estimates of the vertical velocity at the steep wave front and on the back of the wave crest due to the small numerical oscillations. At L6, however, Figure 7.44 shows good agreement between the measured and computed vertical velocity, indicating that the numerical model tends to recover inside the surf zone.

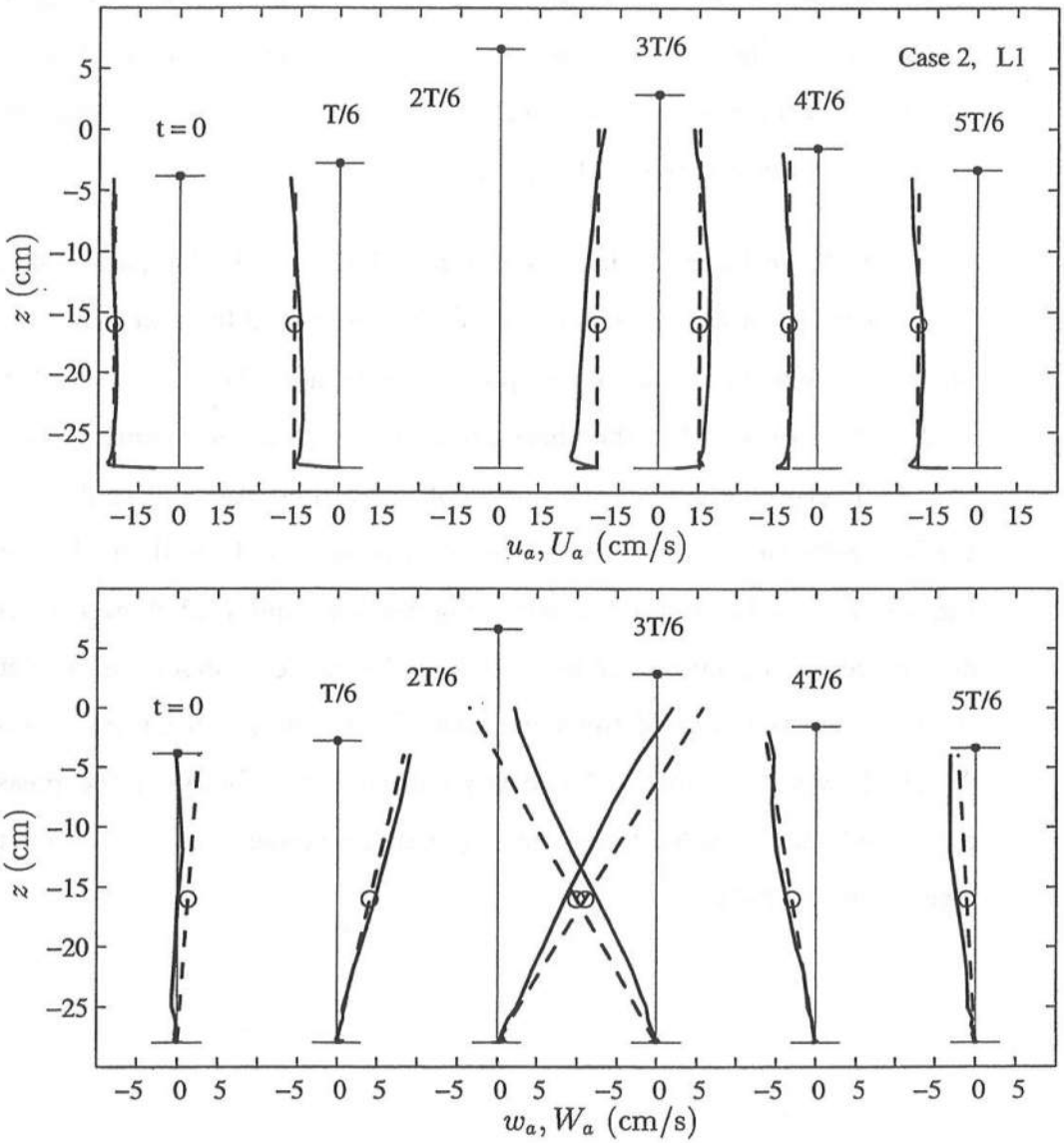

Figure 7.25: Vertical Variations of Horizontal Velocity: Measured, u_a(——), and Computed, U_a(– –○), (Top); Vertical Velocity: Measured, w_a(——), and Computed, W_a(– –○), (Bottom); and Free Surface Elevation: Measured, η_a(——), and Computed, η_{ac}(•), (Both); at Six Phases for Case 2 at L1.

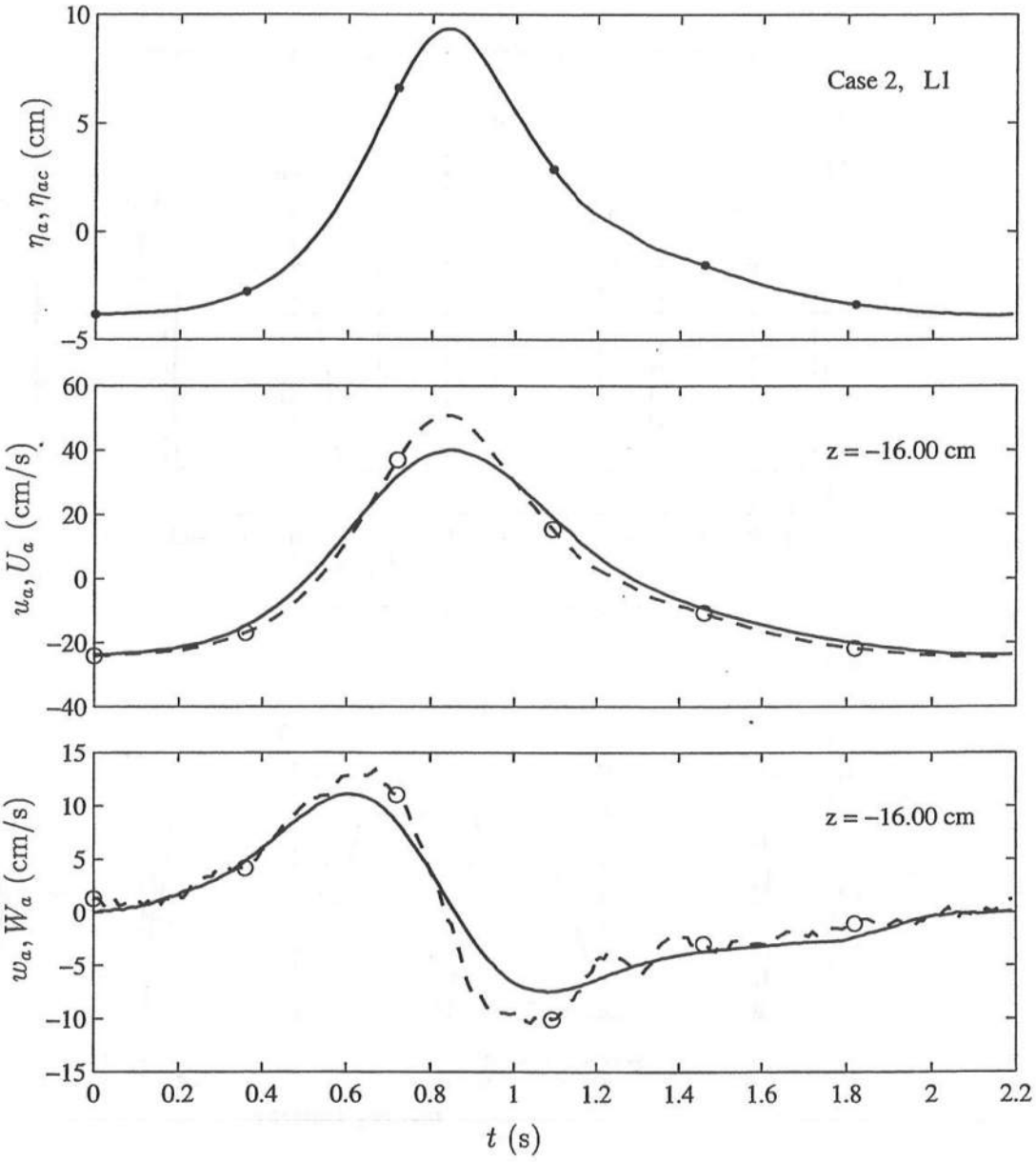

Figure 7.26: Temporal Variations of Free Surface Elevation: Measured, η_a(——), and Computed, η_{ac}(– –•), (Top); Horizontal Velocity: Measured, u_a(——), and Computed, U_a(– –○), (Middle); and Vertical Velocity: Measured, w_a(——), and Computed, W_a(– –○), (Bottom); at $z = -16.00$ cm for Case 2 at L1.

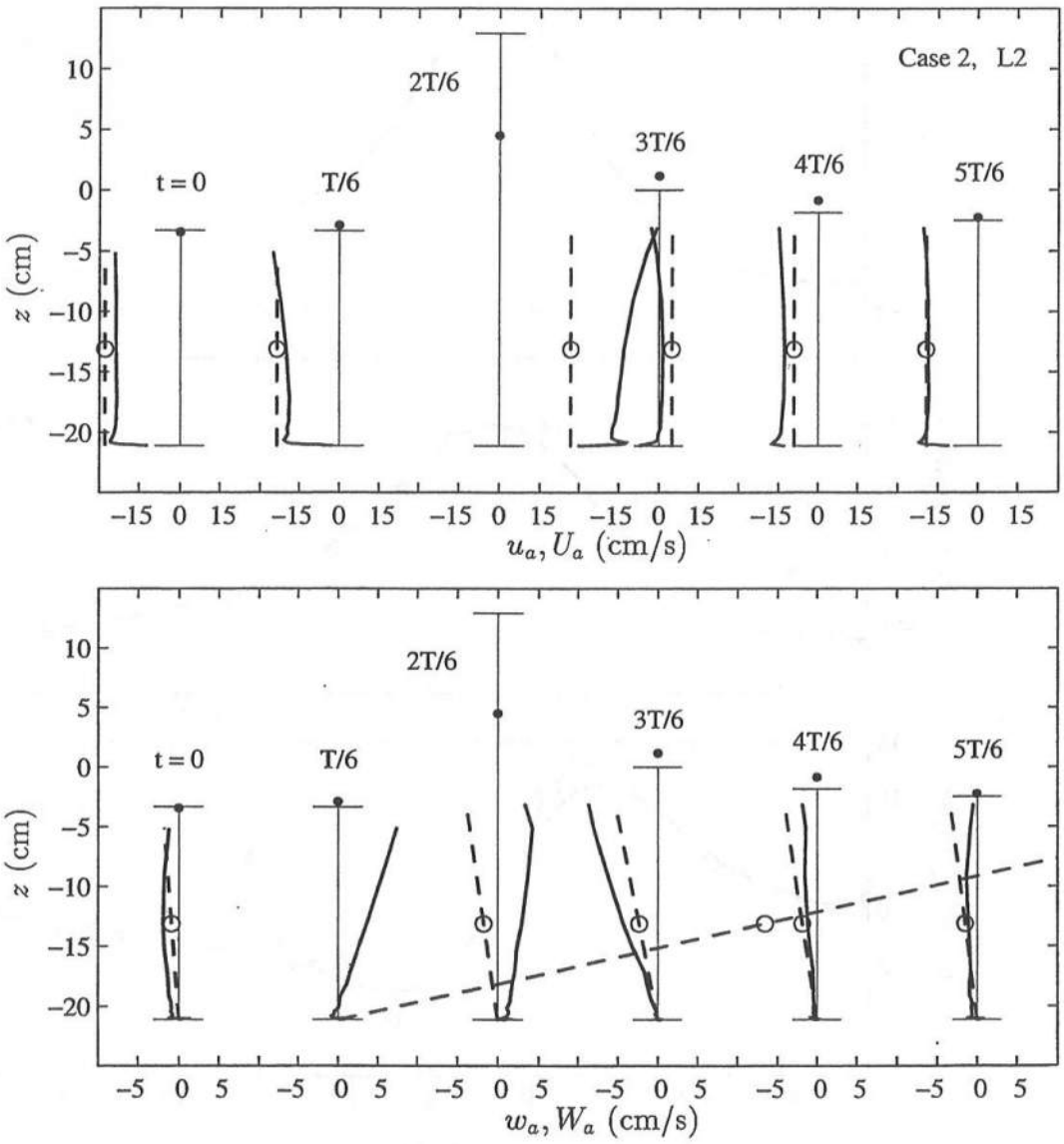

Figure 7.27: Vertical Variations of Horizontal Velocity: Measured, u_a(——), and Computed, U_a(– –○), (Top); Vertical Velocity: Measured, w_a(——), and Computed, W_a(– –○), (Bottom); and Free Surface Elevation: Measured, η_a(——), and Computed, η_{ac}(•), (Both); at Six Phases for Case 2 at L2.

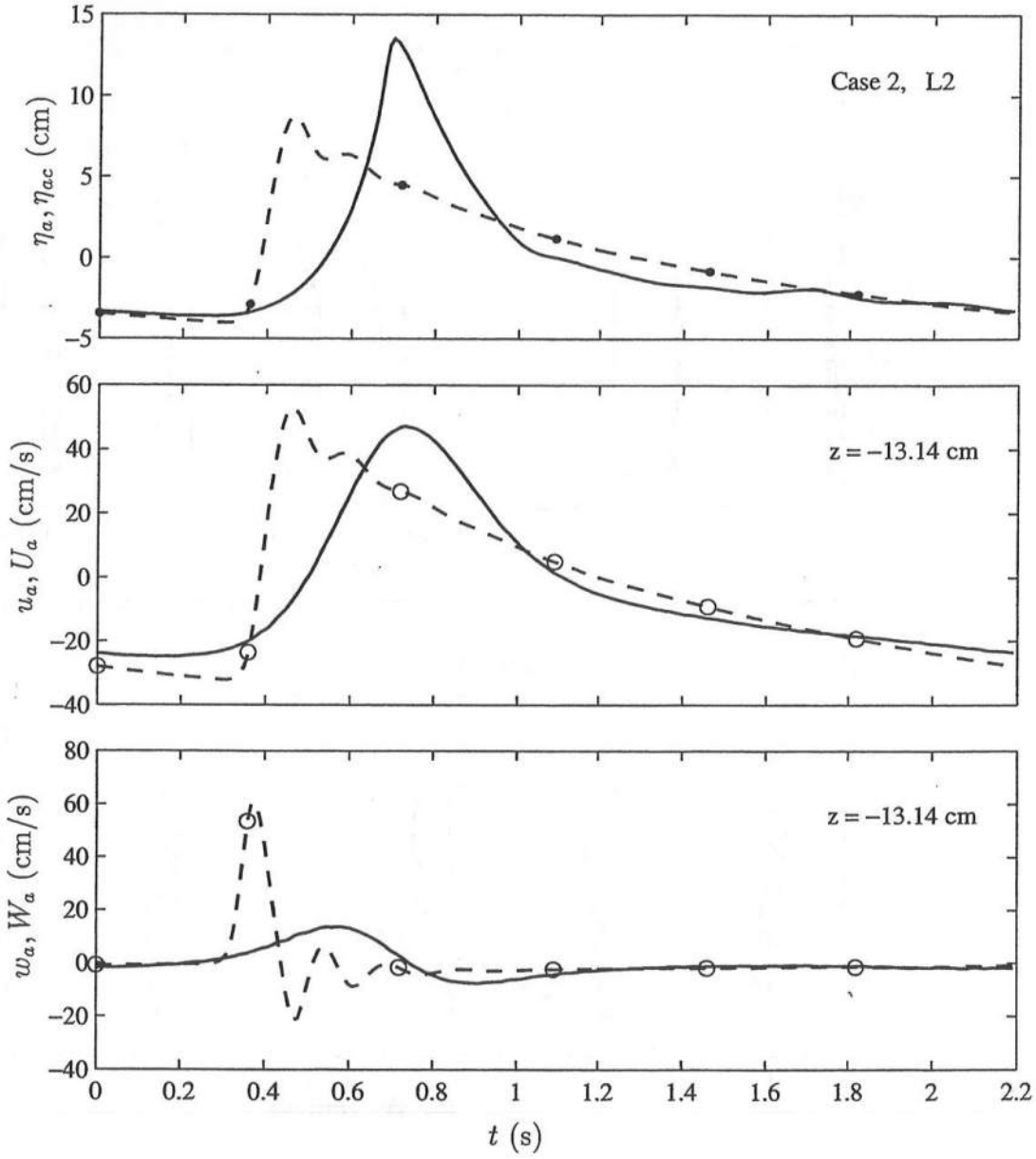

Figure 7.28: Temporal Variations of Free Surface Elevation: Measured, η_a(——), and Computed, η_{ac}(– –•), (Top); Horizontal Velocity: Measured, u_a(——), and Computed, U_a(– –o), (Middle); and Vertical Velocity: Measured, w_a(——), and Computed, W_a(– –o), (Bottom); at $z = -13.14$ cm for Case 2 at L2.

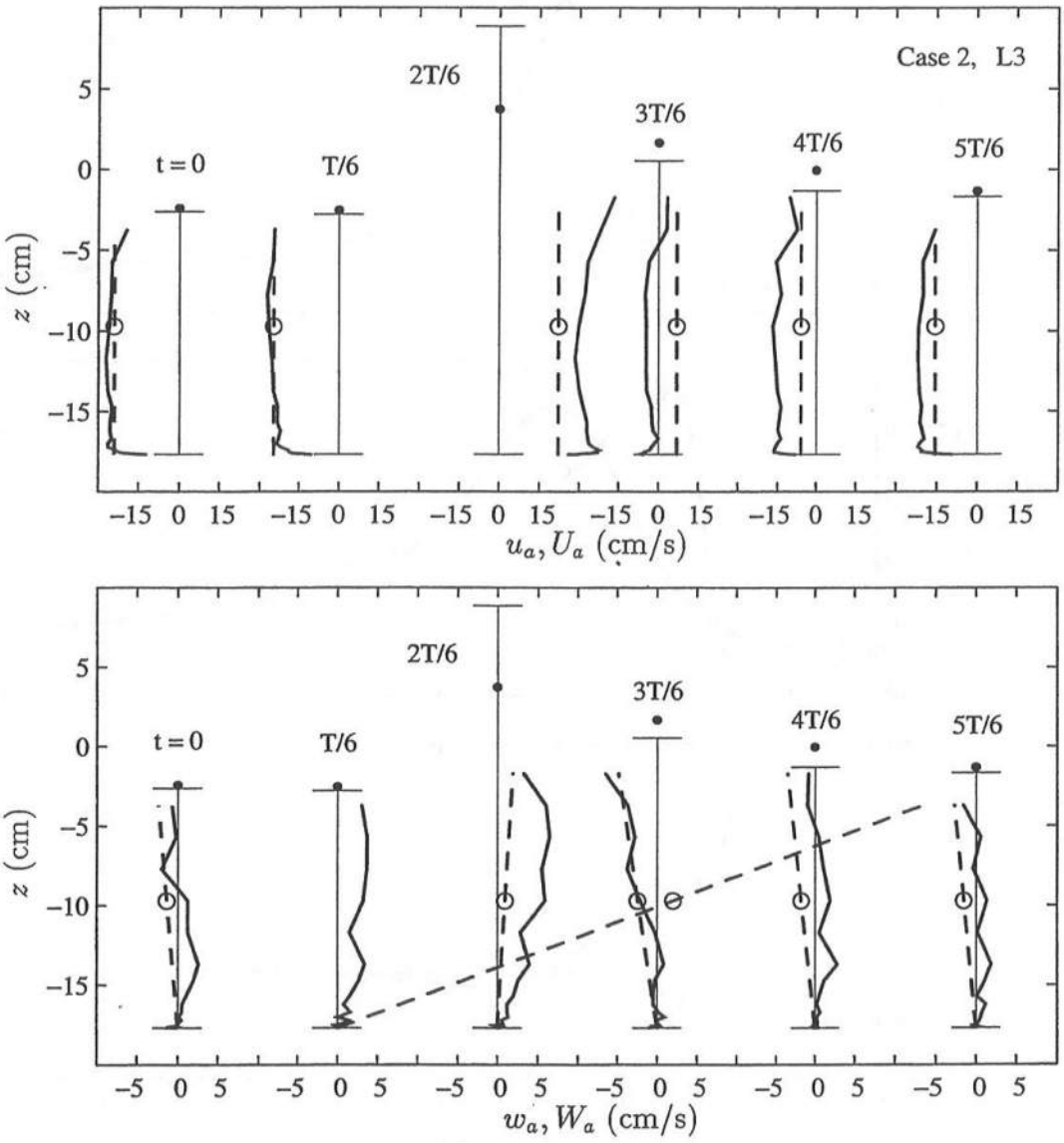

Figure 7.29: Vertical Variations of Horizontal Velocity: Measured, u_a(——), and Computed, U_a(– –○), (Top); Vertical Velocity: Measured, w_a(——), and Computed, W_a(– –○), (Bottom); and Free Surface Elevation: Measured, η_a(——), and Computed, η_{ac}(●), (Both); at Six Phases for Case 2 at L3.

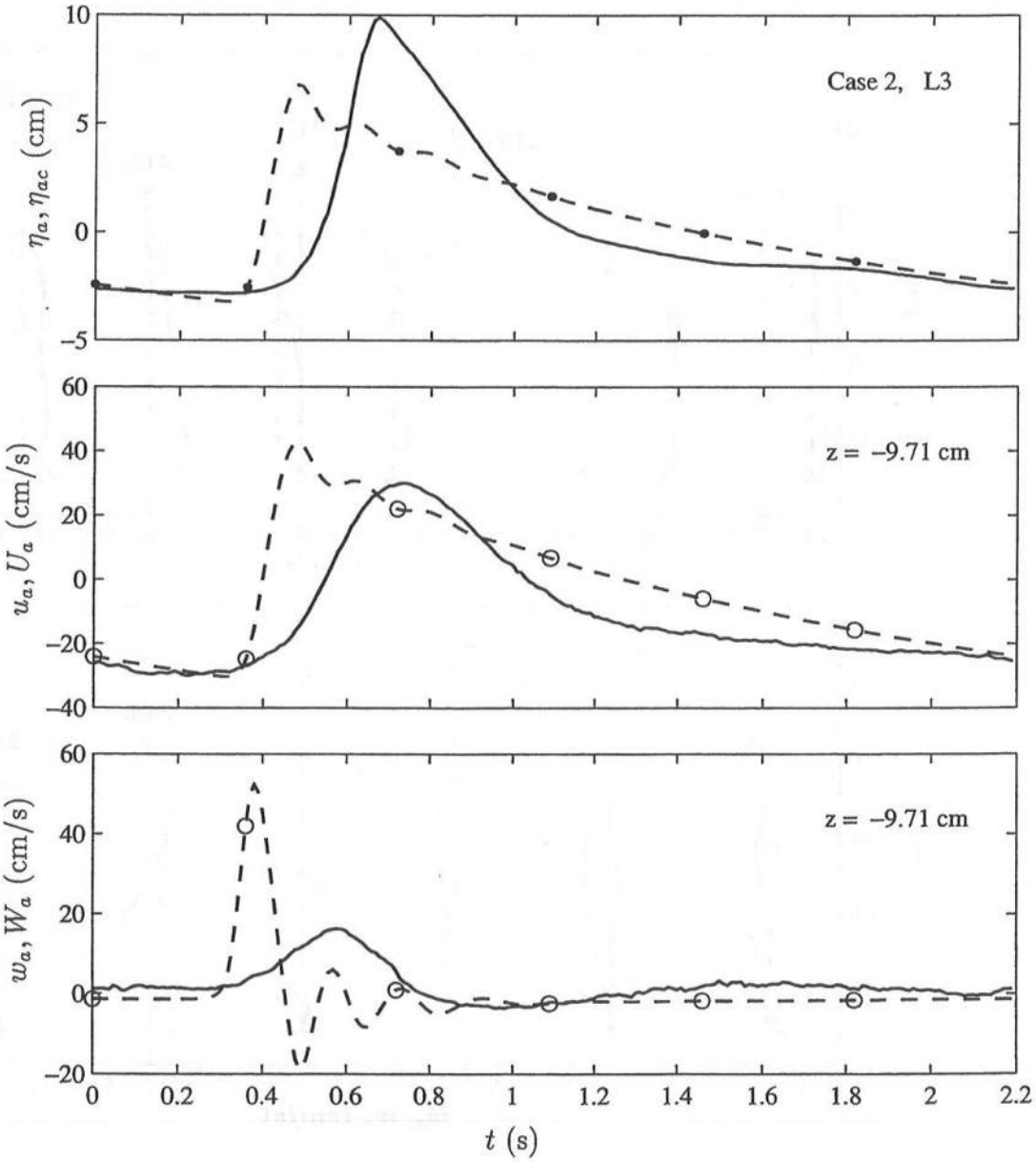

Figure 7.30: Temporal Variations of Free Surface Elevation: Measured, η_a(——), and Computed, η_{ac}(– –•), (Top); Horizontal Velocity: Measured, u_a(——), and Computed, U_a(– –○), (Middle); and Vertical Velocity: Measured, w_a(——), and Computed, W_a(– –○), (Bottom); at $z = -9.71$ cm for Case 2 at L3.

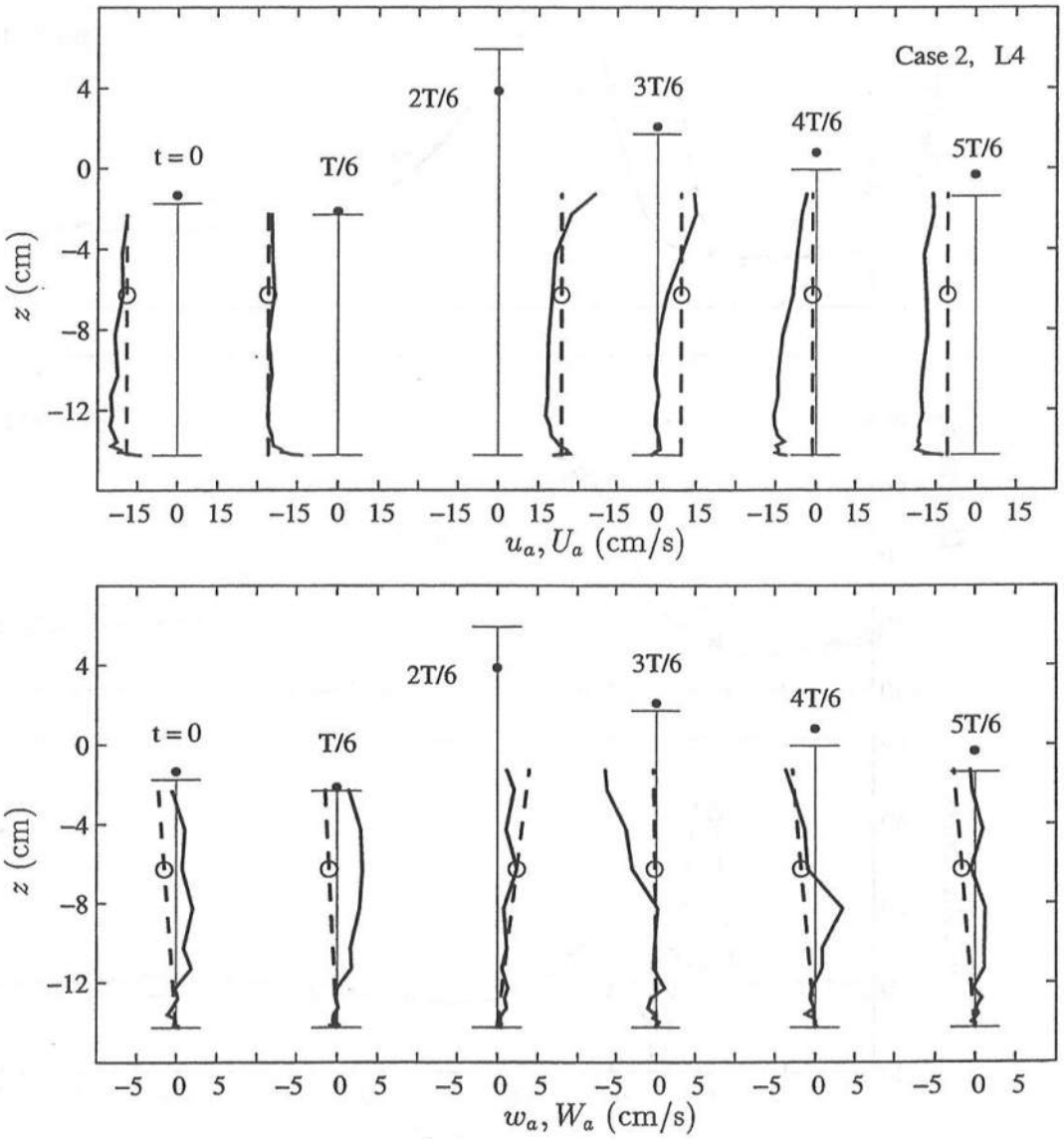

Figure 7.31: Vertical Variations of Horizontal Velocity: Measured, u_a(——), and Computed, U_a(– –○), (Top); Vertical Velocity: Measured, w_a(——), and Computed, W_a(– –○), (Bottom); and Free Surface Elevation: Measured, η_a(——), and Computed, η_{ac}(●), (Both); at Six Phases for Case 2 at L4.

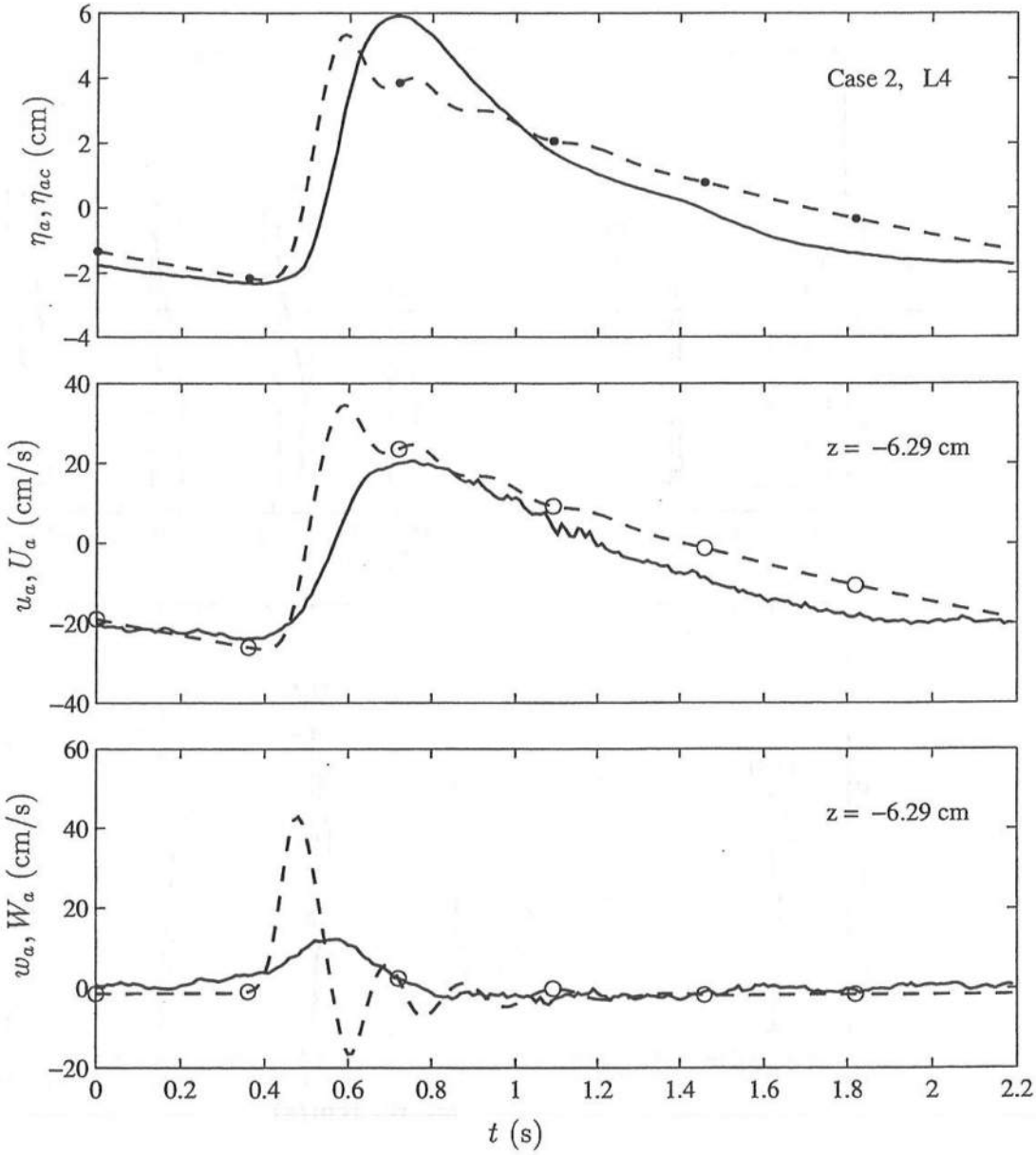

Figure 7.32: Temporal Variations of Free Surface Elevation: Measured, η_a(——), and Computed, η_{ac}(– –•), (Top); Horizontal Velocity: Measured, u_a(——), and Computed, U_a(– –○), (Middle); and Vertical Velocity: Measured, w_a(——), and Computed, W_a(– –○), (Bottom); at $z = -6.29$ cm for Case 2 at L4.

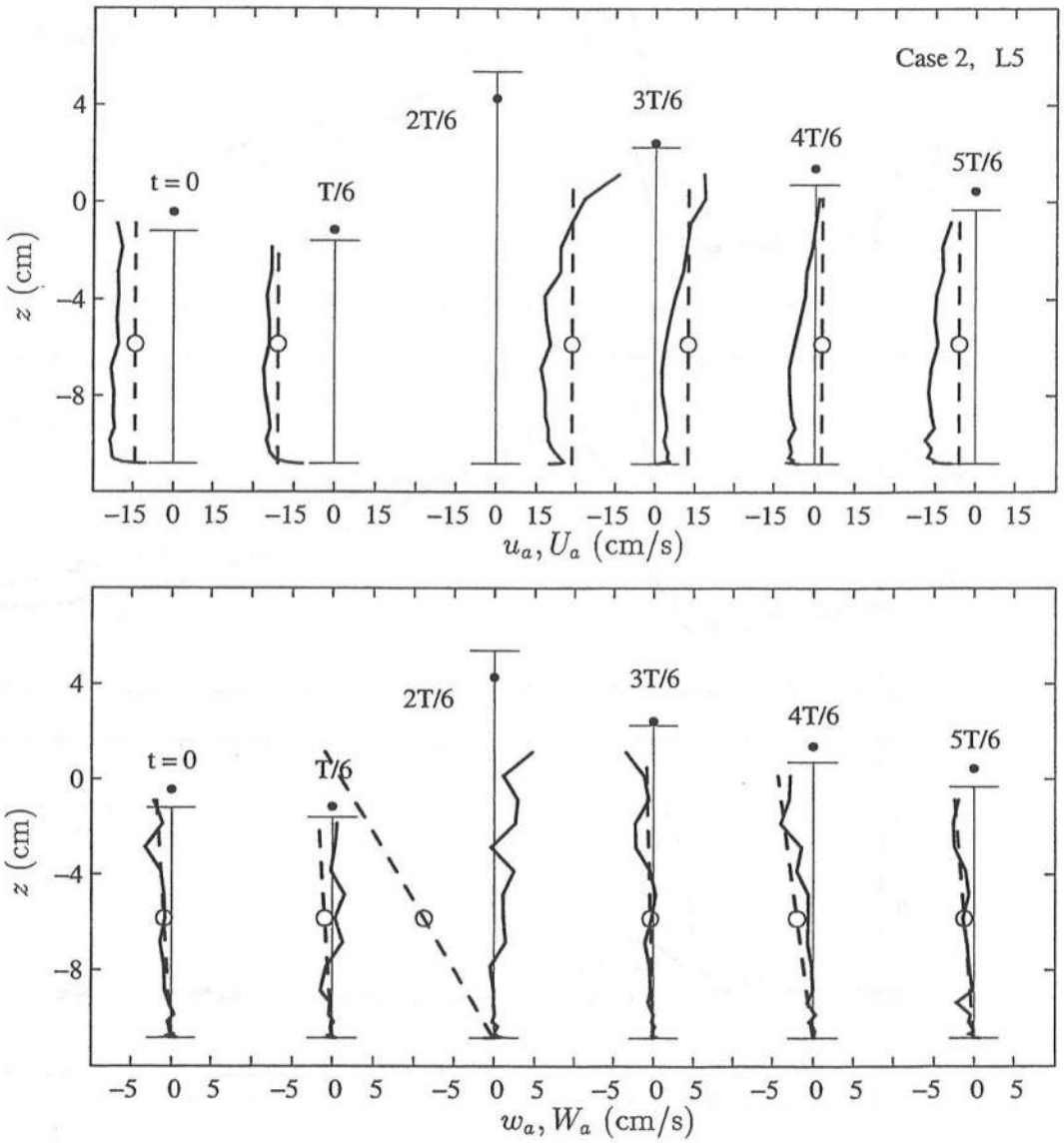

Figure 7.33: Vertical Variations of Horizontal Velocity: Measured, u_a(——), and Computed, U_a(– –○), (Top); Vertical Velocity: Measured, w_a(——), and Computed, W_a(– –○), (Bottom); and Free Surface Elevation: Measured, η_a(——), and Computed, η_{ac}(●), (Both); at Six Phases for Case 2 at L5.

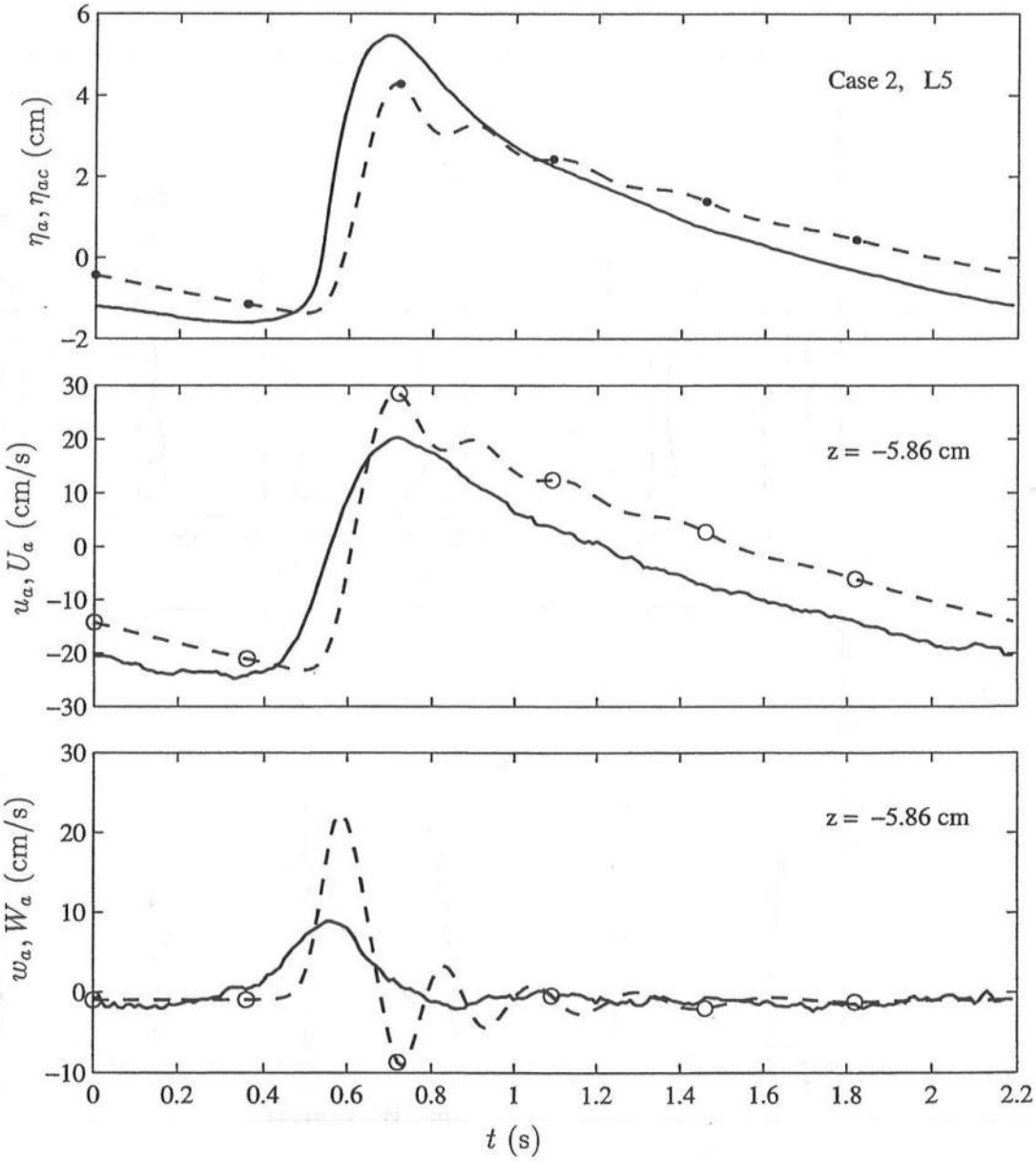

Figure 7.34: Temporal Variations of Free Surface Elevation: Measured, η_a(——), and Computed, η_{ac}(– –•), (Top); Horizontal Velocity: Measured, u_a(——), and Computed, U_a(– –○), (Middle); and Vertical Velocity: Measured, w_a(——), and Computed, W_a(– –○), (Bottom); at $z = -5.86$ cm for Case 2 at L5.

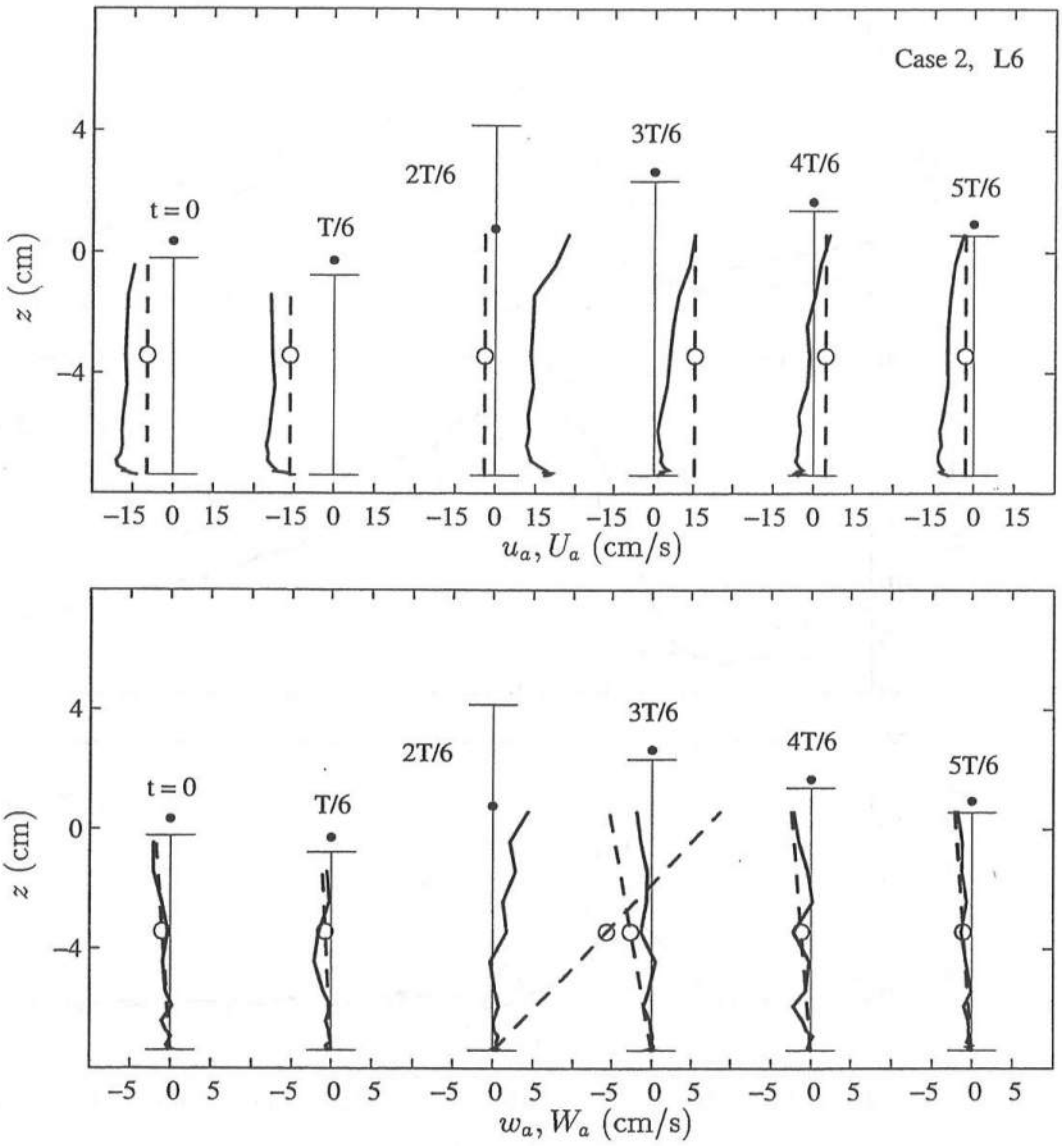

Figure 7.35: Vertical Variations of Horizontal Velocity: Measured, u_a(——), and Computed, U_a(– –○), (Top); Vertical Velocity: Measured, w_a(——), and Computed, W_a(– –○), (Bottom); and Free Surface Elevation: Measured, η_a(——), and Computed, η_{ac}(•), (Both); at Six Phases for Case 2 at L6.

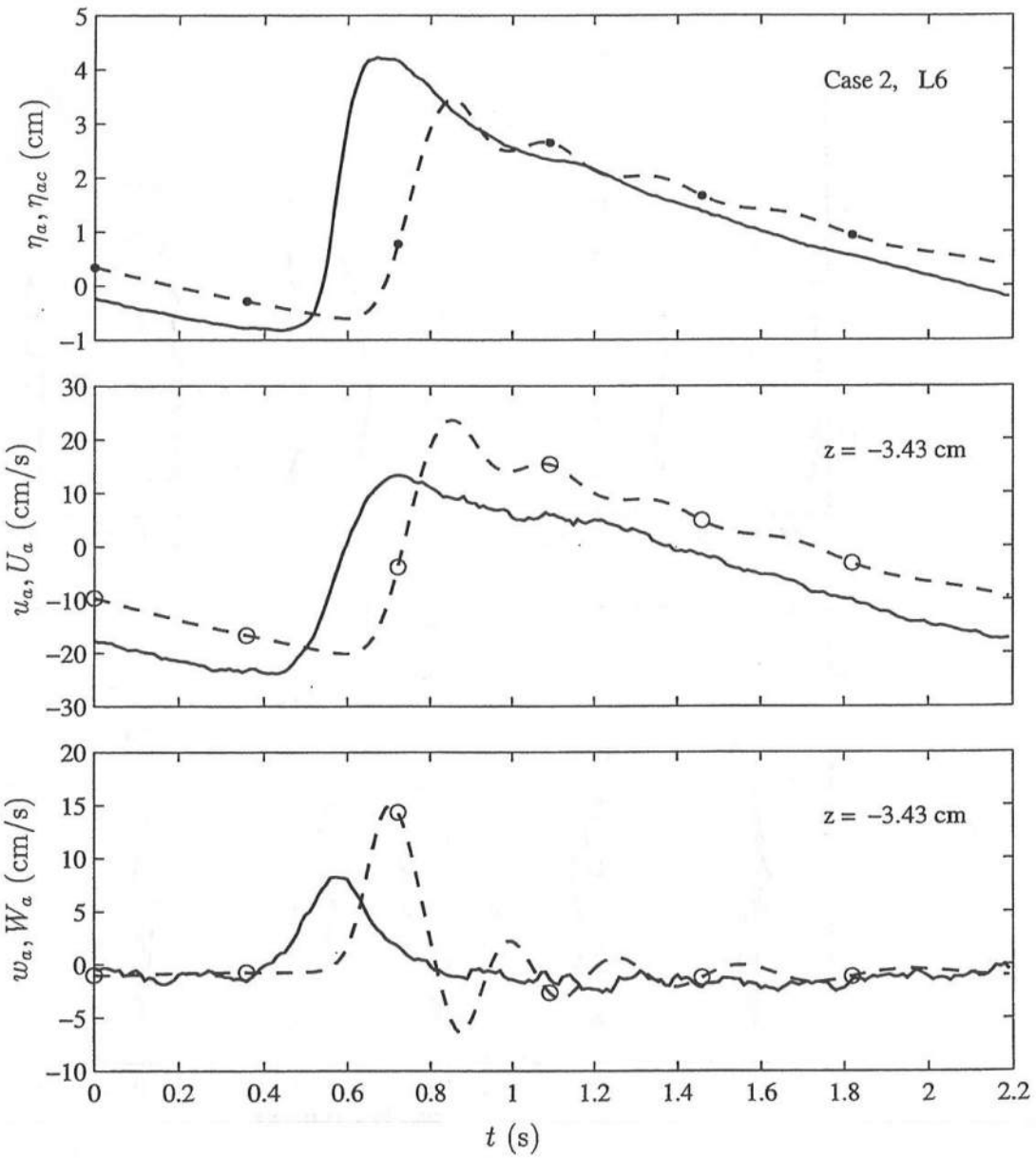

Figure 7.36: Temporal Variations of Free Surface Elevation: Measured, η_a(——), and Computed, η_{ac}(– –•), (Top); Horizontal Velocity: Measured, u_a(——), and Computed, U_a(– –○), (Middle); and Vertical Velocity: Measured, w_a(——), and Computed, W_a(– –○), (Bottom); at $z = -3.43$ cm for Case 2 at L6.

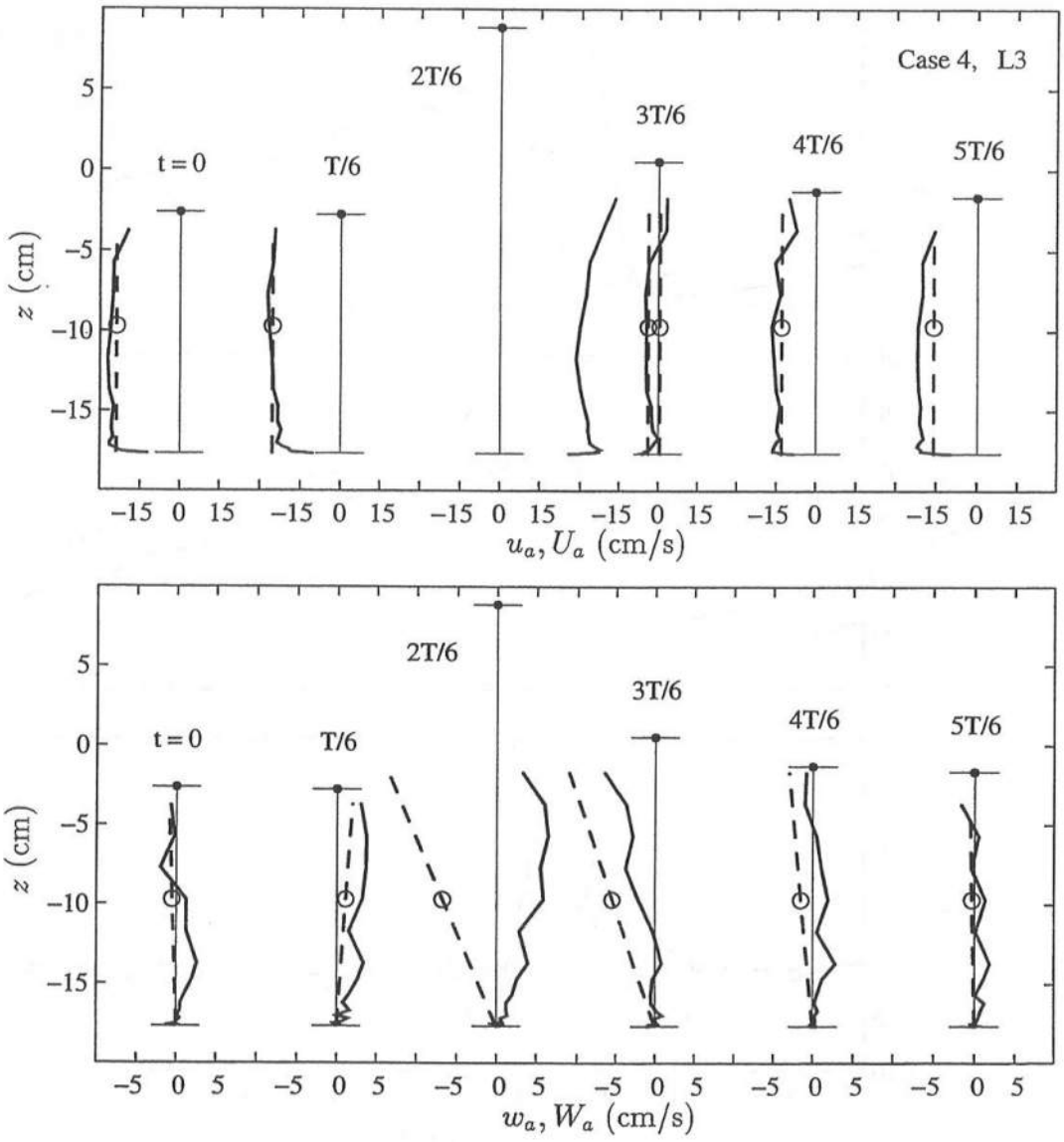

Figure 7.37: Vertical Variations of Horizontal Velocity: Measured, u_a(——), and Computed, U_a(– –○), (Top); Vertical Velocity: Measured, w_a(——), and Computed, W_a(– –○), (Bottom); and Free Surface Elevation: Measured, η_a(——), and Computed, η_{ac}(●), (Both); at Six Phases for Case 4 at L3.

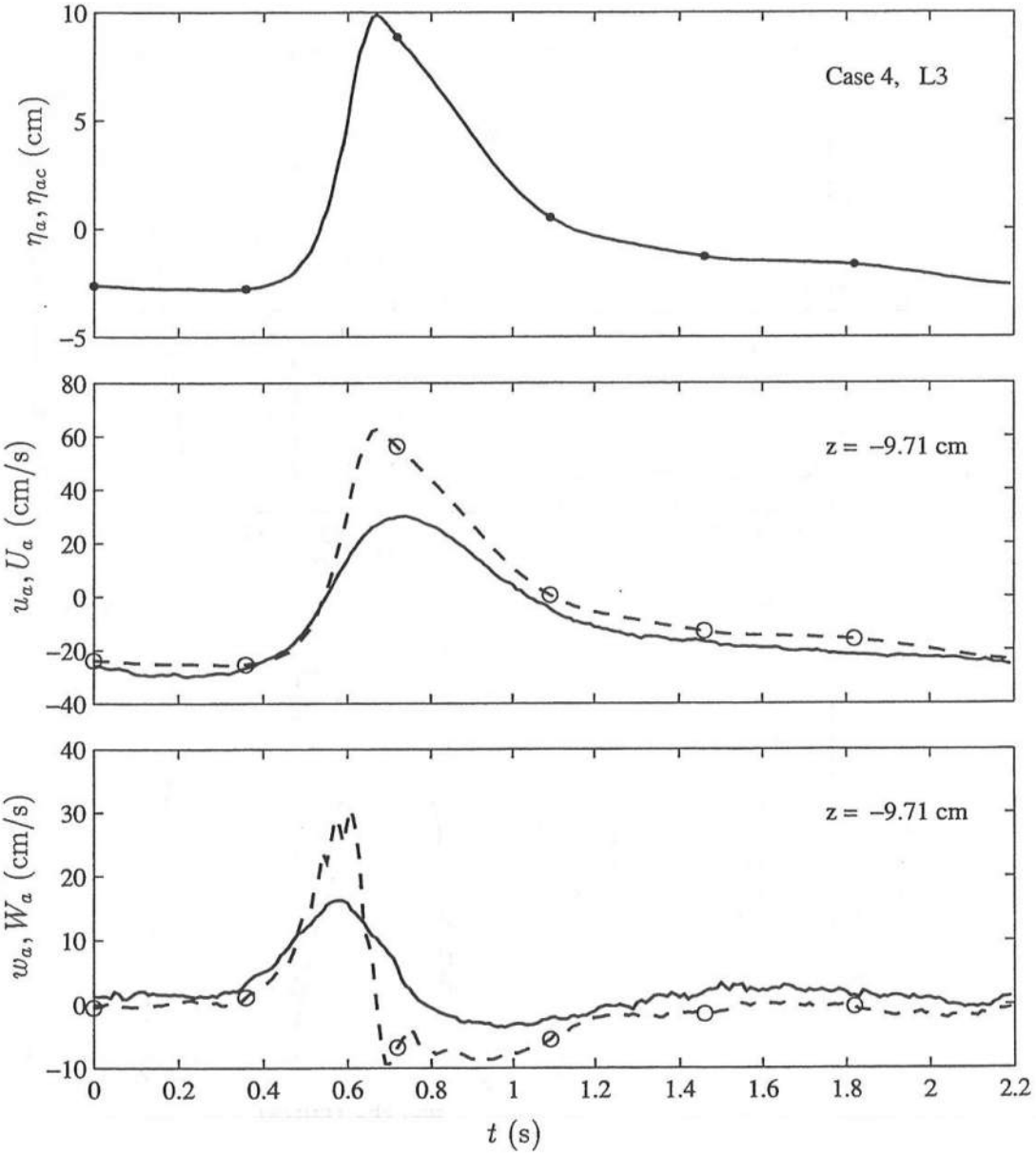

Figure 7.38: Temporal Variations of Free Surface Elevation: Measured, η_a(——), and Computed, η_{ac}(– –•), (Top); Horizontal Velocity: Measured, u_a(——), and Computed, U_a(– –○), (Middle); and Vertical Velocity: Measured, w_a(——), and Computed, W_a(– –○), (Bottom); at $z = -9.71$ cm for Case 4 at L3.

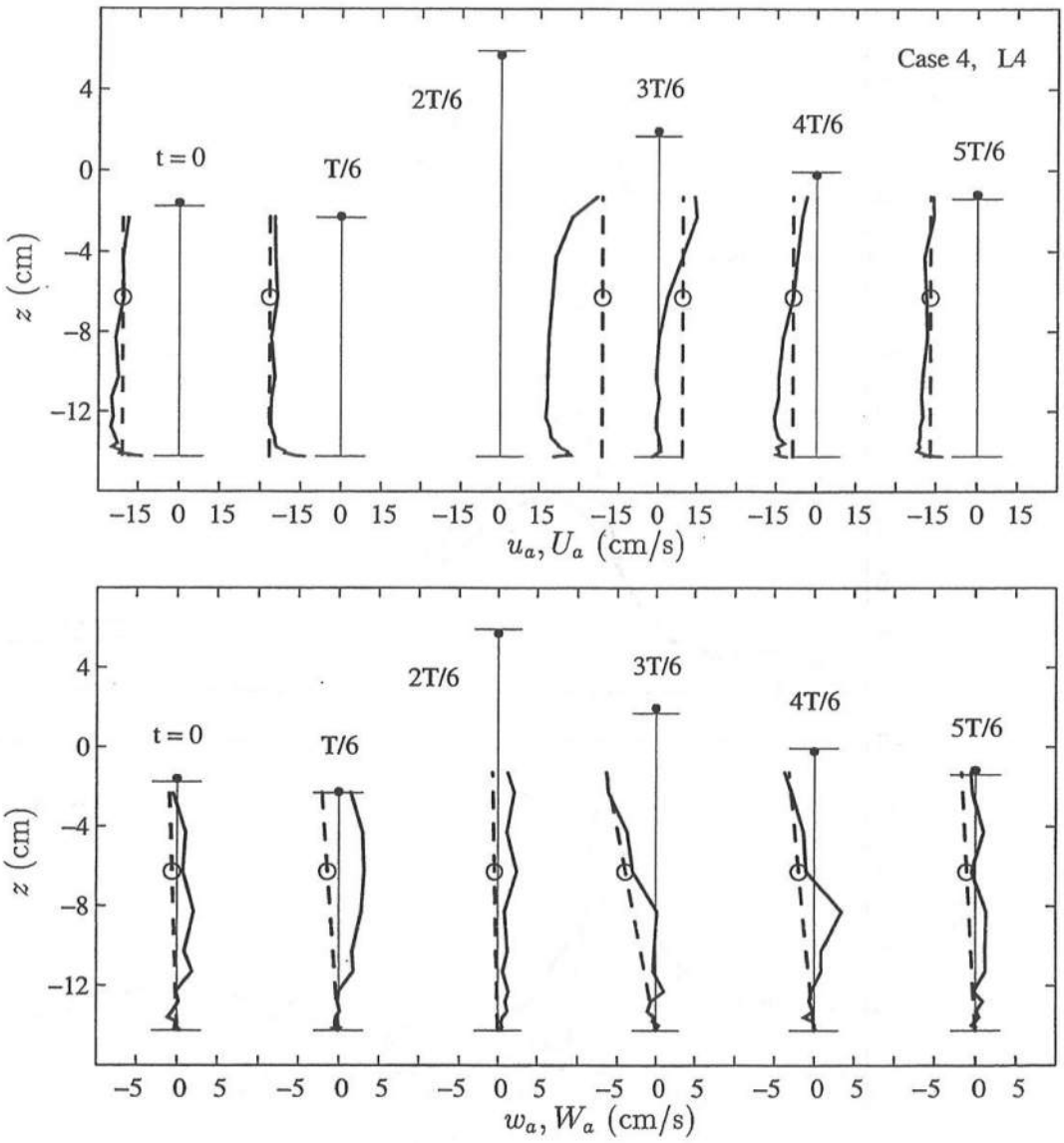

Figure 7.39: Vertical Variations of Horizontal Velocity: Measured, u_a(——), and Computed, U_a(– –○), (Top); Vertical Velocity: Measured, w_a(——), and Computed, W_a(– –○), (Bottom); and Free Surface Elevation: Measured, η_a(——), and Computed, η_{ac}(●), (Both); at Six Phases for Case 4 at L4.

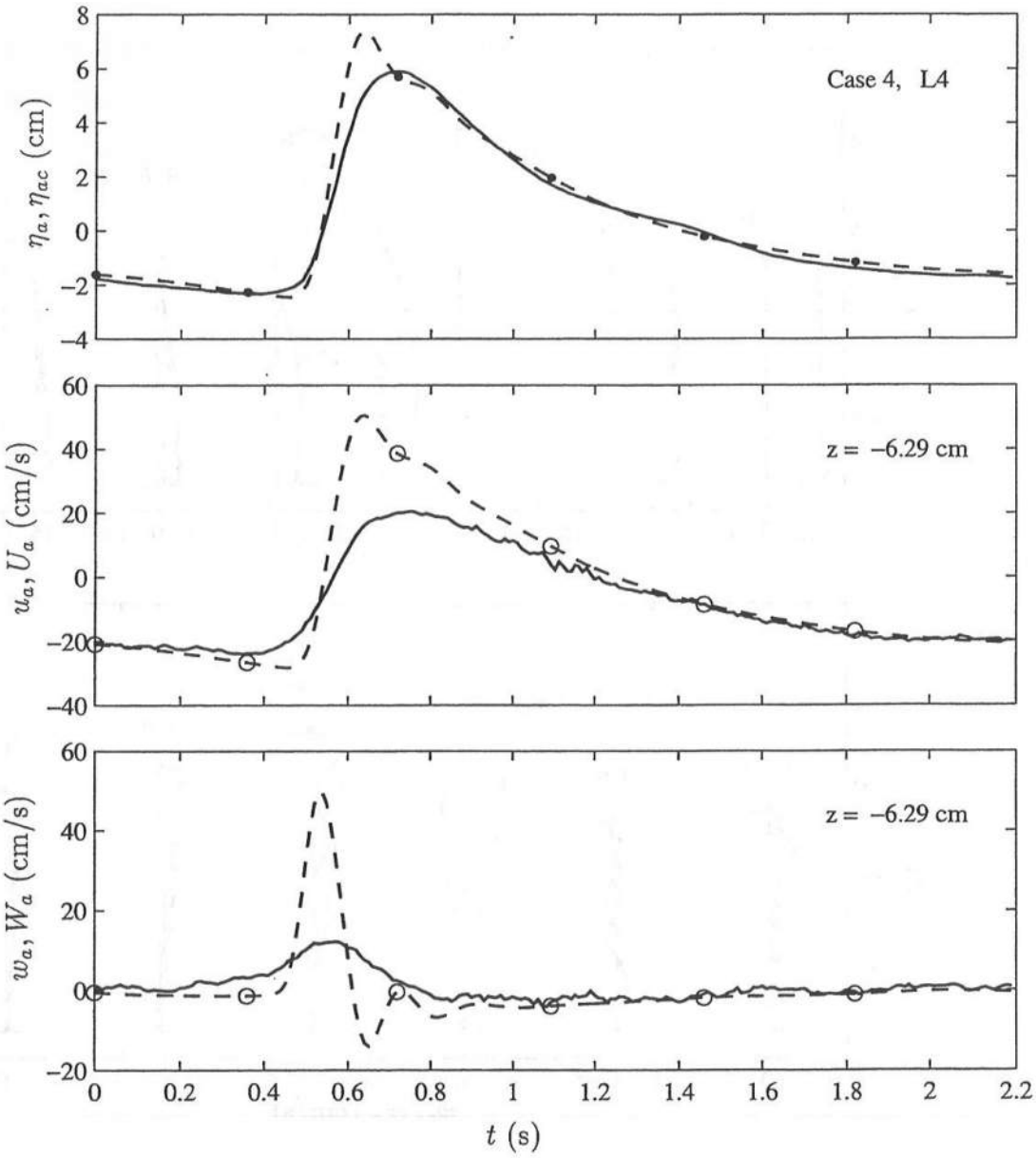

Figure 7.40: Temporal Variations of Free Surface Elevation: Measured, η_a(——), and Computed, η_{ac}(– –•), (Top); Horizontal Velocity: Measured, u_a(——), and Computed, U_a(– –○), (Middle); and Vertical Velocity: Measured, w_a(——), and Computed, W_a(– –○), (Bottom); at $z = -6.29$ cm for Case 4 at L4.

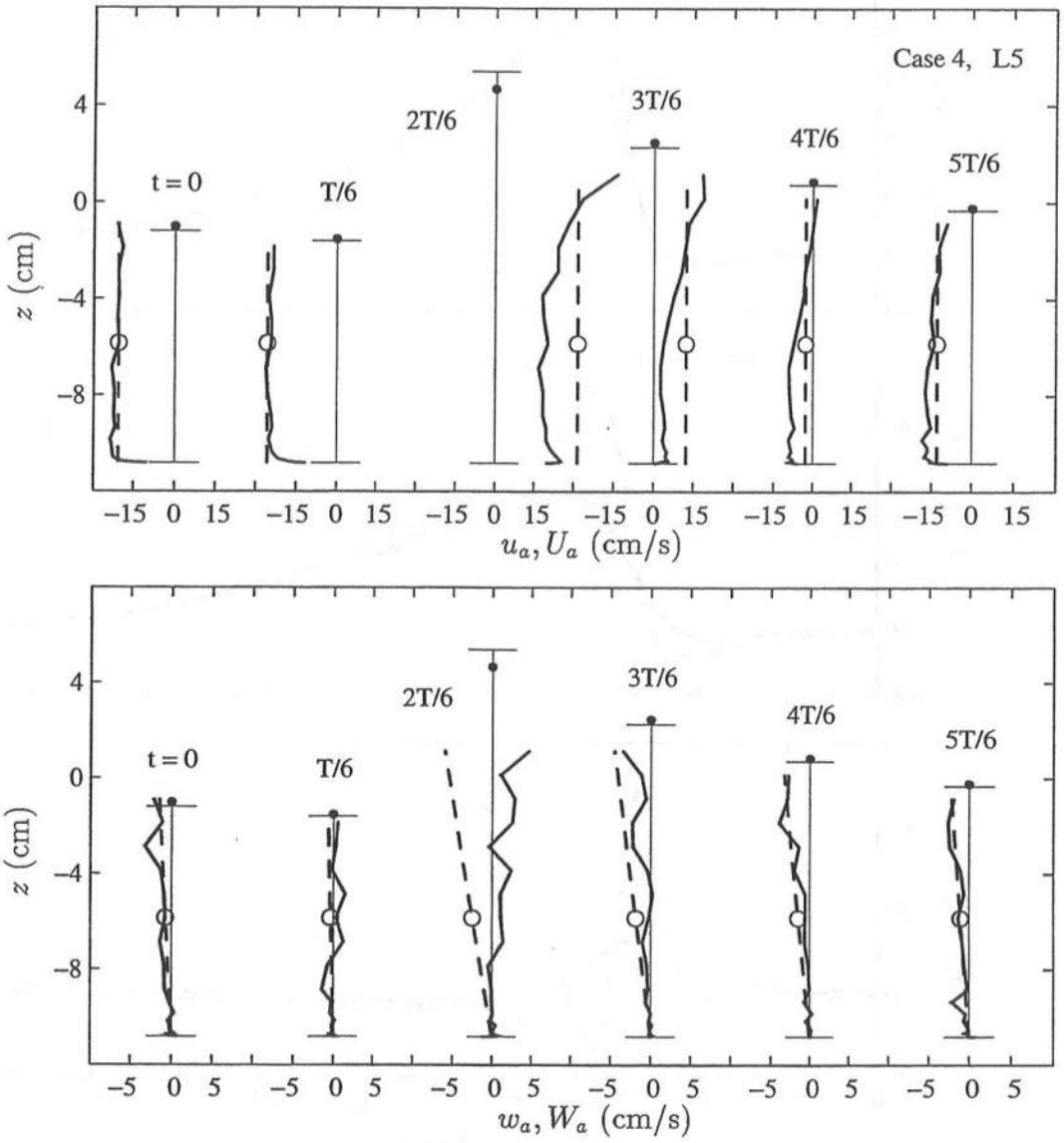

Figure 7.41: Vertical Variations of Horizontal Velocity: Measured, u_a(——), and Computed, U_a(– –○), (Top); Vertical Velocity: Measured, w_a(——), and Computed, W_a(– –○), (Bottom); and Free Surface Elevation: Measured, η_a(——), and Computed, η_{ac}(•), (Both); at Six Phases for Case 4 at L5.

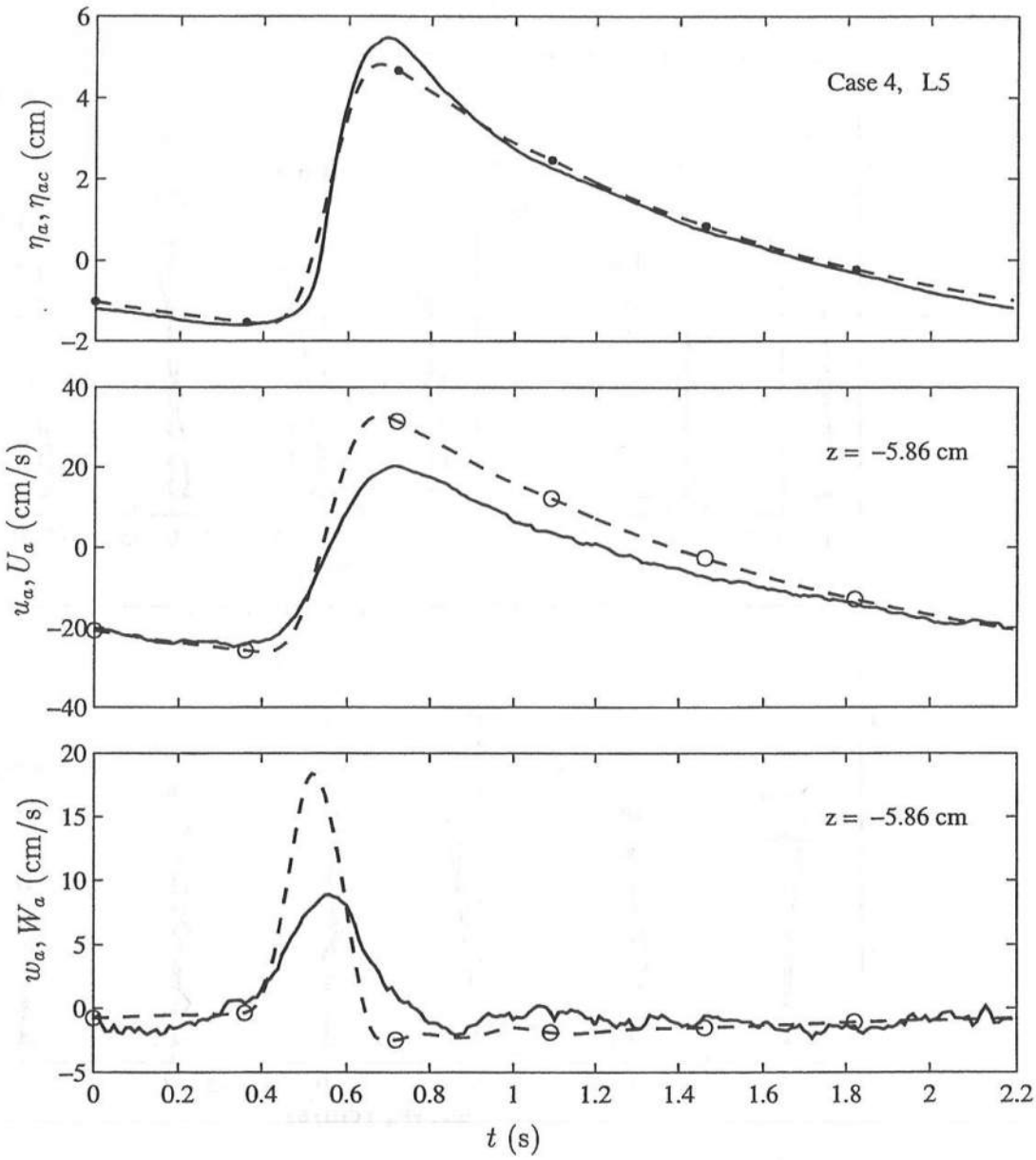

Figure 7.42: Temporal Variations of Free Surface Elevation: Measured, η_a(——), and Computed, η_{ac}(– –•), (Top); Horizontal Velocity: Measured, u_a(——), and Computed, U_a(– –○), (Middle); and Vertical Velocity: Measured, w_a(——), and Computed, W_a(– –○), (Bottom); at $z = -5.86$ cm for Case 4 at L5.

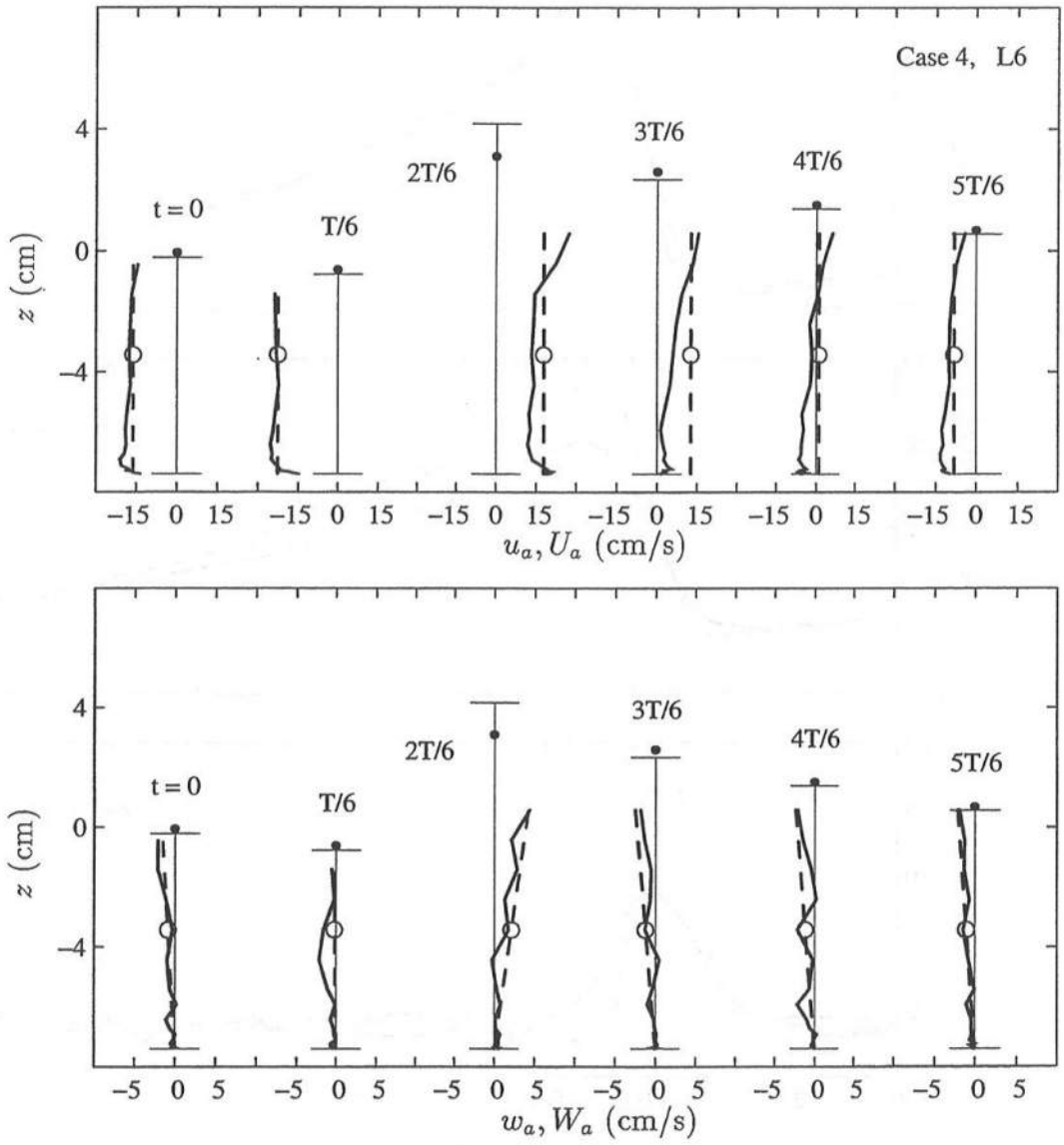

Figure 7.43: Vertical Variations of Horizontal Velocity: Measured, u_a(——), and Computed, U_a(– –○), (Top); Vertical Velocity: Measured, w_a(——), and Computed, W_a(– –○), (Bottom); and Free Surface Elevation: Measured, η_a(——), and Computed, η_{ac}(•), (Both); at Six Phases for Case 4 at L6.

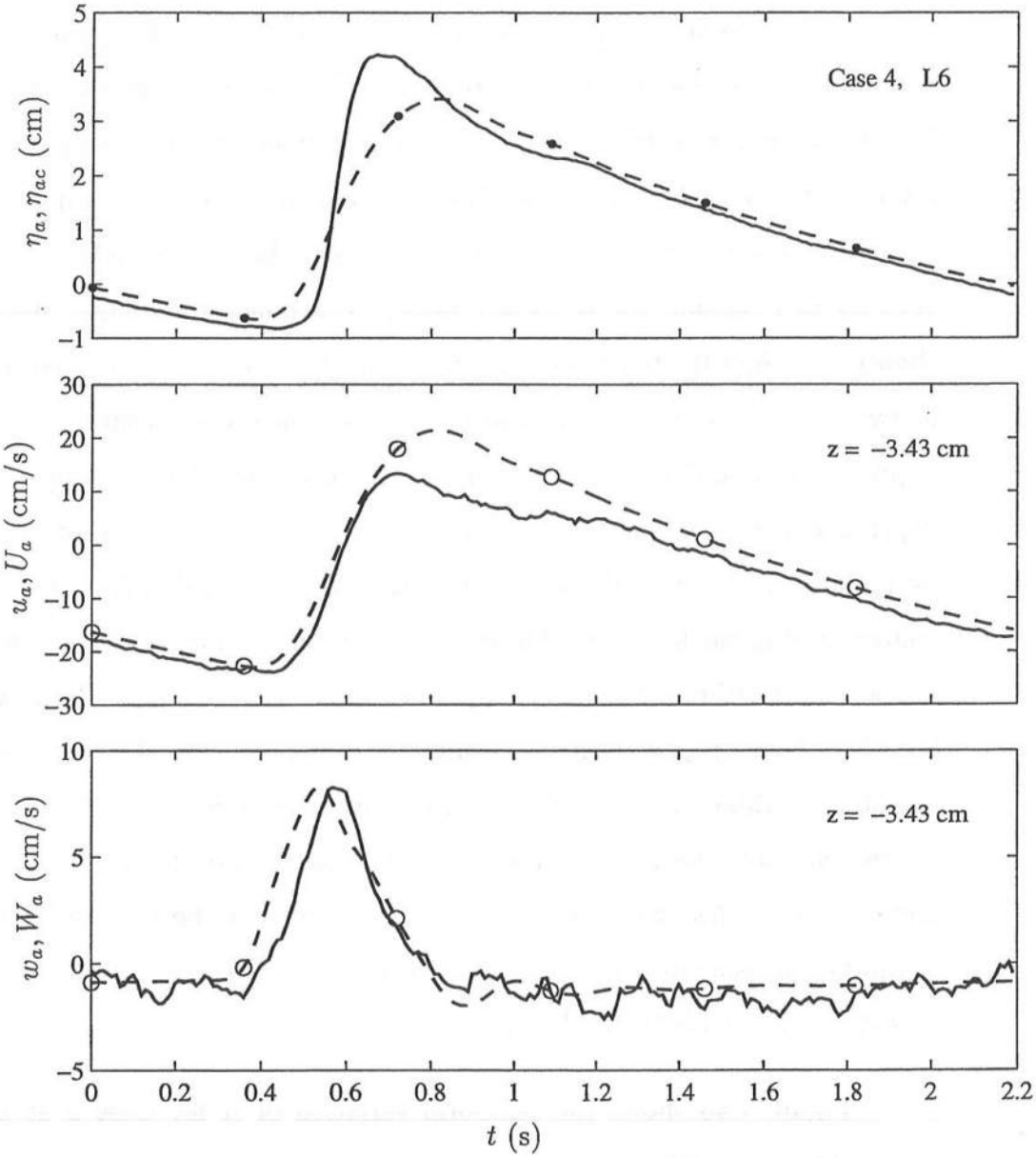

Figure 7.44: Temporal Variations of Free Surface Elevation: Measured, η_a(——), and Computed, η_{ac}(– –•), (Top); Horizontal Velocity: Measured, u_a(——), and Computed, U_a(– –○), (Middle); and Vertical Velocity: Measured, w_a(——), and Computed, W_a(– –○), (Bottom); at $z = -3.43$ cm for Case 4 at L6.

7.6 Bottom Shear Stress Comparisons

Comparisons are made in this section of the temporal variation of the bottom shear stress, τ_b. In Chapter 5, the bottom shear stress was estimated by a least-squares fit of the phase-averaged horizontal velocity in the logarithmic layer of the lower portion of the bottom boundary layer. An empirical friction factor was used to relate the estimated bottom shear stress and the horizontal velocity just outside the boundary layer. The quadratic friction equation was shown to predict the temporal variation of the bottom shear stress within a factor of two. A friction factor was also fitted based on the horizontal velocity at an approximate mid-depth elevation. In this section, the phase-averaged computed depth-averaged horizontal velocity, U_a, is used to predict the bottom shear stress from Equation 7.3 with the assumed friction factor, f. Table 7.4 lists the friction factors used in the figures in this section where the friction factors are denoted as follows: f_w is estimated from u_a at $z_m = 1.6$ cm above the bottom, just outside the boundary layer; f_{mid} is estimated from u_a at $z = z_{mid}$ below the wave trough level as listed in Table 7.3 for each measuring line; and f is the friction factor used for the computations. Table 7.4 shows that the friction factors fitted from the measured velocities vary across the surf zone and that the friction factor for the computations is assumed constant across the surf zone. It is noted that $f_w \simeq f_{mid}$ except at L1 outside the surf zone.

Figure 7.45 shows the temporal variation of τ_b for Case 2 at L1 and is similar to Figure 5.60. The three curves using the quadratic friction equation with f_w, f_{mid}, and f predict the estimated shear stress reasonably at the seaward boundary.

Figures 7.46 and 7.47 show that the temporal variation of the bottom shear stress is not well predicted by the computed depth-averaged velocity, particularly

Table 7.4: Friction Factors for Measured and Computed Bottom Shear Stress Estimates for L1 to L6.

Line No.	Measured f_w	Measured f_{mid}	Computed f
L1	0.025	0.018	0.015, 0.05
L2	0.014	0.014	0.015
L3	0.017	0.016	0.015
L4	0.016	0.018	0.015
L5	0.026	0.027	0.015
L6	0.028	0.031	0.015

near the wave crest. This is expected since the errors in the predicted horizontal velocity are squared in computing the bottom shear stress. This emphasizes the accuracy necessary for hydrodynamics models used as input for predictive sediment transport models.

Figures 7.48, 7.49 and 7.50 for the inner surf zone also show the that the model can predict only qualitatively the temporal variation of the bottom shear stress. Figures 7.51 to 7.54 for Case 4 show that the model does not predict τ_b well in the surf zone. The poor agreement is due to the amplification of the error in the predicted velocity and to the assumption of a constant friction factor. Figure 7.55 shows the temporal variation of τ_b for Case 5 with $f = 0.05$ at L1. This figure shows the sensitivity of the computed bottom shear stress to f. Comparing Figures 7.45 and 7.55, $f = 0.015$ gives better agreement than $f = 0.05$ for this set of laboratory data. It is encouraging to note that $f = 0.015$ was the value calibrated by Raubenheimer *et al.* (1995) using runup data on a gently sloping natural beach.

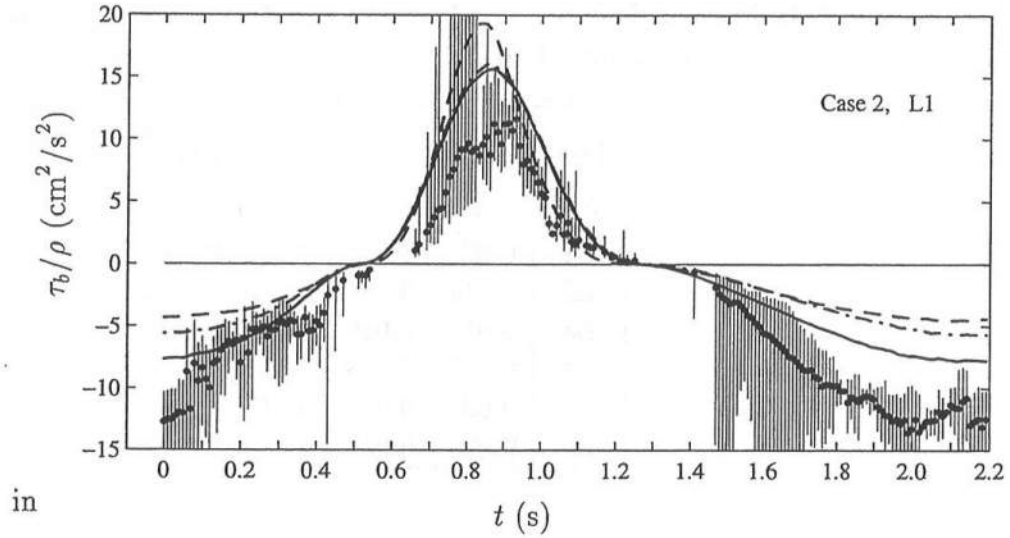

Figure 7.45: Temporal Variation of Bottom Shear Stress, τ_b: Estimated from Shear Velocity (•) with 95% Confidence Limits (——); Fitted Curves with f_w (——) and f_{mid} (–·–); and Computed from U_a (– –) for Case 2 at L1.

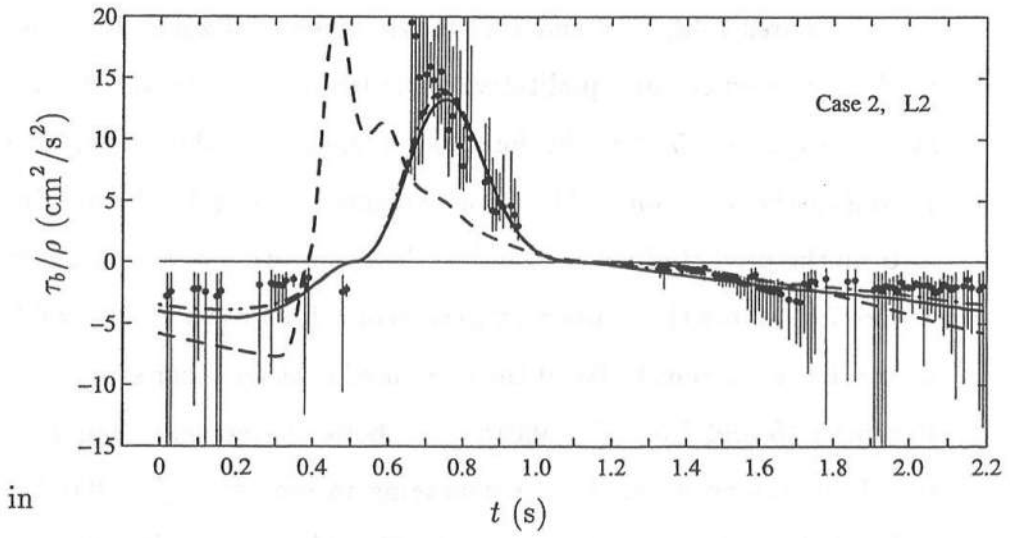

Figure 7.46: Temporal Variation of Bottom Shear Stress, τ_b: Estimated from Shear Velocity (•) with 95% Confidence Limits (——); Fitted Curves with f_w (——) and f_{mid} (–·–); and Computed from U_a (– –) for Case 2 at L2.

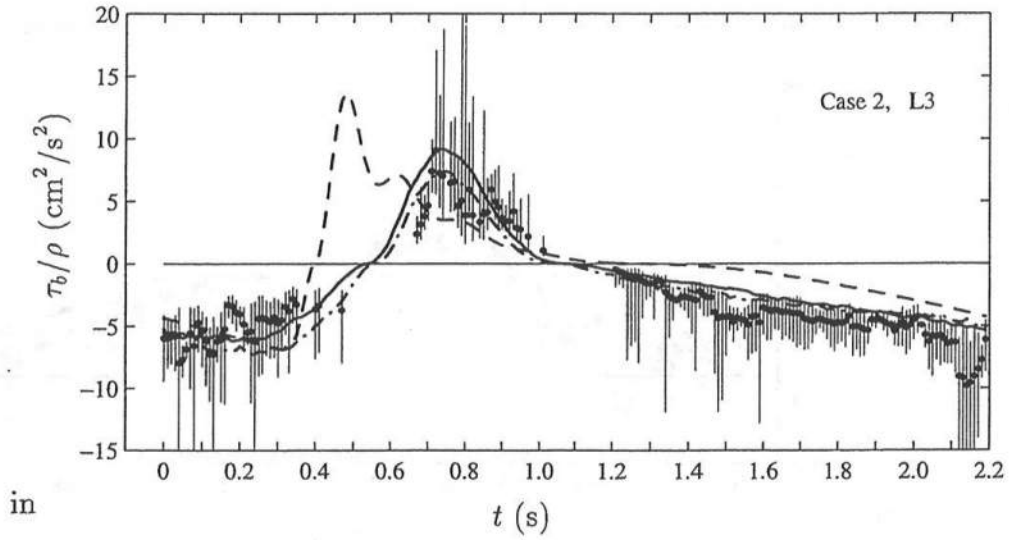

in

Figure 7.47: Temporal Variation of Bottom Shear Stress, τ_b: Estimated from Shear Velocity (•) with 95% Confidence Limits (——); Fitted Curves with f_w (——) and f_{mid} (–·–); and Computed from U_a (– –) for Case 2 at L3.

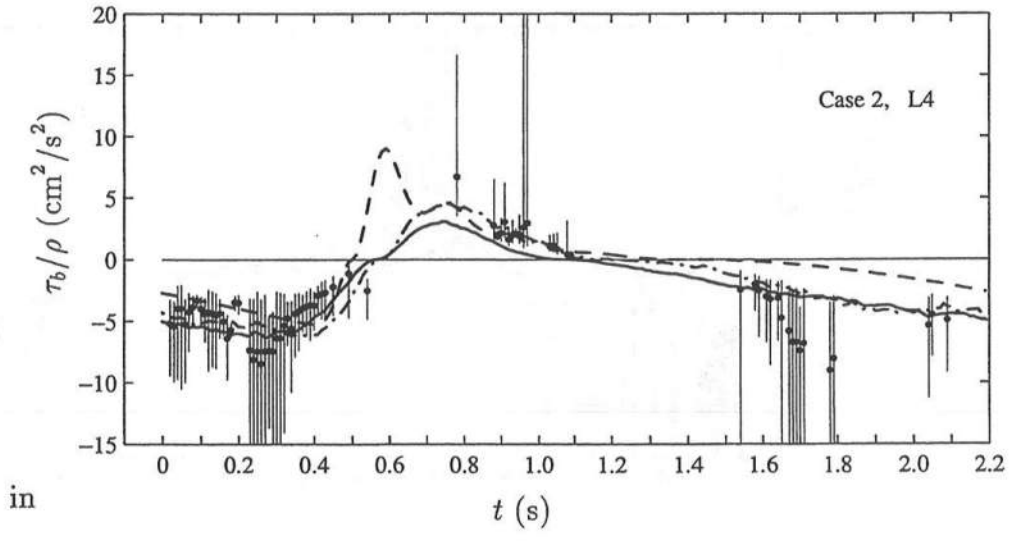

in

Figure 7.48: Temporal Variation of Bottom Shear Stress, τ_b: Estimated from Shear Velocity (•) with 95% Confidence Limits (——); Fitted Curves with f_w (——) and f_{mid} (–·–); and Computed from U_a (– –) for Case 2 at L4.

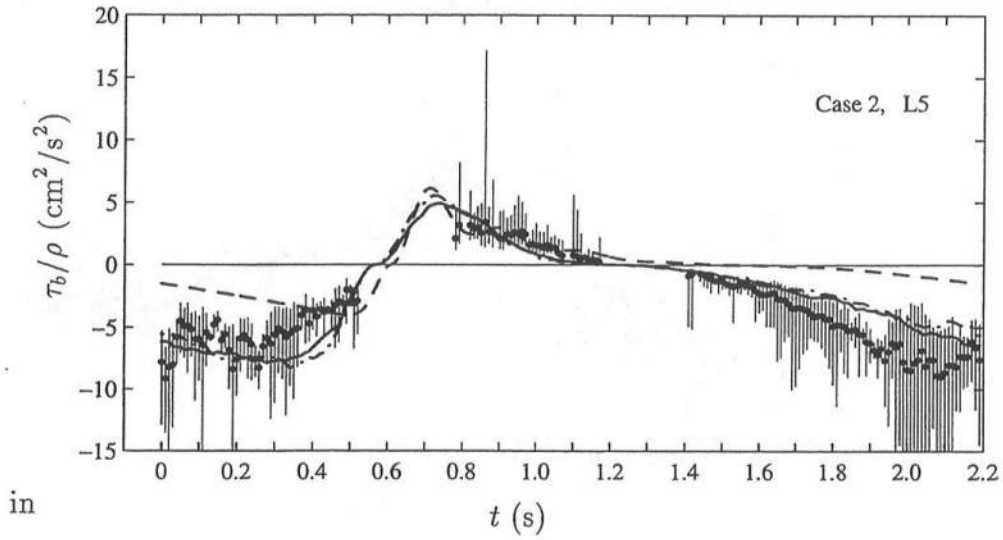

in

Figure 7.49: Temporal Variation of Bottom Shear Stress, τ_b: Estimated from Shear Velocity (•) with 95% Confidence Limits (——); Fitted Curves with f_w (——) and f_{mid} (–·–); and Computed from U_a (– –) for Case 2 at L5.

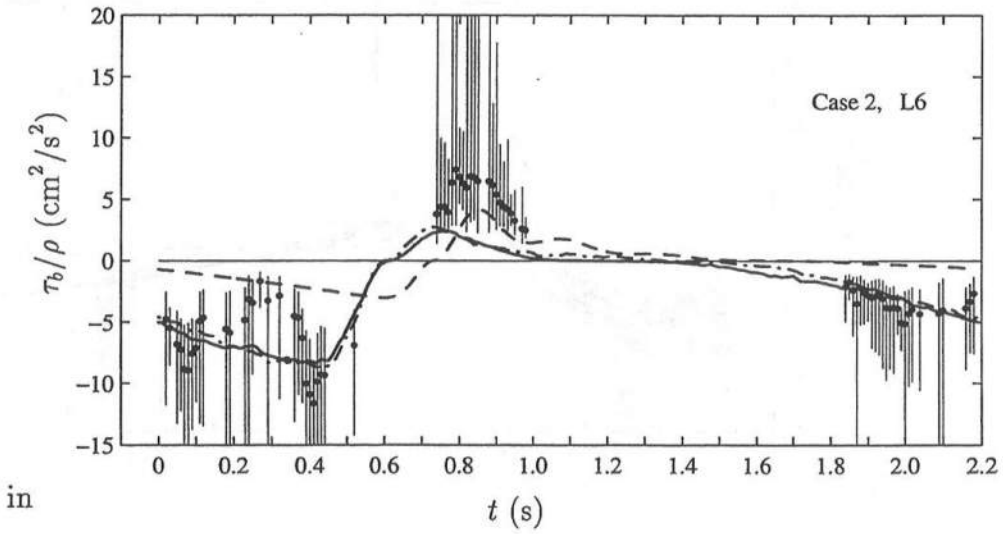

in

Figure 7.50: Temporal Variation of Bottom Shear Stress, τ_b: Estimated from Shear Velocity (•) with 95% Confidence Limits (——); Fitted Curves with f_w (——) and f_{mid} (–·–); and Computed from U_a (– –) for Case 2 at L6.

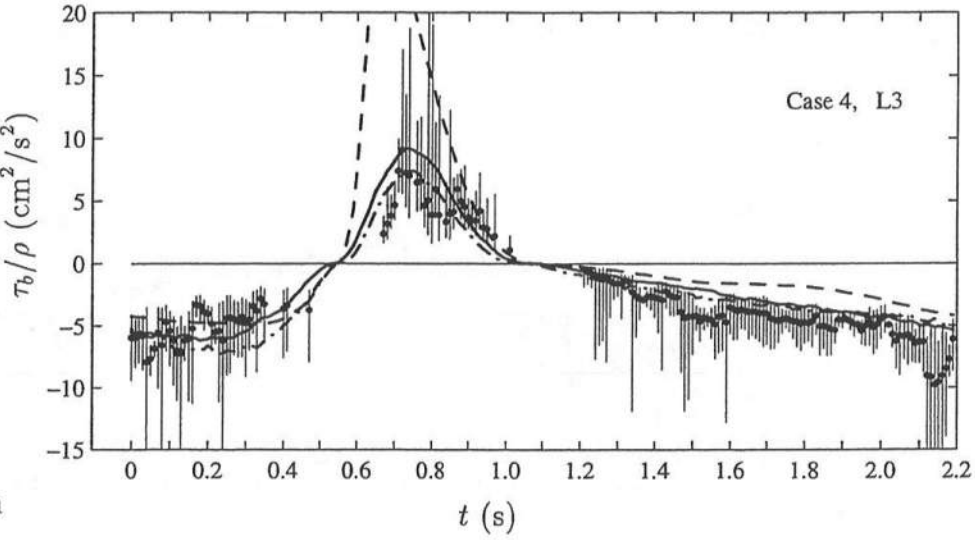

in

Figure 7.51: Temporal Variation of Bottom Shear Stress, τ_b: Estimated from Shear Velocity (•) with 95% Confidence Limits (——); Fitted Curves with f_w (——) and f_{mid} (-·-); and Computed from U_a (– –) for Case 4 at L3.

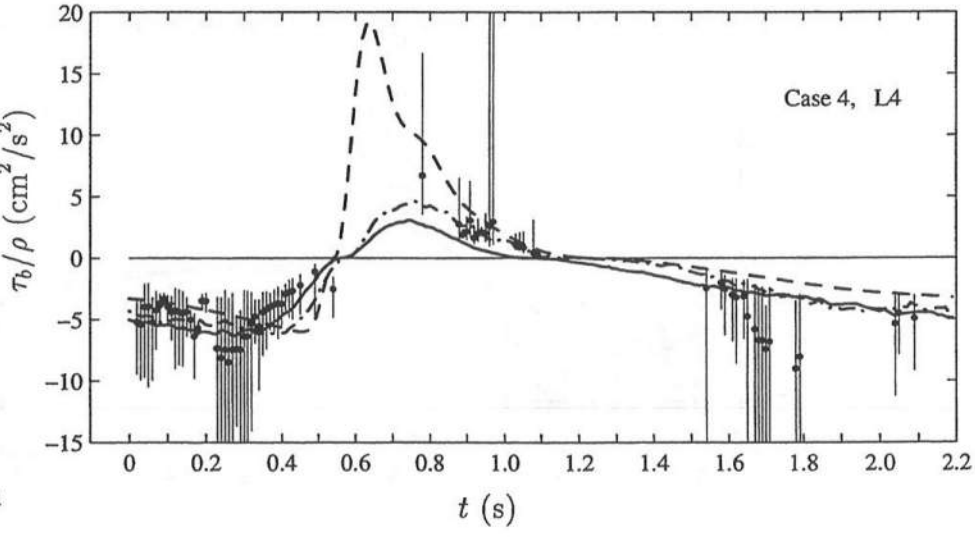

in

Figure 7.52: Temporal Variation of Bottom Shear Stress, τ_b: Estimated from Shear Velocity (•) with 95% Confidence Limits (——); Fitted Curves with f_w (——) and f_{mid} (-·-); and Computed from U_a (– –) for Case 4 at L4.

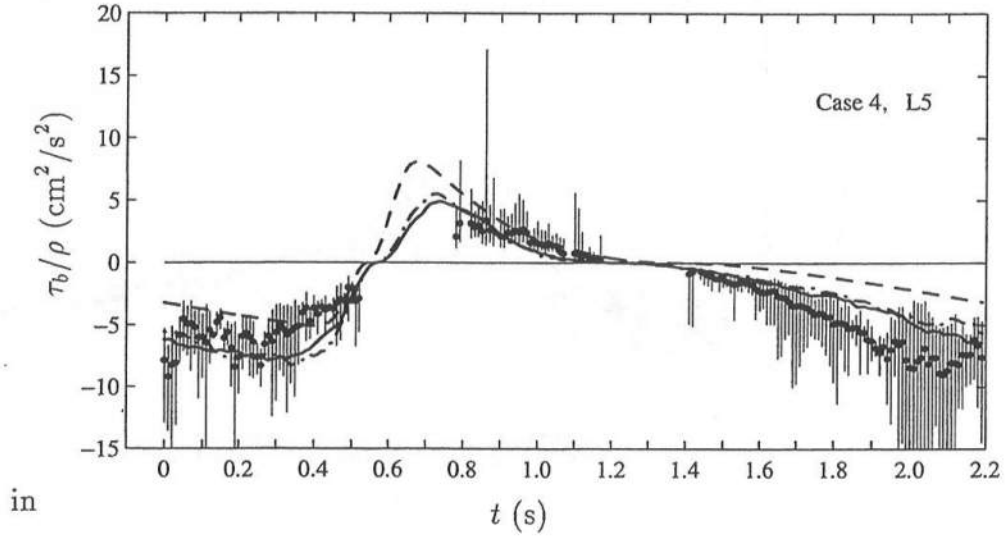

Figure 7.53: Temporal Variation of Bottom Shear Stress, τ_b: Estimated from Shear Velocity (•) with 95% Confidence Limits (——); Fitted Curves with f_w (——) and f_{mid} (-·-); and Computed from U_a (– –) for Case 4 at L5.

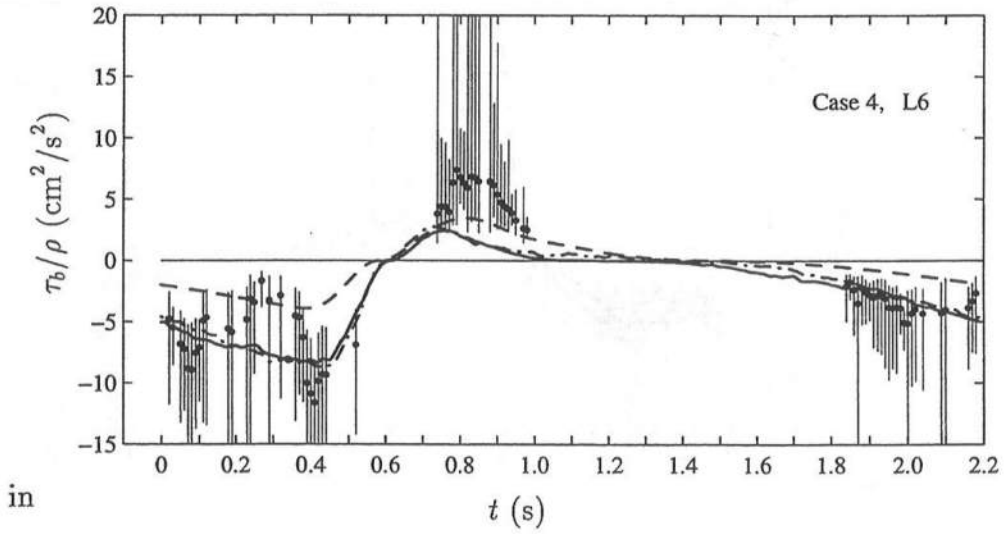

Figure 7.54: Temporal Variation of Bottom Shear Stress, τ_b: Estimated from Shear Velocity (•) with 95% Confidence Limits (——); Fitted Curves with f_w (——) and f_{mid} (-·-); and Computed from U_a (– –) for Case 4 at L6.

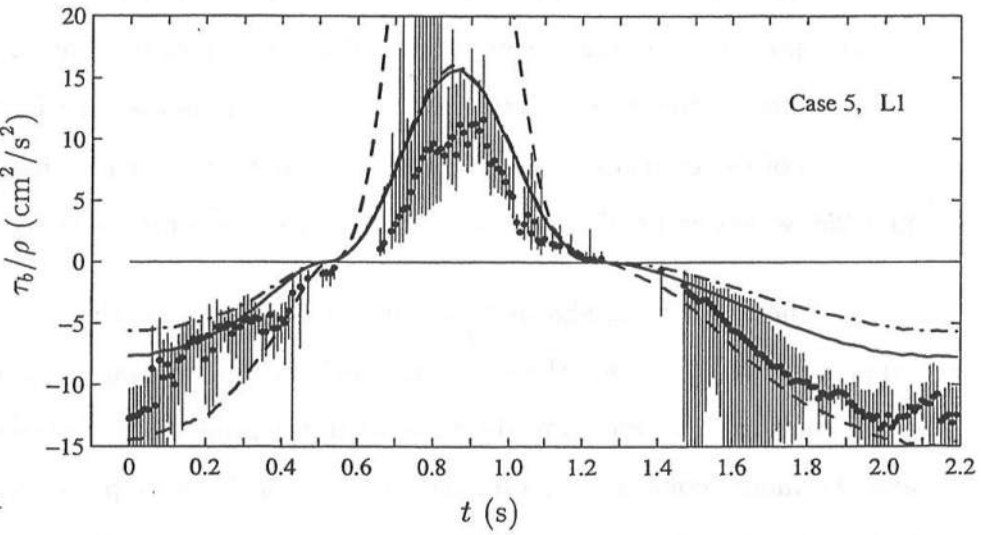

in

Figure 7.55: Temporal Variation of Bottom Shear Stress, τ_b: Estimated from Shear Velocity (•) with 95% Confidence Limits (——); Fitted Curves with f_w (——) and f_{mid} (–·–); and Computed from U_a (– –) for Case 5 at L1.

7.7 Summary of Comparisons with One-Dimensional Numerical Model

In this chapter, the one-dimensional numerical model is used to predict the nonlinear wave characteristics in the surf zone. Six cases were used to evaluate the model's sensitivity to the specification of three options: the bottom friction factor, the location of the seaward boundary, and the specification of the input time series at the seaward boundary.

Transition effects due to the initiation of the model with no wave action in the computational domain were examined for the six cases. The runup time series was used since the effects were amplified at the shoreline. It was found that the duration of the transition effects varied with input options and that truncating the first 250 waves was sufficient to eliminate these effects for the six cases considered.

The model was shown to predict reasonably well the wave profile in the inner surf zone even for the cases in which the model was initiated outside the break point. There was some discrepancy in the predicted phase of the wave front, and the model could not predict the variation of the wave profile in the transition region. For the cases where the model was initiated inside the surf zone, the wave profiles were well predicted across the inner surf zone, and there was less phase error. Comparisons of the phase-averaged free surface elevations showed that the model was fairly insensitive to the assumed friction factor. Comparisons of the standard deviations of the free surface elevations showed that variations specified in the input time series were confined to the front of the computed wave crest and did not vary much across the surf zone.

Comparisons of the horizontal velocities showed that the computed depth-averaged velocity represented the measured profile below trough level fairly well. At the break point and the transition region, the horizontal velocities were not well

predicted under the wave crest since the model does not account for the vertical velocity variation which is expected to be large above the trough level at the break point and in the transition region. In the inner surf zone, the model predicted the measured profiles fairly well, except for the phases where the measured profile were presumably affected by the undertow current.

The computed vertical velocity estimated from the continuity equation represented the measured vertical velocities at least qualitatively over most of the phases. However, the spatial derivatives on U gave poor estimates of the vertical velocity at the steep wave front and on the back of the wave crest due to the small high-frequency numerical oscillations.

The computed bottom shear stress, $\tau_b = \frac{1}{2}\rho f |U| U$, with the constant bottom friction factor, $f = 0.015$, predicted the measured bottom shear stress only qualitatively because the error of the computed velocity is amplified and because the friction factor is not really constant across the surf zone and may vary with time. The assumption of $\tau_b = \frac{1}{2}\rho f |U| U$ is acceptable for computing η and U which are not sensitive to τ_b in the region of the velocity measurements. However, this assumption is not accurate to predict the bottom shear stress.

The limitation of the one-dimensional numerical model indicates the necessity of a two-dimensional numerical model for predicting surf zone hydrodynamics and resulting sediment transport.

Chapter 8

SUMMARY AND CONCLUSIONS

This dissertation was developed with two concurrent themes. The first theme was to asses the applicability of theories developed for non-breaking waves and steady flows using measurements made of surf zone waves in a laboratory. The second theme was to analyze the data to provide useful empirical coefficients for nearshore hydrodynamic modeling. In the study of the bottom boundary layer, the first point was to show whether boundary layer theories developed for oscillatory flows can be applied for the boundary layer under breaking waves. The second point was to estimate the wave friction factor and bottom roughness in the surf zone. In the study of wave generated turbulence, the first point was to show whether the approximation of the local equilibrium of turbulence is a reasonable assumption for breaking waves. The second point was to estimate the mixing length coefficients and dissipation coefficients. Both of these themes were presented in the context of numerical modeling since it is desirable to have a time-dependent numerical model that can predict the nearshore hydrodynamics.

8.1 Summary

Chapter 1 surveyed some of the literature for boundary layer theories related to coastal dynamics and for wave generated turbulence. The review indicated

that much work has been done for wave and current boundary layers outside of the surf zone. There have been very few studies, however, of the boundary layer inside the surf zone; and there is no indication to what extent the theories developed under steady currents and non-breaking waves can be applied to the surf zone. For the case of wave generated turbulence, the review indicated that there have been many recent studies of the turbulent and wave motions inside the surf zone, resulting in some qualitative understanding. However, turbulence due to wave breaking is still a poorly understood subject.

Chapter 2 discussed the formulation of a two-dimensional, time-dependent numerical model for predicting the wave transformation and velocity profiles in the surf zone. The formulation included an analysis of the turbulent kinetic energy transport equation and the implementation of a simple turbulence model based on the mixing length concept. The intent of this chapter was to provide a theoretical context in which the experiments were performed.

Chapter 3 discussed the details of the experiment. The setup of the experiment included adding a physical bottom roughness layer to increase the boundary layer roughness and thickness. Using a two-component laser-Doppler velocimeter, velocity measurements were made at a fraction of the grain height above the bottom so that estimates could be made of the temporal variation of the bottom shear stress and bottom roughness under breaking waves. Several measuring lines were made in the cross-shore direction to include one vertical line seaward of the break point, one line at the breakpoint, one line in the transition region, and three lines in the inner surf zone. Additional velocity measurements were made in the bottom boundary layer to check the variability of the measurements due to irregularities of the bottom and to check the reliability of the method to estimate the bottom shear stress and bottom roughness.

Chapter 4 discussed the reduction of the data. Regular waves were used so that the turbulent signal could be extracted by phase-averaging. The temporal variation of the phase-averaged free surface elevations and statistics as well as the phase-averaged velocities and turbulent stresses were presented in a way that would be useful in evaluating cross-shore hydrodynamic models. The higher order statistics of skewness and kurtosis were discussed briefly in connection with a conditional sampling technique in the hope of detecting large eddies.

Chapter 5 discussed the bottom boundary layer analysis and the estimates of the bottom shear stress and bottom roughness. The logarithmic profile was shown to exist for the bottom boundary layers outside and inside the surf zone. The bottom shear velocity and bottom roughness were estimated using a logarithmic fit of the measured velocities in the bottom portion of the boundary layer. The confidence intervals and sensitivity of the estimates to irregularities in the bottom roughness were reported.

Chapter 6 discussed the wave generated turbulence in relation to the assumption of a local equilibrium of turbulence for wave breaking. Two empirical coefficients were involved in the simple turbulence model, and the temporal and spatial variations of these coefficients were determined. The validity of the local equilibrium assumption was evaluated using the calibrated coefficients and measured turbulent quantities.

In Chapter 7, comparisons were made between the measured data and a one-dimensional, time-dependent numerical model. The model's sensitivity to three input options was discussed. The limitations of the numerical model in predicting the temporal variation of the bottom shear stress were also discussed.

8.2 Conclusions

The main conclusions of this dissertation are as follows:

1. The experiment was successful in obtaining high quality data of the free surface elevations and fluid velocities outside and inside the surf zone, including detailed measurements of the bottom boundary layer. This data will be useful in evaluating cross-shore hydrodynamic models for the undertow and bottom boundary layer.

2. A logarithmic layer was found to exist in the bottom boundary layer for most of the phases over a wave period seaward of the break point and in the surf zone.

3. The least-squares method applied at each phase yielded estimates of the shear velocity and bottom roughness. This method was shown to give consistent results that were not affected by the local irregularities in the bottom roughness.

4. As a first approximation, the bottom roughness may be considered constant across the surf zone, and a simple relation based on the median grain diameter gives a reasonable approximation of the bottom roughness. As a second approximation, the bottom roughness appears to increase slightly with increasing distance shoreward in the surf zone. These conclusions are based on the fixed bed experiments and may not be valid for movable beds.

5. As a first approximation, the friction factor may be assumed constant across the surf zone if the detail of the bottom shear stress variation is not necessary.

6. As a second approximation, the friction factor varies across the surf zone. Jonsson's equation, based on linear wave theory, gives a fairly good estimate of

the measured wave friction factor base on the quadratic friction equation, but it appears to slightly overpredict the measured value in the inner surf zone

7. For the wave generated turbulence, the approximate local equilibrium of turbulence for spilling waves was shown to be a reasonable assumption.

8. Two coefficients of practical importance, the mixing length coefficient and the turbulent dissipation coefficient, were calibrated. The mixing length coefficient was shown to have a small temporal variation and that the assumption of a time-invariant mixing length coefficient was reasonable. The value of this coefficient was significantly different under non-breaking and breaking waves. The dissipation coefficient was shown to have significant vertical and cross-shore variations but a crude estimate was made which could be applied over much of the inner surf zone.

9. The calibrated coefficients were used to show that the eddy viscosity varied gradually over depth and was nearly time-invariant except near trough level with the passing of the turbulent bore.

10. In evaluating the numerical model, the model predicted the cross-shore variation of the wave profile reasonably well. The computed depth-averaged horizontal velocity represented the vertical profile of the measured horizontal velocity below the wave trough level reasonably well except in the transition region.

11. The computed vertical velocity estimated from the continuity equation represented the measured vertical velocity at least qualitatively except under the wave crest. The temporal variation of the bottom shear stress was predicted poorly because errors in the computed horizontal velocity were magnified in the computed bottom shear stress and because the friction factor is not really constant as assumed in the model.

8.3 Suggestions for Future Work

There are several considerations for future work. As was mentioned previously, this experiment considered only spilling waves. The importance of plunging versus spilling waves has been noted, and it would be interesting to study the effects of plunging waves on the bottom boundary layer. In addition, it would be of interest to focus more on the transition region, since this is one of the more difficult regions of the surf zone to model.

This experiment was conducted using a fixed bed. It would be of interest to study the bottom boundary layer with loose sand.

This experiment used only regular waves, and it would be useful to study the effects of irregular waves on the turbulent structure in the surf zone as well as the bottom boundary layer. Further, these waves were of normal incidence, and it would be of interest to study the turbulence induced by multi-directional waves in order to relate the findings of laboratory measurements with field observations.

The implementation of the simple turbulence model in a two-dimensional, time-dependent numerical model seems feasible. Such a model would be useful in providing the detailed hydrodynamics in the surf and swash zone for input to a model of cross-shore sediment transport.

REFERENCES

Adrian, R. J. (1991) "Particle-imaging techniques for experimental fluid mechanics." *Annu. Rev. Fluid Mech.*, 23, 261–304.

Adrian, R. J. (1983) "Laser velocimetry." In *Fluid Mechanics Measurements* ed. R. Goldstein, 155-244. Hemisphere Publishing Co., New York, NY.

ASCE Task Committee on Turbulence Models in Hydraulic Computations (1988) "Turbulence modeling of surface water flow and transport: Part I to V." *J. Hydraulic Engrg.*, ASCE, 114(9), 970–1073.

Bakker, W. T. and van Doorn, T. (1978) "Near-bottom velocities in waves with a current." *Proc. 16th Coast. Engrg. Conf.*, ASCE, 1394–1413.

Battjes, J. A. (1988) "Surf-zone dynamics." *Annu. Rev. Fluid Mech.*, 20, 257–293.

Battjes, J. A. and Janssen, J. P. F. M. (1978) "Energy-loss and set-up due to breaking of random waves." *Proc. 16th Coast. Engrg. Conf.*, ASCE, 569–587.

Battjes, J. A. and Sakai, T. (1981) "Velocity field in a steady breaker." *J. Fluid Mech.*, 111, 421-437.

Beach, R. A. and Sternberg, R. W. (1988) "Suspended sediment transport in the surf zone: Response to cross-shore infragravity motion." *Marine Geol.*, 80, 61–79.

Bendat, J. S. and Piersol, A. G. (1986) *Random Data: Analysis and Measurement Procedures*, John Wiley and Sons, New York, NY.

Benjamin, J. R and Cornell, C. A, (1970) *Probability, Statistics, and Decision for Civil Engineers*, McGraw-Hill, New York, NY.

Cox, D. T. (1989) "Irregular wave runup and reflection on rough, permeable slopes." M.C.E. Thesis, University of Delaware, Newark, Del.

Cox, D. T., Kobayashi, N. and Kriebel, D. L. (1994a) "Numerical model verification using SUPERTANK data in surf and swash zones." *Proc. Coast. Dynamics*, ASCE, 248–262.

Cox, D. T., Kobayashi, N. and Okayasu, A. (1994b) "Vertical variations of fluid velocities and shear stress in surf zones." *Proc. 24th Coast. Engrg. Conf.*, ASCE, (in press).

Cox, D. T., Kobayashi, N. and Okayasu, A. (1994c) 'Bottom shear stress in the surf zone." submitted to *J. Geophys. Res.*

Dantec Electronik (1991) *BURSTware User's Guide*, Dantec Electronik, Skovlunde, Denmark.

Deigaard, R., BroMikkelsen, M. and Fredsøe, J. (1992) "Measurements of the bed shear stress in a surf zone." *Progress Report 73*, Tech. Univ. Denmark, 21–30.

Deigaard, R., Fredsøe, J. and Hedegaard, I. B. (1986) "Suspended sediment in the surf zone." *J. Wtrway. Port Coast. and Oc. Engrg.*, ASCE, 112(1), 115–127.

Deigaard, R., Justesen, P. and Fredsøe, J. (1991) "Modelling of undertow by a one-equation turbulence model." *Coast. Engrg.*, 15, 431–458.

Fletcher, C. A. J. (1991) *Computational Techniques for Fluid Dynamics, Volume I*, Springer-Verlag, New York, NY.

Flick, R. E. and George, R. A. (1990) "Turbulence scales in the surf and swash." *Proc. 22nd Coast. Engrg. Conf.*, ASCE, 557–569.

Flick, R. E., Guza, R. T. and Inman D. L. (1981) "Elevation and velocity measurements of laboratory shoaling waves." *J. Geophys. Res.*, 86 (C5), 4149–4160.

Fredsøe, J. and Deigaard, R. (1992) *Mechanics of Coastal Sediment Transport*, Advanced Series on Ocean Engineering, Vol. 3, World Scientific, New Jersey.

George, R. A., Flick, R. E. and Guza, R. T. (1994) "Observations of turbulence in the surf zone." *J. Geophys. Res.*, 99(C1), 801–810.

Grant, W. D. and Madsen, O. S. (1979) "Combined wave and current interation with a rough bottom." *J. Geophys. Res.*, 84(C4), 1797–1808.

Grant, W. D. and Madsen, O. S. (1986) "The continental shelf bottom boundary layer." *Annu. Rev. Fluid Mech.*, 18, 265–305.

Grant, W. D., Williams, A. J. and Glenn, S. M. (1984) "Bottom stress estimates and their prediction on the Northern California continental shelf during CODE-1: The importance of wave-current interactions" *J. Phys. Ocean.*, 15, 1219–1228.

Grant, W. D., Williams, A. J., Glenn, S.M., Cacchione, D. A. and Drake, D. E. (1983) "High frequency bottom stress variability and its prediction in the CODE region." *Woods Hole Oceanog. Inst. Tech. Rept. WHOI-83-19*, Woods Hole, Mass.

Hanes, D. M. and Bowen, A. J. (1985) "A granular-fluid model for steady intense bed-load transport." *J. Geophys. Res.*, 90(C5), 9149–9158.

Hattori, M. and Aono T. (1985) "Experimental study on turbulence structures under spilling waves." in *The Ocean Surface*, ed. Y. Toba and H. Mitsuyasu, 419–424, D. Reidel, Hingam, Mass.

Hedegaard, I. B., Roelvink, J. A., Southgate, H., Pechon, P., Nicholson, J. and Hamm, L. (1992) "Intercomparison of coastal profile models." *Proc. 23rd Coast. Engrg. Conf.*, ASCE, 2108–2121.

Holman, R. A., Bowen, A. J., Dalrymple, R. A., Dean, R. G., Elgar, S., Flick, R., Freilich, M., Guza, R. T., Hanes, D., Kirby, J., Madsen, O., Sternberg, R. and Svendsen, I. A (1990) "Report on the state of nearshore processes research." Report from the Nearshore Processes Workshop, St. Petersburg, FL, April 1989, Rpt. OSU-CO-90-6, Oregon State University, Corvallis, Oregon.

Horikawa, K. (1981) "Coastal sediment processes." *Annu. Rev. Fluid Mech.*, 13, 9–32.

Huntley, D. A. and Hazen D. G. (1988) "Seabed stress in combined wave and steady flow conditions on the Nova Scotia continental shelf: Field measurements and predictions." *J. Phys. Ocean.*, 18, 347–362.

Jackson, P. S. (1981) "On the displacement height in the logarithmic velocity profile." *J. Fluid Mech.*, 111, 15–25.

Jensen, B. L., Sumer, B. M. and Fredsøe, J. (1989) "Turbulent oscillatory boundary layers at high Reynolds numbers." *J. Fluid Mech.*, 206, 265–297.

Jonsson, I. G. (1966) "Wave boundary layers and friction factors." *Proc. 10th Coast. Engrg. Conf.*, ASCE, 127–148.

Jonsson, I. G. and Carlsen, N. A. (1976) "Experimental and theoretical investigations in an oscillatory turbulent boundary layer." *J. Hydraul. Res.*, 14, 45–60.

Kamphuis, J. W. (1975) "Friction factor under oscillatory waves." *J. Wtrway. Harbors Coast. Engrg.*, ASCE, 101(2), 135–144.

Klopman, G. (1994) "Vertical structure of the flow due to waves and currents." *Progress Report H 840.30, Part II*, Delft Hydraulics, The Netherlands.

Kobayashi, N. (1988) "Review of wave transformation and cross-shore sediment transport processes in surf zones." *J. Coast. Res.*, 4(3), 435–445.

Kobayashi, N., Otta, A. K. and Roy, I. (1987) "Wave reflection and runup on rough slopes." *J. Wtrway. Port Coast. and Oc. Engrg.*, ASCE, 113(3), 282–298.

Kobayashi, N., DeSilva, G. S. and Watson, K. D. (1989) "Wave transformation and swash oscillation on gentle and steep slopes." *J. Geophys. Res.*, 94(C1), 951–966.

Kobayashi, N. and Poff, M. T. (1994) "Numerical model RBREAK2 for random waves on impermeable coastal structures and beaches." *Research Report No. CACR-94-12*, Center for Applied Coastal Research, University of Delaware, Newark, Del.

Kobayashi, N. and Wurjanto, A. (1992) "Irregular wave setup and run-up on beaches." *J. Wtrway. Port Coast. and Oc. Engrg.*, ASCE, 118(4), 368–386.

Komar, P. D. and Holman, R. A. (1986) "Coastal processes and the development of shoreline erosion." *Annu. Rev. Earth Planet. Sci.*, 14, 237–265.

Launder, B. E. and Spalding, D. B. (1972) *Mathematical Models of Turbulence*, Academic Press, New York, NY.

Lin, J. C. and Rockwell, D. (1994) "Instantaneous structure of a breaking wave." *Phys. Fluids*, 6(9), 2877–2879.

Madsen, O. S. (1994) "Spectral wave-current bottom boundary layer flows." *Proc. 24th Coast. Engrg. Conf.*, ASCE, (in press).

Madsen, O. S., Wright, D. L., Boon, J. D. and Chisholm, T. A. (1993) "Wind stress, bed roughness and sediment suspension on the inner shelf during an extreme storm event." *Cont. Shelf Res.*, 13(11), 1303–1324.

Nadaoka, K. and Kondoh, T. (1982) "Laboratory measurements of velocity field structure in the surf zone by LDV." *Coast. Engrg. in Japan*, 25, 125–145.

Nadaoka, K., Hino, M. and Kayano, Y. (1989) "Structure of the turbulent flow field under breaking waves in the surf zone." *J. Fluid Mech.*, 204, 359–387.

Nadaoka, K., Ueno, S. and Igarashi, T. (1988) "Sediment suspension due to large scale eddies in the surf zone." *Proc. 21st Coast. Engrg. Conf.*, ASCE, 1646–1660.

Nairn, R. B., Roelvink, J. A. and Southgate, H. (1990) "Transition zone width and implications for modelling surfzone hydrodynamics." *Proc. 22nd Coast. Engrg. Conf.*, ASCE, 68–81.

Okayasu, A., and Cox, D. T. (1995) "Laboratory study on turbulent velocity field in the surf zone over a rough bed." *Coast. Engrg. in Japan*, (in preparation).

Okayasu, A., Shibayama, T. and Horikawa, K. (1988) "Vertical variation of undertow in the surf zone." *Proc. 21st Coast. Engrg. Conf.*, ASCE, 478–491.

Okayasu, A., Shibayama, T. and Mimura, N. (1986) "Velocity field under plunging waves." *Proc. 20th Coast. Engrg. Conf.*, ASCE, 660–674.

Peregrine, D. H. (1983) "Breaking waves on beaches." *Annu. Rev. Fluid Mech.*, 15, 149–178.

Peregrine and Svendsen (1978) "Spilling breakers, bores and hydraulic jumps." *Proc. 16th Coast. Engrg. Conf.*, ASCE, 540–551.

Petit, H. A. H., Tönjes, P., van Gent, M. R. A. and van den Bosch, P. (1994) "Numerical simulation and validation of plunging breakers using a 2D Navier-Stokes model." *Proc. 24th Coast. Engrg. Conf.*, ASCE, (in press).

Press, W. H., Flannery, B. P., Teukolsky, S. A. and Vetterling, W. T. (1989) *Numerical Recipes: The Art of Scientific Computing (FORTRAN Version).* Cambridge University Press, New York, NY.

Raubenheimer, B., Guza, R. T., Elgar, S. and Kobayashi, N. "Swash on gently sloping beach." *J. Geophys. Res.*, (in press).

Rodi, W. (1980) *Turbulence Models and Their Application in Hydraulics.* Int'l. Assoc. for Hydraul. Res., Delft, The Netherlands.

Sakai, T., Inada, Y. and Sandanbata, I. (1982) "Turbulence generated by wave breaking on beach." *Proc. 18th Coast. Engrg. Conf.*, ASCE, 3–21.

Sakai, T., Mizutani, T., Tanaka, H. and Tada, Y. (1986) "Vortex formation in plunging breaker." *Proc. 20th Coast. Engrg. Conf.*, ASCE, 711–723.

Sakai, T., Sandanbata, I. and Uchida, M. (1984) "Reynolds stress in surf zone." *Proc. 19th Coast. Engrg. Conf.*, ASCE, 42–53.

Schäffer, H. A., Deigaard, R. and Madsen, P. (1992) "A two-dimensional surf zone model based on the Boussinesq equations." *Proc. 23rd Coast. Engrg. Conf.*, ASCE, 576–589.

Simons, R. R., Grass, T. J. and Mansour-Tehrani, M. (1992) "Bottom shear stresses in the boundary layers under waves and currents crossing at right angles." *Proc. 23rd Coast. Engrg. Conf.*, ASCE, 604–617.

Simons, R. R., Grass, T. J., Saleh, W. M. and Mansour-Tehrani, M. (1994) "Bottom shear stresses under random waves with a current superimposed." *Proc. 24th Coast. Engrg. Conf.*, ASCE, (in press).

Sleath, J. F. A. (1987) "Turbulent oscillatory flow over rough beds." *J. Fluid Mech.*, 182, 369–409.

Soulsby, R. L, Hamm, L., Klopman, G., Myrhaug, D., Simons, R. R. and Thomas, G. P. (1993) "Wave-current interaction within and outside the bottom boundary layer." *Coast. Engrg.*, 21, 41-69.

Stive, M. J. F. (1980) "Velocity and pressure field of spilling breakers." *Proc. 17th Coast. Engrg. Conf.*, ASCE, 547–566.

Stive, M. J. F. and De Vriend, H. J. (1994) "Shear stresses and mean flow in shoaling and breaking waves." *Proc. 24rd Coast. Engrg. Conf.*, ASCE, (in press).

Soulsby, R. L, Hamm, L., Klopman, G., Myrhaug, D., Simons, R. R. and Thomas, G. P. (1993) "Wave-current interaction within and outside the bottom boundary layer." *Coast. Engrg.*, 21, 41-69.

Svendsen, I. A. (1987) "Analysis of surf zone turbulence." *J. Geophys. Res.*, 92(C5), 5115–5124.

Svendsen, I. A., Schäffer, H. A. and Hansen J. B. (1987) "The interaction between the undertow and the boundary layer flow on a beach." *J. Geophys. Res.*, 92(C11), 11845–11856.

Svendsen, I. A., Madsen, P. A. and Hansen, B. J. (1978) "Wave characteristics in the surfzone." *Proc. 16th Coast. Engrg. Conf.*, ASCE, 540–551.

Tennekes, H. and Lumley, J. L. (1972) *A First Course in Turbulence*, MIT Press, Cambridge, Mass.

Thornton, E. B. (1979) "Energetics of breaking waves within the surf zone." *J. Geophys. Res.*, 84(C8), 4931–4938.

Thornton, E. B. and Guza, R. T. (1983) "Transformation of wave height distribution." *J. Geophys. Res.*, 88(C10), 5925–5938.

Ting, F. C. K. and Kirby, J. T. (1994) "Observation of undertow and turbulence in a laboratory surf zone." *Coast. Engrg.*, 24, 51-81.

Trowbridge, J. and Madsen, O. S. (1984a) "Turbulent wave boundary layers 1. Model formulation and first-order solution." *J. Geophys. Res.*, 89(C5), 7989–7997.

Trowbridge, J. and Madsen, O. S. (1984b) "Turbulent wave boundary layers 2. Second-order theory and mass transport." *J. Geophys. Res.*, 89(C5), 7999–8007.

Trowbridge, J. and Young, D. (1989) "Sand transport by unbroken water waves under sheet flow conditions." *J. Geophys. Res.*, 94(C8), 10971–10991.

Visual Numerics (1991), *IMSL MATH/LIBRARY User's Manual, Version 2.0*, Houston, Texas.

Wei, G., Kirby, J. T. and Mase, H. (1995) "Implementation of eddy viscosity models in a time-domain Boussinesq wave model." *Proc. 10th Engineering Mechanics Conference*, (in press).

Yaglom, A. M. (1979) "Similarity laws for constant-pressure and pressure-gradient turbulent wall flows." *Annu. Rev. Fluid Mech.*, 11, 505–540.